PHOTO-INITIATED HALIDE RELEASE AND OXIDATION

Michael Davis Turlington

A dissertation submitted to the faculty at the University of North Carolina at Chapel Hill in partial fulfillment of the requirements for the degree of Doctor of Philosophy in the Department of Chemistry.

Chapel Hill
2021

Approved by:

Gerald Meyer

Michel Gagne

Jillian Dempsey

Marcey Waters

David Lawrence

ABSTRACT

Michael Davis Turlington: Photo-Initiated Halide Release and Oxidation
(Under the direction of Gerald J. Meyer)

The ability to control interactions between halides and molecular excited states is of importance in the fields of halide sensing and energy storage. The tools of supramolecular assembly provide a means for fundamental study, as ground-state preorganization precludes the need for diffusion of the short-lived excited states. This dissertation seeks to gain insight into how these assemblies respond to light excitation and to utilize these interactions for energy storage reactions. Towards this end, Chapter 1 briefly reviews strategies that have been developed for halide supramolecular assembly and halide oxidation.

In Chapters 2 and 3, ruthenium polypyridyl complexes with hydrogen-bonding ligands that controlled the stoichiometry and thermodynamics of ground-state halide supramolecular assembly are presented. In Chapter 2, ancillary ligands are shown to induce an excited-state dipole that was oriented toward or away from the assembled halide. When the excited-state dipole was directed towards the halide, coulombic repulsion resulted in its photorelease. Orientation of the excited-state dipole away from the receptor ligand resulted in enhanced halide assembly. In Chapter 3, modifying the hydrogen bonding functional groups was found to tune the ground-state equilibrium constants over two orders of magnitude. In the excited-state, analysis of the photorelease kinetics suggested that the extent of hydrogen bonding with the halide presented a barrier to dissociation.

In Chapter 4, ruthenium complexes with a novel hydrogen-bonding ligand formed 1:2 ruthenium:halide assemblies in organic solution. The excited-state reduction potentials ($Ru^{2+*/+}$)

were tuned by varying the electronic properties of the ancillary ligands. For the most potent photo-oxidant, the luminescent excited-state was statically and dynamically quenched by iodide. Both the static and dynamic components were sensitive to the iodide concentration, suggesting that the supramolecular assembly structure impacted the quenching mechanism.

In Chapter 5, photocatalytic bromide oxidation at a metal-oxide interface in pH 5.6 aqueous electrolyte is investigated. To promote bromide oxidation under these challenging conditions, a dual-sensitizer photoanode was developed that coupled efficient electron injection and bromide oxidation by utilizing a separate reductant and oxidant as sensitizers. A reductive quenching reaction was identified as the primary energy loss pathway in the cell, but the yield was reduced through anode design.

To my life group, my family, and my wife Madeline.
For fueling me in graduate school, particularly with a lot of good food.

ACKNOWLEDGEMENTS

When I arrived in Chapel Hill five years ago, I little thought that my time here would start with a national championship (UNC men's basketball, 2017) and end with a retirement celebration for Hall of Fame coach Roy Williams (2021). Like my favorite basketball team, there have been highs and lows over the past five years, but as I look back on my graduate career, I am especially thankful for the many people that have been with me every step of the way.

To begin, I would like to thank my lab mates. Not only have you set the tone for my graduate school experience, but you also made the day-to-day work in lab both satisfying and fun. I have been inspired by the hard work and dedication that each of you have put into your research. To Ludo, Renato, Jenny, Bruno, Matt K., Evan, Brian, Tim, Wes, Tyler, Eric, Andrew, Andressa, Matt B., Sara, Erica, Tori, Rachel, Yuting, Zander, Daniel, Quentin, Erin, Tashii, Jake, and John, thank you.

To my advisor, Jerry Meyer, thank you for your guidance throughout graduate school and for investing in me as a chemist. You have challenged me to learn and grow, for which I am thankful. I have also been inspired by your commitment to promoting a close-knit group. During the last year, lockdowns and social distancing have made that goal extremely difficult, but I am thankful for the ways that you continued to reach out with ideas for group get-togethers, both virtual and in person.

To my friends and mentors from Furman who continued to encourage me in chemistry, Paul Wagenknecht and Jared Pienkos, thank you.

To my church life group, thank you for Tuesday night discussions, dinners, desserts, and (your choice of a word to complete the alliteration here). Over the past five years, you have providing a space to get away from the daily grind, refocus, and find the source of strength for each day. You have been a wonderful family to me here in Chapel Hill, and I will miss you all.

To the kids that I've taught in Sunday School, thank you for paying attention during the lessons (mostly), wearing me out on the playground with tag, and always surprising me with your understanding of the Bible and Jesus. You have pushed me to better understand what I tried to teach to you. I will continue to pray for you.

To my (rapidly growing) family, I can't begin to thank you for everything. Heidi, Mark, Emily, Chris, Hannah, Chelsea, Alex, and Amy, y'all are the best! Mom and Dad, I love you a lot! To my niece and nephews, stop growing up so quickly!

To my wife Madeline, I'm glad you picked UNC for graduate school too! From our Maple View dates, to completing two proposals in one day (the third year proposal and popping the question), to our wedding, and now almost two years into being married, I can't imagine a more supportive and loving wife. I love you!

TABLE OF CONTENTS

LIST OF FIGURES

LIST OF TABLES

LIST OF SCHEMES

CHAPTER 1: SALT AND LIGHT: HALIDE PHOTOCHEMISTRY

"You are the salt of the earth… You are the light of the world." Matthew 5:13-14

1.1 Halides in Chemistry and Biology

The fresh, salty sent of the sea breeze; the taste of a favorite salty snack (for me, pretzels); the feel of sweat and exhaustion at the end of a hard day's work in the tomato field, a grueling tennis match, or a long triathlon (for some reason called a sprint); these scenes all serve as reminders of the importance of halides in day-to-day life. Halides, commonly encountered in the form of salts, are ubiquitous in the world around us, and in fact play a more significant role in our life that just making green beans edible for young children.

The abundance of the halides (fluoride, chloride, bromide, and iodide) has resulted in their incorporation into numerous roles in biology and the life sciences. Fluoride, for instance, is known to benefit dental health, and has therefore been added to drinking water and toothpaste.[1] However, prolonged exposure to large concentrations of this halide can have unintended and adverse effects on the teeth and bones.[2] The intake of chloride is also necessary for the overall health of the body. However, misregulation of chloride ion transport across cell membranes results in cystic fibrosis for some ~70,000 individuals worldwide.[3] The removal of chloride from seawater (desalination) is also an important goal for providing clean water to the world's population, as saltwater makes up over 97% of the earth's water supply.[4] These few examples provide a glimpse into the important roles of halides in biology and the life sciences.

Humans, and not just nature, have found many uses for the abundant halides. For instance, in much of the twentieth century, silver halides were extensively used in photography as the light-

sensitive agent in photographic films. To capture an image, the absorption of photons by the photosensitive silver halide resulted in the formation of metallic silver, yielding a latent image that could then be magnified.[5,6] Halide photoredox chemistry has also been impactful in a variety of solar energy schemes for fuel generation. For instance, in response to the energy crisis in the 1980s, Texas Instruments was developing photoelectrochemical hydrobromic acid splitting cells for fuel storage.[7,8] Ultimately, the storage of the photoproducts, H_2 and Br_2, which would allow for electric power generation when the sun was down, presented a number of economic and environmental concerns that precluded the early prototypes from being brought to market.

In both the natural processes and manmade technologies that utilize halides, fundamental work investigating the interactions and reactivity of halide species is of importance. The use of visible light as a probe is particularly appealing, as light provides a sensitive and selective means for halide sensing, and can also act as an energy input that promotes electron-transfer and bond forming reactions. To couple visible light absorption with halide sensing/ chemistry, it is necessary to develop sensitizers with excited states that interact with halides. Towards this end, this dissertation seeks to better understand interactions between halides and transition metal excited states, thereby providing control over excited-state halide assembly and reactivity. In section 1.2 and 1.3, strategies for halide assembly and photorelease are presented, with a particular emphasis on halide sensing with visible light. Section 1.4 discusses some of the current strategies that couple light absorption with halide chemistry, and their applications toward energy storage. Section 1.5 briefly outlines the ground- and excited-state properties of the ruthenium polypyridyl complexes that are utilized in this dissertation to couple light absorption with halide release and oxidation.

1.1.1 Abundance

The natural abundance of halogen species such as fluoride, chloride, bromide and iodide makes their ubiquity in chemistry, biology and the life sciences unsurprising. However, practical applications need to account for the fact that the natural abundance of halogen species decreases significantly as the atomic number increases. The halides discussed in this thesis are predominately chloride, bromide, and iodide, as they are both abundant and have properties suitable for the applications described herein. Fluoride, although the most abundant halogen, is difficult to oxidize and its characterization is often complicated by acid-base chemistry, while astatine is unstable.

Chlorine is most commonly present in the form of sodium chloride and represents the 20th most abundant element in the Earth's crust, at 126 ppm.[9] Chloride is found in significantly higher concentrations in seawater, comprising over 1.9% of seawater by weight. Seawater is reported to make up 97% of the Earth's water supply.[10]

Bromine is the 46th most abundant element in the Earth's crust, comprising 2.5 ppm as bromide salts, and, like chlorine, is also more abundant in seawater, making up 65 ppm. This corresponds to a ratio of approximately one bromide for every 660 chloride ions in seawater. Higher bromide concentrations are observed in salt lakes, where bromide is typically extracted.[11] Significant quantities of bromide are extracted from the Dead Sea in particular, where concentrations of bromide ions are as high as 0.4%. Bromine is industrially isolated from seawater by first acidifying seawater and reacting it with chlorine to generate bromine. The bromine is then reacted with soda ash to produce a solution of sodium bromide and bromate. This solution is separated and then treated with sulfuric acid to liberate bromine, which is heated, collected as a vapor, and then condensed as pure liquid bromine.[12]

Iodine, the 61st most abundant element, is the least common of the stable halogens and comprises 0.46 ppm in the Earth's crust. Iodine is commonly found in the form of iodate minerals. The caliche nitrate beds of Chile contain up to 1% iodine by weight and are among the leading sources of iodine. Additionally, natural brine wells in the Chiba area of Japan were discovered to contain up to 100 ppm concentrations of iodine. Seawater contains concentrations of only 0.05 ppm, which is too low for commercial recovery. The lower concentrations observed in seawater versus the Earth's crust are attributed to the biophilic nature of iodine.[13] Thus, the natural brine wells in the Chiba area and the caliche nitrate beds allow Japan and Chile to be the leading commercial sources of iodine.[14]

1.2 Halide Supramolecular Assembly

The importance of halides in the life sciences has necessitated the ability to detect these ions in fluid solution.[15,16] This need spurred a growing interest in halide sensing, but challenges intrinsically linked with anion binding slowed initial progress in the field, especially in comparison to cation sensing. To highlight this contrast, in 1987, when rigorous strategies for halide assembly were beginning to be developed, the Nobel Prize in chemistry was awarded to Cram, Lehn, and Pederson for the development of crown ethers that selectively interacted with Lewis acidic alkali and alkaline earth cations of a specific size and charge.[17] To accomplish the same level of selectivity with halides, it is necessary to account for several precluding factors. Halides, which are larger than their isoelectronic cations, have a smaller charge-to-size ratio that reduces the magnitude of electrostatic interactions. In addition, the solvation energy of halides is typically quite favorable, and these solvent interactions must be overcome for a receptor and a halide to form an assembly. As halide assembly strategies have been developed that overcome these

limitations, the field has grown by leaps and bounds, and now is utilized in many areas of chemistry.

1.2.1 Electrostatic Interactions

Halide receptors have been designed that make use of electrostatic interactions between the positively charged host and the negative halide anion. These interactions have been utilized in work as early as the 1980s to promote halide complexation in even polar solvents like water. For example, the macrocyclic host containing four quaternary ammonium groups (Figure 1.1) was found to assemble with anions such as chloride, bromide, iodide, and *p*-nitrophenolate.[18,19]

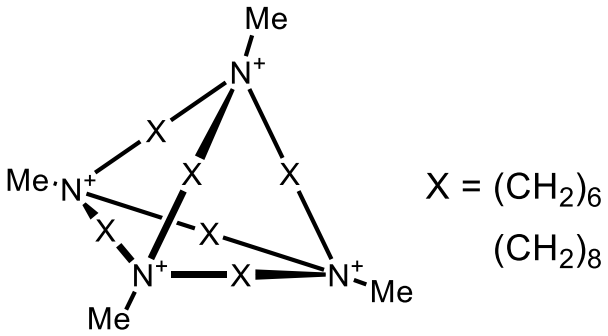

Figure 1.1: Quaternary ammonium complexes for anion assembly.

The size of the internal cavity could be tuned to promote selective association with anions of different sizes. One downside of this method is that a cationic host necessarily is associated with an anion prior to assembly with the desired halide. This counter ion can compete with the halide for the binding site, thereby decreasing the yeild of the desired halide assembly.

1.2.2 Hydrogen Bonding

Hydrogen-bonding interactions are particularly appealing in promoting anion assembly. In general chemistry texts, hydrogen bonding is defined as a noncovalent interaction between a nucleophile and a polarized (δ+) hydrogen atom that is covalently bonded to an electronegative nitrogen, oxygen, or fluorine atom. The δ+ charge on the polarized hydrogen atom facilitates the

noncovalent interaction with the lone pair of electrons on the nucleophile. One important aspect of these hydrogen bonds is that they are directional, unlike the previously discussed electrostatic interactions. This allows greater control when designing receptors that are selective for specific anions. In practice, functional groups like amides, ureas, and alcohols are known to be adept at promoting supramolecular assembly through hydrogen-bonding interactions.

Although general chemistry textbooks tend to restrict hydrogen-bonding to functional groups with N-H, O-H, and F-H bonds, the IUPAC has adopted a broader definition[20] that encompasses any "attractive interaction between a hydrogen atom from a molecule or a molecular fragment X–H in which X is more electronegative than H, and an atom or a group of atoms in the same or a different molecule, in which there is evidence of bond formation." Recent work by Flood et al. has shown that carbon-hydrogen bonds, when highly polarized and incorporated into rigid macrocycles, efficiently promote hydrogen-bonding interactions with halides. For example, the macrocycle shown in Figure 1.2, left, containing four triazol groups forms an assembly with chloride with an equilibrium constant of 1.3×10^5 M^{-1} in CH_2Cl_2, even though only "weak" C-H hydrogen bonds are present to stabilize the halide.[21] A related cryptand-like triazole cage (Figure 1.2, right) facilitated such strong chloride binding, 10^{17} M^{-1} in CH_2Cl_2, that this halide could be extracted from water into CH_2Cl_2.[22]

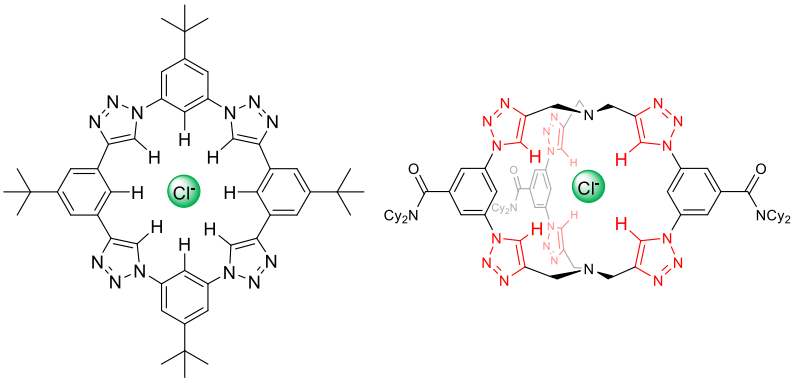

Figure 1.2: Macrocyclic C-H hydrogen-bonding halide receptors developed by Flood et al.

1.2.3 Halogen Bonding

Halogen bonding is a strategy that makes use of polarizable halogen atoms to supramolecular assembly. In molecules with covalent carbon-halogen bonds, electrons in the filled p_z orbital contribute to a σ-bond with the carbon atom, while the electrons in the filled p_x and p_y orbitals form a belt of negative charge around the halide perpendicular to the carbon-halogen bond. This polarization of the halogen results in a σ-hole, or δ+ charge directly opposite the carbon-halogen bond that can interact with halides (Figure 1.3).[23–25]

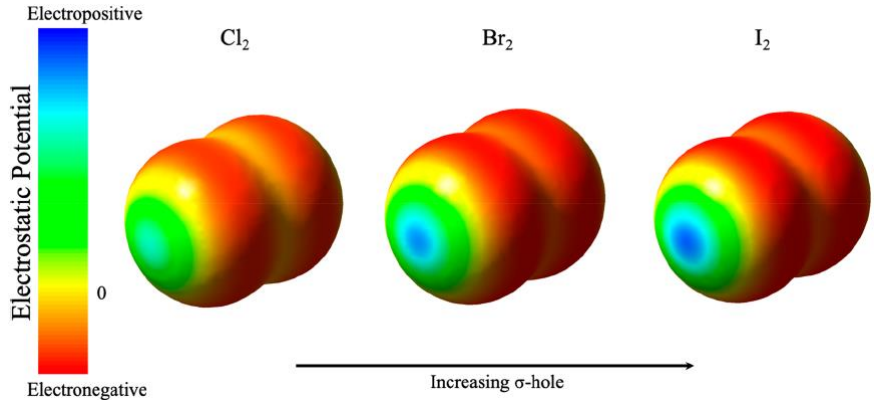

Figure 1.3: Electrostatic potential surfaces mapped onto total electron density for the X_2 species. The electropositive σ-hole increases with the polarizability of the halogen.

The σ-hole increases with the principle quantum number of the halogen, and electron withdrawing groups can further polarize the bond and enhance halogen-bonding interactions. An example of a halogen bond donor is shown in Figure 1.4, which binds chloride and bromide with equilibrium constants of $10^5 – 10^6$ M^{-1} in CH_3CN and CH_2Cl_2, values that are comparable with those obtained with hydrogen bonding hosts.[26]

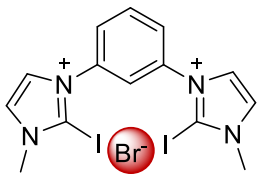

Figure 1.4: Halogen-bonding bis-(iodoimidazolium) compounds for halide assembly.

1.2.2 Applications

The tools required for halide assembly have been optimized to such an extent that a variety of applications have made use of this technique. Beer et al. have used halides as a template to form mechanically interlocked molecules, providing new synthetic routes to these challenging macrocycles.[27,28] Jacobsen et al. have utilized fluoride and chloride association to efficiently catalyze a number of enantioselective reactions, and the methodology has been applied to challenges in total synthesis.[29–32] Strategies that promote halide transport across membranes have also made use of supramolecular assembly.[33–38]

Halide sensing, an application of particular interest in this dissertation, has been a prominent goal in the field,[15] and numerous sensors have been developed that can detect the presence of halides in low concentrations in a range of polar, non-polar, and protic solvents. Many of these sensors report on the presence of halide by producing a measurable electrochemical or optical response upon halide assembly.

Molecular electrochemical sensors report on halide assembly when a change in the reduction potential of the sensor is observed. A representative example is the series of cobaltacene complexes (Figure 1.5), that experienced cathodic shifts of 30 and 85 mV in acetonitrile solutions containing chloride.[39] The electrochemical response was proposed to be a result of chloride assembly, which stabilized the cobaltacene and made it more difficult to reduce. This method allows for some discernment in sensing different anions, as anions that selectively bind with the sensor tend to produce a larger change in the reduction potential.

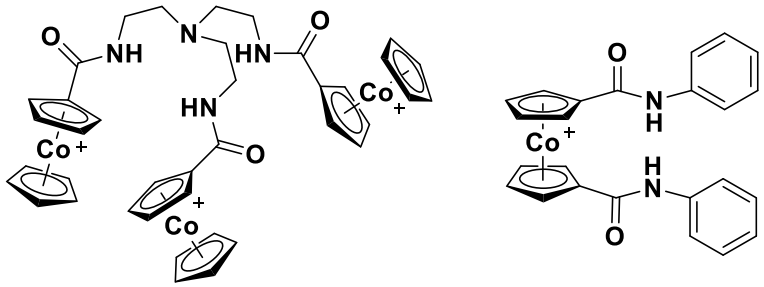

Figure 1.5: Electrochemical cobaltacene sensors for anion detection in organic solvents.

Optical sensors that report on halides with a photoluminescent response are also particularly useful, as this detection method is extremely sensitive. Sensors can be designed such that halide assembly results in enhancement of the luminescence or excited-state quenching, behaviors that have been called "turn-on" and "turn-off" sensing, respectively. The well-studied photophysical properties of ruthenium(II) polypyridyl type complexes make derivatives of these systems well suited for anion sensing using photoluminescence (PL) techniques.[15] Many ruthenium complexes which contain anion receptor sites act as "turn-on" sensors, as they emit more brightly (up to 500%) upon anion binding.[40] A less sensitive technique for anion sensing, that allows for anion detection by eye, takes advantage of anion induced color changes and is called colorimetric sensing. An example of a colorimetric sensor is shown in Figure 1.6, which turns from yellow to purple upon the addition of fluoride.[41] Typically, these color changes are caused by chemical reactions with the sensor, and are often ascribed to the acid-base chemistry of the more basic fluoride anion.

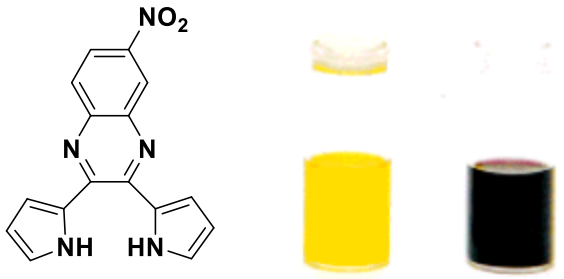

Figure 1.6: Colorimetric dipyrrolylquinoxaline sensor that turns dark purple in the presence of fluoride.

1.3 Halide Release

Although strategies for promoting halide assembly have rapidly advanced in recent years, the reverse process, namely halide release, has been largely overlooked. Understanding the factors that lead to controlled release is important for applications that seek to make use of this concept. In photoactivated therapy for example, the development of nontoxic prodrugs that release an active drug upon light irradiation is envisioned to provide precise temporal and spatial resolution of drug delivery.[42]

To date, halide photorelease is limited to a handful of strategies that include the photoaquation of transition-metal complexes with a halide ligand[43–47] (discussed in Chapter 2, Introduction) and photoisomerization of halide receptors,[48–50] thereby blocking access to the binding site or changing the structure to such an extent that halide binding is not as favorable. Photoaquation typically leads to irreversible halide release, as rebinding of the halide ligand does not occur when the external stimulus is removed. Photoisomerization[48] (Figure 1.7) tends to require high energy ultraviolet light, and an equilibrium between the *cis*- and *trans*- isomers is often observed that leads to incomplete halide release. However, the halide release is reversible, as irradiation with a second wavelength regenerates the host and reverses the equilibrium so that halide assembly is favored.

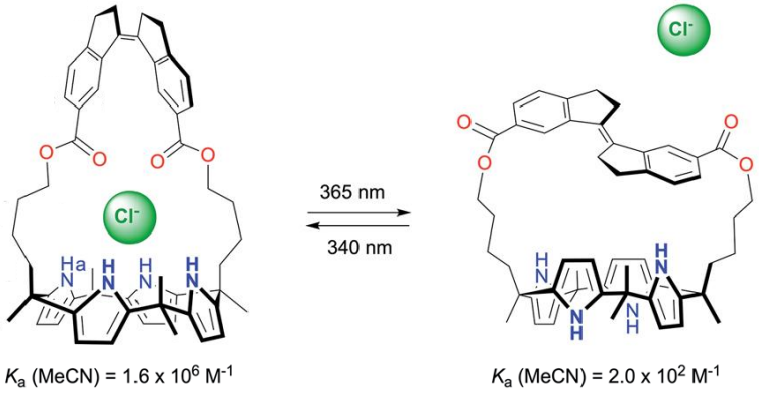

Figure 1.7: Photoswitchable calix[4]pyrrole for halide binding and release.

Completely reversible photorelease mechanisms, which are of particular relevance to this thesis, are known in the cation photorelease literature. For example, pulsed-laser excitation of a rhenium bipyridine complex (Figure 1.8) bearing an azacrown ether in conjugation with the metal center results in cation release on the ns time scale, with subsequent rebinding occurring in about a μs.[51–55] Upon MLCT excitation (Re to bpy), the nitrogen in the azacrown ether contributes significant charge density to the rhenium metal center, which thereby weakens the interaction with the assembled cation. The general strategy of using light to lower the energy barrier for ion release, while also providing an energy input to overcome this barrier, should be generalizable and applicable to halide release. These ideas will be probed more fully in chapters 2 and 3 of this dissertation.

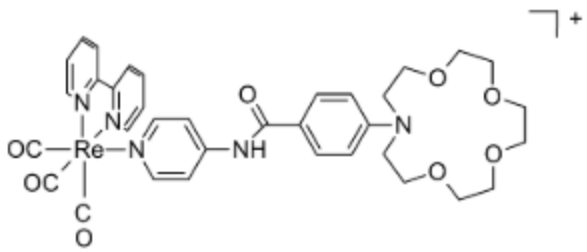

Figure 1.8: Rhenium bipyridine complex for reversible Lewis-acidic cation release.

1.4 Halide Oxidation for Energy Storage

Hydrohalic acid splitting is of great interest for solar hydrogen fuel production. As compared to water splitting, which is a complicated four-electron process that involves multiple proton-coupled electron transfer steps, HX splitting is mechanistically simpler. Halides (X^-) are oxidized to X_2 by a two-electron transfer process that does not involve proton-coupled electron transfers. Hydrohalic acid splitting is the thermodynamically uphill conversion of hydrohalic acid (HX) to yield hydrogen gas (H_2) and the halogen (X_2). The reverse reaction releases free energy, and hence H_2 and X_2 can be stored as solar fuels. In the literature, two main strategies have been implemented to accomplish HX splitting. In Section 1.4.1, homogeneous HX splitting with transition metal and main group catalysts is discussed. In Section 1.4.2, dye-sensitization, an approach commonly used for solar cells, is first described, and then the relevance of this approach to HX splitting is described.

1.4.1 Halide Oxidation Through X_2 Elimination

1.4.1.1 Dirhodium HX Splitting Catalysts

Halide oxidation has been accomplished by the Nocera group in their pioneering work to develop hydrohalic acid (HX) splitting catalysts for solar fuel generation. Excellent reviews are recommended for a detailed description of their approach.[56,57] Bimetallic mixed-valence complexes with a metal−metal bond, were characterized as competent photocatalysts for the two-electron process required to reduce protons to H_2 and oxidize halides to X_2 or $X^{\bullet}$, which then reacted with a halogen trap.[58] Early catalyst (denoted M^n–M^n) behavior was consistent with the catalytic cycle shown in Figure 1.9.[59]

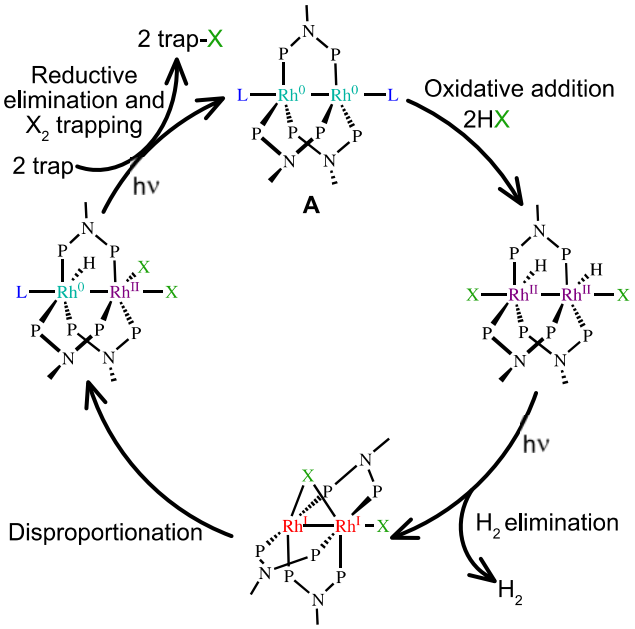

Figure 1.9: Proposed mechanism for HX splitting with complex A.

Oxidative addition of HX to both metal centers gave the dihydride−dihalide M^{n+2}–M^{n+2}. Photoinduced elimination of H_2 yielded the catalyst as M^{n+1}–M^{n+1}, which then underwent halide transfer to give the disproportionation product M^{n}–M^{n+2}. Photoexcitation yielded LMCT excited states that facilitated halogen elimination in the presence of sacrificial olefin reagents, or halogen traps, which regenerated the catalyst (M^{n}–M^{n}), and closed the catalytic cycle.

The first example of the homogeneous catalytic conversion of HX (X = Cl or Br) to H_2 and X_2 was achieved with the dirhodium catalyst A, Figure 1.9.[58] The success of this catalysis was due in part to the ability of the catalyst to support mixed-valency in the metal centers. In these complexes, the three bridging dfpma ligands (dfmpa = bis-[difluorophosphino]methylamine) stabilized the rhodium in the Rh^0, Rh^I, and Rh^{II} oxidation states, as the π-acceptor phosphine orbitals accept charge density from the nitrogen or the metal. This aided in the disproportionation reaction which yielded an intermediate that underwent reductive elimination upon irradiation with UV light, Figure 1.9. This elimination reaction, which is of interest in the context of this thesis,

has subsequently been studied in significant detail as the low monochromatic quantum yield for the halogen elimination step (0.6%) was found to limit the overall efficiency.[60–62]

1.4.1.2 Bimetallic Catalysts for X_2 Elimination.

The elimination of X_2 also proceeded through the use of bimetallic complexes where one metal mediates H_2 formation, and a second, more oxidizing metal such as platinum, gold, or iridium facilitates the difficult M−X bond activation required for halogen elimination.[63–65] This strategy was successfully employed in a $Pt^{III}(d^7)$−$Au^{II}(d^9)$ complex (Figure 1.10, B) where the quantum yield for the photoelimination of chlorine with visible light in the presence of a halogen trap was 5.7%.[63] Subsequent work on this and other bimetallic complexes, Figure 1.10 (B−D), resulted in even higher quantum yields for chlorine photoelimination with values ranging from 10% to 38%. Complexes containing Pt(III) typically gave the highest quantum yields. Catalysts based on this design, but with main group elements such as tellurium (Te) or antimony (Sb), Figure 1.10 (E−F), instead of a second transition metal center, were also shown to facilitate the two-electron reactivity at the transition metal center with comparable quantum yields (4− 14%) for X_2 formation.[66,67]

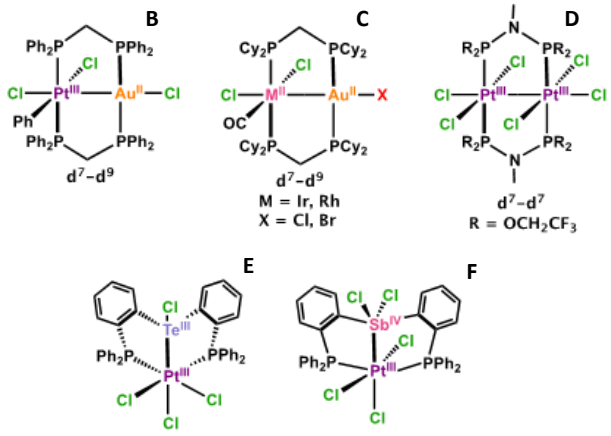

Figure 1.10: Bimetallic complexes for halogen elimination.

The mechanism of chloride photoelimination in main group transition metal platinum complexes was recently investigated.[68] Pulsed-light excitation revealed the presence of reaction intermediates in a family of Pt(III) complexes. These intermediates did not correspond to the reductive elimination products, and the authors attributed them to the singly reduced Pt complexes caused by the release of a halogen atom X•. Photocrystallography of Q supported this assignment, as a single Pt−Cl bond was elongated upon irradiation, which suggested stepwise cleavage of Pt−Cl bonds instead of a concerted reductive elimination reaction. The halogen elimination quantum yield was shown to decrease as the strength of the Pt−Cl bond increased. Although this correlation was expected, it showed that the development of both highly endothermic and efficient energy storage reactions are at odds.

1.4.1.3 Main Group HX Splitting Catalysts

The work on main group participation in transition metal based HX splitting has launched investigations into complexes where a main group element is the sole mediator for halogen elimination. Many main group elements in fact seem ideal for this application, as they preferably perform two-electron redox chemistry, as the one-electron processes are more energetically demanding.[69–72] Examples of halogen elimination remain uncommon, but examples of tellurium[73–75] and antimony[76,77] have been reported. An early example, shown in Figure 1.11, top, reported by Seferos et al. utilized a tellurophene functional group, where the tellurium center had accessible II and IV oxidation states.[73] In this work, illumination of the dihalide−Te(IV) complex reductively eliminated a halogen atom, but variation of the halide (X = Cl, Br) and halogen trap concentration only gave a maximum efficiency of 0.19%. DFT calculation suggested that the nature of the HOMO−LUMO transition was responsible for the low quantum yield, as the excited state did not

have significant Te−X antibonding character but was instead delocalized across the entire molecule.

In subsequent work, Seferos et al. designed Te−X_2 compounds, Figure 1.11, bottom, in which the lowest energy excited state was localized on the tellurophene and was comprised of significant Te−X antibonding character.[75] Irradiation of the lowest energy absorption band resulted in rapid halogen elimination. A halogen elimination quantum yield of nearly 17% (when X = Br) at trap concentrations of 5 M was determined, which was 85 times greater than the previously reported tellurophene.[73] This quantum yield compared favorably with many of the leading transition metal complexes.[64,65] Similar observations were made by ^{1}H NMR when Te−Br_2 was irradiated in the presence of 0.9 M of DMBD halogen trap. Over 20 s of illumination, the resonances associated with Te−Br_2 decreased with a concomitant rise in those associated with Te, therefore confirming the light-induced halogen elimination. Mechanistic studies on a series of tellurophenes suggest that the bromine elimination occurred through a stepwise pathway.[74]

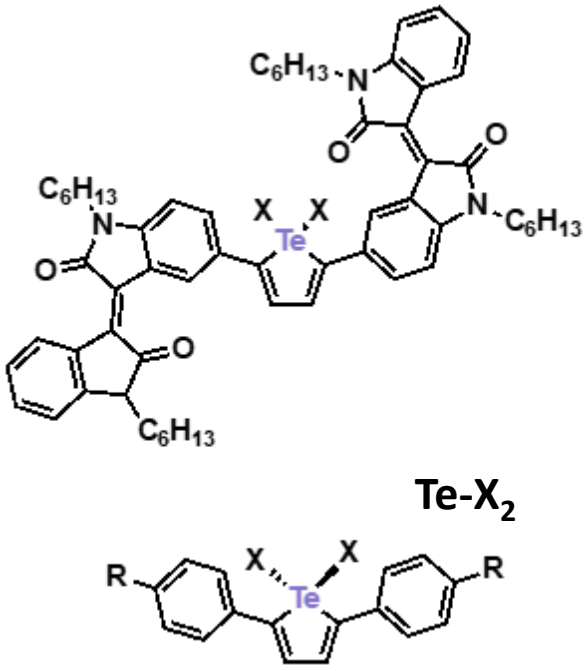

Figure 1.11: Tellurophenes as reported by Seferos et al.

A recent report by Gabbaï et al. has shown that antimony can also participate in the reductive elimination of halogen atoms.[76] In the antimony−palladium complex G shown in Figure 1.12, reaction with chlorine did not result in oxidative addition at the palladium center, as was expected from related work on platinum−antimony complexes.[67] Instead, addition occurred across the palladium−antimony bond, formally oxidizing both atoms by one, which yielded complex H. Density functional theory calculations indicated that the lowest energy excited state of this complex was antibonding with respect to the Pd−Cl and Sb−Cl bonds, and irradiation indeed lead to the photoelimination of Cl_2 with a quantum yield of 0.58% when halogen trap concentrations of 2.0 M were used.

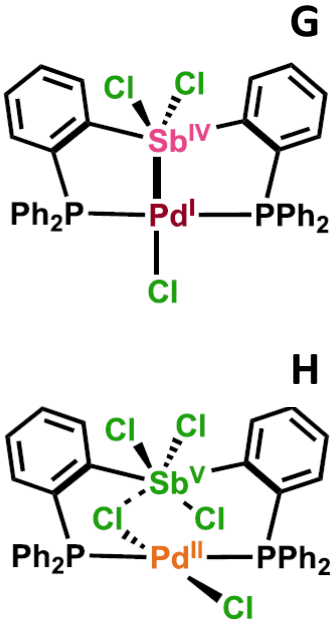

Figure 1.12: Antimony−palladium complexes as reported by Gabbaï et al.

Nocera et al. have provided a subsequent example of halogen elimination mediated solely by antimony.[77] The Sb III and V oxidation states appeared well suited for halogen oxidative addition and reductive elimination, and the authors were able to exploit this when the main group Sb metal was complexed by a corrole ligand. Crystallography, ^{1}H NMR, and UV−vis absorption

spectroscopy revealed that changes in the antimony oxidation state were accompanied by significant structural changes. In the III oxidation state, the antimony resided above the plane of the ligand, but oxidative addition of either $PhICl_2$ or Br_2 resulted in an octahedral complex where the Sb^V resided in the ligand plane. Qualitative conversion from Sb^V–Br and Sb^V–Cl to Sb^{III} was achieved through steady-state photolysis as is shown in Figure 1.13. With the various excitation wavelengths tested, Sb^V–Br was found to give higher reductive elimination quantum yields than Sb^V–Cl. For Sb^V–Br, a maximum ϕ of 0.88% was achieved with 435 nm excitation, while Sb^V–Cl had a maximum ϕ of 0.17% with 315 nm excitation. Trap-free halogen elimination from Sb^V–Br and Sb^V–Cl could not be achieved, as the halogen atoms reacted with the corrole ligand. The reported quantum yields were similar to many of the tellurophene complexes studied by Seferos et al.[73–75]

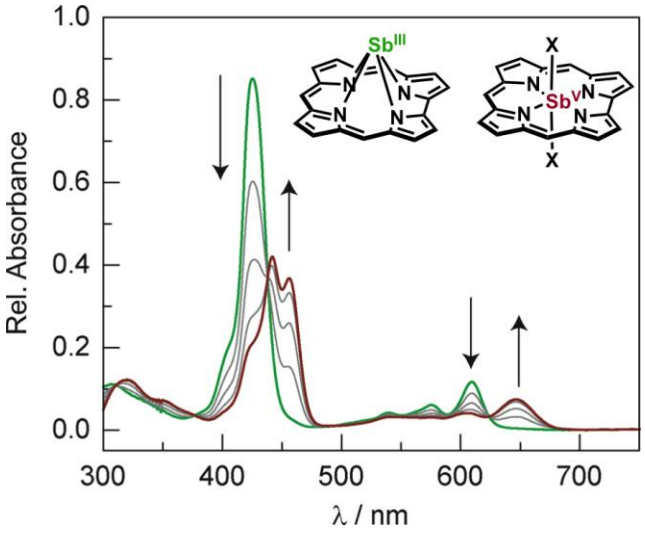

Figure 1.13: Steady-state photolysis (λ_{exc} > 305 nm) of Sb^V–Corrole in degassed THF. The initial spectrum (green) converts to that of Sb^{III}–Corrole (brown) over the course of 2 min.

1.4.1.4 Monomeric and Bimetallic Gold and Platinum HX Splitting Catalysts

To more extensively focus on the halide oxidation step of HX splitting catalysis, transition metal complexes have been developed that only perform the halide oxidation reaction. Recently, advances have been achieved with monomeric transition metal complexes that successfully

catalyze this reaction. Nocera et al. have reported a series of mono and bimetallic Au^{III}–halide complexes, I–K in Figure 1.14, in which the metal center supported the complete two electron chemistry required for the reductive elimination of X_2.[78] In this work, X_2 formation was driven through photochemical elimination from the gold center in both the monomeric and bimetallic complexes. Although the mechanism was not definitively established, halogen trapping with olefins gave products that were predominately consistent with X_2 and not halogen radical formation, suggesting a concerted X_2 reductive elimination mechanism.

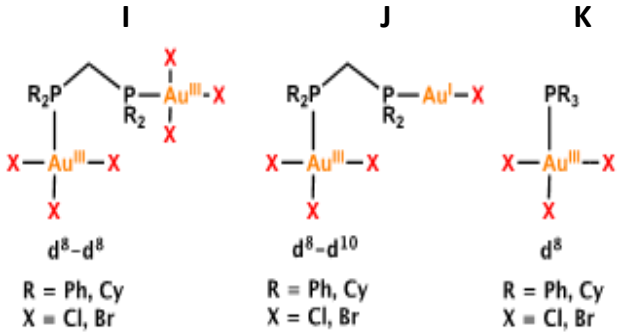

Figure 1.14: Mono- and bimetallic gold complexes as reported by Nocera et al.

The series of $Pt(PEt_3)_2(R)(Br)_3$ complexes shown in Figure 1.15 was reported by Sharp et al. for the reductive elimination of Br_2.[79,80] In the R = CF_3Ph case, a Br_2 elimination quantum yield of 82% was achieved, while the other complexes had quantum yields ranging from <1% to 59%. The wide range of quantum yields could not be directly attributed to a single parameter such as the free energy for elimination or the steric bulk of the complexes. Halogen trap products were characterized to help determine the photoelimination mechanism. When DMB was used as the trap, the major product was the dibrominated alkane DMB-Br_2, which suggested that Br_2 was formed as a direct photoproduct. However, minor trap products (DMB-Br) from $Br^{\bullet}$ and HBr addition were formed in higher yields when larger concentrations of the trap were present.

Importantly, the authors concluded that the reactive excited states could react directly with the olefin trap, thereby changing the mechanism of bromine photoelimination.

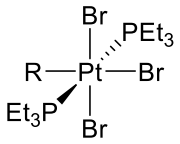

Figure 1.15: Platinum complexes as reported by Sharp et al.

1.4.1.5 Halogen Photoelimination from First Row Transition Metals

First row transition metals have been underexplored for halide oxidation, largely due to the short-lived nature of their excited states. However, LMCT transitions from a halide ligand to a nickel(III) center were recently shown to form dissociative excited states, yielding a halogen radical and a reduced nickel(II) complex (Figure 1.16).[81,82] The formation of X_2 species through this strategy was complicated by the back reaction (Cl• + Ni(II) → Ni(III)−Cl) that was thermodynamically favorable (ΔG° = −24 kcal mol−1) and fast, as the photodissociated nickel(II) and halogen radical were in close proximity. To circumvent this problem, Nocera et al. designed nickel complexes in which the secondary coordination sphere assisted with halogen dissociation. Aromatic ligands, which form relatively long-lived charge-transfer complexes with halogen atoms,[83] were built into the ligand framework that trapped photolabile halogen atoms and prevented the back reaction with the reduced metal species. Pulsed-light excitation of the complexes revealed a long-lived (3 μs) transient species after excitation, and the spectral features were similar to previously characterized arene-to-chlorine charge-transfer bands, Figure 16.[84–86] Further evidence in favor of the charge-transfer adduct was obtained by incorporation of electron donating groups on the aryl ligand, which red-shifted the lowest energy absorption band of the transient species.[82]

Remarkable yields of X_2 product were measured with 370 nm excitation of these Ni complexes. For example, when the secondary coordination sphere was controlled, the quantum yield for photodissociation exceeded 95%. In control experiments where the nickel complexes did not have this design feature, the quantum yield was drastically reduced (20%), although inclusion of benzene as a cosolvent enhanced the elimination yields to 62%.

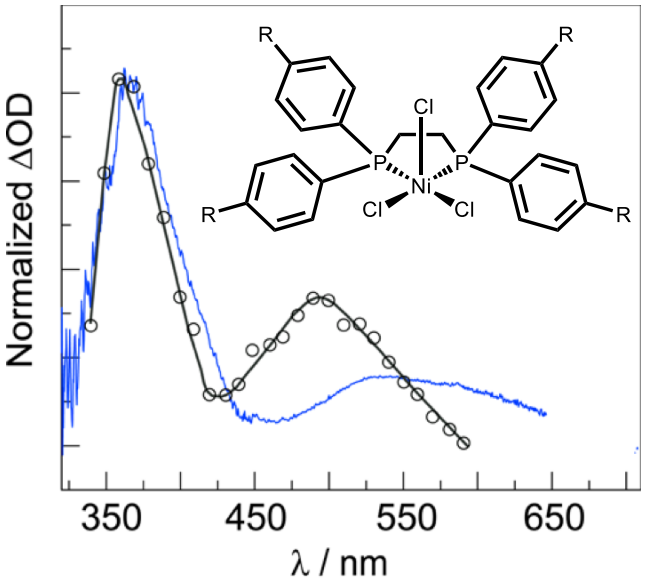

Figure 1.16: Comparison between the absorption spectra of the transient species generated by laser flash photolysis of the represented nickel complex (blue) and the chloride atom charge transfer adduct of benzene (black) also generated by laser flash photolysis.

1.4.2 Dye-Sensitized Halide Oxidation

1.4.2.1 Dye-Sensitized Solar Cells

The dye-sensitized solar cell (DSSC, Figure 1.17) introduced by Gratzel and O'Reagan in 1991, is a photovoltaic composed of a mesoporous metal-oxide thin film, typically TiO_2, that is sensitized to visible light by a molecular dye, here called a sensitizer (S).[87] Upon visible light excitation the cell generates electrical power through a number of electron transfer reactions as described below, and as shown in Figure 1.17.

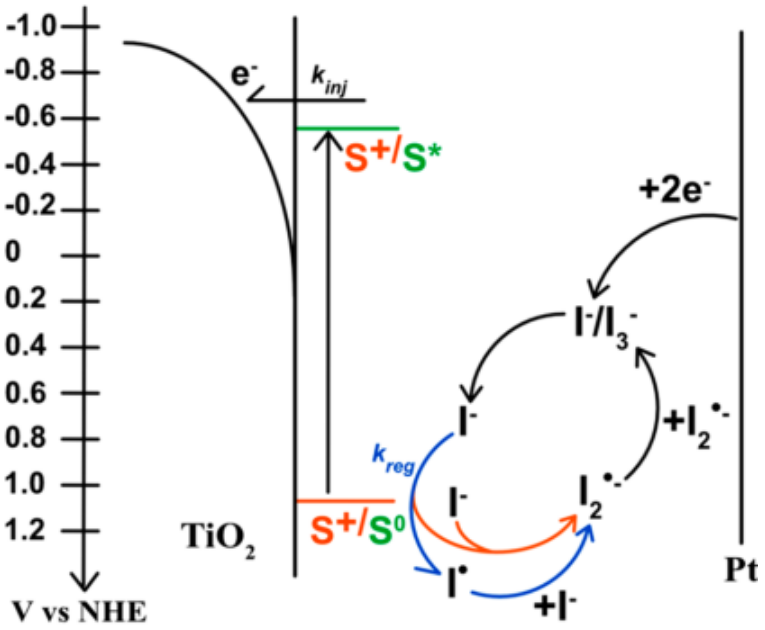

Figure 1.17: Schematic representation of a dye-sensitized solar cell where an excited-state sensitizer S* injects an electron (k_{inj}) into the TiO_2 acceptor states. The oxidized sensitizer is regenerated (k_{reg}) by iodide either through a single-atom pathway (blue arrow) or through a concerted pathway (orange arrow).

First, absorption of a photon by the sensitizer results in an excited state (S*) that injects an electron into the acceptor states of the metal oxide, yielding an oxidized sensitizer (S^+). The injected electron diffuses to the back contact, where it is transported through an external circuit to a metallic counter electrode. At the counter electrode, a redox mediator, typically I_3^-, is reduced to form I^-. The redox mediator then diffuses through solution and regenerates the oxidized sensitizer (S) so that no net chemistry occurs. The mechanism of sensitizer regeneration at the metal oxide surface by the I^-/I_3^- redox mediator has been systematically studied, and is of interest in the context of this dissertation research. The two pathways which have been proposed for sensitizer regeneration, depicted in Figure 1.17 (blue and orange arrows), and are called the single atom and concerted pathways, and are shown in more detail in equations 1 and 2.

$$TiO_2(e^-)|S^+ + I^- \rightarrow TiO_2(e^-)|S + I^\bullet + (I^-) \rightarrow I_2^{\bullet -} \quad (1)$$

$$TiO_2(e^-)|S^+ + 2I^- \rightarrow TiO_2(e^-)|S + I_2^{\bullet -} \quad (2)$$

In the single atom pathway, S^+ is proposed to oxidize I^- by one electron, yielding the iodine radical, $I^\bullet$. The iodine radical may then diffuse through solution until it encounters I^-, at which point a bond formation reaction occurs to give $I_2^{\bullet -}$. In the concerted reaction, both the electron transfer and bond formation are proposed to occur in a single step, which requires 300 meV less of free energy.[88–90] Although the single atom pathway is proposed to occur in these regenerative solar cells, only indirect evidence for the concerted pathway has been reported. Mechanistic studies at the interface can be complicated by the absorbance of the metal-oxide, etc., and so studies in fluid solution have been undertaken to more intimately probe iodide oxidation mechanisms. Chapter 4 of this dissertation presents one such study.

1.4.2.2 Hydrohalic Acid Splitting in Dye-Sensitized Photoelectric Synthesis Cells

Recently, the DSSC approach has been utilized for applications in solar fuels generation. In this approach, called a dye-sensitized photoelectrosynthesis cell, or DSPEC, the photoanode and cathode are separated into two half cells and divided by a proton exchange membrane.[91] In each half cell, important oxidation and reduction reactions are performed, that when combined correspond to water splitting or hydrohalic acid splitting (Figure 1.18). Hydrohalic acid splitting was a particularly appealing initial target, as the commonly used ruthenium polypyridyl sensitizers are capable of performing iodide oxidation in a DSSC. Therefore, it was expected that a single ruthenium sensitizer could be utilized as the light absorber and halide oxidation catalyst in a DSPEC.

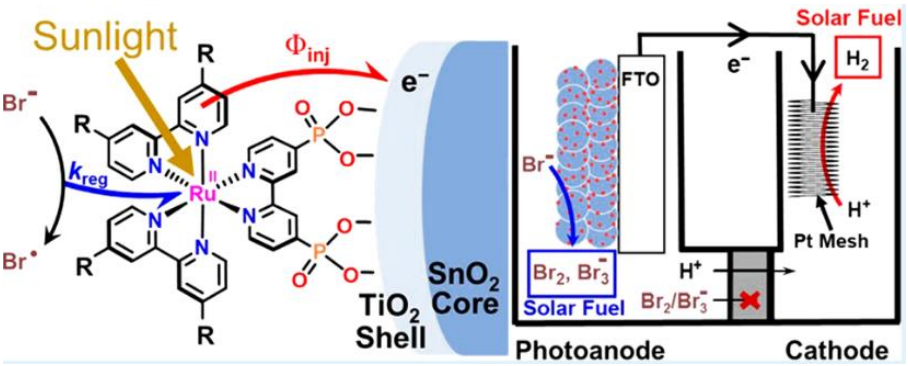

Figure 1.18: Dye-sensitized photoelectrosynthesis cell (DSPEC) in which light induced HX oxidation yielding X_2 and $2H^+$ is performed at the photoanode while H^+ reduction is performed at the cathode. Proton transfer across the two electrodes' compartment is achieved through a proton exchange membrane.

Initial reports investigating hydrobromic acid splitting utilized a $Ru(btfmb)_2P$ catalyst, shown in Figure 18 where R = CF_3, anchored to a core-shell SnO_2/TiO_2 metal oxide surface.[92] In 1N hydrobromic acid, white light illumination (100 mW cm^{-2}) produced sustained photocurrents, and the products of hydrobromic acid splitting, H_2 and Br_2, were quantified. Faradaic efficiencies of 71% for Br_2 and 94% for H_2 production were obtained.

In subsequent work, a series of four ruthenium polypyridyl complexes were prepared where the electronic properties of the ancillary ligands were tuned to give more potent photoreductants or more potent ground-state oxidants.[93] As expected, electron donating groups on the ancillary ligands resulted in a more negative $Ru^{III/2+*}$ potential, yielding stronger photoreductants and larger injection quantum yields. However, these electron donating groups also lowered the $Ru^{III/II}$ potential from 1.85 to 1.35 V vs NHE, which resulted in a five order of magnitude decrease in the regeneration rate constant with bromide. In this work, neither the dye with the largest rate constant for bromide oxidation or the dye with the largest injection quantum yield generated the most efficient hydrohalic acid splitting cell. Instead, the dye that was best able to balance these two parameters was the most competent hydrobromic acid splitting catalyst.

The implications of this study to dye-sensitized halide oxidation for energy storage applications are numerous. First, when a single dye is responsible for both electron injection and halide oxidation, it is difficult to maintain unity injection quantum yields while still efficiently catalyzing halide oxidation. This would be especially challenging under more alkaline conditions where many energy storage applications are more efficient, as the acceptor states of the metal oxide are higher in energy, rendering electron injection more difficult. To combat this, one could envision using a dye that is both a more potent excited-state reductant and a stronger ground-state oxidant. However, this would require more free energy to be stored in the excited state, which would result in less absorption of visible light, as high energy ultraviolet light would be required to excite the sensitizer. A second option is to design a photoanode that utilizes two dyes with distinct properties, one of which is optimized to perform efficient electron injection, while the second is optimized for bromide oxidation. This second approach is the topic of Chapter 5 of this dissertation.

1.5 Ruthenium Polypyridyl Complexes

The majority of the work completed in this thesis utilizes ruthenium polypyridyl complexes, as a number of properties make them suitable for halide supramolecular assembly and halide oxidation. The ease of synthesis allows a large number of functional groups to be incorporated into the bipyridine ligand scaffold. For instance, amide functional groups, combined with the native 2+ charge of the metal center, make these ideal candidates for halide assembly. The absorption of visible light resulting in a long-lived luminescent excited-state generates a potent photo-oxidation/reductant that can diffuse through solution and perform excited-state reactions. A brief overview of the relevant ground- and excited-state properties of $[Ru(bpy)_3]^{2+}$ and related complexes is presented below.

1.5.1 Ground-State Electronic Structure

Ruthenium, a second row transition metal commonly found in the 2+ oxidation state, is the sixth most rare metal in the earth's crust. Placing the 2+ metal ion into an octahedral ligand field environment results in the d-orbital splitting shown in Figure 1.19, left, yielding a low-spin d^6 complex.

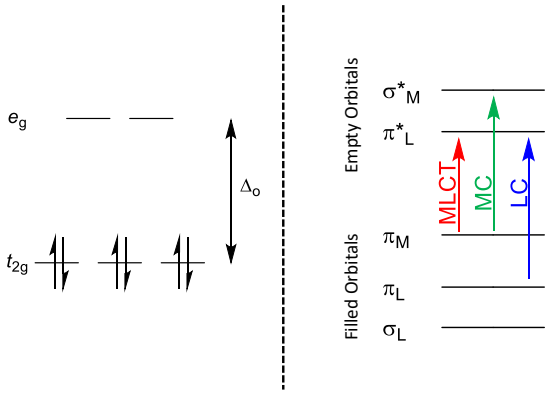

Figure 1.19: (left) Ligand field diagram for a low spin, d^6 ruthenium ion in an octahedral ligand environment. (right) Simplified molecular orbital diagram showing the lowest energy optical transitions for $[Ru(bpy)_3]^{2+}$ and related complexes.

A more complete picture of the ground-state electronic structure is achieved by considering mixing of the metal d orbitals with the ligand orbitals in a molecular orbital diagram.[94] Ligation of the metal center with three bidentate bipyridine ligands in an octahedral geometry results in σ-bonding interactions between the lone-pair of electrons on the nitrogen atoms of the bipyridine ligand and the d_{z^2} and $d_{x^2-y^2}$ orbitals of ruthenium. This mixing results in a set of molecular orbitals with the stabilized bonding orbitals being predominately ligand based (σ_L) and the destabilized antibonding orbitals being predominately d_{z^2} and $d_{x^2-y^2}$ (σ^*_M, e_g orbitals from ligand field theory) in character. The remaining filled metal *d* orbitals (d_{xy}, d_{xz}, and d_{yz}) are able to π-backbond into the π* orbitals of the ligands, which stabilizes these orbitals (π_M, t_{2g} set in ligand field theory) and increases the splitting (Δ_0) between the metal centered orbitals. The MO theory (Figure 1.19, right) predicts that the highest occupied molecular orbitals (HOMO) are metal centered in nature, while

the lowest unoccupied molecular orbitals (LUMO) are π* orbitals on the ligands. Therefore, the lowest energy electronic absorption is a metal-to-ligand charge-transfer transition. Additionally, one would expect ligand localized π-to-π* transitions and metal centered d-d transitions to be present as well, but at a higher energy than the MLCT transitions.

The ground state absorption spectrum of $[Ru(bpy)_3]^{2+}$ is shown in Figure 1.20. The main features are a broad absorption centered around 450 nm ascribed to the MLCT transition, while the sharp absorption feature at higher energy (~300 nm) is consistent with ligand-centered π-to-π* transitions. Both of these transitions are spin and symmetry allowed, resulting in large extinction coefficients (ε_{MLCT} typically from $1\text{-}2\times10^4$ M^{-1} s^{-1}). This is in contrast to the metal centered d-d transitions, which are symmetry forbidden and have low extinction coefficients, and are likely buried under the charge-transfer transitions.[95]

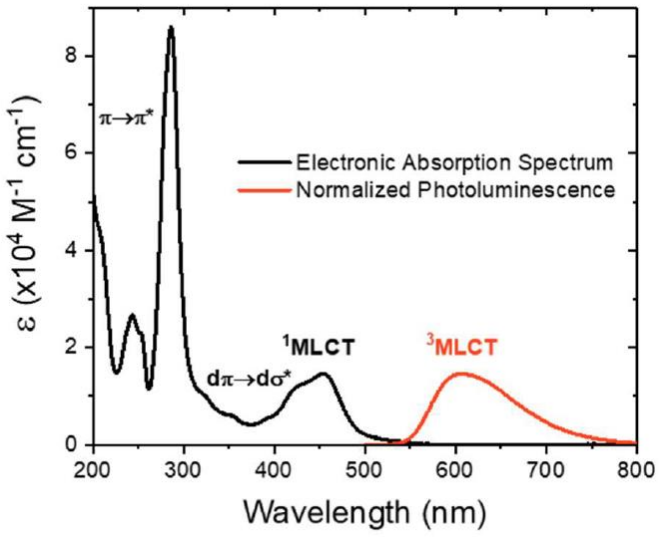

Figure 1.20: Absorption (black) and photoluminescence (red) spectra of $[Ru(bpy)_3]^{2+}$ in CH_3CN solution.

1.5.1 Excited-State Electronic Structure

Visible light excitation of $[Ru(bpy)_3]^{2+}$ is found to result in room temperature photoluminescence (Figure 1.20, red). A simplified Jablonski diagram is presented in Figure 1.21

to explain the photophysics of the luminescent excited-state. The absorption of a photon of the appropriate energy by $[Ru(bpy)_3]^{2+}$ results in the singlet excited state (^{1}MLCT). The large spin-orbit coupling of the ruthenium metal facilitates intersystem crossing (ISC) to the ^{3}MLCT state, which can then decay back to the ground state through radiative or nonradiative pathways.[94]

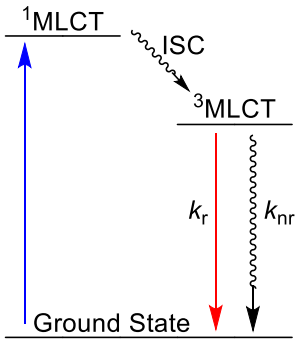

Figure 1.21: Simplified Jablonski diagram showing deactivation pathways for the $[Ru(bpy)_3]^{2+}$ excited state.

The photoluminescence spectrum of $[Ru(bpy)_3]^{2+}$ displays a sizable Stokes-like shift (λ_{max} of 620 nm) while the excited-state lifetime tends to be quite long lived (~1 μs), in agreement with luminescence from the triplet state. As described above, the ^{3}MLCT excited-state can relax back to the ground state through radiative (k_r) and nonradiative (k_{nr}) pathways. The rate constants for these relaxation pathways are related to the excited-state lifetime, τ, as shown in equation 3.

$$\tau = \frac{1}{k_r + k_{nr}} \tag{3}$$

Additionally, the rate constants can be used to determine the quantum yield for photoluminescence, Φ, using equation 4.

$$\Phi = \frac{k_r}{k_r + k_{nr}} \tag{4}$$

By measuring Φ and τ then, it is possible to use these equations to experimentally determine k_r and k_{nr}. For $[Ru(bpy)_3]^{2+}$ and related complexes, numerous studies have shown that k_{nr} tends to be the dominate factor in determining Φ and τ, as the nonradiative rate constants are usually on the order

of 10^6 s^{-1}. The radiative rate constants tend to be much smaller, on the order of 10^4 s^{-1}, although the solvent medium has been shown to influence these rate constants.[96]

An additional pathway that can contribute to excited-state decay is deactivation by an external quencher. Excited-state quenching occurs through a variety of mechanisms including energy transfer and oxidative or reductive electron transfer. Of most relevance to this thesis is the reductive quenching of ruthenium polypyridyl excited states by a halide quencher. A typical reductive quenching mechanism is depicted in Figure 1.22.

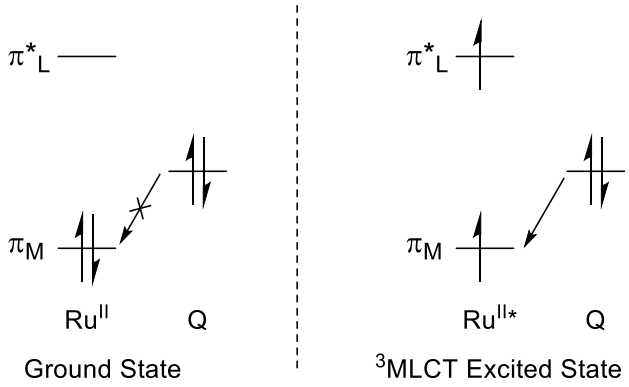

Figure 1.22: Electronic structures of the ground- and excited-states of $[Ru(bpy)_3]^{2+}$.In the excited state, $[Ru(bpy)_3]^{2+}$ is both a more potent oxidant and reductant.

In Figure 1.22, left, the ground-state of a $[Ru(bpy)_3]^{2+}$ complex is depicted, along with the HOMO of a quencher on a relative energy axis. In the ground-state, reduction of $[Ru(bpy)_3]^{2+}$ by the quencher is an uphill reaction and does not occur. However, light excitation (Figure 22, right), which promotes an electron to the $[Ru(bpy)_3]^{2+}$ π^* orbitals of the ligand, generates a stronger oxidant, resulting in a downhill reaction that favors reductive quenching of the excited-state. If the luminescent excited state lives long enough in solution to encounter the quencher, reductive quenching may occur. It is also evident from this figure that the excited state of $[Ru(bpy)_3]^{2+}$ is a more potent reductant, and if a quencher with a LUMO of the correct energy is present, oxidative

quenching of the excited state will be observed. The ground- and excited-state reduction potentials of $[Ru(bpy)_3]^{2+}$ are shown in Figure 1.23.[97]

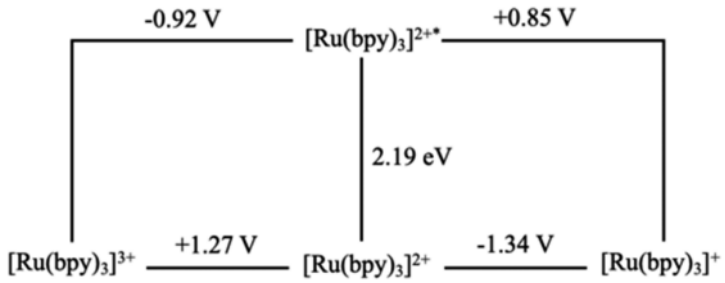

Figure 1.23: Formal reduction potential for $[Ru(bpy)_3]^{2+}$* in CH_3CN at a fixed ionic stregth of 0.1. Potentials are referenced vs SCE (+0.244 vs NHE).

1.5.3 Excited State Quenching and Stern-Volmer Analysis

In 1919, Otto Stern and Max Volmer provided an analysis that allows the quenching of luminescent excited states in fluid solution to be quantified.[98] In this analysis, when the concentration of the excited state is kept constant, a decrease in the photoluminescence intensity (PLI) or the excited-state lifetime, τ, can be related to the change in the quencher concentration to give information about the quenching rate constant and quenching mechanisms. This information is gleaned from plots of PLI_0/PLI or τ_0/τ versus the quencher concentration, examples of which are shown in Figure 1.24 for $[Ru(deeb)_3]^{2+}$ in CH_3CN (a-c) and in CH_2Cl_2 (d-f).[99]

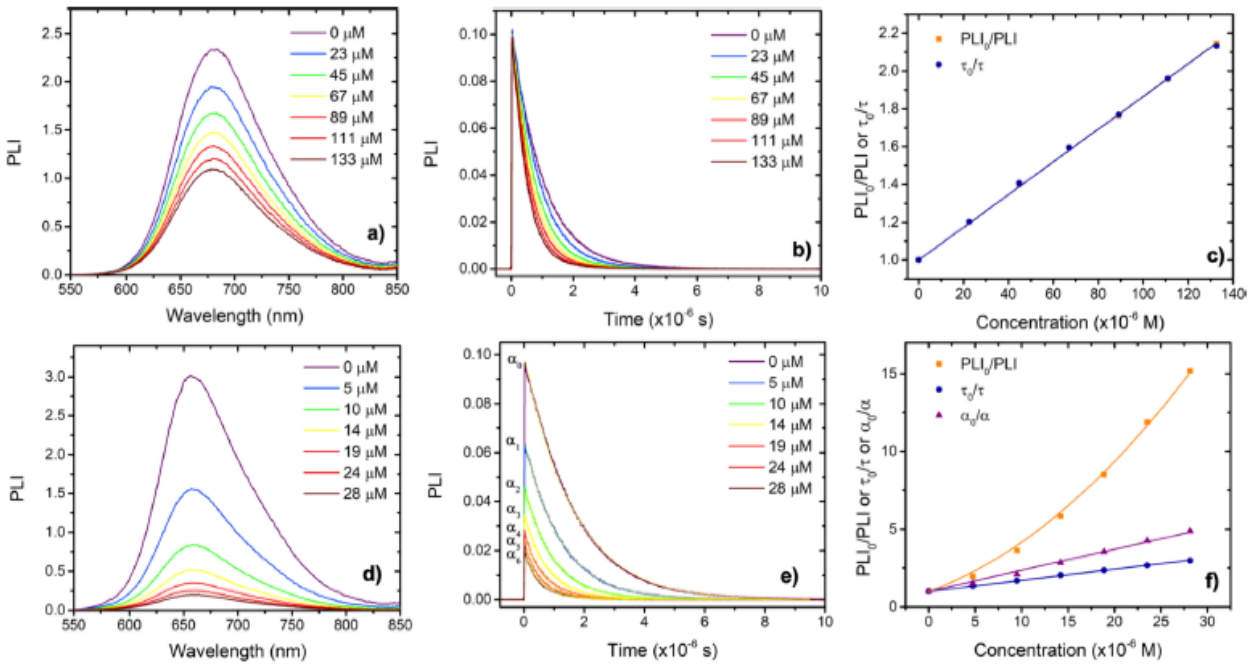

Figure 1.24: Excited-state quenching of [Ru(bpy)2(deeb)]2+* by iodide in CH3CN (a,b,c) and in CH2Cl2 (d,e,f). Steady-state (a,d) and time-resolved (b,e) photoluminescence quenching with increasing concentration of iodide. The decrease of signal amplitude in (e) is associated with static quenching, whereas a decrease in excited-state lifetime is correlated to dynamic quenching. (c,f) Stern−Volmer plot using either the integrated photoluminescence (PLI), the excited-state lifetime (τ), or the initial amplitude of the time-resolved photoluminescence (α). The equilibrium constant is extracted from the amplitudes (α_0/α), whereas the quenching rate constants, k_q, are abstracted from excited-state lifetime (τ_0/τ).

One possible outcome from a Stern-Volmer experiment is that both plots of PLI_0/PLI or $\tau_0,/\tau$ versus the quencher concentration are linear and coincident (Figure 1.24, a,b,c), suggesting that a dynamic quenching mechanism is operative and that the excited state reaction is first-order in the quencher concentration. In dynamic quenching, the excited state and the quencher must diffuse together to form an encounter complex, allowing quenching to occur. In this case, the slope obtained from the Stern-Volmer analysis (equation 5) gives the Stern-Volmer quenching constant (K_{SV}), the inverse of which is the quencher concentration required to quench half of the excited states.

$$PLI_0/PLI \text{ or } \tau_0/\tau = 1 + K_{SV}[Q] \quad (5)$$

$$k_q = K_{SV}/\tau \quad (6)$$

K_{SV} is directly related to the bimolecular quenching rate constant k_q through the excited-state lifetime in the absence of quencher, as shown in equation 6.

A second mechanism, called static quenching, occurs when the quencher preassociates with the ruthenium complex in the ground state prior to light excitation. This results in a ground-state adduct, which, when excited, is non-luminescent and leads to a decrease in the initial photoluminescence intensity. In the extreme case where every quencher forms an adduct, no diffusional quenching is observed resulting in Stern-Volmer plots where τ does not change with increasing quencher concentration. Evidence for this mechanism is observed when there is a decrease in the initial amplitude, A, in the time resolved photoluminescence, but no decrease in τ. When static quenching is operative, the Stern-Volmer relationship, given in equation 7 provides the equilibrium constant, K_S, for adduct formation.

$$PLI_0/PLI \text{ or } A_0/A = 1 + K_S[Q] \tag{7}$$

It is possible in quenching experiments to observe both static and dynamic quenching simultaneously. In these cases, both a decrease in the initial amplitude and in the lifetime in the time-resolved photoluminescence are observed (Figure 24, e,f,g). Additionally, the Stern-Volmer analysis of the steady-state photoluminescence results in upward curvature, as there is now a quadratic dependence on the quencher concentration, as is shown in equation 8.

$$\frac{PLI_0}{PLI} = \frac{A_0}{A} \times \frac{\tau_0}{\tau} = 1 + (K_s + K_D)[Q] + K_D K_S[Q]^2 \tag{8}$$

REFERENCES

(1) Wade, C. R.; Broomsgrove, A. E. J.; Aldridge, S.; Gabbaı, F. P. *Chem. Rev.* **2010**, *110*, 3958–3984.

(2) Carton, R. J. *Fluoride* **2006**, *39*, 163.

(3) Cutting, G. R. *Nat. Rev. Genet.* **2014**, *16*, 45–56.

(4) Werber, J. R.; Osuji, C. O.; Elimelech, M. *Nat. Rev. Mater.* **2016**, *1*.

(5) Gould, I. R.; Lenhard, J. R.; Muenter, A. A.; Godleski, S. A.; Farid, S. *J. Am. Chem. Soc.* **2000**, *122*, 11934–11943.

(6) Fyson, J. R.; Twist, P. J.; Gould, I. R. In *Electron Transfer in Chemistry*; 2001; Vol. V, pp 285–378.

(7) Luttmer, J. D.; Konrad, D.; Trachtenberg, I. *J. Electrochem. Soc.* **1985**, *132*, 1054–1058.

(8) Luttmer, J. D.; Trachtenberg, I. *J. Electrochem. Soc.* **1985**, *132*, 1312–1315.

(9) Greenwood, N. N.; Earnshaw, A. *Chemistry of the Elements*, 2nd ed.; Elsevier Butterworth-Heinemann: Oxford, UK, 1997.

(10) Du, J.; Chen, Z.; Chen, C.; Meyer, T. J. *J. Am. Chem. Soc.* **2015**, *137*, 3193–3196.

(11) Tallmadge, J. A.; Butt, J. B.; Solomon, H. J. *Ind. Eng. Chem.* **1964**, *56*, 44–65.

(12) Stewart, L. C. *Ind. Eng. Chem.* **1931**, *26*, 361–369.

(13) Elderfield, H.; Truesdale, V. W. *Earth Planet. Sci. Lett.* **1980**, *50*, 105–114.

(14) Amachi, S. *Microbes Env.* **2008**, *23* (4), 269–276.

(15) Beer, P. D.; Gale, P. A. *Angew. Chemie Int. ed. English* **2001**, *40* (3), 486–516.

(16) Evans, N. H.; Beer, P. D. *Angew. Chemie Int. Ed. English* **2014**, *53* (44), 11716–11754.

(17) Cram, D. J. *Science (80-.).* **1988**, *240*, 760–767.

(18) Schmidtchen, F. P. *Angew. Chem. Int. Ed. Engl.* **1981**, *20*, 466–468.

(19) Schmidtchen, F. P.; Mullerb, G. *J. Chem. Soc., Chem. Comm* **1984**, 1115–1116.

(20) Arunan, E.; Desiraju, G. R.; Klein, R. A.; Sadlej, J.; Scheiner, S.; Alkorta, I.; Clary, D. C.; Crabtree, R. H.; Dannenberg, J. J.; Hobza, P.; Kjaergaard, H. G.; Legon, A. C.; Mennucci,

B.; Nesbitt, D. J. *Pure Appl. Chem.* **2011**, *83* (8), 1637–1641.

(21) Li, Y.; Flood, A. H. *Angew. Chemie Int. Ed.* **2008**, *47* (14), 2649–2652.

(22) Liu, Y.; Zhao, W.; Chen, C.-H.; Flood, A. H. *Science (80-.).* **2019**, *365*, 159–161.

(23) Cavallo, G.; Metrangolo, P.; Milani, R.; Pilati, T.; Priimagi, A.; Resnati, G.; Terraneo, G. *Chem. Rev.* **2016**, *116*, 2478–2601.

(24) Gilday, L. C.; Robinson, S. W.; Barendt, T. A.; Langton, M. J.; Mullaney, B. R.; Beer, P. D. *Chem. Rev.* **2015**, *115*, 7118–7195.

(25) Lim, J. Y. C.; Beer, P. D. *Chem* **2018**, *4*, 731–783.

(26) Walter, S. M.; Kniep, F.; Rout, L.; Schmidtchen, F. P.; Herdtweck, E.; Huber, S. M. *J. Am. Chem. Soc.* **2012**, *134*, 8507–8512.

(27) Barendt, T. A.; Ferreira, L.; Marques, I.; Félix, V.; Beer, P. D. *J. Am. Chem. Soc.* **2017**, *139* (26), 9026–9037.

(28) Lim, J. Y. C.; Marques, I.; Félix, V.; Beer, P. D. *Angew. Chemie Int. Ed.* **2018**, *57* (2), 584–588.

(29) Brown, A. R.; Kuo, W.-H.; Jacobsen, E. N. *J. Am. Chem. Soc.* **2010**, *132* (27), 9286–9288.

(30) Birrell, J. A.; Desrosiers, J. N.; Jacobsen, E. N. *J. Am. Chem. Soc.* **2011**, *133* (35), 13872–13875.

(31) Reisman, S. E.; Doyle, A. G.; Jacobsen, E. N. *J. Am. Chem. Soc.* **2008**, *130* (23), 7198–7199.

(32) Raheem, I. T.; Thiara, P. S.; Peterson, E. A.; Jacobsen, E. N. *J. Am. Chem. Soc.* **2007**, *129* (44), 13404–13405.

(33) Koulov, A. V.; Lambert, T. N.; Shukla, R.; Jain, M.; Boon, J. M.; Smith, B. D.; Li, H.; Sheppard, D. N.; Joos, J. B.; Clare, J. P.; Davis, A. P. *Angew. Chemie - Int. Ed.* **2003**, *42* (40), 4931–4933.

(34) McNally, B. A.; Koulov, A. V.; Lambert, T. N.; Smith, B. D.; Joos, J. B.; Sisson, A. L.; Clare, J. P.; Sgarlata, V.; Judd, L. W.; Magro, G.; Davis, A. P. *Chem. - A Eur. J.* **2008**, *14* (31), 9599–9606.

(35) Hussain, S.; Brotherhood, P. R.; Judd, L. W.; Davis, A. P. *J. Am. Chem. Soc.* **2011**, *133* (6), 1614–1617.

(36) Berezin, S. K.; Davis, J. T. *Society* **2009**, *131* (February), 2458–2459.

(37) Sessler, J. L.; Eller, L. R.; Cho, W. S.; Nicolaou, S.; Aguilar, A.; Lee, J. T.; Lynch, V. M.; Magda, D. J. *Angew. Chemie - Int. Ed.* **2005**, *44* (37), 5989–5992.

(38) Winstanley, K. J.; Allen, S. J.; Smith, D. K. *Chem. Commun.* **2009**, No. 28, 4299–4301.

(39) Beer, P. D.; Hesek, D.; Hodacova, J.; Stokes, S. E. *J. Chem. Soc., Chem. Comm* **1992**, *3*, 270–272.

(40) Beer, P. D.; Timoshenko, V.; Maestri, M.; Passaniti, P.; Balzani, V. *Chem. Commun.* **1999**, 1755–1756.

(41) Black, C. B.; Andrioletti, B.; Try, A. C.; Ruiperez, C.; Sessler, J. L. *J. Am. Chem. Soc.* **1999**, *121* (44), 10438–10439.

(42) Battistin, F.; Balducci, G.; Wei, J.; Renfrew, A. K.; Alessio, E. *Eur. J. Inorg. Chem.* **2018**, 1469–1480.

(43) Glebov, E. M.; Pozdnyakov, I. P.; Plyusnin, V. F.; Khmelinskii, I. *J. Photochem. Photobiol. C Photochem. Rev.* **2015**, *24*, 1–15.

(44) Balzani, V.; Manfrin, F.; Moggi, L. *Inorg. Chem.* **1967**, *6* (2), 354–358.

(45) Balzani, V.; Carassiti, V. *J. Phys. Chem.* **1968**, *72* (2), 383–388.

(46) Pozdnyakov, I. P.; Glebov, E. M.; Plyusnin, V. F.; Tkachenko, N. V.; Lemmetyinen, H. *Chem. Phys. Lett.* **2007**, *442* (1–3), 78–83.

(47) Glebov, E. M.; Plyusnin, V. F.; Grivin, V. P.; Venediktov, a. B.; Korenev, S. V. *Russ. Chem. Bull.* **2007**, *56* (12), 2357–2363.

(48) Villaron, D.; Siegler, M. A.; Wezenberg, S. J. *Chem. Sci.* **2021**, *12*, 3188–3193.

(49) Kokan, Z.; Chmielewski, M. J. *J. Am. Chem. Soc.* **2018**, *140*, 16010–16014.

(50) Hua, Y.; Flood, A. H. *J. Am. Chem. Soc.* **2010**, *132*, 12838–12840.

(51) MacQueen, D. B.; Schanze, K. S. *J. Am. Chem. Soc.* **1991**, *113* (16), 6108–6110.

(52) Lewis, J. D.; Moore, J. N. *Chem. Commun. (Camb).* **2003**, No. 23, 2858–2859.

(53) Lewis, J. D.; Perutz, R. N.; Moore, J. N. *J. Phys. Chem. A* **2004**, *108* (42), 9037–9047.

(54) Lewis, J. D.; Clark, I. P.; Moore, J. N. *J. Phys. Chem. A* **2007**, *111* (1), 50–58.

(55) Lewis, J. D.; Towrie, M.; Moore, J. N. *J. Phys. Chem. A* **2008**, *112* (17), 3852–3864.

(56) Teets, T. S.; Nocera, D. G. *Chem. Commun.* **2011**, *47*, 9268–9274.

(57) Esswein, A. J.; Nocera, D. G. *Chem. Rev.* **2007**, *107*, 4022–4047.

(58) Heyduk, A. F.; Nocera, D. G. *Science (80-.).* **2001**, *293*, 1639–1642.

(59) Esswein, A. J.; Veige, A. S.; Nocera, D. G. *J. Am. Chem. Soc.* **2005**, *127*, 16641–16651.

(60) Powers, D. C.; Anderson, B. L.; Hwang, S. J.; Powers, T. M.; Pe, L. M.; Hall, M. B.; Zheng, S.; Chen, Y.; Nocera, D. G. **2014**.

(61) Powers, D. C.; Chambers, M. B.; Teets, T. S.; Elgrishi, N.; Anderson, B. L.; Nocera, D. G. *Chem. Sci.* **2013**, *4*, 2880–2885.

(62) Powers, D. C.; Hwang, S. J.; Zheng, S.-L.; Nocera, D. G. *Inorg. Chem.* **2014**, *53*, 9122–9128.

(63) Cook, T. R.; Esswein, A. J.; Nocera, D. G. *J. Am. Chem. Soc.* **2007**, *129*, 10094–10095.

(64) Cook, T. R.; Surendranath, Y.; Nocera, D. G. *J. Am. Chem. Soc.* **2009**, *131*, 28–29.

(65) Teets, T. S.; Lutterman, D. A.; Nocera, D. G. *Inorg. Chem.* **2010**, *49*, 3035–3043.

(66) Lin, T.-P.; Gabbai, F. P. *J. Am. Chem. Soc.* **2012**, *134*, 12230–12238.

(67) Yang, H.; Gabbai, F. P. *J. Am. Chem. Soc.* **2014**, *136*, 10866–10869.

(68) Powers, D. C.; Hwang, S. J.; Anderson, B. L.; Yang, H.; Zheng, S.-L.; Chen, Y.-S.; Cook, T. R.; Gabbai, F. P.; Nocera, D. G. *Inorg. Chem.* **2016**, *53*, 11815–11820.

(69) Dunn, N. L.; Ha, M.; Radosevich, A. T. *J. Am. Chem. Soc.* **2012**, *134*, 11330–11333.

(70) Jones, J. S.; Gabbai, F. P. *Acc. Chem. Res.* **2016**, *49*, 857–867.

(71) Protchenko, A. V; Bates, J. I.; Saleh, L. M. A.; Blake, M. P.; Schwarz, A. D.; Kolychev, E. L.; Thompson, A. L.; Jones, C.; Mountford, P.; Aldridge, S. *J. Am. Chem. Soc.* **2016**, *138*, 4555–4564.

(72) Stauber, J. M.; Muller, P.; Dai, Y.; Wu, G.; Nocera, D. G.; Cummins, C. C. *Chem. Sci.* **2016**, *7*, 6928–6933.

(73) Carrera, E. I.; Mccormick, T. M.; Kapp, M. J.; Lough, A. J.; Seferos, D. S. *Inorg. Chem.* **2013**, *52*, 13779–13790.

(74) Carrera, E. I.; Lanterna, A. E.; Lough, A. J.; Scaiano, J. C.; Seferos, D. S. *J. Am. Chem. Soc.* **2016**, *138*, 2678–2689.

(75) Carrera, E. I.; Seferos, D. S. *Dalt. Trans.* **2015**, *44*, 2092–2096.

(76) Sahu, S.; Gabbai, F. P. *J. Am. Chem. Soc.* **2017**, *139*, 5035–5038.

(77) Lemon, C. M.; Hwang, S. J.; Maher, A. G.; Powers, D. C.; Nocera, D. G. *Inorg. Chem.* **2018**, *57*, 5333–5342.

(78) Teets, T. S.; Nocera, D. G. *J. Am. Chem. Soc.* **2009**, *131*, 7411–7420.

(79) Karikachery, A. R.; Lee, H. B.; Masjedi, M.; Ross, A.; Moody, M. A.; Cai, X.; Chui, M.; Hoff, C. D.; Sharp, P. R. *Inorg. Chem.* **2013**, *52*, 4113–4119.

(80) Perera, T. A.; Masjedi, M.; Sharp, P. R. *Inorg. Chem.* **2014**, *53*, 7608–7621.

(81) Hwang, S. J.; Powers, D. C.; Maher, A. G.; Anderson, B. L.; Hadt, R. G.; Zheng, S.-L.; Chen, Y.-S.; Nocera, D. G. *J. Am. Chem. Soc.* **2015**, *137*, 6472–6475.

(82) Hwang, S. J.; Anderson, B. L.; Powers, D. C.; Maher, A. G.; Hadt, R. G.; Nocera, D. G. *Organometallics* **2015**, *34*, 4766–4774.

(83) Chateauneuf, J. E. *Chem. Phys. Lett.* **1989**, *164*, 577–580.

(84) Bossy, J. M.; Buhler, R. E.; Ebert, M. *J. Am. Chem. Soc.* **1970**, *92*, 1099–1101.

(85) Strong, R. L.; Rand, S. J.; Britt, J. A. *J. Am. Chem. Soc.* **1960**, *82*, 5053–5057.

(86) Buhler, R. E.; Ebert, M. *Nature* **1967**, *214*, 1220–1221.

(87) O'Regan, B.; Gratzel, M. *Nature* **1991**, *353*, 737–740.

(88) Nord, G.; Pedersen, B.; Farverl, O. *Inorg. Chem.* **1978**, *17* (8), 2233–2238.

(89) Stanbury, D. M.; Wilmarth, W. K.; Khalaf, S.; Po, H. N.; Byrd, J. E. *Inorg. Chem.* **1980**, *19*, 2715–2722.

(90) Nord, G. *Comments Inorg. Chem.* **1992**, *13*, 221–239.

(91) Brennaman, M. K.; Dillon, R. J.; Alibabaei, L.; Gish, M. K.; Dares, C. J.; Ashford, D. L.; House, R. L.; Meyer, G. J.; Papanikolas, J. M.; Meyer, T. J. *J. Am. Chem. Soc.* **2016**, *138*, 13085–13102.

(92) Brady, M. D.; Sampaio, R. N.; Wang, D.; Meyer, T. J.; Meyer, G. J. *J. Am. Chem. Soc.* **2017**, *139*, 15612–15615.

(93) Brady, M. D.; Troian-Gautier, L.; Sampaio, R. N.; Motley, T. C.; Meyer, G. J. *ACS Appl. Mater. Interfaces* **2018**, *10*, 31312–31323.

(94) Juris, A.; Balzani, V.; Barigelletti, F.; Campagna, S.; Belser, P.; Von Zelewsky, A. *Coord. Chem. Rev.* **1988**, *84*, 85–277.

(95) Kalyanasundaram, K. *Coord. Chem. Rev.* **1982**, *46*, 159–244.

(96) Chen, P.; Meyer, T. J. *Chem. Rev.* **1998**, *98*, 1439–1477.

(97) Thompson, D. W.; Ito, A.; Meyer, T. J. *Pure Appl. Chem.* **2013**, *85* (7), 1257–1305.

(98) Stern, O.; Volmer, M. *Phys. Zeitschrift* **1919**, *20*, 183–188.

(99) Troian-Gautier, L.; Turlington, M. D.; Wehlin, S. A. M.; Maurer, A. B.; Brady, M. D.; Swords, W. B.; Meyer, G. J. *Chem. Rev.* **2019**, *119*, 4628–4683.

CHAPTER 2: LIGAND CONTROL OF SUPRAMOLECULAR CHLORIDE PHOTORELEASE[1]

2.1 Introduction

The important role halide ions play in chemistry and biology has inspired research into halide sensing.[1–10] The contactless nature of luminescent sensors is particularly attractive for fundamental study and has led to the rational design of chromophores that specifically recognize halides. Amides and functional groups capable of H-bonding have, in particular, been shown to recognize halide ions present in solution.[11–13] In spite of the remarkable advances in halide sensing, receptors that reversibly bind, and then promote controlled halide release have not been developed.

To date, halide release is limited to transition metal complexes that utilize reactive excited states for photoaquation of a halide ligand, as in non-luminescent Pt^{IV} complexes.[14] For example, ultraviolet or d-d excitation of $[PtBr_6]^{2-}$ in water results in Br^- release with a quantum yield (ϕ) of 0.4.[15–18] Similarliy, illumination of $[PtCl_6]^{2-}$ also gave the aquation product and free Cl^-, but the mechanism was complicated by additional redox chemistry.[19,20] Seminal work in the 1970s on thermal and photochemical release of ligands from Cr(III) complexes, such as $[Cr(NH_3)_5Cl]^{2+}$ revealed preferential photoaquation reactions that differed from the thermal aquation.[21] For $[Cr(NH_3)_5Cl]^{2+}$, photoaquation primarily causes release of NH_3 (ϕ = 0.35), and only minimal Cl^- release ($\phi = 2\times10^{-4}$).[21] Adamson's empirical rules for these reactions have been used to design

[1] This chapter previously appeared as an article in the journal Inorganic Chemistry. The original citation is as follows: Turlington, M. D.; Troian-Gautier, L.; Sampaio, R. N.; Beauvilliers, E. E.; Meyer, G. J. Ligand Control of Supramolecular Chloride Release. *Inorg. Chem.* **2018**, *57*, 5624-5631.

transition metal complexes that preferentially release halide from the metal coordination sphere upon illumination.[22] For example, *trans*-$[Cr(en)_2Cl_2]^+$ undergoes photoaquation of a chloride ligand with a ϕ from 0.32-0.35 in acidic aqueous solution.[23] The corresponding *cis* and *trans* $[Co(en)_2Cl_2]^+$ complexes shows similar photochemistry, but with a much lower efficiency (ϕ from 10^{-3} to 10^{-4}).[24,25] Significantly, this ligand field photochemistry is irreversible and therefore differs from this report.

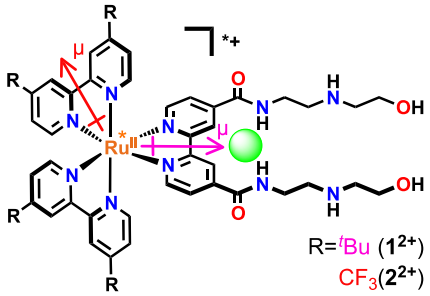

Figure 2.1: Proposed supramolecular assembly structure of 1^{2+} or 2^{2+} and chloride (green sphere). The dipole orientation is indicated for the excited-state of 1^{2+} (pink) and for 2^{2+} (red).

Herein two chromophores were designed which exploit receptor properties for supramolecular association with halide and excited-state characteristics relevant for reversible halide release. The chromophores shown in **Figure 2.1** include a common ligand for halide coordination and a net charge of 2+ for electrostatic attraction. The second important design element is the orientation of the excited-state dipole. In chromophore $\mathbf{1}^{2+}$ the metal-to-ligand charge transfer (MLCT) excited state dipole is directed toward the halide binding site, while for $\mathbf{2}^{2+}$ it is directed away. This orientation had no significant influence on ground-state halide association, but did have a profound influence on the photoluminescence of both excited states. In the case of $\mathbf{1}^{2+}$, the excited-state equilibrium constant for chloride association was 20 times smaller than that of the ground state, and light excitation of the adduct $[\mathbf{1}^{2+}, Cl^-]^+$ resulted in photorelease of the chloride ion. In the case of $\mathbf{2}^{2+}$, no evidence for chloride release was observed but rather a 45-fold increase in the equilibrium constant was determined through the Förster cycle. Hence,

supramolecular assembly can be utilized to recognize and photorelease chloride, behavior that may one day enable additional applications such as quantifying halide transport across artificial and natural membranes relevant to sea water desalination and cystic fibrosis related diseases.[26–28]

2.2 Experimental Section

2.2.1 Materials

Dichloromethane (CH_2Cl_2, Burdick and Jackson, 99.98 %) was used as received. Argon and nitrogen gas (Airgas, 99.998 %) were passed through a Drierite drying tube before use. Ammonium hexafluorophosphate (NH_4PF_6, Sigma-Aldrich, ≥ 98 %), tetrabutylammonium chloride (TBACl, Sigma-Aldrich, purum ≥ 97 %), tetrabutylammonium perchlorate ($TBAPF_6$, Sigma-Aldrich, for electrochemical analysis, ≥ 98 %), sodium tetrakis[3,5-bis(trifluoromethyl)phenyl]borate ($NaB(ArF)_4$, ArkPharm, 97%) and ruthenium trichloride hydrate (Oakwood Chemicals), were used as received. NMR solvents were purchased from Cambridge Isotope Laboratories, Inc. $Ru(dtb)_2Cl_2•2H_2O$ and $Ru(btfmb)_2Cl_2$ were synthesized according to a literature procedure.[29,30] All other chemicals were obtained from commercial distributors with minimum purity of 98 % and used as received. All solutions were purged with argon for at least 30 minutes before all electrochemical, titration and transient photoluminescence (PL) experiments.

2.2.2 Nuclear Magnetic Resonance

Characteristic NMR spectra were obtained at room temperature on a Bruker Avance III 400 or 500 MHz spectrometer. Solvent residual peaks were used as internal standards for ^1H (δ = 2.50 ppm for DMSO, 1.94 for CD_3CN, and 5.32 for CD_2Cl_2) and ^{13}C (39.52 ppm for DMSO) chemical shift referencing. NMR spectra were processed using MNOVA.

2.2.3 Mass Spectrometry

Samples were analyzed with a hybrid LTQ FT (ICR 7T) (ThermoFisher, Bremen, Germany) mass spectrometer.

2.2.4 UV−Vis Absorption

UV−vis absorption spectra were recorded on a Varian Cary 60 UV−vis spectrophotometer with a resolution of 1 nm.

2.2.5 Steady-State PL

Steady-state PL spectra were recorded on a Horiba Fluorolog 3 fluorimeter and corrected by calibration with a standard tungsten-halogen lamp. Samples were excited at 450 nm. The intensity was integrated for 0.1 s at 1 nm resolution and averaged over 3 scans. The PL quantum yields were measured by the optically dilute method using $[Ru(bpy)_3][PF_6]_2$ in acetonitrile (Φ = 0.062) as a quantum yield standard.[31]

2.2.6 Time-Resolved Photoluminescence

Time-resolved PL data were acquired on a nitrogen dye laser with excitation centered at 500 nm. Pulsed light excitation was achieved with a Photon Technology International (PTI) GL-301 dye laser that was pumped by a PTI GL-3300 nitrogen laser. The PL was detected by a Hamamatsu R928 PMT optically coupled to a ScienceTech Model 9010 monochromator terminated into a LeCroy Waverunner LT322 oscilloscope. Decays were monitored at the PL maximum and averaged over 90 scans. Non-radiative and radiative rate constants were calculated from the quantum yields, $\Phi = k_r/(k_r + k_{nr})$ and lifetimes, $\tau = 1/(k_r + k_{nr})$.

2.2.7 Transient Photoluminescence

Transient photoluminescence data were obtained on the nitrogen dye laser described above. Excited-State decay traces were obtained every 10 nm from 560 to 770 nm and averaged over 60

scans. The amplitude of each PL decay after a specific time-delay from the laser pulse (45 ns to 3 μs at given intervals) was plotted versus the wavelength, and the data was normalized to give the transient PL spectra shown in **Figure 3**.

2.2.8 Excited-State Equilibrium

The solutions to the rates in equations 1 and 2 are described elsewhere.[32–34] Since PL does not report on the concentrations of the excited state complexes $\mathbf{1}^{2+}$ and $[\mathbf{1}^{2+},Cl^-]^+$, the constants *a* and *b* were introduced for the appropriate conversion. Values for k_1 and k_2 were obtained in the absence or presence of 200 equivalents of chloride. At these boundary conditions, the time-resolved PL traces displayed first-order kinetics, indicating that only one emissive species was present.

2.2.9 Electrochemistry

Square wave voltammetry was performed with a BASi Epsilon potentiostat in a standard three-electrode cell in CH_2Cl_2 electrolyte. The cells consisted of a platinum working electrode and a platinum mesh as an auxiliary electrode. A non-aqueous silver/silver chloride electrode (Pine) was used as a reference electrode that was referenced to an internal ferrocene (724 mV vs. NHE)[35] or decamethylferrocene ($Me_{10}Fc$) standard (250 mV vs. NHE).[36] The experiments were performed with 1.0 mM ruthenium solutions in 0.1M $TBAClO_4$.

2.2.10 Halide Titrations

UV−vis, PL, and time-resolved measurements were performed in CH_2Cl_2 using approximately 10 μM solutions of $\mathbf{1}^{2+}$ and $\mathbf{2}^{2+}$. Titration measurements were performed for each of the spectroscopies using TBACl through additions of 0.25 equivalents. Throughout all titrations the concentration of ruthenium complexes remained unchanged. In order to do so, a stock solution of each complex with an absorbance of ~0.1 at 450 nm in the desired solvent was prepared. The

stock solution was transferred into a spectrophotometric quartz cuvette (5 mL). A titration solution was then prepared with 25 mL of the complex's stock solution. TBACl was added to the stock solution to obtain the desired concentration of halide. These solutions were then titrated to the quartz cuvette.

The ^{1}H NMR titrations were performed using Bruker Avance III 500 MHz spectrometer equipped with a broadband inverse (BBI) probe using 1 mM ruthenium complex in 600 µL of deuterated solvent and 0.20 equivalent of TBACl was added in 10 µL additions. The ruthenium concentration was kept unchanged through preparation of a titration solution that contained both the desired complex and the desired halide. Each spectrum was averaged over 16 scans.

Data analysis for all experiments was performed using OriginLab, version 9.0. Data fitting was preformed using a Levenberg-Marquardt iteration method. Benesi-Hildebrand type analysis was performed in Mathematica, version 10.

2.2.11 Synthesis

Synthesis of daea: To 1.0 g (3.7 mmol) of 4,4′-dimethylester-2,2′-bipyridine in 20 mL of methanol was added 5 mL (5.15 g, 49 mmol) of 2-(2-Aminoethylamino)ethanolamine. The mixture was refluxed for 4 hours. After cooling, ~25 mL of acetone was added to the resulting mixture that was then filtered on a sintered glass frit. The precipitate was washed with a copious amount of acetone and dried in an evacuated oven overnight at 150 °C to yield the title compound as a white powder (1.1 g, 72%). ^{1}H NMR (500 MHz, DMSO-d_6) δ 8.93 (t, J = 5.6 Hz, 2H), 8.86 (d, J = 5.0 Hz, 2H), 8.79 (d, J = 1.6 Hz, 2H), 7.85 (dd, J = 5.0, 1.7 Hz, 2H), 4.48 (t, J = 5.3 Hz, 2H), 3.44 (q, J = 5.5 Hz, 4H), 3.38 (q, J = 6.3 Hz, 4H), 2.72 (t, J = 6.5 Hz, 4H), 2.60 (t, J = 5.8 Hz, 4H). ^{13}C NMR (126 MHz DMSO-d_6) δ 164.63, 155.51, 150.03, 142.99, 121.99, 118.25, 60.47, 51.51, 48.39, 39.52.

[Ru(dtb)$_2$(daea)](PF$_6$)$_2$, (1^{2+}): To a 10 mL glass microwave vial was added Ru(dtb)$_2$Cl$_2$•2H$_2$O (100 mg, 0.14 mmol), **daea** (70 mg, 0.17 mmol) and 5 mL of water containing 3 drops of concentrated HCl. The mixture was heated under microwave radiation by an Anton Paar Monowave 300 at 150 ºC for 10 minutes. The mixture was brought to room temperature and filtered on a sintered glass frit. The filtrate was then neutralized with sodium bicarbonate and stirred for 15 minutes. A saturated aqueous NH_4PF_6 solution was then added and the formed precipitated was filtered on a sintered glass frit and washed with water. The precipitate was then dried under vacuum to give the desired product (127 mg, 67%). ^{1}H NMR (CD_3CN, 500 MHz): 9.02 (s, 2H), 8.48 (dd, 4H), 7.84 (d, 2H), 7.73 (d, 2H), 7.55 (d, 4H), 7.42 (dd, 2H), 7.35 (dd, 2H), 3.56 (t, 4H), 3.51 (m, 4H), 2.85 (t, 4H), 2.73 (t, 4H), 1.41 (s, 18H), 1.39 (s, 18H). HRMS (ESI-MS) m/z: $[M+Na]^+$ Calcd for $C_{56}H_{76}N_{10}O_4P_2Ru_1F_{12}Na_1$ 1367.28; Found 1367.43.

[Ru(btfmb)$_2$(daea)](PF$_6$)$_2$, (2^{2+}): To a 50 mL round bottom flask was added Ru(btfmb)$_2$Cl$_2$ (200 mg, 0.26 mmol), **daea** (110 mg, 0.26 mmol), $AgNO_3$ (90 mg, 0.53 mmol) and 16 mL H_2O:EtOH (1:1, v:v). The mixture was purged with N_2 for 30 minutes and then refluxed for 5 hours under N_2. After cooling, the mixture was filtered and the solvent was removed from the filtrate, giving a red solid. The solid was dissolved in minimal H_2O (about 3 mL) and was precipitated by the addition of a saturated aqueous NH_4PF_6 solution. The solid was collected by filtration, washed with excess water, and dried under vacuum. The title compound was finally obtained as a dark red solid (128 mg, 35%). ^{1}H NMR (CD_3CN, 500 MHz): 9.02 (s, 2H), 8.96 (s, 4H), 8.18 (s, 2H), 7.97 (dd, 4H), 7.87 (d, 2H), 7.74 (m, 6H), 3.72 (m, 8H), 3.24 (t, 4H), 3.11 (t, 4H). HRMS (ESI-MS) m/z: $[M]^{2+}$ Calcd for $C_{44}H_{40}F_{12}N_{10}O_4Ru$: 551.10429, Found 551.1049.

This complex as isolated was not soluble in CH_2Cl_2, which prevented its characterization in that solvent. To enhance the solubility in CH_2Cl_2, ion metathesis to the B(ArF)$_4$ salt was performed

following a previously published procedure.[37,38] Briefly, a 95% yield of $[Ru(dtfmb)_2(daea)](NO_3)_2$ was assumed for the solid obtained from the reaction mixture after evaporation, as described above. This solid was dissolved in minimal H_2O (5 mL), and $NaB(ArF)_4$ (200 mg, 2 equivalents relative to the predicted ruthenium yield) in MeOH (3 mL) was added, causing a precipitate to form. The solid was collected by filtration and washed with excess H_2O. All subsequent experiments were performed using the $B(ArF)_4$ salt of the complex.

2.3 Results and Discussion

The diamide ligand for halide recognition shown in **Figure 2.1** is abbreviated **daea** and was synthesized by refluxing 4,4′-dimethylester-2,2′-bipyridine in the presence of a large excess of 2-[(2-aminoethyl)amino]ethanol in methanol for 4h. Microwave irradiation of this ligand with $Ru(dtb)_2Cl_2$ (dtb = 4,4′-di-*tert*-butyl-2,2′-bipyridine) in H_2O gave complex $\mathbf{1}^{2+}$ that was further isolated as the PF_6 salt. Complex $\mathbf{2}^{2+}$ was obtained by refluxing the **daea** ligand with $Ru(btfmb)_2Cl_2$ (btfmb = 4,4′-bis(trifluoromethyl)-2,2′-bipyridine) and silver nitrate in H_2O: MeOH (1:1) for 5h. Ion metathesis was finally performed to obtain $\mathbf{2}^{2+}$ as a $B(ArF)_4$ salt. (Figure **S2.1-S2.6**) All subsequent experiments were performed in CH_2Cl_2. Square wave voltammetry was used to determine the $Ru^{III/II}$ and ligand-based reduction potentials. Due to the electron withdrawing **btfmb** ligand, the $Ru^{III/II}$ potential of $\mathbf{2}^{2+}$ was found to be 300 mV more positive than that of $\mathbf{1}^{2+}$, and the first ligand based reduction potentials were -880 mV and -470 mV vs NHE for $\mathbf{1}^{2+}$ and $\mathbf{2}^{2+}$, respectively (**Figure S2.7**).

The use of ^1H NMR spectroscopy provided insights into the coordination environment of the chloride ions. Anions are known to affect the local magnetic environment of neighboring nuclei, such that the chemical shift can report on the specific location of a halide ion.[39–42] Tetrabutylammonium chloride titrations into solutions of $\mathbf{1}^{2+}$ and $\mathbf{2}^{2+}$ showed that the 3,3′ protons

on the **daea** ligand, as well as the amide protons, displayed significant downfield shifts, while the other resonances remained unchanged (**Figure S2.8 and S2.9**). These downfield shifts saturated after one equivalent of chloride was added, pointing towards a one-to-one stoichiometry. The ^{1}H NMR data indicates that a single chloride ion binds to the two amide groups and the acidic H atoms of the bipyridine ligand, which elongates the C- and N-H bonds and thereby reduces the electron density at these protons, causing downfield shifts of the signals.[40] This behavior has been observed for halide self-assembly to related chromophores.[40,41,43]

The UV-Visible absorption spectra of $\mathbf{1}^{2+}$ and $\mathbf{2}^{2+}$ in CH_2Cl_2 were typical of ruthenium polypyridyl complexes (**Figure 2.2**). The broad absorption from 400 to 500 nm was ascribed to metal-to-ligand charge-transfer (MLCT) transitions, while the features at or below 300 nm were assigned to ligand centered π to π^* transitions. Upon absorption of visible light, both complexes displayed room temperature photoluminescence (PL) with maxima at 665 and 600 nm for $\mathbf{1}^{2+}$ and $\mathbf{2}^{2+}$, respectively.

Chloride titrations into solutions of $\mathbf{1}^{2+}$ or $\mathbf{2}^{2+}$ induced significant spectral shifts in the MLCT absorption band that saturated after about one equivalent, consistent with strong ion-pairing of chloride, **Figure 2.2**. A Benesi-Hildebrand analysis revealed a large equilibrium constant of 3.9×10^{6} M^{-1} for $\mathbf{1}^{2+}$ (**Figure S2.10**).[40,44] An accurate K_{eq} determination for $\mathbf{2}^{2+}$ was hindered by precipitation of the chromophore and potential ligand substitution at high chloride concentrations, however the absorption changes over the chloride concentration allowed were in good agreement with that of $\mathbf{1}^{2+}$ from which a value of 4×10^{6} M^{-1} was estimated (**Figure S2.11**). Supramolecular assembly was also observed with Br^- and I^-, but excited-state reactivity complicated further analysis with these halides. Additionally, experiments in more polar solvents such as CH_3CN revealed ground-state equilibrium constants that were systematically one to two orders of

magnitude smaller (6.7×10^4 M^{-1} for $\mathbf{1}^{2+}$ with Cl^-) than those observed in CH_2Cl_2, which has also been observed for related compounds.[41]

Table 2.1. Photophysical Properties of Complexes $\mathbf{1}^{2+}$, $\mathbf{2}^{2+}$ and their chloride-ion-paired analogues in CH_2Cl_2.

	λ_{max} (nm)		τ	ϕ_{PL}	k_r	k_{nr}
	Abs	PL	(μs)		($\times10^4$ s^{-1})	($\times10^5$ s^{-1})
1^{2+}	474	665	1.18	0.061	5.2	8.0
$[1^{2+},Cl^-]$	471	640	1.33	0.12	6.8	4.80
2^{2+}	459	600	1.36	0.095	7.0	6.7
$[2^{2+},Cl^-]$	469	630	1.78[a]	-b	-b	-b

[a]Estimated from the time-resolved PL of $\mathbf{2}^{2+}$ at one equivalent of chloride. [b]Unable to be determined due to precipitation of the complex at high chloride concentrations.

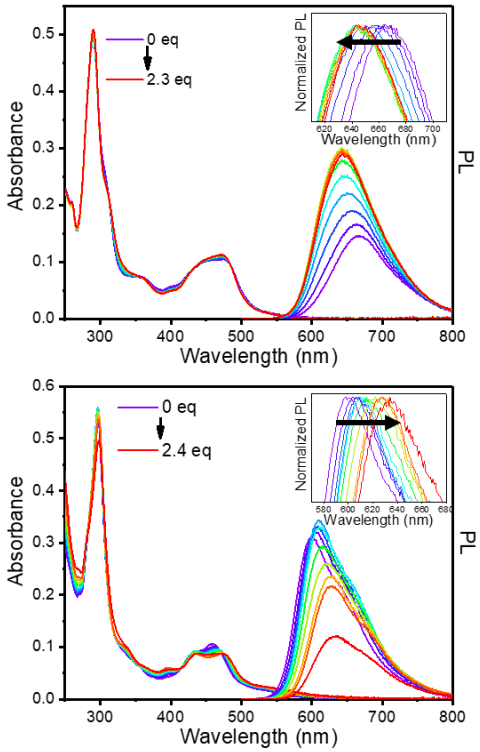

Figure 2.2: Absorption and PL changes of 1^{2+} (top) and 2^{2+} (bottom) upon titration of chloride from 0 to 2.3/2.4 equivalents in CH_2Cl_2. Inset shows the normalized PL shifts upon titration of chloride.

The steady state PL spectra also shifted in energy as chloride was titrated into the solution. In the case of $\mathbf{1}^{2+}$*, the PL maximum blue-shifted and increased in intensity with increased Cl^- concentrations to about one equivalent. Previous reports have attributed related excited-state interactions to halide-induced planarization of the two pyridyl rings.[30,45] For $\mathbf{2}^{2+}$*, the excited-state

was localized on the **btfmb** ancillary ligand (as discussed below), and a red-shift in the PL was observed upon chloride titration. The red-shift was accompanied by a change in the PL intensity, but precipitation and potential ligand substitution at higher chloride concentrations precluded a more detailed analysis. Indeed, precipitation in these experiments was observed as a baseline shift in the delta absorbance spectrum (**Figure S2.11**), which was also concurrent with a moderate growth at 570 nm that could correspond to ligand substitution.[43,46] Both of these results contribute to the decrease in photoluminescence intensity.

The fact that the supramolecular assembly of chloride ions caused a PL blue-shift for $\mathbf{1}^{2+}$* and a PL red-shift for $\mathbf{2}^{2+}$* can be understood based on the location of the associated halide ion relative to the excited-state dipole. For this class of chromophores, Blakley and De Armond have shown that the charge transfer dipole is directed toward the ligand that is most easily reduced.[47] The first reduction potential of $\mathbf{1}^{2+}$ is -880 mV vs. NHE, which compares favorably to that of the related $[Ru(bpy\text{-}CONHEt)_3]^{2+}$ (-880 mV vs NHE),[48] but not that of $[Ru(dtb)_3]^{2+}$ (-1000 mV).[49] Therefore, in $\mathbf{1}^{2+}$ the excited-state dipole is directed toward the **daea** ligand, and the luminescent excited-state was well formulated as $[Ru^{III}(daea^{-})(dtb)_2]^{2+}$*, with the dipole directed toward the halide binding site. Hence halide self-assembly in the excited state is formally described with an anionic ligand that destabilizes the excited-state resulting in a blue-shift in photoluminescence.

In contrast, the electron withdrawing groups in $\mathbf{2}^{2+}$ lower the reduction potential to -470 mV, that compares reasonably with the -530 mV first reduction of $[Ru(btfmb)_3]^{2+}$.[50] The excited-state of $\mathbf{2}^{2+}$ is hence well formulated as $[Ru^{III}(daea)(btfmb^{-})(btfmb)]^{2+}$*. Hence, halide supramolecular assembly involves a ligand that is not directly aligned with the charge transfer dipole that stabilizes the excited-state resulting in a red-shifted PL spectrum.

Pulsed light excitation provided photoluminescence decays that were well described by a first-order kinetic model and yielded lifetimes of τ = 1.18 μs and 1.36 μs for $\mathbf{1}^{2+}$ and $\mathbf{2}^{2+}$, respectively. Chloride titration studies with $\mathbf{1}^{2+}$ led to the appearance of bi-exponential kinetics (**Figure S2.12 and S2.13**). At large chloride concentrations, a single exponential decay was again recovered with τ = 1.33 μs. Quantum yield measurements performed in the absence and presence of excess chloride allowed the radiative and non-radiative rate constants for excited state decay to be determined, **Table 2.1**. This analysis revealed that the increased lifetime and PL intensity associated with Cl^- assembly to $\mathbf{1}^{2+}$, resulted from an approximately two-fold change in the non-radiative rate constant. The analogous titration study with $\mathbf{2}^{2+}$ was frustrated by precipitation and potential ligand substitution, however no evidence for bi-exponential excited state relaxation was observed.

The PL spectrum recorded at fixed delay times after pulsed light excitation were measured and found to be very informative. Representative data are shown in **Figure 2.3** for $\mathbf{1}^{2+}$ and $\mathbf{2}^{2+}$ with one equivalent of chloride, abbreviated $[\mathbf{1}^{2+},Cl^-]^+$ and $[\mathbf{2}^{2+},Cl^-]^+$ respectively. In the case of $\mathbf{1}^{2+}$, the PL spectrum measured 3 μs after excitation was considerably red shifted from that measured at a 45 ns delay time. Spectra recorded at intermediate times showed a continuous spectral shift to lower energy. This transient data is consistent with light excitation resulting in Cl^- release followed by re-equilibration.

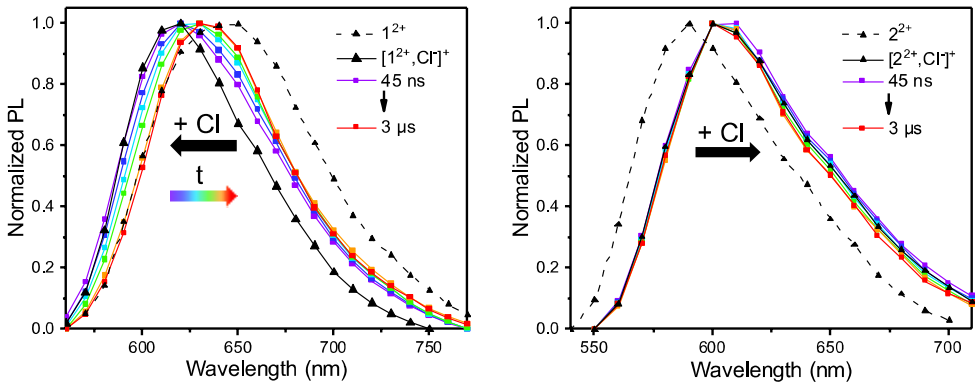

Figure 2.3: Transient photoluminescence spectra obtained 45 ns (purple square) and at longer (purple to red) time delays after pulsed 500 nm laser excitation of $[Ru(dtb)_2(daea)]^{2+}$, 1^{2+} (left) and $[Ru(btfmb)_2(daea)]^{2+}$, 2^{2+} (right) in the presence of one equivalent of chloride. The photoluminescence spectra of the non-ion-paired complexes is also given for reference (Black triangle, dashed lined). The bold black arrow indicated the spectral shift expected for chloride self-assembly. The colored arrow indicates the time dependent spectral shift.

For $\mathbf{2}^{2+}$, the addition of chloride did not affect the time-resolved PL, which was well described by a first order kinetic model throughout the titration. Transient PL experiments of $\mathbf{2}^{2+}$ with an equivalent of chloride did not show any time-dependent color change. It should be noted that the PL spectra measured in these transient experiments were different from the steady state spectral data in **Table 2.1** and **Figure 2.2** that were corrected for the fluorimeter spectral response.

A square scheme with ground and excited-state equilibrium is proposed like those commonly used to understand photo- acid/base chemistry, **Figure 2.4**.[30,32–34,51] The ground state equilibrium is associated with the excited-state equilibrium through light absorption to yield the thermally equilibrated photoluminescent excited-state. The differential rate equations for the two excited-state species A* and B*, where A is either $\mathbf{1}^{2+}$ or $\mathbf{2}^{2+}$ and B is either $[\mathbf{1}^{2+},Cl^-]^+$ or $[\mathbf{2}^{2+},Cl^-]^+$, are given in equations 1 and 2. The analytical solutions for these equations have been derived elsewhere[32–34] and were used to fit the experimental data. An interesting point is that the rate constants extracted from a bi-exponential fit do not correspond to relaxation of the two excited-states present (i.e. k_1 and k_2), but rather report on the entire equilibrium system and hence provide the excited-state equilibrium constant, K^*_{eq}.

$$\frac{d[A*]}{dt} = -(k_{12} + k_1)[A^*] + (k_{21})[B^*] \quad (1)$$

$$\frac{d[B*]}{dt} = -(k_{21} + k_2)[B^*] + (k_{12})[A^*] \quad (2)$$

Application of this kinetic analysis to $\mathbf{1}^{2+}$* gave the forward (k_{12} = 1.8×10^{11} M^{-1} s^{-1}) and reverse (k_{21} = 9.1×10^5 s^{-1}) rate constants that corresponds to K*$_{eq}$ = 1.7×10^5 M^{-1} which differs from that of the ground state by a factor of 20 (K$_{eq}$ = 3.9×10^6 M^{-1}).

It should be emphasized that this analysis is for the thermally equilibrated excited-state, and the rate constant for chloride dissociation in the initially formed Franck-Condon excited-state may be much larger as relaxation back to the luminescent excited state occurs with the transfer of considerable electron density from the **daea** ligand back to the metal. The kinetic data is nevertheless important for understanding the behavior of the luminescent excited state. For example, 500 ns after photoexcitation of [$\mathbf{1}^{2+}$,Cl$^-$]$^+$ about 45% of the excited states have dissociated chloride (**Figure S2.14**).

Complex [$\mathbf{2}^{2+}$,Cl$^-$]$^+$ displayed remarkably different excited state behavior than [$\mathbf{1}^{2+}$,Cl$^-$]$^+$. In the time-resolved PL, the decay kinetics remained first-order even after the addition of chloride. Also, photoexcitation of the ion-paired complex did not result in time dependent shifts in the PL spectra. Nonetheless, in regards to the red-shift of the photoluminescence between $\mathbf{2}^{2+}$ and [$\mathbf{2}^{2+}$,Cl$^-$]$^+$, an increased binding constant is expected. This was confirmed through Förster cycle analysis that showed a 45-fold increase in the excited-state equilibrium constant (**Table 2.2**).

Table 2.2. Equilibrium constants for 1^{2+} and 2^{2+} with chloride in the ground and excited-state.

	K$_{eq}$ (M^{-1})	K$_{eq}$* (M^{-1})	k_{12} (10^{11} M^{-1} s^{-1})	k_{21} (10^5 s^{-1})
[1^{2+},Cl$^-$]$^+$	3.9×10^6	1.7×10^5	1.8	9.1
[2^{2+},Cl$^-$]$^+$	4×10^6 [a]	1.9×10^8 [b]	[c]	[c]

[a]The incertainty was larger for this equilibrium due to precipitation of the complex at high chloride concentrations. [b]Estimated using a Förster cycle. [c]There was no spectroscopic evidence for differing ground and excited-state equilibrium, precluding kinetic analysis.

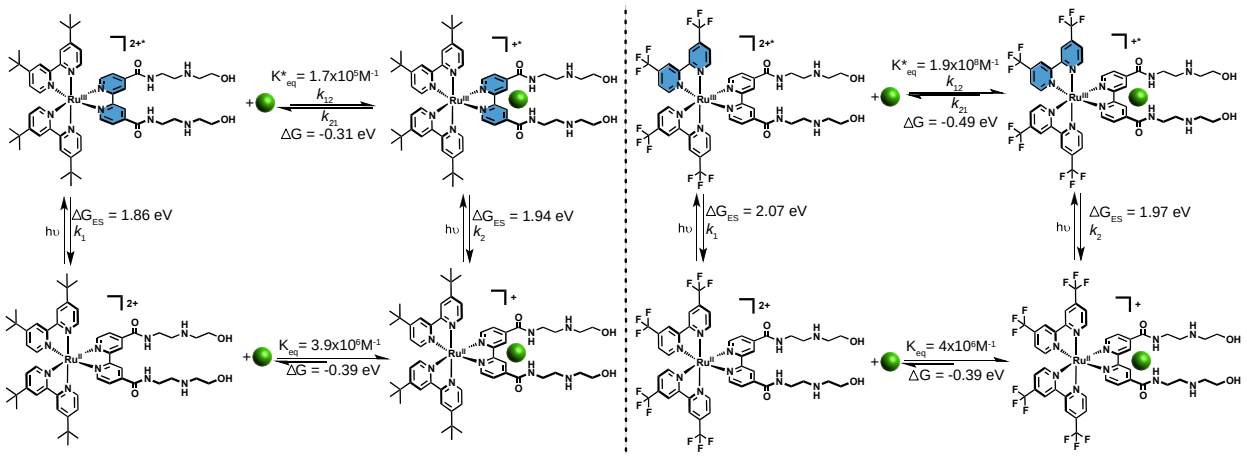

Figure 2.4: Square Scheme for ground and excited-state equilibria of $[Ru(dtb)_2(daea)]^{2+}$, 1^{2+} (left) and $[Ru(btfmb)_2(daea)]^{2+}$, 2^{2+} (right) in the presence of chloride. The blue shading indicates the location of the electron in the MLCT excited-state, while the green sphere represents chloride. Förster cycle analysis was used to calculate K^*_{eq} for 1^{2+} and 2^{2+}. The calculated K^*_{eq} for 1^{2+} is consistent with the kinetic analysis from the square scheme.

The supramolecular assembly of chloride ions resulted in excited states that either retained, $[\mathbf{2}^{2+}, Cl^-]^+$*, or released, $[\mathbf{1}^{2+}, Cl^-]^+$*, chloride ions. The former are useful for chloride sensing,[1,2,12,13] while the latter may be exploited for delivery.[52–57] The photo-release described here has the advantage of rapid release of Cl^- in about 150 ns. The self-assembly of the photo-released Cl^- was advantageous for signal averaging with pulsed lasers, but is not ideal for many other applications. For biological and desalination applications,[26–28] halide self-assembly must occur in water where irreversible release may be desired. The supramolecular assembly described here takes advantage of the Coulombic attraction of the dication chromophore and the halide anion, as well as the H-bonding properties of the **daea** ligand. The low dielectric constant of the organic solvent utilized here enhances the Coulombic attraction, and for application in aqueous environments, the halide recognition ability of the ligand would require enhancement. The difference in ground and excited state equilibrium constants combined with advances in halide sensing in water,[1] suggests that fine tuning can be realized.

2.4 Conclusions

Two ruthenium chromophores, $[Ru(dtb)_2(daea)]^{2+}$ ($\mathbf{1}^{2+}$) and $[Ru(btfmb)_2(daea)]_{2+}$ ($\mathbf{2}^{2+}$), exhibited very different excited state behaviors in the supramolecular assembly with chloride. When the excited state dipole was directed away from the **daea** halide receptor ligand, as was the case for $[\mathbf{2}^{2+},Cl^-]^+$, the equilibrium constant for chloride assembly in the excited state was greater than in the ground state. In dramatic contrast, when the excited-state dipole was oriented toward the chloride anion, as was the case for $[\mathbf{1}^{2+},Cl^-]^+$, the excited-state equilibrium constant was reduced by a factor of 20 from that of the ground state, which resulted in the rapid loss of the chloride ion upon light absorption. Preliminary results show that this approach is generalizable across the halide series, although excited-state reactivity was observed with iodide. However, such reactivity can be avoided through tuning of the excited-state reduction potentials.

Most practical applications of this advance would require aqueous conditions. The compounds presented herein are unlikely to even bind halides from water, as halide binding is inversely proportional to the solvent dielectric constant.[3] Indeed, about a two order of magnitude decrease in equilibrium constant was found here when the solvent was changed from dichloromethane ($\varepsilon = 8.9$) to acetonitrile ($\varepsilon = 37.5$), which is in agreement with previous findings.[41] Transposition to water ($\varepsilon = 80.1$) presents further challenges, as favorable solvent-solute interactions must also be overcome.[58] However, significant advances in halide binding in water and organic solvent/water mixtures have been achieved through the use of rigid receptor ligands and supramolecular complexes such as cavitand, where the local polar environment is controlled at the molecular level.[58–60] Utilization of these supramolecular complexes with the correctly tuned excited-state properties could one day lead to enhanced anion binding or photorelease in polar solvents. Overall, this data and analysis show that with appropriate synthetic design, chromophores

that rapidly release or completely retain a chloride ion when excited with visible light can be realized in fluid solution.

2.5 Supporting Information

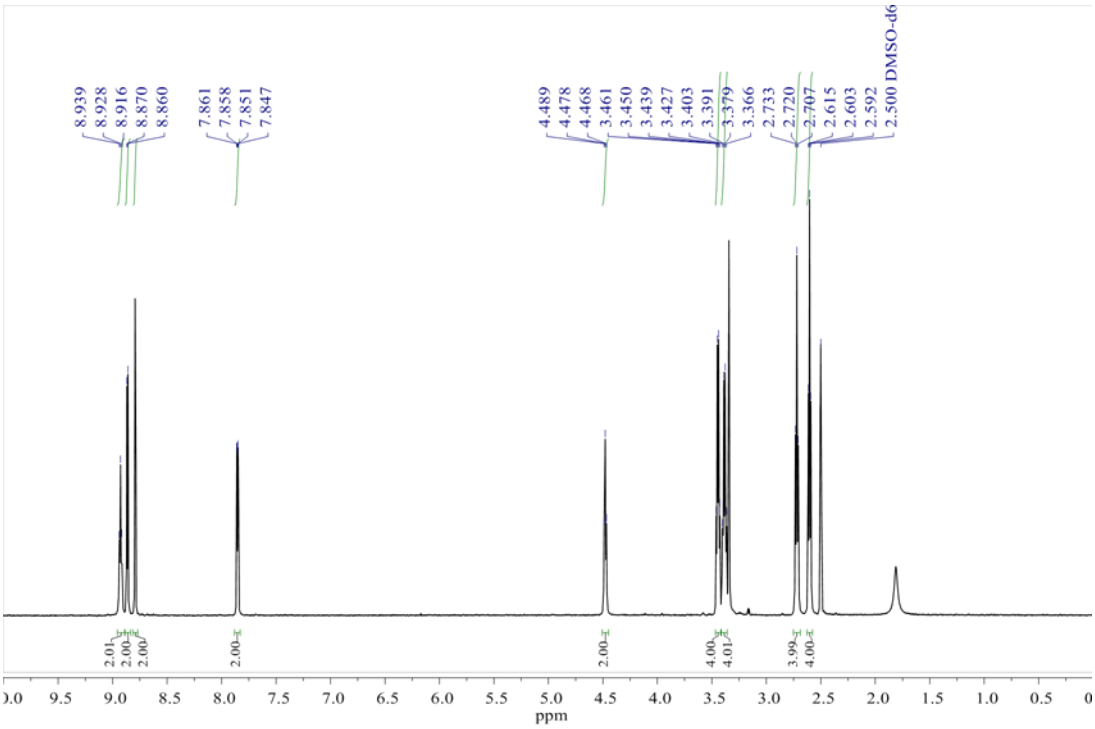

Figure S2.1: ^{1}H NMR of daea in DMSO at 500 MHz and 298 K.

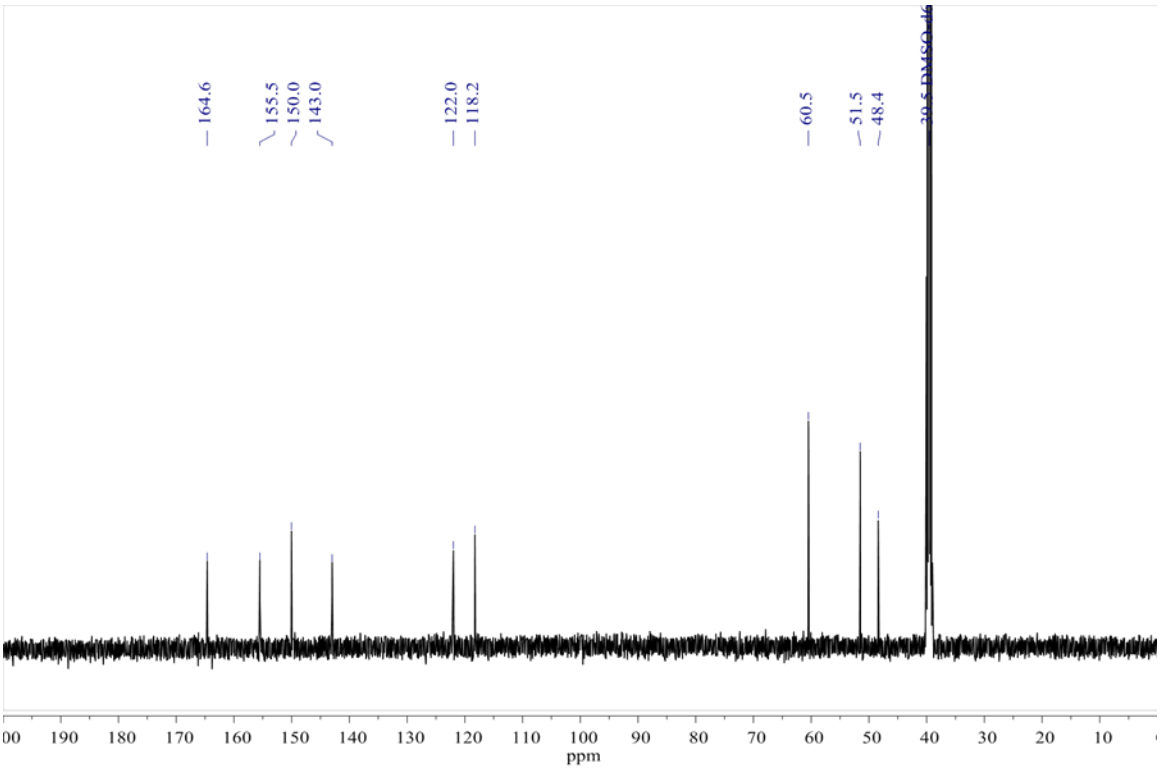

Figure S2.2: ^{13}C NMR of daea in DMSO at 126 MHz and 298 K.

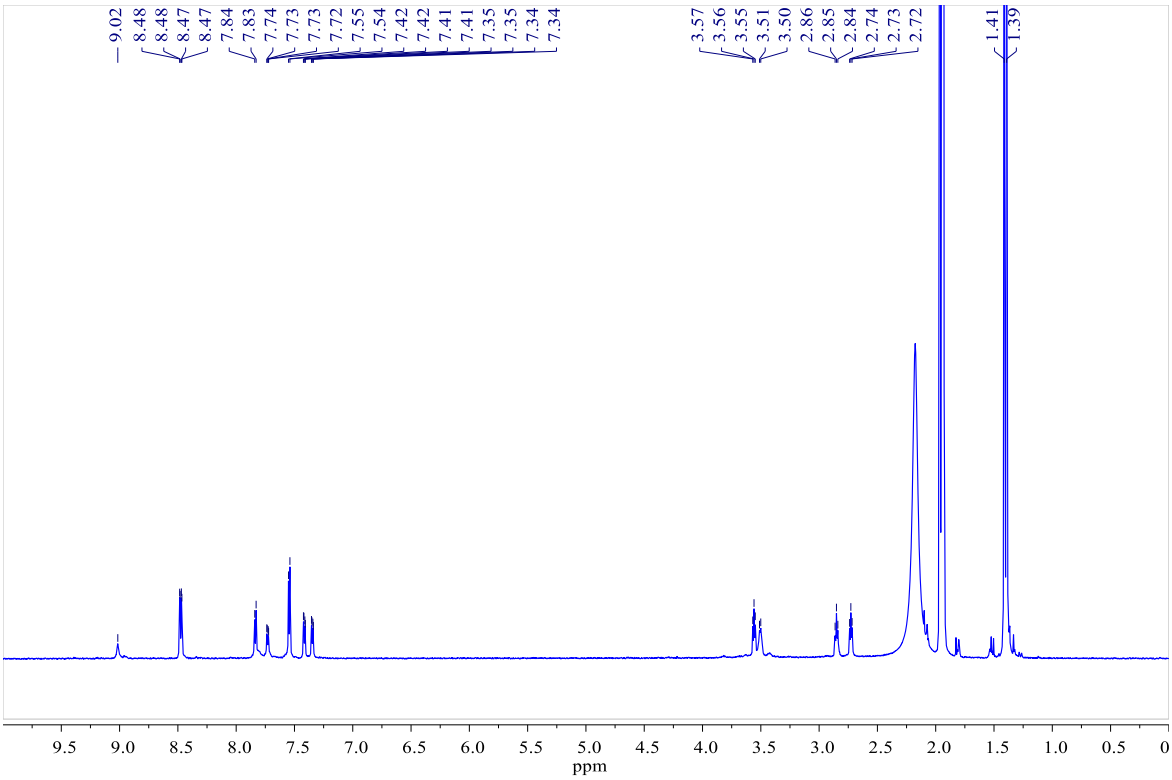

Figure S2.3: ^{1}H NMR of $[Ru(dtb)_2(daea)](PF_6)_2$ in CD_3CN at 500 MHz and 298 K.

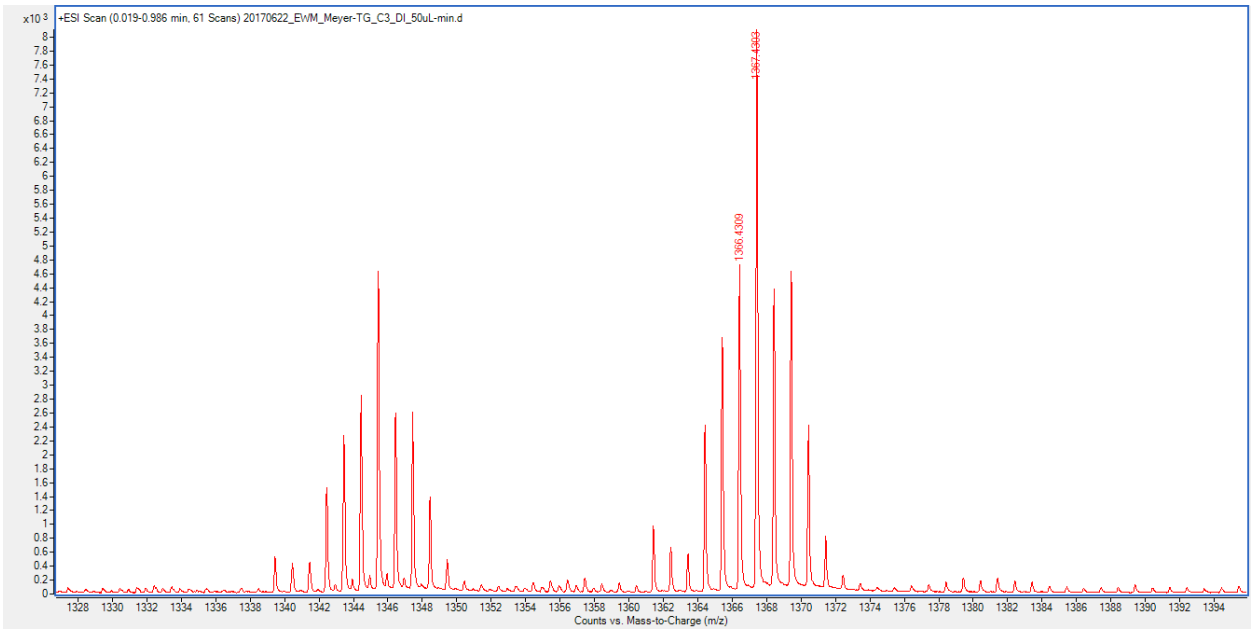

Figure S2.4: High-Resolution Mass Spectrum of $[Ru(dtb)_2(daea)](PF_6)_2$.

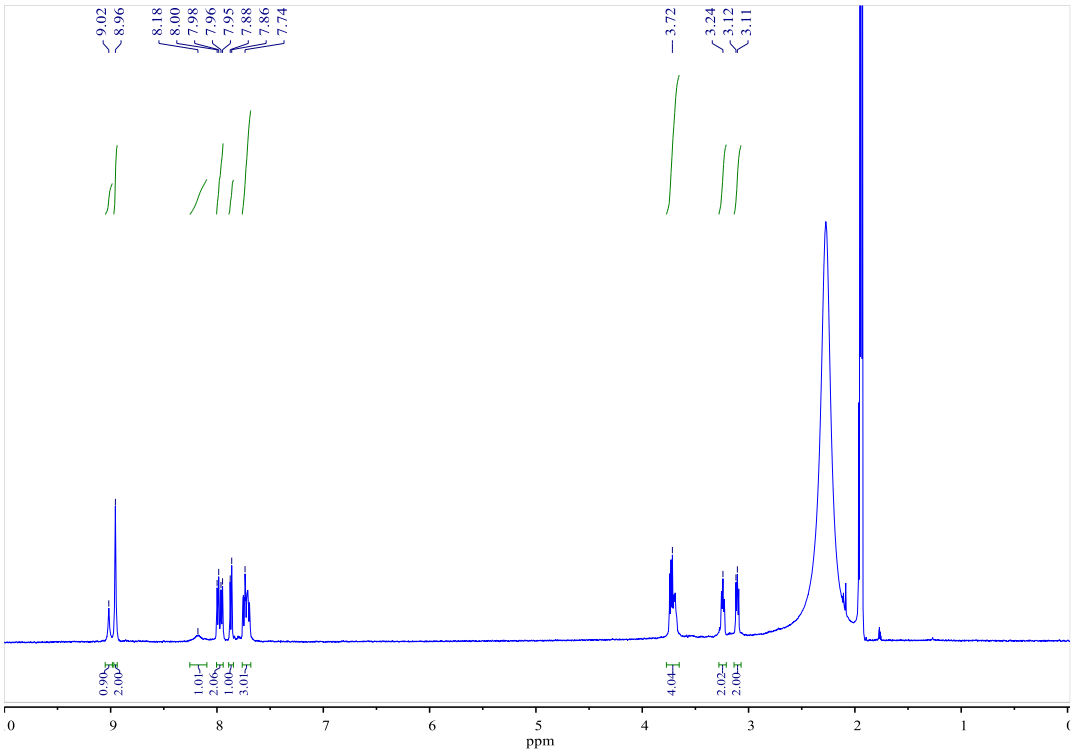

Figure S2.5: ^{1}H NMR of [Ru(btfmb)$_2$(daea)](PF$_6$)$_2$ in CD$_3$CN at 500 MHz and 298 K.

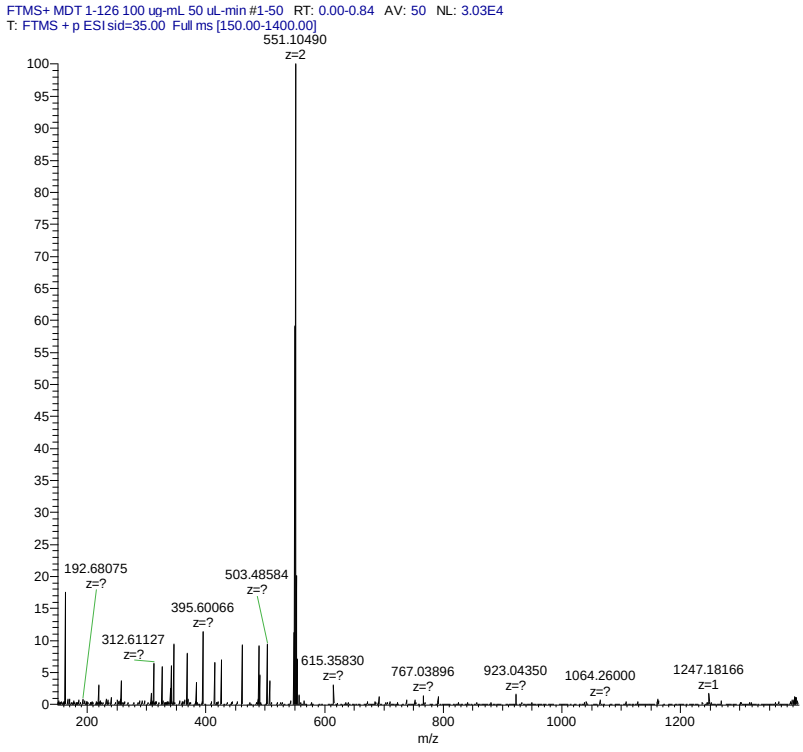

Figure S2.6: High-Resolution Mass Spectrum of [Ru(btfmb)$_2$(daea)](PF$_6$)$_2$.

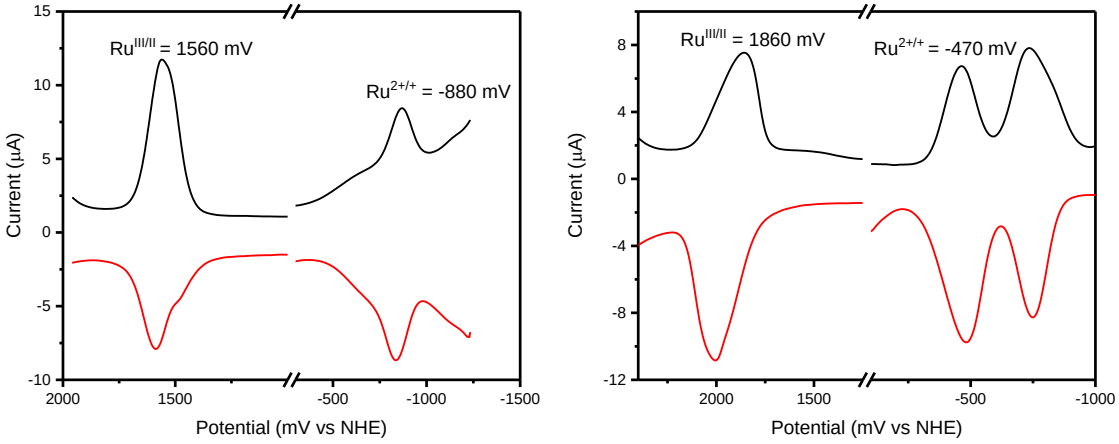

Figure S2.7: Square-wave voltammogram of 1^{2+} (left) and 2^{2+} (right) at 1.0 mM concentrations in CH_2Cl_2 with 0.1 M tetrabutylammonium perchlorate in solution. The potentials are referenced to NHE.

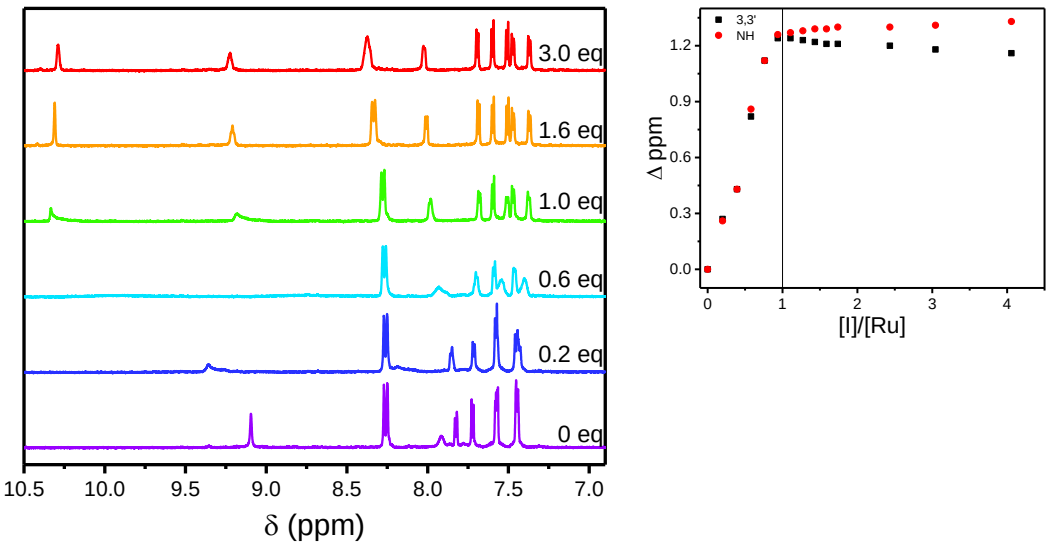

Figure S2.8: ^{1}H NMR of 1^{2+} in CD_2Cl_2 as TBACl is titrated into solution (left). Changes in ppm of the 3,3′ and amide (NH) protons on the daea ligand with increasing chloride concentration (right). These changes saturate at a [I]/[Ru] = 1.

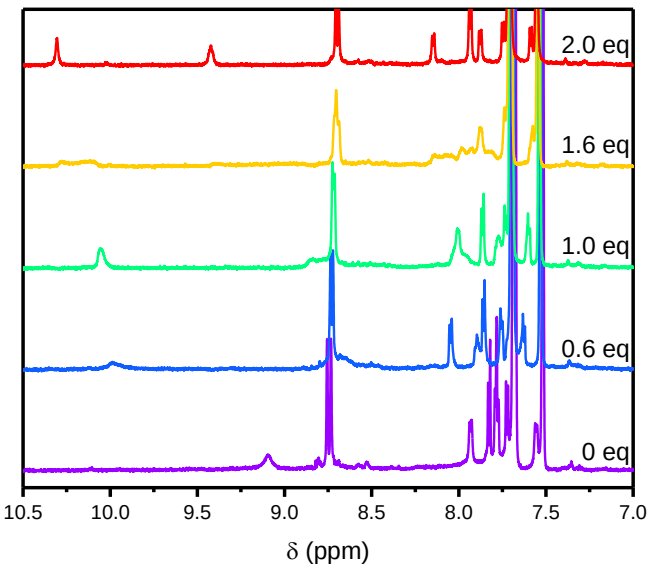

Figure S2.9: ^{1}H NMR of 2^{2+} ($B(ArF)_4$ salt) in CD_2Cl_2 as TBACl is titrated into the solution.

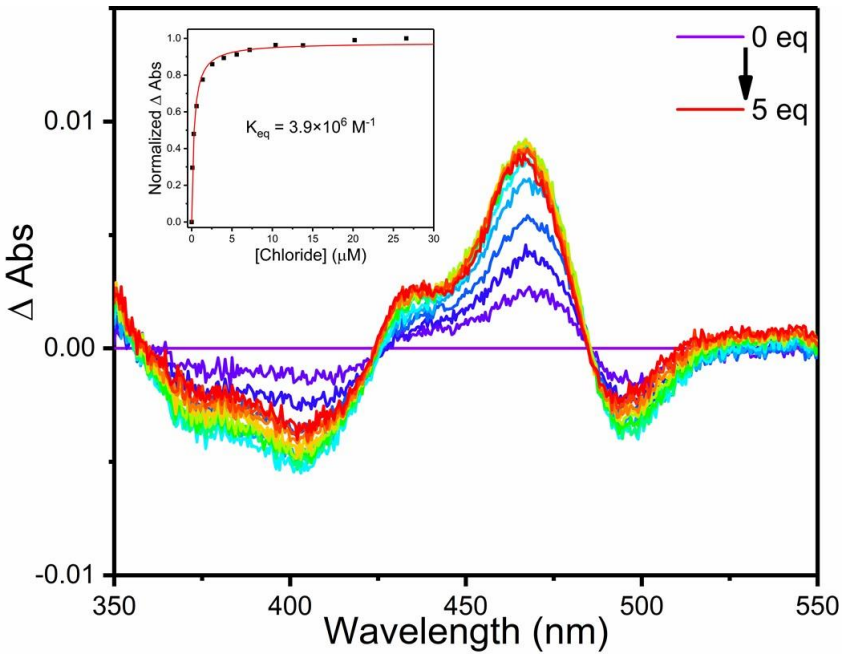

Figure S2.10: Difference absorption spectra of 1^{2+} in CH_2Cl_2 as tetrabutylammonium chloride (TBACl) is titrated into solution. Inset shows Benesi-Hildebrand analysis which was used to give the ground state binding constant.

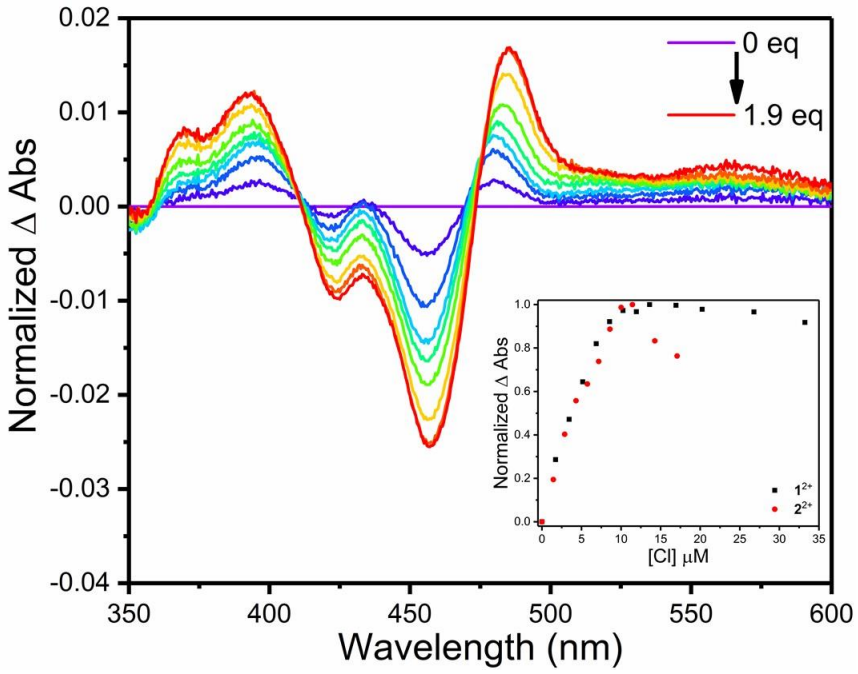

Figure S2.11: Difference absorption spectra of 2^{2+} in CH_2Cl_2 as TBACl is titrated into solution. The inset shows the absorption changes with increasing chloride concentration for 1^{2+} and 2^{2+}. These changes indicate a similar binding constant for the two complexes.

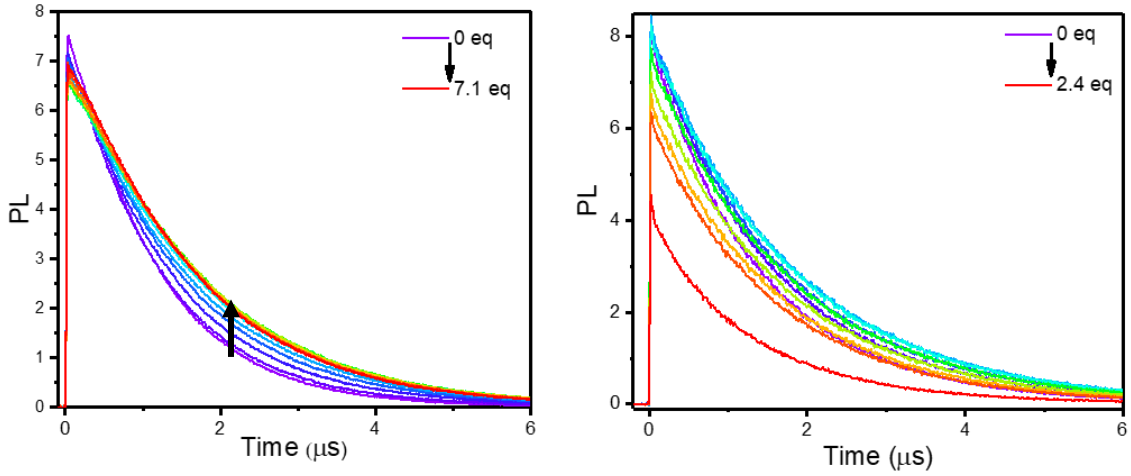

Figure S2.12: Time-resolved photoluminescence decay traces of 1^{2+} (left) and 2^{2+} (right) in CH_2Cl_2 as TBACl is titrated into solution.

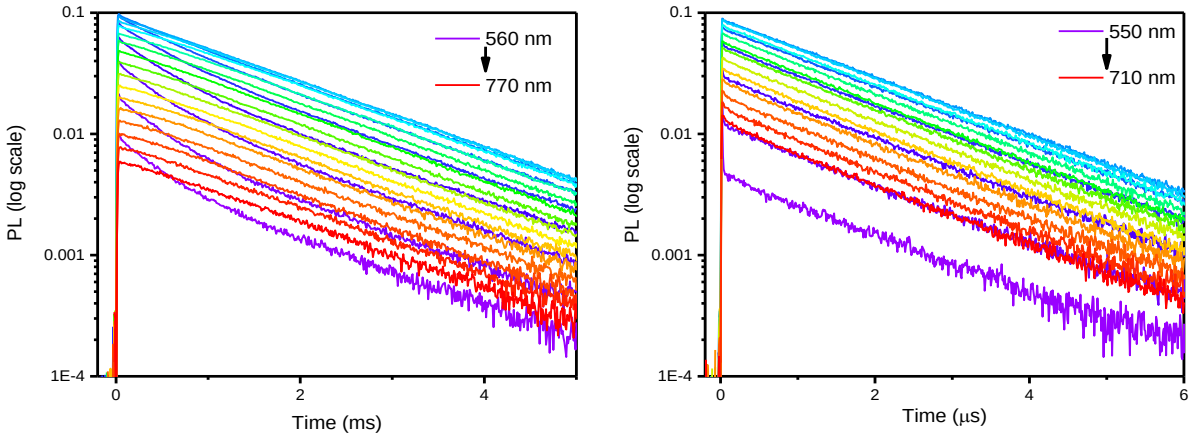

Figure S2.13: PL traces of 1^{2+} (left, measured from 560 to 770 nm with 10 nm increment) and 2^{2+} (right, measured from 550 to 710 nm with 10 nm increment) in CH_2Cl_2 with one equivalent of added chloride. The log scale of the PL intensity shows biexponential kinetic behavior for $[1^{2+},Cl^-]^+$ and single exponential kinetic behavior for $[2^{2+},Cl^-]^+$.

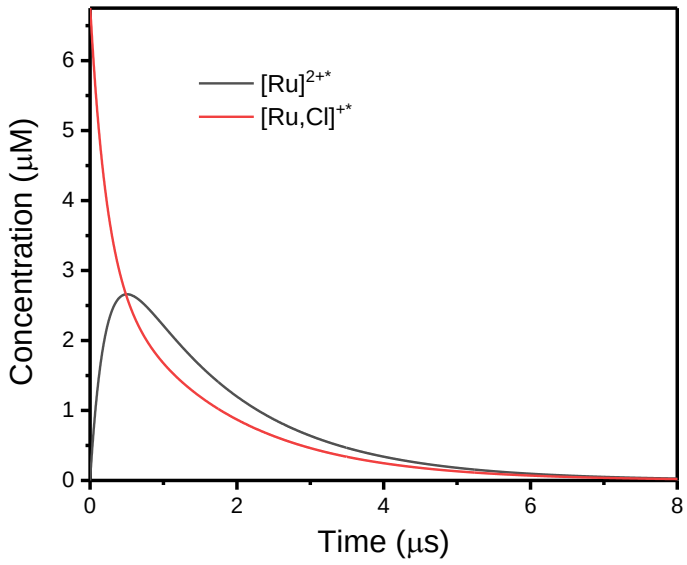

Figure S2.14: Results from the square-scheme analysis which show the concentrations changes of 1^{2+} and ion-paired $[1^{2+},Cl^-]^+$ upon excitation.

REFERENCES

(1) Beer, P. D; Gale, P. A. Anion Recognition and Sensing: The State of the Art and Future Perspectives. *Angew. Chem. Int. Ed.* **2001**, *40*, 486–516.

(2) Evans, N. H.; Beer, P. D. Advances in Anion Supramolecular Chemistry: From Recognition to Chemical Applications. *Angew. Chem. Int. Ed.* **2014**, *53*, 11716–11754.

(3) Liu, Y.; Sengupta, A.; Raghavachari, K.; Flood, A. H. Anion Binding in Solution: Beyond the Electrostatic Regime. *Chem.* **2017**, *3*, 411–427.

(4) Rebarz, M.; Marcélis, L.; Menand, M.; Cornut, D.; Moucheron, C.; Jabin, I.; Kirsch-De Mesmaeker, A. Revisited Photophysics and Photochemistry of a Ru-TAP Complex Using Chloride Ions and a Calix[6]crypturea. *Inorg. Chem.* **2014**, *53*, 2635–2644.

(5) Brunetti, E.; Picron, J. F.; Flidrova, K.; Bruylants, G.; Bartik, K.; Jabin, I. Fluorescent Chemosensors for Anions and Contact Ion Pairs with a Cavity-Based Selectivity. *J. Org. Chem.* **2014**, *79*, 6179–6188.

(6) Goursaud, M.; De Bernardin, P.; Cort, A. D.; Bartik, K.; Bruylants, G. Monitoring Fluoride Binding in DMSO: Why is a Singular Binding Behavior Observed? *Eur. J. Org. Chem.* **2012**, 3570–3574.

(7) Lau, Y. H.; Rutledge, P. J.; Watkinson, M.; Todd, M. H. Chemical sensors that incorporate click-derived triazoles. *Chem. Soc. Rev.* **2011**, *40*, 2848–2866.

(8) Cort, A. D.; Bernardin, P. D.; Forte, G.; Mihan, F. Y. Metal–Salophen-Based Receptors for Anions. *Chem. Soc. Rev.* **2010**, *39*, 3863–3874.

(9) Cametti, M.; Rissanen, K. Recognition and sensing of fluoride anion. *Chem. Commun.* **2009**, 2809–2829.

(10) Cametti, M.; Cort, A. D.; Bartik, K. Fluoride Binding in Water: A New Environment for a Known Receptor. *ChemPhysChem* **2008**, *9*, 2168–2171.

(11) Bisson, A. P.; Lynch, V. M.; Monahan, M. K. C.; Anslyn, E. V. Recognition of Anions through NH-π Hydrogen Bonds in a Bicyclic Cyclophane- Selectivity for Nitrate. *Angew. Chem. Int. Ed. Engl.* **1997**, *36*, 2340–2342.

(12) Szemes, F.; Hesek, D.; Chen, Z.; Dent, S. W.; Drew, M. G. B.; Goulden, A. J.; Graydon, A. R.; Grieve, A.; Mortimer, R. J.; Wear, T.; Weightman, J. S.; Beer, P. D. Synthesis and Characterization of Novel Acyclic, Macrocyclic, and Calix[4]arene Ruthenium(II) Bipyridyl Receptor Molecules That Recognize and Sense Anions. Inorg. Chem. 1996, 35, 5868–5879.

(13) Uppadine, L. H.; Drew, M. G. B.; Beer, P. D. Anion Selectivity Properties of Ruthenium(II)

tris(5,5′-diamide-2,2′-bipyridine) Receptors Dictated by Solvent and Amide Substituent. *Chem. Commun.* **2001**, 291–292.

(14) Glebov, E. M.; Pozdnyakov, I. P.; Plyusnin, V. F.; Khmelinskii, I. Primary Reactions in the Photochemistry of Hexahalide Complexes of Platinum Group Metals: A Minireview. *J. Photochem. Photobiol. C Photochem. Rev.* **2015**, *24*, 1–15.

(15) Balzani, V.; Manfrin, F.; Moggi, L. Photochemistry of Coordination Compounds. XVI. Hexabromoplatinate(IV) and Hexaiodoplatinate(IV) Ions. *Inorg. Chem.* **1967**, *6*, 354–358.

(16) Balzani, V.; Carassiti, V. Photochemistry of Some Square-Planar and Octahedral Platinum Complexes. *J. Phys. Chem.* **1968**, *72*, 383–388.

(17) Pozdnyakov, I. P.; Glebov, E. M.; Plyusnin, V. F.; Tkachenko, N. V.; Lemmetyinen, H. Primary Processes in Photophysics and Photochemistry of $PtBr_6^{2-}$ Complex Studied by Femtosecond Pump–Probe Spectroscopy. *Chem. Phys. Lett.* **2007**, *442*, 78–83.

(18) Glebov, E. M.; Plyusnin, V. F.; Grivin, V. P.; Venediktov, A. B.; Korenev, S. V. Photochemistry of $PtBr_6^{2-}$ in Aqueous Solution. *Russ. Chem. Bull.* **2007**, *56*, 2357–2363.

(19) Wright, R. C.; Laurence, G. S. Production of Platinum(III) by Flash Photolysis of $PtCl_6^{2-}$**.** *J. Chem. Soc., Chem. Comm.* **1972**, 132–133.

(20) Znakovskaya, I. V.; Sosedova, Y. A.; Glebov, E. M.; Grivin, V. P.; Plyusnin, V. F. Intermediates Formed by Laser Flash Photolysis of $[PtCl_6]^{2-}$ in Aqueous Solutions. *Photochem. Photobiol. Sci.* **2005**, *4*, 897–902.

(21) Wong, C. F. C.; Kirk, A. D. Chloride Quantum Yields from Photolysis of Chloropentammine and Chloropentakisalkynlamino Chromium(III) Complexes. *Can. J. Chem.* **1974**, *52*, 3384–3386.

(22) Adamson, A. W. Photochemistry of Complex Ions. The Role of Quartet Excited States in the Photochemistry of Chromium (III) Complexes. *J. Phys. Chem.* **1967**, *71*, 798–808.

(23) Kirk, A. D.; Moss, K. C.; Valentin, J. G. Photochemistry of the *cis*- and *trans*-Dichlorobisethylenediamine Chromium(III) Cations in Acidic Solutions. Observation of a Stereochemical Change in Photoaquation. *Can. J. Chem.* **1971**, *49*, 1524–1528.

(24) Sheridan, P. S.; Adamson, A. W. Photochemistry of Complex Ions. *cis*-$[Co(en)_2Cl_2]^+$ and $_{cis}$-$[Co(en)_2(H_2O)Cl]^{2+}$. *J. Am. Chem. Soc.* **1974**, *96*, 3032–3038.

(25) Pribush, R. A.; Poon, C. K.; Bruce, C. M.; Adamson, A. W. Photochemistry of Complex Ions. Photochemistry of Cobalt(III) Acidoammines. *J. Am. Chem. Soc.* **1974**, *96*, 3027–3032.

(26) Werber, J. R.; Osuji, C. O.; Elimelech, M. Materials for Next-Generation Desalination and

Water Purification Membranes. *Nat. Rev. Mater.* **2016**, *1*, 1–15.

(27) White, W.; Sanborn, C. D.; Reiter, R. S.; Fabian, D. M.; Ardo, S. Observation of Photovoltaic Action from Photoacid-Modified Nafion Due to Light-Driven Ion Transport. *J. Am. Chem. Soc.* **2017**, *139*, 11726–11733.

(28) Cutting, G. R. Cystic fibrosis genetics: from molecular understanding to clinical application. *Nat. Rev. Genet.* **2015**, *16*, 45–56.

(29) Hadda, T. B.; Le Bozec, H. Preparation and Characterization of Ruthenium Complexes with the New 4,4′,4″-tri-*tert*-butylterpyridine Ligand and with 4,4′-di-*tert*-butylbipyridine. *Polyhedron* **1988**, *7*, 575−577.

(30) O'Donnell, R. M.; Sampaio, R. N.; Li, G.; Johansson, P. G.; Ward, C. L.; Meyer, G. J. Photoacidic and Photobasic Behavior of Transition Metal Compounds with Carboxylic Acid Group(s). *J. Am. Chem. Soc.* **2016**, *138*, 3891–3903.

(31) Crosby, G. A.; Demas, J. N. The Measurement of Photoluminescence Quantum Yields. A Review. *J. Phys. Chem.* **1971**, *75*, 991–1024.

(32) Loken, M. R.; Hayes, J. W.; Gohlke, J. R.; Brand, L. Excited-State Proton Transfer as a Biological Probe. Determination of Rate Constants by Means of Nanosecond Fluorometry. *Biochemistry* **1972**, *11*, 4479–4786.

(33) Demas, J. N. In *Excited State Lifetime Measurements*; Demas, J. N., Ed., Academic Press: New York, 1983; p 43.

(34) Laws, W. R.; Brand, L. Analysis of Two-State Excited-State Reactions. The Fluorescence Decay of 2-Naphthol. *J. Phys. Chem.* **1979**, *83*, 795–802.

(35) Connelly, N. G.; Geiger, W. E. Chemical Redox Agents for Organometallic Chemistry. *Chem. Rev.* **1996**, *96*, 877–910.

(36) Noviandri, I.; Brown, K. N.; Fleming, D. S.; Gulyas, P. T.; Lay, P. A.; Masters, A. F.; Phillips, L. The Decamethylferrocenium/Decamethylferrocene Redox Couple: A Superior Redox Standard to the Ferrocenium/Ferrocene Redox Couple for Studying Solvent Effects on the Thermodynamics of Electron Transfer. *J. Phys. Chem. B* **1999**, *103*, 6713–6722.

(37) Lin, S.; Ischay, M. A.; Fry, C. G.; Yoon, T. P. Radical Cation Diels-Alder Cycloadditions by Visible Light Photocatalysis. *J. Am. Chem. Soc.* **2011**, *133*, 19350–19353.

(38) Ischay, M. A.; Ament, M. S.; Yoon, T. P. Crossed intermolecular [2 + 2] cycloaddition of styrenes by visible light photocatalysis. *Chem. Sci.* **2012**, *3*, 2807–2811.

(39) Fielding, L. Determination of Association Constants (K_a) from Solution NMR Data. *Tetrahedron* **2000**, *56*, 6151–6170.

(40) Ward, W. M.; Farnum, B. H.; Siegler, M.; Meyer, G. J. Chloride Ion-Pairing with Ru(II) Polypyridyl Compounds in Dichloromethane. *J. Phys. Chem. A* **2013**, *117*, 8883–8894.

(41) Troian-Gautier, L.; Beauvilliers, E. E.; Swords, W. B.; Meyer, G. J. Redox Active Ion-Paired Excited States Undergo Dynamic Electron Transfer. *J. Am. Chem. Soc.* **2016**, *138*, 16815–16826.

(42) Swords, W. B.; Li, G.; Meyer, G. J. Iodide Ion Pairing with Highly Charged Ruthenium Polypyridyl Cations in CH_3CN. *Inorg. Chem.* **2015**, *54*, 4512–4519.

(43) Wehlin, S. A. M.; Troian-Gautier, L.; Li, G.; Meyer, G. J. Chloride Oxidation by Ruthenium Excited-states in Solution. *J. Am. Chem. Soc.* **2017**, *139*, 12093–12906.

(44) Benesi, H. A.; Hildebrand, J. H. A Spectrophotometric Investigation of the Interaction of Iodine with Aromatic Hydrocarbons. *J. Am. Chem. Soc.* **1949**, *71*, 2703–2707.

(45) Gu, J.; Yan, Y.; Helbig, B. J.; Huang, Z.; Lian, T.; Schmehl, R. H. The Influence of Ligand Localized Excited States on the Photophysics of Second Row and Third Row Transition Metal Terpyridyl Complexes : Recent Examples and a Case Study. *Coord. Chem. Rev.* **2015**, *282–283*, 100–109.

(46) Li, G.; Brady, M. D.; Meyer, G. J. Visible Light Driven Bromide Oxidation and Ligand Substitution Photochemistry of a Ru Diimine Complex. J. Am. Chem. Soc. 2018, [Online early access]. DOI: 10.1021/jacs.8b00944.

(47) Blakley, R. L.; Dearmond, M. K. Unique Spectroscopic Properties of Mixed-Ligand Complexes with 2,2′-Dipyridylamine: A Dual Luminescence from a Ruthenium(II) Complex. *J. Am. Chem. Soc.* **1987**, *109*, 4895–4901.

(48) Elliott, C. M.; Hershenhart, E. J. Electrochemical and Spectral Investigations of Ring-Substituted Bipyridine Complexes of Ruthenium. *J. Am. Chem. Soc.* **1982**, *104*, 7519–7526.

(49) Martir, D. R.; Averardi, M.; Escudero, D.; Jacquemin, D.; Zysman-Colman, E. Photoinduced Electron Transfer in Supramolecular Ruthenium–Porphyrin Sssemblies. *Dalton Trans.* **2017**, *46*, 2255–2262.

(50) Jang, H. J.; Hopkins, S. L.; Siegler, M. A.; Bonnet, S. Frontier Orbitals of Photosubstitutionally Active Ruthenium Complexes: An Experimental Study of the Spectator Ligands' Electronic Properties Influence on Photoreactivity. *Dalton Trans.* **2017**, *46*, 9969–9980.

(51) Ireland, J. F.; Wyatt, P. A. H. In *Advances in Physical Organic Chemistry*; V. Gold, Ed., Academic Press: New York, 1976, Vol. 12, p. 131.

(52) Zhou, D.; Khatmullin, R.; Walpita, J.; Miller, N. A.; Luk, H. L.; Vyas, S.; Hadad, C. M.; Glusac, K. D. Mechanistic Study of the Photochemical Hydroxide Ion Release from 9-

Hydroxy-10-methyl-9-phenyl-9,10-dihydroacridine. *J. Am. Chem. Soc.* **2012**, *134* , 11301–11303.

(53) Xie, Y.; Ilic, S.; Skaro, S.; Maslak, V.; Glusac, K. D.; Excited-State Hydroxide Ion Release From a Series of Acridinol Photobases. *J. Phys. Chem. A* **2017**, *121*, 448–457.

(54) Hidayatullah, A. N.; Wachter, E.; Heidary, D. K.; Parkin, S.; Glazer, E. C. Photoactive Ru(II) Complexes With Dioxinophenanthroline Ligands Are Potent Cytotoxic Agents. *Inorg. Chem.* **2014**, *53*, 10030–10032.

(55) Wachter, E.; Glazer, E. C. Mechanistic Study on the Photochemical "Light Switch" Behavior of $[Ru(bpy)_2dmdppz]^{2+}$. *J. Phys. Chem. A* **2014**, *118*, 10474–10486.

(56) Kohler, L.; Nease, L.; Vo, P.; Garofolo, J.; Heidary, D. K.; Thummel, R. P.; Glazer, E. C. Photochemical and Photobiological Activity of Ru(II) Homoleptic and Heteroleptic Complexes Containing Methylated Bipyridyl-type Ligands. *Inorg. Chem.* **2017**, *56*, 12214–12223.

(57) Qu, F.; Park, S.; Martinez, K.; Gray, J. L.; Thowfeik, F. S.; Lundeen, J. A.; Kuhn, A. E.; Charboneau, D. J.; Gerlach, D. L.; Lockart, M. M.; Law, J. A.; Jernigan, K. L.; Chambers, N.; Zeller, M.; Piro, N. A.; Kassel, W. S.; Schmehl, R. H.; Paul, J. J.; Merino, E. J.; Kim, Y.; Papish, E. T. Ruthenium Complexes are pH-Activated Metallo Prodrugs (pHAMPs) with Light-Triggered Selective Toxicity Toward Cancer Cells. *Inorg. Chem.* **2017**, *56*, 7519–7532.

(58) Kubik, S. Anion Recognition in Water. *Chem. Soc. Rev.* **2010**, *39*, 3648–3663.

(59) Langton, M. J.; Serpell, C. J.; Beer, P. D. Anion Recognition in Water: Recent Advances from a Supramolecular and Macromolecular Perspective. *Angew. Chem. Int. Ed.* **2016**, *55*, 1974–1987.

(60) Wenzel, M.; Weigand, J. J. Recent Advances in Anion Recognition. *J. Incl. Phenom. Macrocycl. Chem.* **2017**, *89*, 247–251.

CHAPTER 3: CONTROL OF EXCITED-STATE SUPRAMOLECULAR ASSEMBLY LEADING TO HALIDE PHOTORELEASE[2]

3.1 Introduction

Supramolecular assembly of halides is well established as a tool for halide sensing,[1] but recent advances have allowed this chemistry to be exploited in a growing array of applications spanning templated synthesis,[2–4] catalysis,[5–8] and halide transport across membranes.[9–14] These applications rely on intermolecular forces like hydrogen and halogen bonding, among others, to facilitate ground-state assembly structures with halides that then perform desired chemistry. Recent work has shown that the formation of ground-state assembly structures between ruthenium polypyridyl complexes and iodide affects the excited-state electron transfer reactivity between the two species.[15,16] These results imply that control over excited-state supramolecular assembly is necessary for influencing the mechanisms and kinetics of important energy storing reactions. However, to our knowledge, little work has characterized the response of ground-state halide assembly structures to photoexcitation.

Recently, it was reported that equilibrium constants for chloride assembly differed in the ground (K_{eq}) and excited states, K^*_{eq}.[17] In that report, two ruthenium polypyridyl complexes were designed with a common halide receptor ligand and with a luminescent metal-to-ligand charge-transfer (MLCT) excited-state that was oriented toward or away from the associated halide. In heteroleptic Ru(II) complexes, the photoluminescent excited state in fluid solution is known to be

[2] This chapter previously appeared as an article in the journal Inorganic Chemistry. The original citation is as follows: Turlington, M. D.; Troian-Gautier, L.; Sampaio, R. N.; Beauvilliers, E. E.; Meyer, G. J. Control of Excited-State Supramolecular Assembly Leading to Halide Photorelease. *Inorg. Chem.* **2019**, *58*, 5, 3316–3328.

localized on the most easily reduced ligand. Hence, when electron withdrawing CF_3 groups were present on the ancillary ligands, the excited-state dipole was oriented away from the receptor ligand. In contrast, when the ancillary ligands contained electron donating *t*-butyl groups, the excited-state dipole was oriented toward the receptor ligand. The excited-state localization had little effect on the assembly structure or the ground-state equilibrium constants (K_{eq}) with chloride. When the excited state was localized on the halide receptor ligand, photoexcitation reduced the equilibrium constant (K^*_{eq}) by a factor of 20, which resulted in chloride photorelease. Conversely, when the excited state was localized away from the associated halide, the K^*_{eq} value was increased by 45-fold. These results showed that molecular excited-states provide novel control over halide supramolecular assembly that could enable future applications with visible light in sea-water desalination and cystic-fibrosis related diseases.[18–20]

Herein, the ground- and excited-state properties that contribute to halide photorelease are more thoroughly investigated. Toward this end, a series of six ruthenium complexes (**Figure 3.1**) for supramolecular assembly with chloride and bromide are presented. As reported previously, iodide quenched the ruthenium excited-state, which precluded a detailed characterization of photorelease with this halide.[15] In this series of complexes, the functional groups on the halide receptor ligands were systematically varied, while the ancillary ligands remained constant. All complexes formed strong ground-state assembly structures with chloride and bromide in CH_2Cl_2. Functional group variations on the receptor ligands tuned the equilibrium constants across two orders of magnitude, and the fractional contribution of each functional group to the total equilibrium constant was determined. Excitation of the amide-functionalized halide assemblies resulted in a Coulombic repulsion between the halide and the excited state that facilitated halide release. The rate constants for this dissociation were sensitive to the hydrogen-bond donors on the

receptor ligand, indicating that hydrogen-bonding interactions provide a significant barrier to halide photorelease. These results, which reveal molecular design principles that can be used to control excited-state supramolecular assembly, are discussed in relationship to applications that involve halide release in polar solvents.

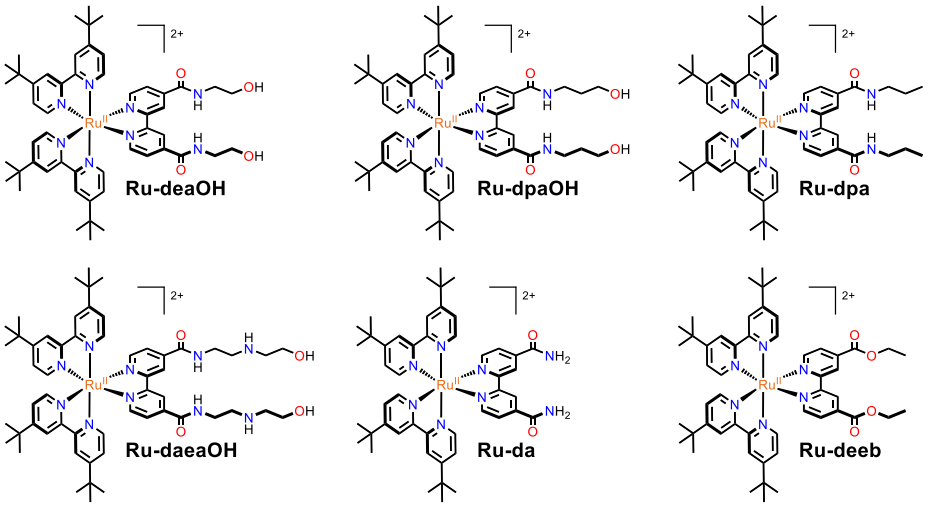

Figure 3.1: Ruthenium polypyridyl complexes for supramolecular assembly with halides used in this study. The ligand abbreviations (deaOH, dpaOH, dpa, daeaOH, da, deeb) are descriptive of the substituents in the 4,4′ position of the amide or ester functionalized ligands. The lowercase letters describe the length of the alkyl chain (ex. dea = diethylaminde, dpa = dipropylamide) while an uppercase OH when present indicates a terminal alcohol. The abbreviation deeb stands for diethylester bipyridine.

3.2 Results

The synthetic pathway for the complexes discussed herein is shown in **Figure 3.2**. The amide containing bipyridine ligands (**deaOH**, **dpaOH**, **dpa**, and **daeaOH**) were obtained by refluxing 4,4′-diethylester-2,2′-bipyridine (**deeb**) or 4,4′-dimethylester-2,2′-bipyridine and a large excess of the appropriate amine in methanol for 4 h. The yields ranged from 54-92 % (**Figure 3.2**, Path A). Ligand **da** was synthesized through another route (**Figure 3.2**, Path B), wherein 4,4′-dicarboxylic acid-2,2′-bipyridine was refluxed in the presence of thionyl chloride to give the highly reactive acid chloride. The addition of ammonia gas to the dissolved intermediate caused **da** to precipitate. The ruthenium complexes were synthesized by microwave irradiation of $Ru(dtb)_2Cl_2$ (**dtb** = 4,4′-di-*tert*-butyl-2,2′-bipyridine) and the appropriate ligand in EtOH or H_2O:EtOH

mixtures and were further isolated as the PF_6^- salt, with yields ranging from 70-90 percent (**Figures S3.1- S3.18**).

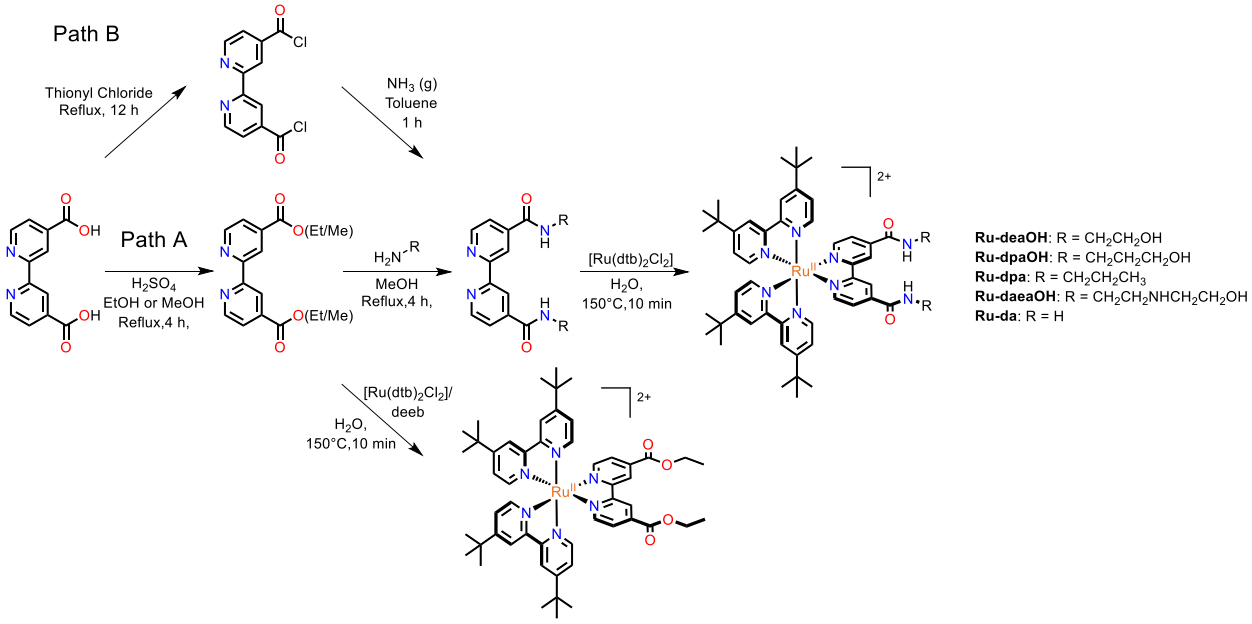

Figure 3.2: Synthetic pathway used to prepare the discussed complexes. See experimental section for additional details.

Cyclic and square-wave voltammetry in CH_2Cl_2 revealed quasi-reversible $Ru^{III/II}$ and ligand-based reductions for all complexes. For the amide derivatized complexes, the first ligand-based reduction fell within a narrow range of -820 to -910 mV vs. NHE, while the first reduction of **Ru-deeb** occurred at -680 mV. The metal centered $Ru^{III/II}$ potentials of all complexes spanned from 1560 to 1680 mV (**Table 3.1**).

The UV-Visible absorption spectra of all complexes in CH_2Cl_2 were typical of ruthenium polypyridyl complexes. The broad absorption bands from 400 to 500 nm were ascribed to metal-to-ligand charge transfer (MLCT) transitions, while the features at or below 300 nm were assigned to ligand centered transitions. The addition of tetrabutylammonium (TBA) chloride or bromide salts to approximately 10 μM solutions of the ruthenium complexes induced changes in the absorption spectra, particularly to the MLCT band (**Figure 3.3** and **S3.19**). These changes were

manifest primarily as increases in the MLCT intensity of the amide complexes (**Figure 3.3**, left), while **Ru-deeb** mainly experienced a red shift of the MLCT band (**Figure 3.3**, right). The spectral shifts saturated at high halide concentrations, and a Benesi-Hildebrand type analysis of the absorbance changes gave ground state equilibrium constants (K_{eq}) ranging from 10^5 to $>10^6$ M^{-1} (**Table 3.1**).[21,22] For complexes **Ru-deaOH**, **Ru-dpaOH**, and **Ru-dpa**, the binding isotherms were so steep ($>10^6$ M^{-1}) that K_{eq} values could not be resolved through standard UV-Vis titrations, and so competitive binding experiments were performed.[23,24] The ions TBA triflate (**Figure S3.20**) and TBA tetrafluoroborate (**Figure S3.21**) were found to be suitable competitors for **Ru-deaOH** and **Ru-dpa** respectively, and displayed one-to-one binding with the ruthenium complexes with an equilibrium constant (K_{comp}) in the 10^4 to 10^5 M^{-1} range. In competitive binding experiments, a fixed concentration of the competitor was present as the halide was titrated into the solution. This competitive equilibrium allowed the desired equilibrium constant to be quantified with Equation 1.[23,24] As expected, increasing the competitor concentration from 200 μM (50 equiv.) to 1 mM (200 equiv.) progressively reduced the observed equilibrium constant (K_{obs}) with halides (**Table S3.1**), and gave within error the same values for the calculated K_{eq}.

$$K_{eq} = K_{obs}\left(1 + K_{comp}[comp]\right) \quad (1)$$

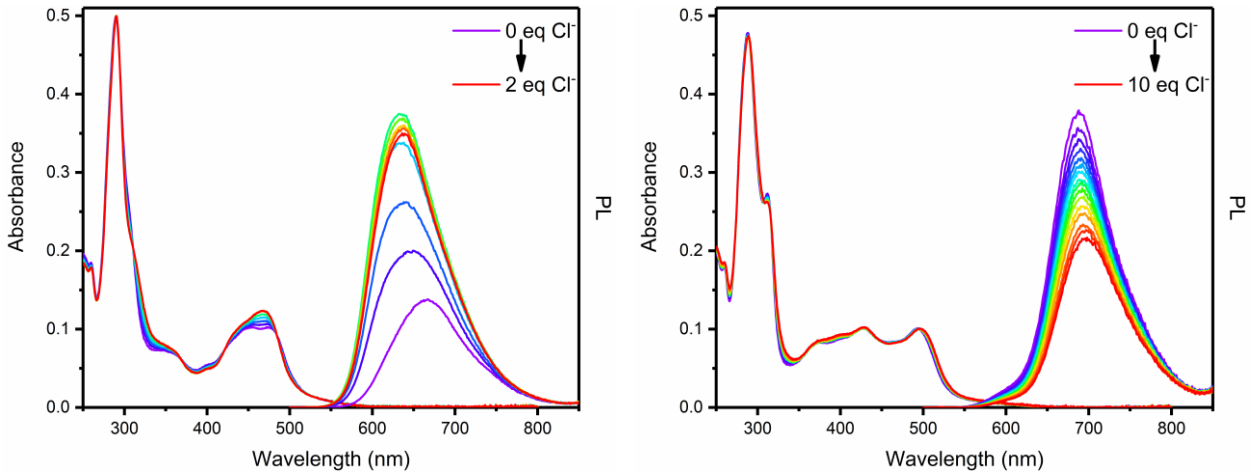

Figure 3.3: Absorbance and photoluminescence (PL) (λ_{ex} = 450 nm) spectra of Ru-dpa (left) and Ru-deeb (right) in CH_2Cl_2 at room temperature as TBA chloride was titrated into solution.

Titrations of chloride and bromide into 1 mM ruthenium solutions in CD_2Cl_2 were monitored by ^{1}H NMR spectroscopy (**Figure 3.4** and **S3.22**). For the amide functionalized complexes, the 3,3′ hydrogens on the amide functionalized ligand, as well as the amide hydrogens, displayed large downfield shifts as halide was added to the solution. At halide concentrations between 0-1 equivalent, significant broadening of these resonances was observed. Additionally, for **Ru-deaOH** and **Ru-dpaOH**, the hydroxyl resonances also drastically shifted downfield. The remaining aromatic and aliphatic resonances did not experience significant shifts in the presence of halide. With **Ru-deeb**, the analogous chloride and bromide titrations produced vastly different results, where the most significant shifts corresponded to the simultaneous deshielding of the 3,3′ hydrogens on the dtb ligand and the 6,6′ hydrogens on the deeb ligand. Significantly, the 3,3′ hydrogens on the deeb ligand did not shift during the course of the titration. The spectral changes for the amide complexes saturated after the addition of approximately one equivalent of halide, which was indicative of 1:1 contact ion pair formation. The 3,3′f dtb hydrogens of **Ru-deeb** continuously shifted even up to three equivalents of halide, but a Job plot (**Figure S3.23**) revealed

that this complex also forms a 1:1 ion pair.[25] This data provided no evidence for halide interactions with the deeb ligand in these CD_2Cl_2 solutions.[22,26]

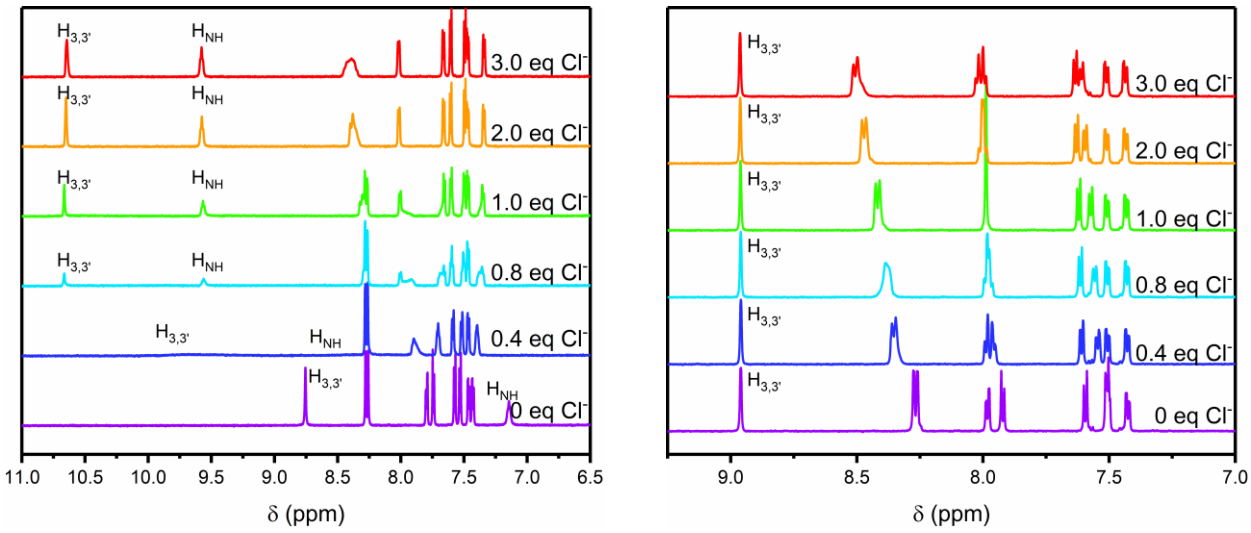

Figure 3.4: The aromatic region of the ^{1}H NMR spectra of Ru-dpa (left) and Ru-deeb (right) as chloride was titrated into CD_2Cl_2. The $H_{3,3'}$ label designates the 3,3′ hydrogens on the dpa (left) or deeb (right) ligands.

Steady state and time resolved photoluminescence (PL) were used to study the excited states of the free and ion-paired complexes. Upon absorption of visible light, all complexes displayed room temperature PL with maximum ranging from 665 to 688 nm. The steady state PL spectra of the complexes were sensitive to the halide concentration (**Figure 3.3** and **S3.19**). For the amide containing complexes, the PL spectrum blue shifted and experienced a 2 to 3-fold increase in intensity with increasing chloride or bromide concentrations, corresponding to an increase in the PL quantum yield. These changes typically saturated between one and two equivalents of halide. For **Ru-deeb**, the addition of chloride and bromide quenched the PL and caused a slight red shift in the spectra.

The PL maximum of the free and ion-paired complexes was taken as a crude estimate of the free energy stored in the excited state (ΔG_{ES}). These values (**Table 3.1**) in conjunction with the ground state K_{eq}, allowed the excited state equilibrium constants (K^*_{eq}) to be calculated through Förster Cycle analysis (**Figure S3.24**). For the amide functionalized complexes, equilibrium

constants for halide ion pairing decreased upon excitation, but for **Ru-deeb**, K^*_{eq} was greater than K_{eq}.

Table 3.1. Photophysical Properties of the Complexes and their Ion-Paired Analogues in CH_2Cl_2

	K_{eq}	K^*_{eq}	λmax PL					E^0 (V vs. NHE)	
complex	(M^{-1})	(M^{-1})	(nm)	τ(μs)	Φ_{PL}	k_r ($\times10^4$ s^{-1})	k_{nr} ($\times10^5$ s^{-1})	$Ru^{III/II}$	$Ru^{2+/+}$
Ru-deaOH	—	—	670	1.32	0.083	6.3	7.0	1.68	-0.82
Cl^-	3.6×10^7[a]	2.4×10^6	645	1.66	0.170	9.0	4.6	1.72	-0.86
Br^-	4.4×10^7[a]	2.9×10^6	647	1.65	0.120	6.8	4.9	—	—
Ru-dpaOH	—	—	668	1.14	0.130	12	7.6	1.56	-0.85
Cl^-	$>10^6$[b]	[c]	643	1.59	0.310	16	3.6	1.60	-0.90
Br^-	$>10^6$[b]	[c]	643	1.66	0.230	14	4.7	—	—
Ru-dpa	—	—	667	1.17	0.150	13	7.3	1.60	-0.91
Cl^-	2.8×10^7[a]	5.7×10^5	633	1.92	0.390	20	3.2	1.67	-0.94
Br^-	8.0×10^6[a]	2.4×10^5	637	1.88	0.390	21	3.3	—	—
Ru-daeaOH	—	—	665	1.18	0.061	5.2	8.0	1.56	-0.88
Cl^-	3.5×10^6	1.6×10^5	643	1.33	0.120	6.8	4.8	1.57	[d]
Br^-	1.7×10^6	2.4×10^5	650	1.60	0.100	6.4	5.6	—	—
Ru-da	—	—	677	0.95	0.090	9.5	9.6	1.56	-0.82
Cl^-	5.7×10^5	2.9×10^4	650	1.49	0.250	15	4.4	1.61	-0.97
Br^-	5.6×10^5	2.9×10^4	650	1.57	0.220	14	5.0	—	—
Ru-deeb	—	—	688	1.03	0.081	7.9	8.9	1.62	-0.68
Cl^-	9.7×10^4	2.1×10^5	696	0.87	0.067	7.7	11	1.66	-0.67
Br^-	1.0×10^5	2.2×10^5	695	0.87	0.067	7.7	11	—	—

[a]Determined through competitive binding experiments. [b]Equilibrium constant was too large to be measured and no suitable competitor was found; therefore, a minimum is given. [c]As K_{eq} could not be determined, K^*_{eq} could not be calculated. [d]Could not be determined.

The excited-state decay data were well described by a first-order kinetic model and yielded lifetimes, τ, on the order of a microsecond. However, the addition of halide to the amide complexes yielded kinetics that were no longer first-order, but which were instead successfully modeled by biexponential kinetics. Excited-state quenching was excluded as the cause of this kinetic behavior, as the complexes were not strong enough photo-oxidants to oxidize chloride or bromide.[27–29] Additionally, a biexponential fit using a weighted average of the lifetime of the free and ion-paired species (Ru^{2+} and $[Ru^{2+},X^-]^+$) did not model the kinetic data. When a large excess of halide was present (from 100-200 equivalents), first-order decay kinetics were recovered, from which the lifetime of the ion-paired complexes was obtained. Ion-pairing was found to increase the excited-state lifetime by 200-500 ns.

The biexponential decay kinetics at intermediate halide concentrations were further probed through transient PL experiments (**Figure S3.25**) and were found to report on the excited-state equilibrium, as predicted by the square-scheme discussed below. With one equivalent of chloride or bromide present, the PL of the amide complexes was found to red shift with time after pulsed laser excitation (**Figure 3.5** and **S3.26**). Note that the PL maxima obtained in the transient experiments were not the same as those described in **Table 3.1** or **Figure 3.3**, as the transient spectra were not corrected for the instrument response. The transient kinetic data were successfully modeled using a square-scheme kinetic analysis to determine the forward (k^*_{12}) and reverse (k^*_{21}) rate constants for ion pairing in the excited state.[17,30–34]

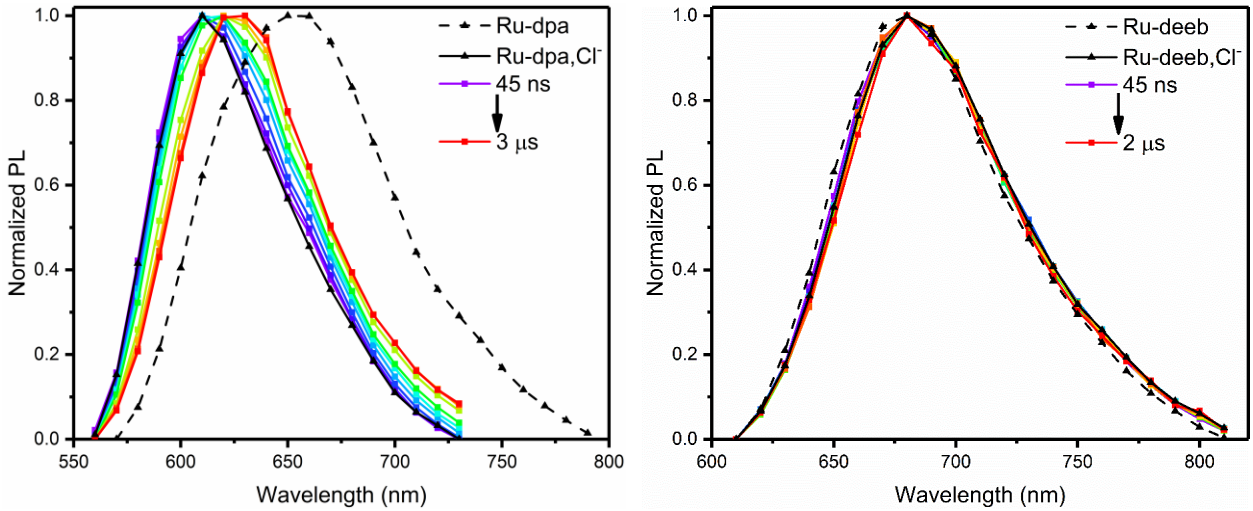

Figure 3.5: The PL spectra of Ru-dpa (left) and Ru-deeb (right) measured at 45 ns and longer time delays after pulsed 500 nm excitation in the presence of one equivalent of chloride in CH_2Cl_2. For reference, the PL spectra of the non-ion-paired complexes are included (black triangles, dashed line).

For **Ru-deeb**, the time-resolved PL data remained single exponential even in the presence of halide, although a decrease in the lifetime was observed. In previous reports, this behavior was attributed to an average lifetime arising from the mixture of the free and ion paired species, which had similar excited-state lifetimes.[22] Using the methods described in these reports, K^*_{eq} for [**Ru-deeb**,Cl^-]$^+$ was calculated to be 2.1×10^5 M^{-1}.[22,35] This value was in good agreement with that

obtained from a Förster Cycle. Transient PL experiments did not reveal time-dependent shifts in the PL, so the kinetics of the excited-state equilibrium could not be resolved.

3.3 Discussion

The experimental data clearly indicate that the ground- and excited-state equilibrium constants for halide binding can be controlled through molecular design. The results are in agreement with a recent study that reported how visible light excitation can be utilized to photorelease chloride ions, provided that the excited-state was localized on a bipyridine ligand with an associated chloride ion.[17] This comparative study was undertaken to understand the generality of the previous report and to better understand how functional group variation at the receptor ligand influences the ground- and excited-state equilibrium.

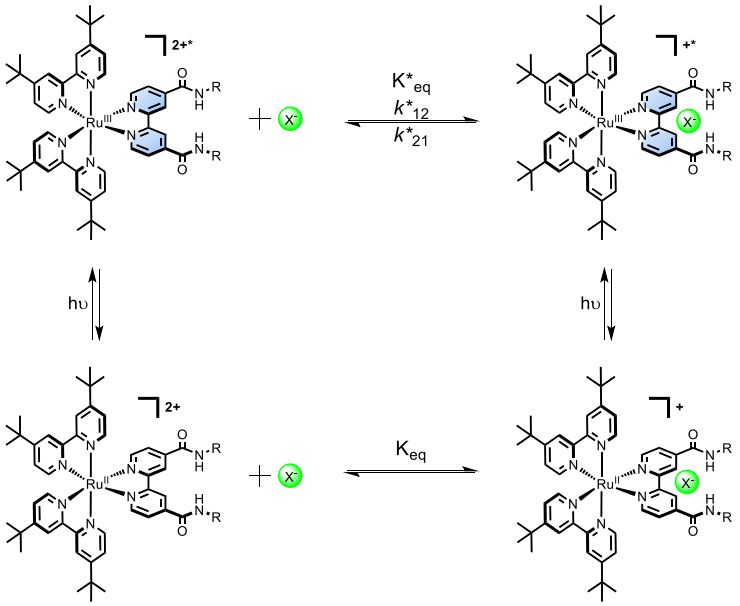

Figure 3.6: Square scheme for ground- and excited-state equilibria with halides. The blue shading represents the excited-state localization and the green sphere represents the halide. Note that the absorption of light promotes excitation to the Franck-Condon excited state, which then undergoes fast vibrational relaxation and intersystem crossing to the photoluminescent excited state. Photoluminescence from this state yields the singlet ground state. For simplicity, the square scheme only represents the singlet ground state and the photoluminescent excited state, which are assumed to be the only relevant states in halide binding and photorelease.

Table 3.2. Excited-State Kinetic and Thermodynamic Parameters

complex	ΔG^0_{GS} eV	ΔG^0_{ES} eV	ΔG^0_{GS}-ΔG^0_{ES} eV	k^*_{12} M^{-1} s^{-1}($\times 10^{11}$)[a]	k^*_{21} s^{-1} ($\times 10^5$)
Ru-deaOH	—	—	—	—	—
+Cl^-	-0.45	-0.38	-0.07	2.4	2.3
+Br^-	-0.45	-0.38	-0.07	2.2	1.5
Ru-dpa	—	—	—	—	—
+Cl^-	-0.44	-0.34	-0.10	2.2	4.5
+Br^-	-0.41	-0.32	-0.09	1.7	6.4
Ru-daeaOH	—	—	—	—	—
+Cl^-	-0.39	-0.31	-0.08	1.8	9.1
+Br^-	-0.37	-0.32	-0.05	2.1	8.7
Ru-da	—	—	—	—	—
+Cl^-	-0.34	-0.26	-0.08	1.27	47.1
+Br^-	-0.34	-0.26	-0.08	0.63	15.7
Ru-deeb	—	—	—	—	—
+Cl^-	-0.30	-0.32	0.02	[b]	[b]
+Br^-	-0.30	-0.32	0.02	[b]	[b]

[a]The k^*_{12} values on the order of 10^{11} M^{-1} s^{-1} are consistent with a diffusion limited rate, as calculated in the appendix of the supporting information. [b]As the time-resolved PL did not provide evidence for differing ground- and excited-state equilibria, the kinetic analysis could not be performed.

A useful starting point for considering these equilibria is the square scheme shown in **Figure 3.6**. The standard Gibbs free energy changes for the ground- and excited-states of the six complexes investigated are reported in **Table 3.2**. Related square schemes have been widely used to quantify the excited-state pK_a's of photo-acids and –bases, as well as excimer and exciplex formation.[30–34] Note that in the square scheme in **Figure 3.6**, "hυ" refers to light population of the photoluminescent excited state. Indeed, this is a simplification as light absorption creates a Franck-Condon state the subsequently relaxes to the photoluminescent state through vibrational relaxation and intersystem crossing. For all the ruthenium complexes reported here, the ground-state equilibrium with chloride and bromide is highly favored in CH_2Cl_2, and the free energies of halide binding provide insights into halide coordination chemistry. In the thermally equilibrated excited-state, the square scheme kinetic analysis and the corresponding differential rate equations (Equation 2 and 3, where A is Ru^{2+} and B is Ru^{2+},X^-) are used to model the experimental data. The analytical solutions for these differential rate equations have been derived elsewhere[31–33] and are

here used to determine the excited-state equilibrium constant and the forward (k^*_{12}) and reverse (k^*_{21}) rate constants. Significantly, biexponential excited-state decay kinetics, which are predicted by the square scheme,[31–33] are observed here for the amide-functionalized complexes. This discussion of ground- and excited-state supramolecular assembly included in the broader context of halide assembly indicates that control of the ground- and the excited-state equilibria with halide can lead to practical applications and fundamental insight into halide coordination chemistry.

$$\frac{d[A*]}{dt} = -(k_{12} + k_1)[A^*] + (k_{21})[B^*] \quad (2)$$

$$\frac{d[B*]}{dt} = -(k_{21} + k_2)[B^*] + (k_{12})[A^*] \quad (3)$$

3.3.1 Ground-State Supramolecular Assembly

The ruthenium polypyridyl complexes investigated in this study are designed to associate with halides through supramolecular assembly. Toward this end, hydrogen-bonding functional groups[36] such as amides and alcohols are built into the ligand framework to provide a specific site for halide assembly.[37] The cationic charge of each complex, as well as the use of the low dielectric solvent CH_2Cl_2 ($\varepsilon = 8.93$), also facilitate supramolecular assembly. Finally, the ancillary ligands are designed with sterically bulky *t*-butyl groups to block other halide interactions with the molecule. The characteristic spectral features of these complexes are sensitive to chloride and bromide, providing evidence for supramolecular assembly formation.

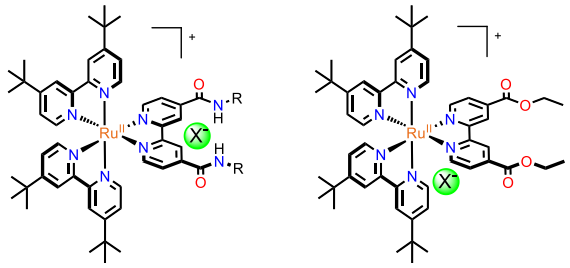

Figure 3.7: Ion-pairing location for the amide complexes (left) and Ru-deeb (right) as determined by ^{1}H NMR spectroscopy.

A powerful technique for resolving the location of the bound halide that also describes the specific hydrogen-bonding interactions that occur within the ion pair is ^{1}H NMR spectroscopy. In previous studies on related complexes, hydrogen bonding with halides was reported to lengthen the covalent bonds that were involved in the hydrogen-bonding interaction, resulting in downfield shifts of specific ^{1}H NMR signals.[15,17,22,27,38,39] The results herein are consistent with that finding. For the complexes with amide functionalized ligands, the 3,3′ C-H bonds and amide N-H bonds on the receptor ligand are most responsive to halide, whereas for **Ru-deeb**, the 3,3′ hydrogens on the dtb ligand and the 6,6′ hydrogens on the deeb ligand were most influenced. This indicates that supramolecular assembly with halides is highly sensitive to the functional groups present within the molecule. For the amide-derivatized complexes, the amide groups clearly provide a halide binding site. However, for **Ru-deeb**, the halide does not associate with a specific ligand, but instead is located between ligands and in close proximity to the positively charged ruthenium. These interactions are depicted in **Figure 3.7**.

Table 3.3. Spectral Shifts of Relevant ^{1}H NMR Signals as Halide is Added

	Δ ppm					
	$H_{3,3'}$		H_{NH}		H_{OH}	
complex	Cl^-	Br^-	Cl^-	Br^-	Cl^-	Br^-
Ru-deaOH	1.42	1.24	1.68	1.34	1.96	1.12
Ru-dpaOH	1.98	1.35	1.72	1.54	1.17	0.56
Ru-dpa	1.90	1.66	2.44	2.20	N/A	N/A
Ru-daeaOH	1.24	0.99	1.33	1.02	[a]	[a]
Ru-da	1.71	1.54	2.36	2.13	N/A	N/A

[a]Were not observed in the ^{1}H NMR spectrum

The magnitude of the downfield shift (Δppm) of specific resonances in the ^{1}H NMR spectra (**Table 3.3**) upon halide addition was found to vary significantly based on the complex and the identity of the halide. It is important to note here that Δppm does not correlate with the equilibrium constant. In other words, the complexes with the largest Δppm do not have the largest K_{eq} values and vice versa. However, in this series of complexes where binding uniformly occurs at the amide functionalized ligand (excluding **Ru-deeb**), the Δppm value provides insight into functional group effects on the supramolecular assembly. It is clear that the 3,3′ C-H, amide N-H, and alcohol O-H (if present) bonds are most significantly affected by the presence of halide. Amide[37,40–45] and hydroxyl[46,47] groups are known to form hydrogen bonding interactions with anions, and hydrogen bonding with C-H groups, although rare, can also occur when that bond is highly polarized or the binding site is highly structured.[48–51] In **Ru-deeb**, the most likely contributors to hydrogen bonding are the most acidic 3,3′ hydrogens (9.02 ppm) on the deeb ligand. Of the complexes studied herein, the electron-withdrawing ester groups are best able to polarize this 3,3′ C-H bond, and **Ru-deeb** should therefore provide the highest likelihood of hydrogen-bonding interactions at this site. However, halide addition does not perturb these 3,3′ C-H bonds, which suggests that this functional group does not form significant hydrogen-bonding interactions with halides. In the amide derivatives, the 3,3′ C-H bonds are slightly less polarized (9.02-8.81 ppm) than those of **Ru-deeb**, making them even less likely to engage in hydrogen-bonding interactions. The observed halide induced shifts at this position in the amide complexes are therefore attributed to halide induced repulsion of electron density in the C-H bond, which deshields the hydrogen atom. The magnitude of this effect is consistent with the distance between the halide and the 3,3′ hydrogens, as discussed below.

As stated previously, hydrogen bonding with amide and alcohol groups is proposed to lengthen the covalent N-H and O-H bonds.[22] For example, **Ru-deaOH** and **Ru-dpaOH** contain the same hydrogen bonding groups but differ by a single methylene spacer in the aliphatic chain of the amide ligand (**Figure 3.8**, right). The O-H bond of **Ru-deaOH** is lengthened more in the presence of halide than that of **Ru-dpaOH**, while the **Ru-dpaOH** N-H bond is elongated more significantly with halide than that of **Ru-deaOH**. This indicates that the length of the aliphatic chain allows the alcohol group on **Ru-deaOH** to interact more fully with halides, which in turn positions the halide farther from the amide group. This analysis is consistent with the electronic repulsion experienced by the 3,3′ C-H bond. In **Ru-deaOH**, the halide is positioned slightly farther from the 3,3′ C-H group, which results in less significant changes to that bond. For **Ru-dpaOH**, the halide is localized closer to the amide group, and the proximity to the 3,3′ C-H bonds increases the electronic repulsion. Complexes **Ru-dpa** (**Figure 3.8**, left) and **Ru-da**, which do not contain alcohol groups, provide further evidence for this interpretation. In these complexes, the amide groups are the sole contributors to hydrogen bonding interactions, and the N-H bond lengths are elongated by nearly 40% more than in the complexes with alcohol groups.

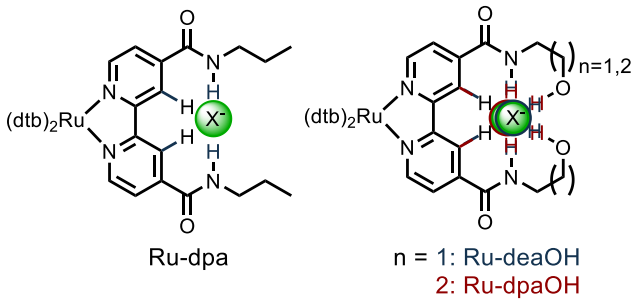

Figure 3.8: Depiction of the relative C-H, N-H, and O-H bond length changes experienced by Ru-dpa (left) and Ru-deaOH (blue hydrogens, right) or Ru-dpaOH (red hydrogens, right) upon supramolecular assembly with halides. The complexes without alcohol groups (left) have significantly longer amide N-H bonds than the alcohol containing complexes (right). In complexes with alcohol groups, the changes in O-H and N-H bond lengths trend in opposite directions as the chain length increases from ethyl to propyl.

The ground-state equilibrium constants provide an additional means by which to characterize functional group effects on the supramolecular assembly structure, which is highly favored in all complexes ($K_{eq} \geq 10^5\ M^{-1}$) in CH_2Cl_2. For **Ru-deaOH**, **Ru-dpaOH**, and **Ru-dpa**, the equilibrium constants for halide binding were so large that they could not be resolved. To overcome this limitation, competitive binding experiments[23,24] (depicted in **Scheme 3.1**) were performed to determine the true equilibrium constant. In this work, competitors were sought that displayed a 1:1 stoichiometry with the ruthenium complex and an equilibrium constant approximately one to two orders of magnitude less than that of the halide. The presence of a fixed concentration of an appropriate competitor during halide titrations enabled extraction of the desired K_{eq} with halide. Suitable competitors, TBA triflate and TBA tetrafluoroborate, were found for **Ru-deaOH** and **Ru-dpa** respectively, which allowed for their equilibrium constants with chloride and bromide to be determined using Equation 1. An adequate competitor was not found for **Ru-dpaOH**.

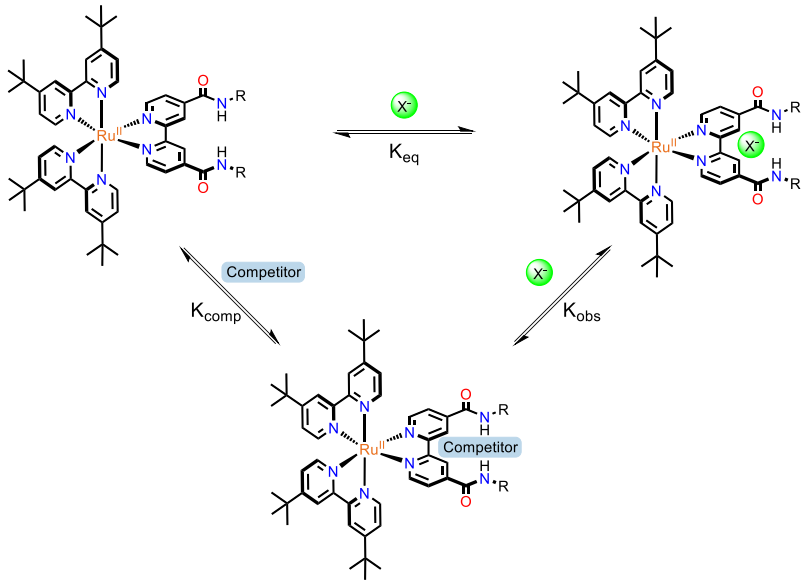

Scheme 3.1: The equilibrium constants (K_{eq}) for Ru-deaOH, Ru-dpaOH, and Ru-dpa with halide were too large to be resolved. However, the competitive equilibrium in the presence of a competitor and halide gave an observed equilibrium constant (K_{obs}) which could be used to calculate K_{eq} with Equation 1.

The functional groups on the receptor ligands drastically affect the equilibrium constants with halides, which span two orders of magnitude and increase in the order of **Ru-deeb** < **Ru-da** < **Ru-daeaOH** < **Ru-dpa** < **Ru-deaOH**. A comparison of the K_{eq} values with chloride (Table 3.1) enables one to partition the fraction that each functional group contributes to the equilibrium constant. For example, **Ru-deeb**, which contains two ester groups instead of amide functional groups, displays the weakest equilibrium constant (1×10^5 M^{-1}). As discussed above, this complex does not contain specific functional groups that stabilize halides through a well-defined assembly structure, and so the halide assembly is mainly attributed to the Coulombic attraction with the 2+ charge. Complexes with amide groups, like **Ru-da** and **Ru-dpa**, provide a specific hydrogen-bonding site for halide association, which enhances the K_{eq} by at least a factor of five. Finally, complexes with alcohol groups on the receptor ligand (**Ru-deaOH** and **Ru-dpaOH**, with the exception of **Ru-daeaOH**) associate so strongly with halides that K_{eq} could not be resolved in the absence of a competitor. These results suggest that the hydrogen-bonding functional groups additively contribute to the K_{eq} values.

The cumulative effect of functional group variation can be seen through a comparison of the ground-state free energies (ΔG^o_{GS}) for halide assembly. The complexes **Ru-deeb**, **Ru-dpa**, and **Ru-deaOH** were chosen for this comparison as the variations in the steric bulk of the receptor ligand are minimal, while the chemical composition of that ligand is changed in a modular fashion. In CH_2Cl_2, the free energy for both chloride and bromide assembly with a 2+ ruthenium polypyridyl complex that does not have a specific receptor ligand for halides (**Ru-deeb**) is -0.30 eV. The addition of hydrogen bonding amide groups (**Ru-dpa**) increased the magnitude of ΔG^o_{GS} (-0.41 and -0.44 eV) by 37-47% for bromide and chloride, respectively. Finally, the combination

of alcohol and amide groups (**Ru-deaOH**) provided a 50% increase in ΔG^{o}_{GS} (-0.45 eV) with both halides as compared to the **Ru-deeb** case.

Some apparent outliers are observed in this analysis, but these exceptions can be explained through consideration of the steric bulk or additional functional groups surrounding the amides. For example, **Ru-daeaOH,** contains a terminal alcohol group but has a smaller K_{eq} value (3.5×10^{6} M^{-1}) than **Ru-dpa** (2.8×10^{7} M^{-1}), which has no terminal alcohol. The alcohol group of **Ru-daeaOH** was not resolved by ^{1}H NMR, which precluded the observation of interactions between the alcohol and the halide. However, halide interactions with the 3,3′ C-H and N-H bonds are significantly less than those of the other complexes, suggesting on average an increased distance between these groups and the halide. This is consistent with the amine group in the daeaOH ligand destabilizing the associated halide, which in turn lowers the K_{eq}. The drastically different equilibrium constants of **Ru-dpa** (2.8×10^{7} M^{-1}) and **Ru-da** (5.7×10^{5} M^{-1}) is also surprising, as both complexes have the same hydrogen bonding functional groups. In the ^{1}H NMR spectrum of **Ru-dpa**, the aliphatic propyl resonances shift downfield with increasing halide concentration, indicating that this group contributes to halide association. The alkyl chain likely enhances the interaction by better encompassing the halide and preventing its dissociation. This suggests that tuning the sterics of the receptor ligand is important for optimal supramolecular assembly.

To summarize, in these complexes, contributions from molecular charge, hydrogen bonding functional groups, and steric bulk all affect ground-state halide assembly in CH_2Cl_2. The inherent 2+ charge of the ruthenium complexes contributes significantly to halide binding in this solvent, while the amide functional groups provide a binding site that further stabilizes the halide. Additional functional groups such as alcohols can influence the halide location within the supramolecular assembly and enhance stability yet again. Finally, the appropriate steric bulk is

important for allowing halides to approach the receptor site and for preventing their dissociation after assembly.

3.3.2 Excited-State Supramolecular Assembly

In a prior report, we have shown that halide photorelease can be achieved with ruthenium complexes that forms a 1:1 ion-pair with chloride.[17] This behavior was clearly observed after pulsed-laser excitation of an ion-paired complex $[Ru^{2+},Cl^{-}]^{+}$ that resulted in time-dependent shifts in the PL spectra, consistent with chloride photorelease and PL from the free ruthenium complex. In that report, the excited-state dipole orientation was paramount for controlling the excited-state assembly with halides. Excited-state localization on the receptor ligand led to halide photorelease, while excited-state localization away from that ligand led to enhanced halide binding. In this study, the excited-state dipole is oriented toward the ester or amide functionalized ligands, leading to halide photorelease for all complexes except **Ru-deeb**. The differences in the excited-state kinetic and thermodynamic parameters (**Figure 3.6**) between complexes are here related to the functional groups on the receptor ligand.

Photoexcitation greatly affects the excited state supramolecular assembly of all complexes, leading to photoinduced release of halides from the amide-containing complexes and enhanced binding in **Ru-deeb**. For instance, the PL maxima of the complexes as monitored by steady-state PL spectroscopy shift significantly during the course of chloride and bromide titrations. For the amide complexes, the PL blue-shifts up to 810 cm^{-1} and is accompanied by a 2-3 fold increase in intensity. For **Ru-deeb**, supramolecular assembly results in a slight red shift and a concurrent decrease in the PL intensity. The opposing PL shifts to low (**Ru-deeb**) or high (amide complexes) energy are due to the excited-state dipole orientation relative to the location of the halide.[17]

It has been shown for this class of complexes that the MLCT excited-state is localized on a single ligand, and that ligand is the one which is most easily reduced.[52] These complexes were designed such that in the MLCT excited-state, an electron resides on the amide or ester functionalized ligand, and this was confirmed through electrochemical experiments which showed that the first reduction potential of the complexes most closely aligned with $[Ru(bpy\text{-}CONHEt)_3]^{2+/+}$ (-880 mV vs NHE)[53] or $[Ru(deeb)_3]^{2+/+}$ (-720 mV vs NHE),[54] and not $[Ru(dtb)_3]^{2+/+}$ (-1000 mV vs NHE).[55] In the amide complexes where the excited-state dipole is oriented toward the ligand that binds the halide, the MLCT excited state is destabilized by Coulombic repulsion with the halide, which results in a higher energy PL.

For **Ru-deeb**, the MLCT excited-state is localized on the deeb ligand. However, an assembled halide does not associate directly with this ligand, but is instead in close proximity to the Ru(II) center. Therefore, upon absorption of a photon, the excited-state dipole is not directed toward the halide. Photoexcitation, which formally generates a Ru(III) metal, thereby increases the Coulombic attraction to the halide. This stabilizes the excited-state, as manifest in the lower energy PL spectrum. Concurrent with this red shift is a decrease in the PL intensity, which is caused by an increase in the non-radiative rate constants (k_{nr}) as predicted through the energy gap law, and which has been reported previously.[22,39]

The halide induced shifts in the steady-state PL were used to calculate the excited-state binding constants (K^*_{eq}) through Förster cycle analysis (**Figure S3.24**). The K^*_{eq} values for the amide complexes were found to be at least an order of magnitude less than the ground state K_{eq} values, as was expected based on the excited-state dipole orientation. For **Ru-deeb**, supramolecular assembly is stronger in the excited state by a factor of two.

To assess how the excited-state orientation affects the equilibrium constants for supramolecular assembly, the difference in free energy between the ground and excited-state ion pairs (ΔG^0_{GS}-ΔG^0_{ES}) was calculated (**Table 3.2**). A negative value provides an estimate of the destabilization in the excited state, while a positive value is indicative of enhanced binding. For all of the amide complexes, the free energy of supramolecular halide assembly decreases in the excited-state by -80 ± 10 meV. This shows that upon excitation, a halide associated with the amide ligands of **Ru-deaOH**, **Ru-dpa**, **Ru-daeaOH**, or **Ru-da** will be destabilized by 80 meV, behavior that is attributed mainly to the Coulombic repulsion of the halide with the excited-state. The different functional groups on these ligands have no discernable impact on the repulsion that is felt by the halide. Due to the similarities of the complexes, the electron density in the thermally equilibrated MLCT excited-state is likely distributed primarily on the coordinating nitrogen atoms, as has been suggested for ruthenium polypyridyl complexes.[56] Additionally, the distance between the ion-paired halide and these nitrogen atoms does not vary significantly from complex to complex. As the small structural differences between ligands do not affect these contributors to the excited state repulsion, photoexcitation reduces the free energy of halide binding by about the same amount in each complex. Thus, the trend in ground-state equilibrium constants (**Ru-da** < **Ru-daeaOH** < **Ru-dpa** < **Ru-deaOH**) is retained in the excited-state.

Although the difference between the ground- and excited-state equilibria are controlled primarily by the excited-state localization, the kinetics of photorelease are sensitive to individual functional group variations between the ligands. Examination of these rate constants is beneficial to understand the observed photorelease. The rate constants for halide association, k^*_{12}, are all within error the same, and on the order of 10^{11} M^{-1} s^{-1}. This value is in agreement with the calculated diffusion limit as described in eq S1 (Appendix, SI).[57] This suggests that the association

of the ruthenium complex and the halide in the excited-state is diffusion limited. Therefore, the K^*_{eq} values are determined by the rate constant for photorelease, k^*_{21}, for each complex. These rate constants correspond to halide dissociation from the ligand on the ns to μs time scale. As halide release is a unimolecular reaction, the dissociation could proceed on the timescale of molecular vibrations (ps), but as the rate is much slower, a barrier for halide photorelease is inferred. This barrier likely involves solvent reorganization to solvate the ruthenium complex and the halide, but this contribution is expected to be approximately the same for all complexes. The energy required to break the hydrogen-bonding interactions between the receptor ligand and the halide is also expected to contribute to this barrier. In this series, k^*_{21} was found to increase in the order of **Ru-deaOH** < **Ru-dpa** < **Ru-daeaOH** < **Ru-da**. This implies that **Ru-deaOH** has the largest barrier for halide photorelease, while **Ru-da** has the lowest barrier. Unsurprisingly, the trend for increasing k^*_{21} is the opposite of that observed for the ground-state equilibrium constants. This reinforces the result that hydrogen-bonding functional groups significantly stabilize halide assemblies, as these interactions provide a significant barrier to halide release in the excited state.

The excited-state kinetics and thermodynamics discussed above pose many challenges that hinder anion photorelease in polar solvents such as CH_3CN or water. For example, supramolecular assembly is known to be inversely proportional to the dielectric of the solvent.[58] In fact, previous work on **Ru-deaOH** determined that K_{eq} with chloride in CH_3CN is 8.5×10^5 M^{-1},[15] as compared to the K_{eq} of 3.6×10^7 M^{-1} reported here in CH_2Cl_2. To even facilitate supramolecular assembly through hydrogen bonding interactions in polar solvents, it would be necessary to design a complex with many strong hydrogen bond donors that outcompete the solvent's ability to stabilize halide. However, the presence of these groups inevitably increases the barrier for halide photorelease. This approach would also adversely affect the halide dissociation rate constants (k_{21}). As the

energy barrier for the halide release would necessarily be large, k_{21} would be slow, and so long-lived excited states would be needed to ensure that the halide would be released before relaxation to the ground state.

To address these challenges, it is helpful to look to the alkali and alkaline earth metal cation binding literature, where several strategies have been employed to photoinitiate metal release in polar solvents like water and CH_3CN. Many of the techniques offer varying degrees of reversibility. For instance, photoreactivity[59–62] (irreversible) or photoisomerization[63,64] (partially reversible) of cation receptors leads to large increases in cation concentrations in polar solvents, and even under biological conditions. Completely reversible photorelease mechanisms, which are of particular interest to this work, have been achieved with rhenium bipyridine complexes bearing an azacrown-ether conjugated to the metal center.[65–69] In cation binding studies in CH_3CN, pulsed-laser excitation of the assembly structures led to photorelease of the associated cations that was attributed to the conjugation of the azacrown nitrogen with the metal center. Upon MLCT (Re to bpy) excitation, this nitrogen contributed significant charge density to the metal center, weakening its interaction with the cation in the crown ether. In this case, photoexcitation not only provided an energy input to overcome the barrier for cation release, but also directly reduced the barrier by weakening interactions that contributed to cation association. A similar strategy could be utilized to facilitate anion photorelease in polar solvents. If the specific functional groups that recognized anions also accepted significant charge density in the excited state, the intermolecular forces that contribute to anion assembly would inherently be weakened. This approach could lead to complexes that strongly bind halides in the ground state in polar solvents, but which have a modest barrier to halide photorelease in the excited state.

3.4 Conclusions

A series of ruthenium polypyridyl complexes containing ester or amide functionalized bipyridine ligands formed strong assembly structures ($K_{eq} \geq \times 10^5$ M^{-1}) with chloride and bromide in CH_2Cl_2. Amide and alcohol functional groups on the receptor ligand significantly enhanced the equilibrium constant, as compared to a complex (**Ru-deeb**) without these groups. This allowed K_{eq} to be tuned by over two orders of magnitude. Photoexcitation of the ion-paired complexes led to a modest enhancement in the equilibrium constant (K^*_{eq}) of **Ru-deeb**, while an order of magnitude decrease in K^*_{eq} was observed for the amide complexes. The decrease in K^*_{eq} resulted in the photorelease of associated halide ions. The excited-state rate constants for halide dissociation (k_{21}) were largest for the complexes with the fewest hydrogen-bond donors (**Ru-da**), while the presence of functional groups that stabilized halides contributed to an energy barrier that decreased the rate of photorelease. The results show that excited-state supramolecular assembly can be controlled through molecular design.

3.5 Experimental

3.5.1 Materials

Sulfuric acid (H_2SO_4, Fisher, 98 %, Certified ACS Plus), methanol (Fisher, Certified ACS), chloroform (Fisher, Certified ACS), ethanolamine (Sigma-Aldrich, ≥ 98 %), acetone (Sigma-Aldrich, Certified ACS), acetonitrile (CH_3CN, Burdick and Jackson, 99.98 %), and dichloromethane (CH_2Cl_2, Burdick and Jackson, 99.98 %) were used as received. Argon gas (Airgas, 99.998 %) was passed through a Drierite drying tube before use. Ammonium hexafluorophosphate (NH_4PF_6, Sigma-Aldrich, ≥ 98 %), tetrabutylammonium chloride (TBACl, Sigma-Aldrich, purum ≥ 97 %), tetrabutylammonium bromide (TBABr, Acros Organics, 99+ %), tetrabutylammonium perchlorate ($TBAClO_4$, Sigma-Aldrich, for electrochemical analysis, ≥ 99

%), and ruthenium trichloride hydrate (Oakwood Chemicals, 97 %) were used as received. NMR solvents were purchased from Cambridge Isotope Laboratories, Inc. $Ru(dtb)_2Cl_2•2H_2O$,[70] 4,4′-dicarboxy-2,2′-bipyridine,[71] 4,4′-dimethylester-2,2′-bipyridine,[15] 4,4′-diethylester-2,2′-bipyridine (deeb),[72] $[Ru(dtb)_2(dea)](PF_6)_2$, (**Ru-deaOH**),[15] and $[Ru(dtb)_2(daea)](PF_6)_2$ (**Ru-daeaOH**)[17] were synthesized according to previous procedures. All solutions were sparged with argon for at least 30 minutes before all titration and transient PL experiments.

3.5.2 Synthesis of ligands

General method for synthesis of amide functionalized ligands. To 4,4′-dimethylester- or 4,4′-diethylester-2,2′-bipyridine in methanol was added an excess of the appropriate amine. The mixture was refluxed for 4 h. Upon cooling, acetone was added to the mixture, and the solid was collected by vacuum filtration on a sintered glass frit. The precipitate was washed with excess acetone and dried under vacuum at 100 °C, yielding a white powder.

deaOH: Refluxing 4,4′-diethylester-2,2′-bipyridine (2.0 g, 6.7 mmol) and ethanolamine (10 mL, 166 mmol) in methanol (40 mL) yielded 1.7 g (77%) of dea. ^{1}H NMR (d_6-DMSO, 500 MHz): 8.91 (2H, t), 8.85 (2H, d), 8.78 (2H, s), 7.85 (2H, dd), 4.83 (2H, t), 3.55 (4H, m), 3.38 (4H, m).

dpaOH: Refluxing 4,4′-dimethylester-2,2′-bipyridine (1.0 g, 3.7 mmol) and 3-amino-1-propanol (5 mL, 83 mmol) in methanol (20 mL) yielded 1.1 g (92%) of dpa. ^{1}H NMR (d_6-DMSO, 600 MHz): 8.95 (2H, t), 8.87 (2H, d), 8.78 (2H, s), 7.85 (2H, dd), 4.52 (2H, t), 3.48 (4H, m), 3.36 (4H, m), 1.71 (4H, p). ^{13}C NMR (d_6-DMSO, 150 MHz): 164.57, 155.52, 150.07, 143.03, 121.95, 118.22, 58.56, 36.81, 32.24.

dpa: Refluxing diethylester-2,2′-bipyridine (0.5 g, 1.6 mmol) and propylamine (3 mL) in methanol (10 mL) yielded 0.292 g (54%) of dpa. ^{1}H NMR (d_6-DMSO, 500 MHz): 8.96 (2H, t),

8.87 (2H, d), 8.79 (2H, s), 7.85 (2H, dd), 3.26 (4H, m), 1.57 (4H, m), 0.91 (6H, t). ^{13}C NMR (d_6-DMSO, 150 MHz): 164.53, 155.53, 150.07, 143.09, 121.97, 118.22, 41.18, 22.26, 11.53.

daeaOH: Refluxing dimethylester-2,2′-bipyridine (1.0 g, 3.7 mmol) and 2-[(2-aminoethyl)amino]ethanolamine (5 mL, 49 mmol) in methanol (20 mL) yielded 1.1 g (72%) of daea. ^{1}H NMR (d_6-DMSO, 500MHz): 8.93 (2H, t), 8.86 (2H, d), 8.79 (2H, d), 7.85 (2H, dd), 4.48 (2H, t), 3.44 (4H, q), 3.38 (4H, q), 2.72 (4H, t), 2.60 (4H, t).

Synthesis of da: 4,4′-dicarboxy-2,2′-bipyridine (10g, 41.0 mmol) was refluxed under argon overnight in thionyl chloride (100 mL). The solvent was then removed from the mixture under reduced pressure and the residue was dissolved in toluene. NH_3(g) was bubbled through the reaction mixture for one hour, causing a precipitate to form. The precipitate was filtered and then washed with a minimum amount of DMSO, and finally with excess acetone. The final product was obtained as a white powder (4.3g, 42 %). ^{1}H NMR (d_6-DMSO, 600 MHz): 8.86 (2H, dd), 8.80 (2H, dd), 8.42 (2H, s), 7.87 (2H, dd), 7.79 (2H, s). ^{13}C NMR (d_6-DMSO, 150 MHz): 166.30, 155.62, 150.04, 142.80, 122.00, 118.53.

Synthesis of deeb: 4,4′-dicarboxy-2,2′-bipyridine (5g, 20.5 mmol) and H_2SO_4 (5 mL) were refluxed in ethanol (100 mL) for 5 days. The reaction mixture was added to $CHCl_3$ (200 mL), and H_2O (150 mL) was added. The aqueous layer was extracted with $CHCl_3$. The organic fraction was dried with $MgSO_4$, and the solvent was removed under vacuum, yielded 5.28 g (85%) of deeb. ^{1}H NMR ($CDCl_3$, 500 MHz): 8.93 (2H, s), 8.85 (2H, d), 7.90 (2H, dd), 4.45 (4H, q), 1.43 (6H, t).

3.5.3 Synthesis of ruthenium complexes

General method for synthesis of ruthenium complexes **Ru-deaOH**, **Ru-dpaOH**, **Ru-dpa**, **Ru-daeaOH**, and **Ru-deeb**. To a 10 mL glass microwave vial was added $Ru(dtb)_2Cl_2$•$2H_2O$, one equivalent of the appropriate ligand, and ~5 mL of EtOH or a 1:1 mixture of H_2O: EtOH. The

mixture was heated under microwave radiation by an Anton Paar Monowave 300 at 150 °C for 10 minutes. The red solution was filtered, and the solvent was removed by rotary evaporation. The resulting solid was dissolved in minimal H_2O, and a few drops of saturated aqueous NH_4PF_6 was added, causing a precipitate to form. The solid was collected with vacuum filtration, washed with excess H_2O, and dried under vacuum at 100 °C overnight, yielding a red solid.

[Ru(dtb)$_2$(deaOH)](PF$_6$)$_2$, (Ru-deaOH): $Ru(dtb)_2Cl_2$ (75 mg, 0.096 mmol), deaOH (32 mg, 0.097 mmol) and ~5 mL H_2O: EtOH (1:1) was heated at 150 °C for 10 min under microwave irradiation, yielding 86 mg (71%) of **Ru-deaOH**. ^{1}H NMR (CD_2Cl_2, 400 MHz): 8.95 (2H, s), 8.27 (4H, d), 7.83 (2H, dd), 7.77 (2H, d), 7.60 (2H, t), 7.57 (4H, q), 7.45 (4H, td), 3.78 (4H, m), 3.58 (4H, m), 2.86 (2H, s), 1.42 (18H, s), 1.40 (18H, s).

[Ru(dtb)$_2$(dpaOH)](PF$_6$)$_2$, (Ru-dpaOH): $Ru(dtb)_2Cl_2$ (75 mg, 0.096 mmol), dpaOH (34 mg, 0.095 mmol), and ~5 mL H_2O: EtOH was heated at 150 °C for 10 min under microwave irradiation, yielding 110 mg (89%) of **Ru-dpaOH**. ^{1}H NMR (CD_2Cl_2, 400 MHz): 8.84 (2H, d), 8.27 (4H, dd), 7.81 (2H, dd), 7.77 (2H, d), 7.72 (2H, t), 7.57 (2H, d), 7.53 (2H, d), 7.46 (2H, dd), 7.43 (2H, dd), 3.70 (4H, t), 3.61 (4H, q), 1.82 (4H, p), 1.43 (18 H, s) 1.41 (18 H). HRMS (ESI-MS). Calcd for $C_{54}H_{70}F_{12}N_8O_4P_2Ru_1Na_1$ ($[M + Na]^+$): *m/z* 1309.37. Found: *m/z* 1309.37.

[Ru(dtb)$_2$(dpa)](PF$_6$)$_2$, (Ru-dpa): $Ru(dtb)_2Cl_2$ (75 mg, 0.096 mmol), dpa (31 mg, 0.095 mmol), and ~5 mL H_2O: EtOH was heated at 150 °C for 10 min under microwave irradiation, yielding 80 mg (66%) of **Ru-dpa**. ^{1}H NMR (CD_3CN, 500 MHz): 8.91 (2H, d), 8.48 (4H, dd), 7.84 (2H, d), 7.70 (2H, dd), 7.54 (4H, dd), 7.51 (2H, t), 7.42 (2H, dd), 7.35 (2H, dd), 3.37 (m, 4H), 1.63 (4H, h), 1.41 (18h, s), 1.39 (18h, s), 0.96 (6H, t). HRMS (ESI-MS). Calcd for $C_{54}H_{70}F_6N_8O_2P_1Ru_1$ ($[M]^{2+}$): *m/z* 482.24. Found: *m/z* 482.23.

[Ru(dtb)$_2$(daeaOH)](PF$_6$)$_2$, (Ru-daeaOH): Ru(dtb)$_2$Cl$_2$ (75 mg, 0.096 mmol), daeaOH (40 mg, 0.096 mmol) and ~5 mL H2O: EtOH (1:1) was heated at 150 °C for 10 min under microwave irradiation, yielding 96 mg (74%) of **Ru-daeaOH**. ^{1}H NMR (CD$_3$CN, 500 MHz): 9.02 (s, 2H), 8.48 (dd, 4H), 7.84 (d, 2H), 7.73 (d, 2H), 7.55 (d, 4H), 7.42 (dd, 2H), 7.35 (dd, 2H), 3.56 (t, 4H), 3.51 (m, 4H), 2.85 (t, 4H), 2.73 (t, 4H), 1.41 (s, 18H), 1.39 (s, 18H).

[Ru(dtb)$_2$(deeb)](PF$_6$)$_2$, (Ru-deeb): Ru(dtb)$_2$Cl$_2$ (100 mg, 0.141 mmol), deeb (42 mg, 0.140 mmol) and ~5 mL EtOH was heated at 150 °C for 10 min under microwave irradiation, yielding 144 mg (83%) of **Ru-deeb**. ^{1}H NMR (CD$_3$CN, 500 MHz): 9.02 (2H, d), 8.48 (4H, dd), 7.90 (2H, d), 7.83 (2H, dd), 7.52 (4H, dd), 7.42 (2H, dd), 7.34 (2H, dd), 4.45 (4H, q), 1.41 (24 H, m), 1.39 (18H, s). HRMS (ESI-MS). Calcd for: C$_{52}$H$_{64}$N$_6$O$_4$Ru$_1$ ([M]2+): *m/z* 469.2. Found: *m/z* 469.2.

[Ru(dtb)$_2$(da)](PF$_6$)$_2$, (Ru-da): [Ru(dtb)$_2$Cl$_2$] (500 mg, 0.071 mmol) and da (188 mg, 0.078 mmol) were dissolved in 12 mL of a 1:1 water/ethanol mixture and refluxed overnight under argon. After reaction, the mixture was brought to room temperature and evaporated to dryness under vacuum. The residue was dissolved in 5 mL of water, and upon addition of a saturated aqueous NH$_4$PF$_6$ solution, a precipitate formed. The precipitate was collected by filtration and purified by column chromatography on alumina using CH$_3$CN/ H$_2$O mixture, yielding 341 mg (41%) of **Ru-da**. ^{1}H NMR (CD$_2$Cl$_2$, 500 MHz): 8.87 (2H, s), 8.27 (4H, dd), 7.83 (2H, dd), 7.79 (2H, d), 7.57 (2H, d), 7.54 (2H, d), 7.46 (2H, dd), 7.44 (2H, dd), 7.07 (2H, s), 6.02 (2H), 1.43 (18H, s), 1.41 (18H, s). HRMS (ESI-MS). Calcd for C$_{48}$H$_{58}$F$_{12}$N$_8$O$_2$P$_2$Ru$_1$Na$_1$ ([M + Na]$^+$): *m/z* 1193.29. Found: *m/z* 1193.29.

3.5.4 Nuclear Magnetic Resonance

Characteristic NMR spectra were obtained at room temperature on a Bruker Avance III 400, 500 or 600 MHz spectrometer. Solvent residual peaks were used as internal standards for ^{1}H (δ =7.26 ppm for $CDCl_3$, 2.50 ppm for DMSO, 5.32 for CD_2Cl_2, 1.94 for CD_3CN) and ^{13}C (δ = 77.16 ppm for $CDCl_3$, 39.52 ppm for DMSO) chemical shift referencing. NMR spectra were processed using MNOVA.

3.5.5 Mass Spectrometry

Samples were analyzed with a hybrid LTQ FT (ICR 7T) (ThermoFisher, Bremen, Germany) mass spectrometer. Samples were introduced via a micro-electrospray source at a flow rate of 3 µL/min. Xcalibur (ThermoFisher, Breman, Germany) was used to analyze the data. Each mass spectrum was averaged over 200 time domains. Electrospray source conditions were set as: spray voltage 4.7 kV, sheath gas (nitrogen) 3 arb, auxiliary gas (nitrogen) 0 arb, sweep gas (nitrogen) 0 arb, capillary temperature 275 ºC, capillary voltage 35 V and tube lens voltage 110 V. The mass range was set to 150-2000 m/z. All measurements were recorded at a resolution setting of 100,000. Solutions were analyzed at 0.1 mg/mL or less based on responsiveness to the ESI mechanism. Low-resolution mass spectrometry (linear ion trap) provided independent verification of molecular weight distributions.

3.5.6 UV−Vis Absorption

UV−vis absorption spectra were recorded on a Varian Cary 60 UV−vis spectrophotometer with a resolution of 1 nm.

3.5.7 Steady-State PL

Steady-state PL spectra were recorded on a Horiba Fluorolog 3 fluorimeter and corrected by calibration with a standard tungsten-halogen lamp. Samples were excited at 450 nm. The

intensity was integrated for 0.1 s at 1 nm resolution and averaged over 3 scans. The PL quantum yields were measured by the optically dilute method using $[Ru(bpy)_3]Cl_2$ in acetonitrile (Φ = 0.062) as a quantum yield standard.[73]

3.5.8 Time-Resolved Photoluminescence

Time-resolved PL data were acquired on a nitrogen dye laser with excitation centered at 445 nm. Pulsed light excitation was achieved with a Photon Technology International (PTI) GL-301 dye laser that was pumped by a PTI GL-3300 nitrogen laser. The PL was detected by a Hamamatsu R928 PMT optically coupled to a ScienceTech Model 9010 monochromator terminated into a LeCroy Waverunner LT322 oscilloscope. Decays were monitored at the PL maximum and averaged over 180 scans. Nonradiative and radiative rate constants were calculated from the quantum yields, $\Phi = k_r/(k_r + k_{nr})$ and lifetimes, $\tau = 1/(k_r + k_{nr})$.

3.5.9 Transient Photoluminescence

Transient photoluminescence data were obtained on the nitrogen dye laser described above. Excited-State decay traces were obtained every 10 nm from 560 to 770 nm and averaged over 60 scans. The amplitude of each PL decay after a specific time-delay from the laser pulse (45 ns to 3 μs at given intervals) was plotted versus the wavelength, and the data was normalized to give the transient PL spectra shown in **Figure 5**.

3.5.10 Excited-State Equilibrium

The square scheme analysis used to resolve the excited-state kinetics are described elsewhere.[31–33]

3.5.11 Electrochemistry

Square wave voltammetry was performed with a BASi Epsilon potentiostat in a standard three-cell in CH_2Cl_2 electrolytes. The cells consisted of a platinum working electrode and a

platinum mesh as an auxiliary electrode. A non-aqueous silver/silver chloride electrode (Pine) was used as a reference electrode that was referenced to an internal ferrocene (724 mV vs. NHE)[74] or decamethylferrocene[75] ($Me_{10}Fc$) standard (250 mV vs. NHE).

3.5.12 Halide Titrations

UV−vis, PL, and time-resolved measurements were performed in CH_2Cl_2 or CH_3CN using ~10 μM solutions of the ruthenium complexes. Titration measurements were performed for each of the spectroscopies with TBACl or TBABr through additions of 0.25 equivalents. Throughout all titrations, the concentration of complexes remained unchanged. In order to do so, a stock solution of each complex with an absorbance of ~0.1 at 450 nm (~6-10 μM) in the desired solvent was prepared. The stock solution was transferred into a spectrophotometric quartz cuvette (5 mL). A titration solution was then prepared with 25 mL of the complex's stock solution. TBACl or TBABr were added to the stock solution to obtain the desired concentration of halide. These solutions were then titrated to the quartz cuvette.

To perform the competitive binding experiments with **Ru-deaOH** and **Ru-dpa**, ruthenium solutions with an absorbance of ~0.1 at 450 nm were prepared as described above. The desired amount of competitor (TBA triflate for **Ru-deaOH**, TBA tetrafluoroborate for **Ru-dpa**) was then added to the ruthenium solution to give a stock solution that contained excess (0.280 – 1.19 mM) competitor concentration. Three stock solutions were prepared with a 50, 100, and 200:1 ratio of competitor to ruthenium. Then, 5 mL of the stock solution was transferred to a quartz cuvette. A titrating solution was also prepared by dissolving the desired amount of TBACl or TBABr in 10 mL of the stock solution. The observed equilibrium constant (K_{obs}) at each competitor concentration was used to determine the halide equilibrium constant (K_{eq}) with Equation 1, and the three trials were averaged to give the reported values.

The ^{1}H NMR titrations were performed using a Bruker Avance III 500 MHz spectrometer equipped with a broadband inverse (BBI) probe using 1 mM ruthenium complex in 600 µL of deuterated solvent and 0.25 equivalent additions of TBACl or TBAI were added in 10 µL additions. The ruthenium concentration was kept unchanged through preparation of a titration solution that contained both the ruthenium complex and the desired halide. Each spectrum was averaged over 16 scans.

Data analysis for all experiments was performed using Origin 2017. Data fitting was preformed using a Levenberg-Marquardt iteration method. Benesi-Hildebrand type analysis was performed in Mathematica, version 11.

3.6 Supporting Information

Ligand Characterization

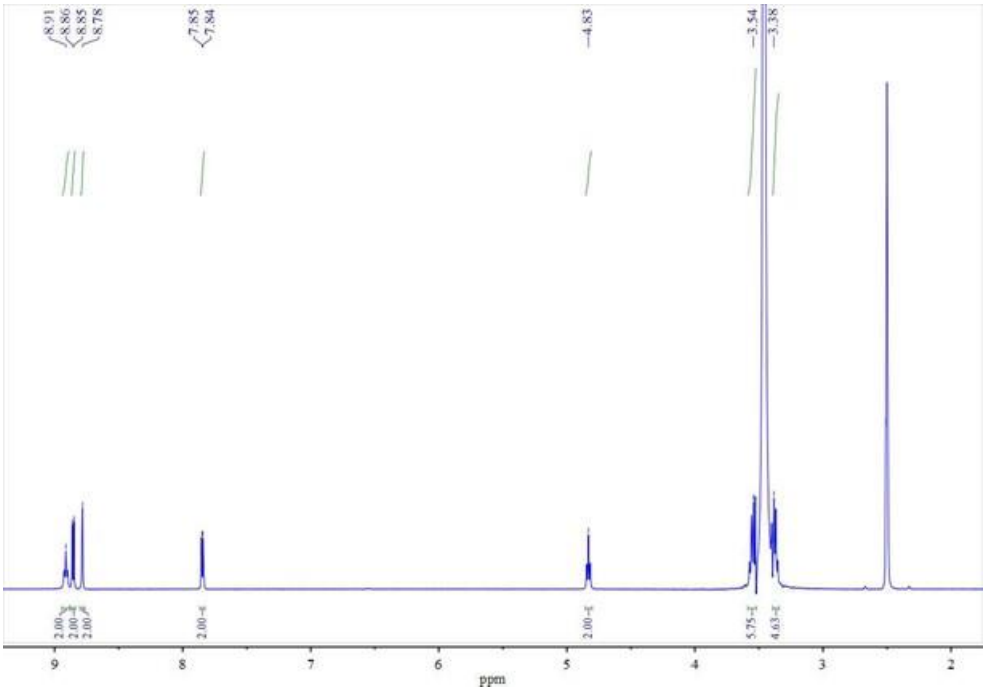

Figure S3.1: The ^{1}H NMR spectrum of deaOH in DMSO at 298 K.

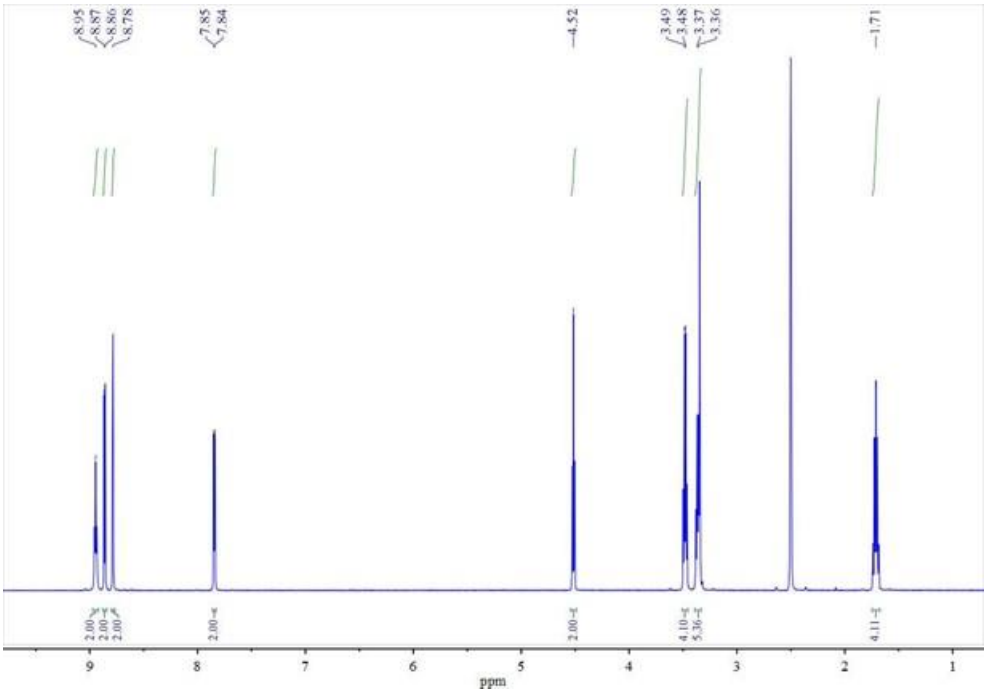

Figure S3.2: The ^{1}H NMR spectrum of dpaOH in DMSO at 298 K.

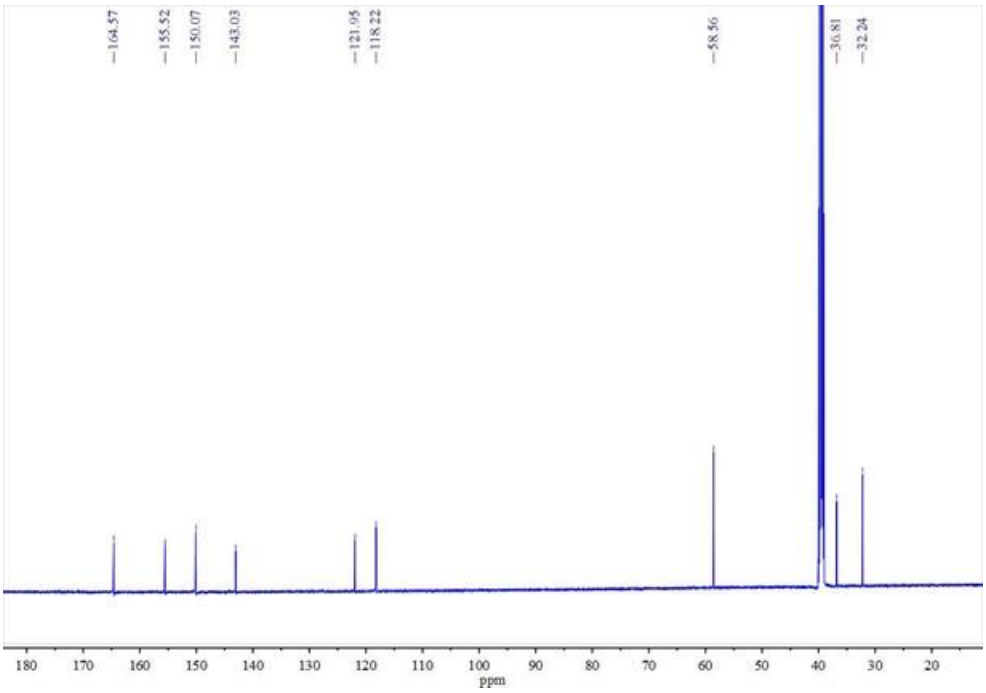

Figure S3.3: The ^{13}C NMR spectrum of dpaOH in DMSO at 298 K.

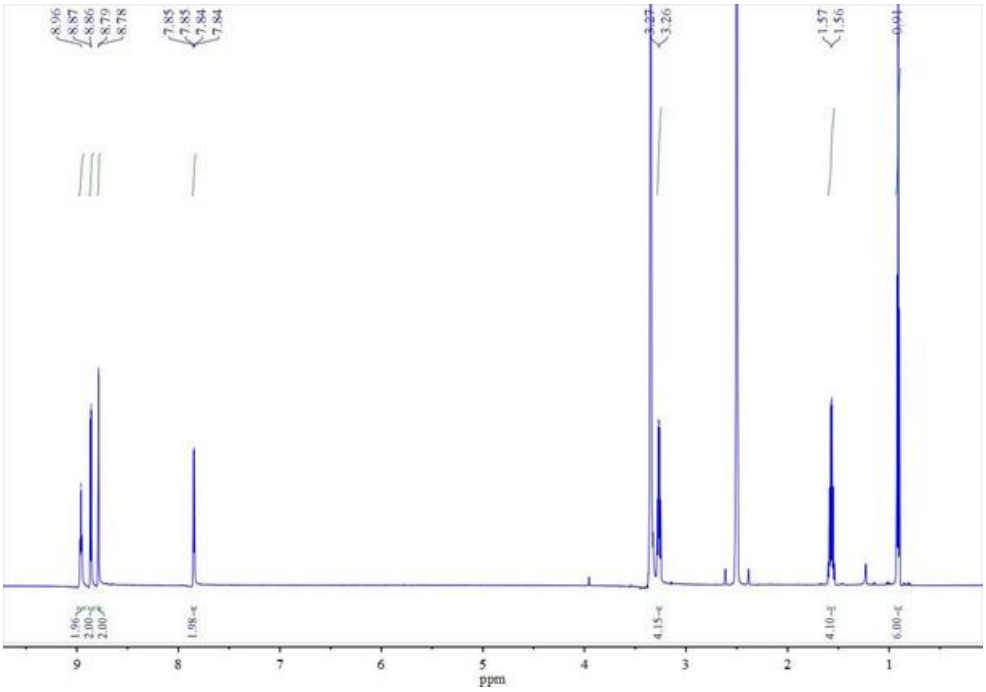

Figure S3.4: The ^{1}H NMR spectrum of dpa in DMSO at 298 K.

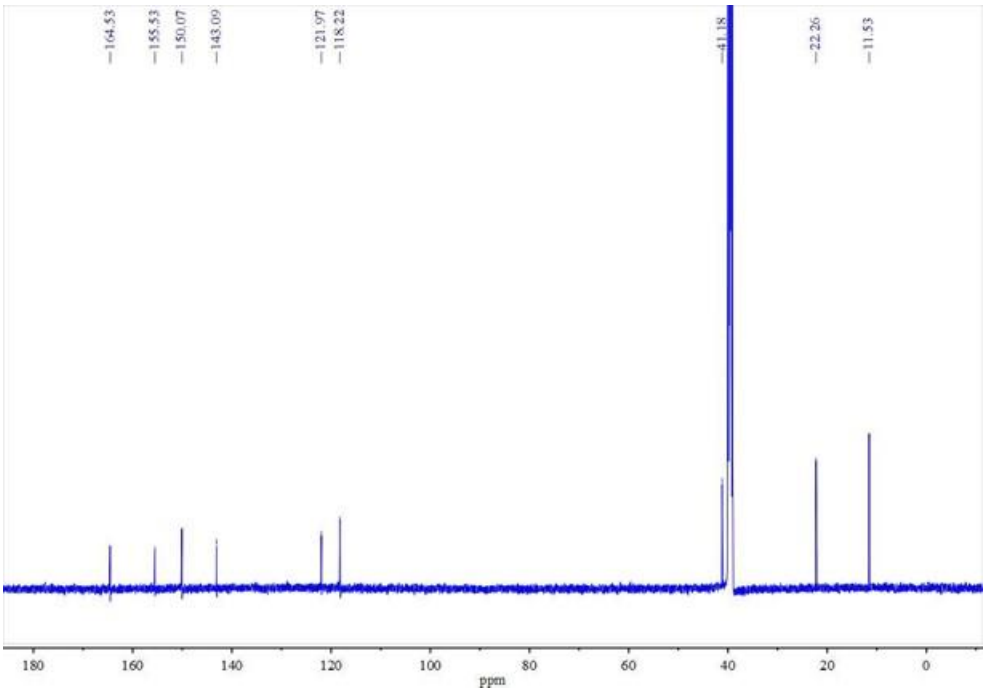

Figure S3. 5: The ^{13}C NMR spectrum of dpa in DMSO at 298 K.

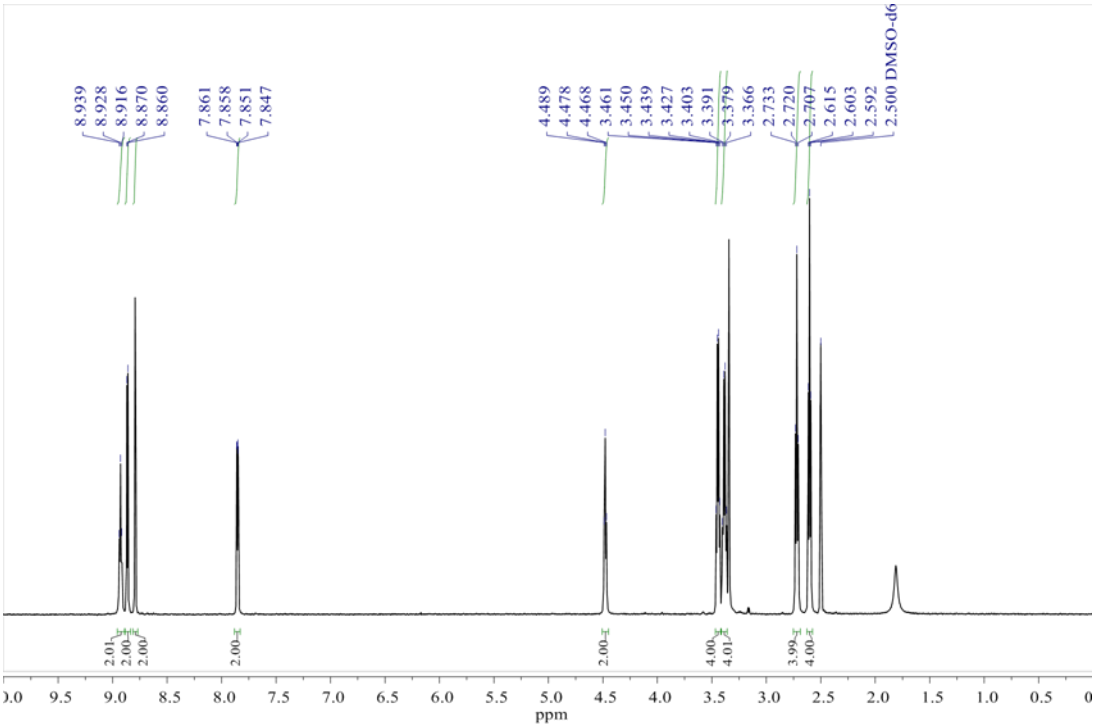

Figure S3.6: The ^{1}H NMR spectrum of daeaOH in DMSO at 298 K.

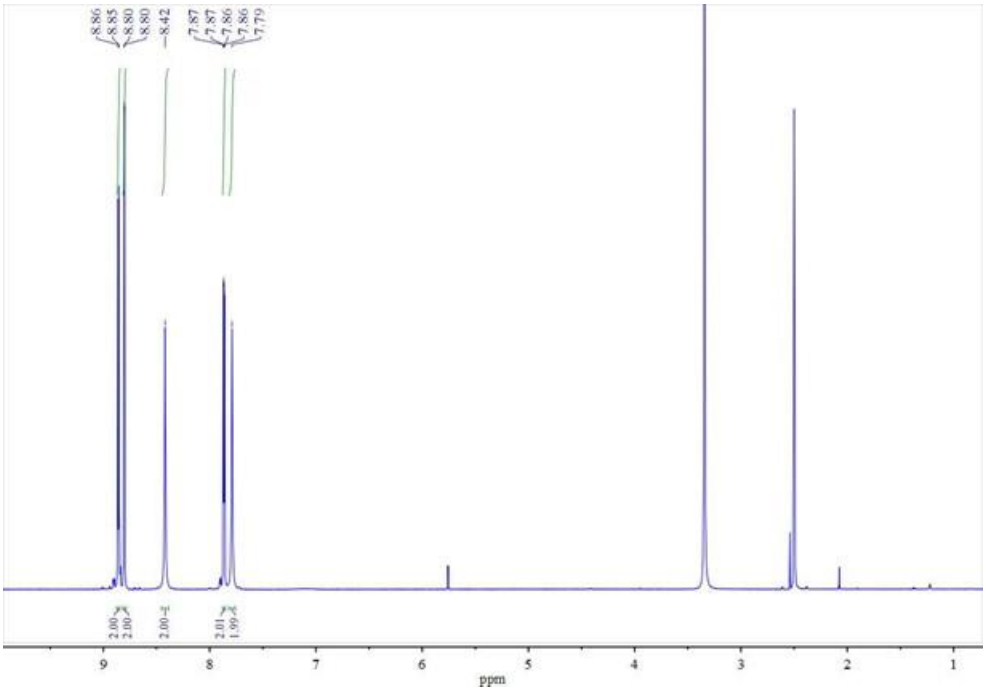

Figure S3.7: The ^{1}H NMR spectrum of da in DMSO at 298 K.

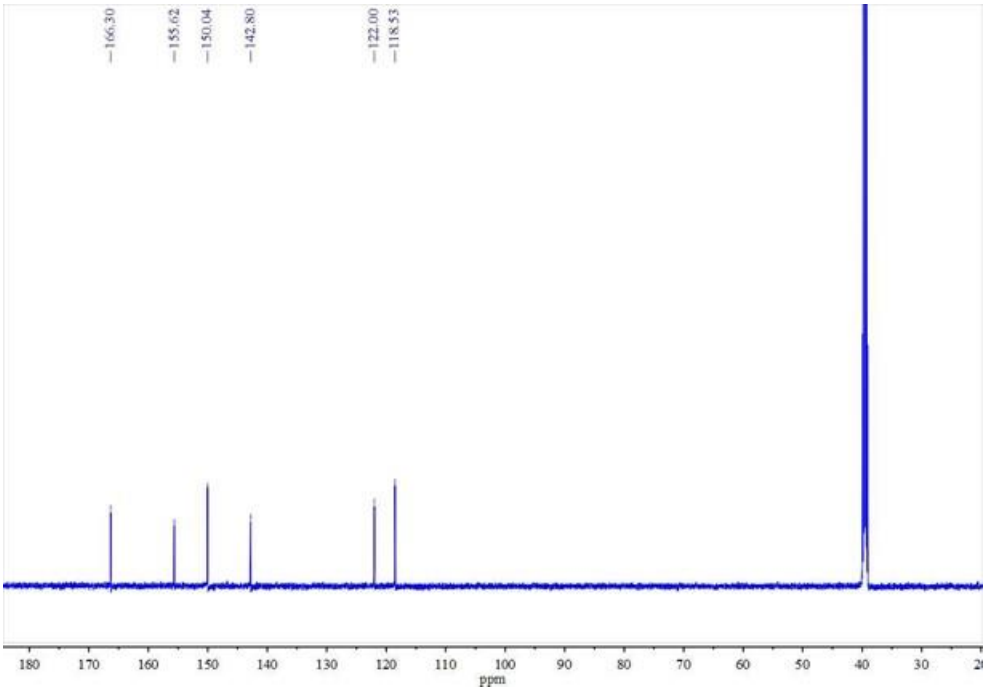

Figure S3.8: The ^{13}C NMR spectrum of da in DMSO at 298 K.

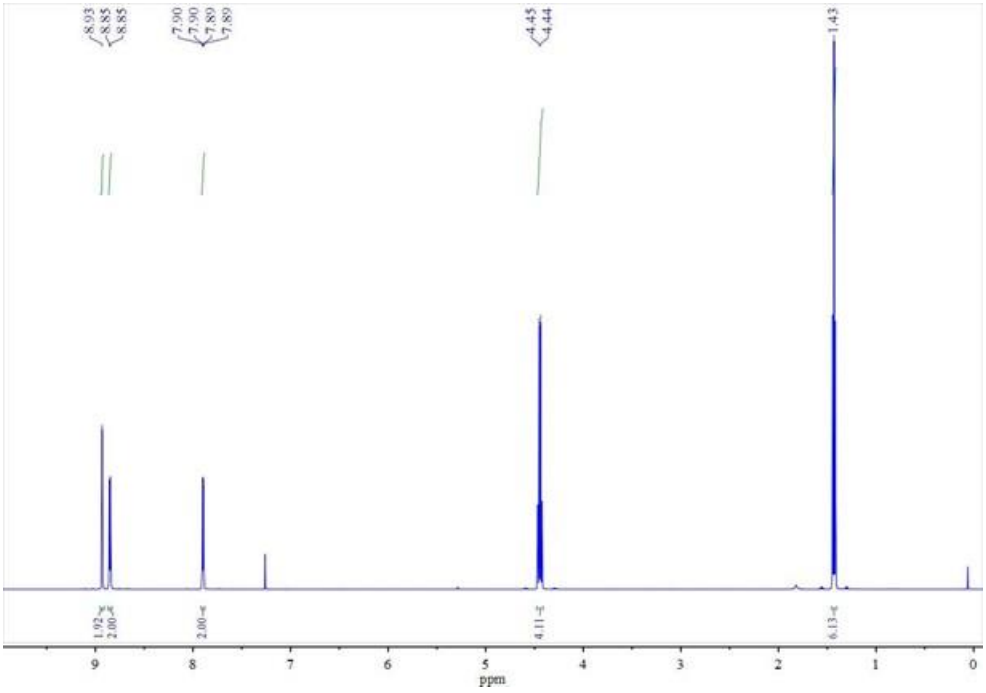

Figure S3.9: The ^{1}H NMR spectrum of deeb in $CDCl_3$ at 298 K.

Complex Characterization

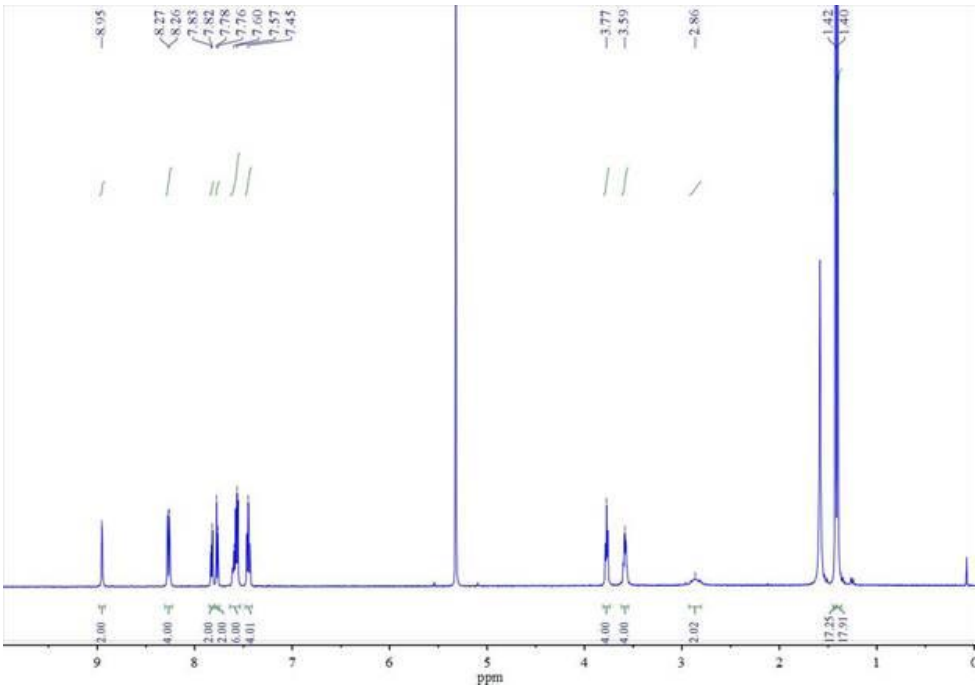

Figure S3.10: The ^{1}H NMR spectrum of Ru-deaOH in CD_2Cl_2 at 298 K.

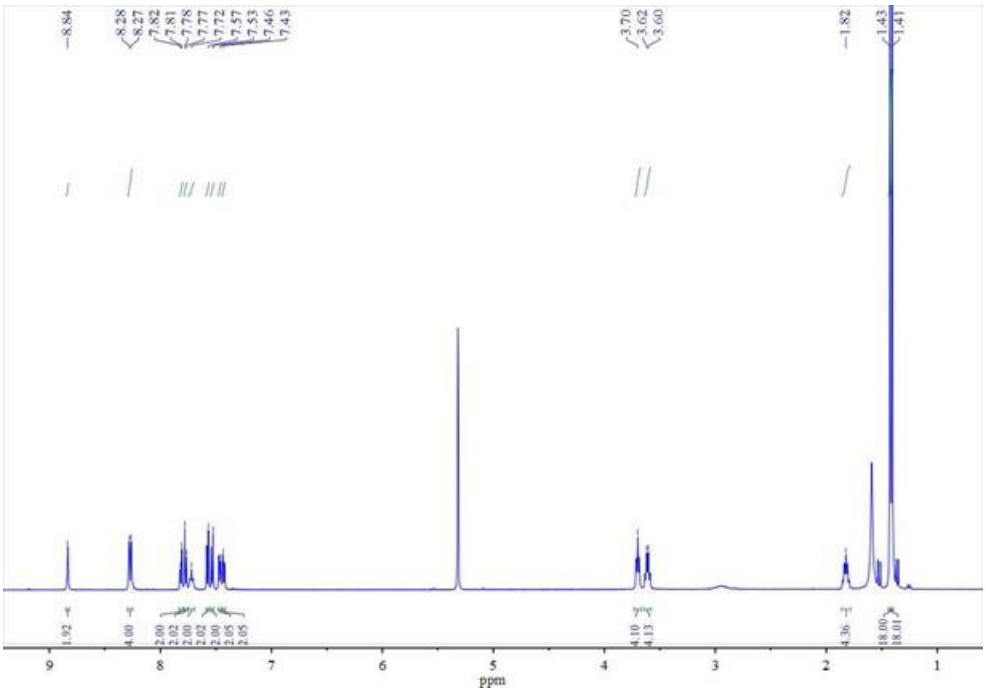

Figure S3.11: The ^{1}H NMR spectrum of Ru-dpaOH in CD_2Cl_2 at 298 K.

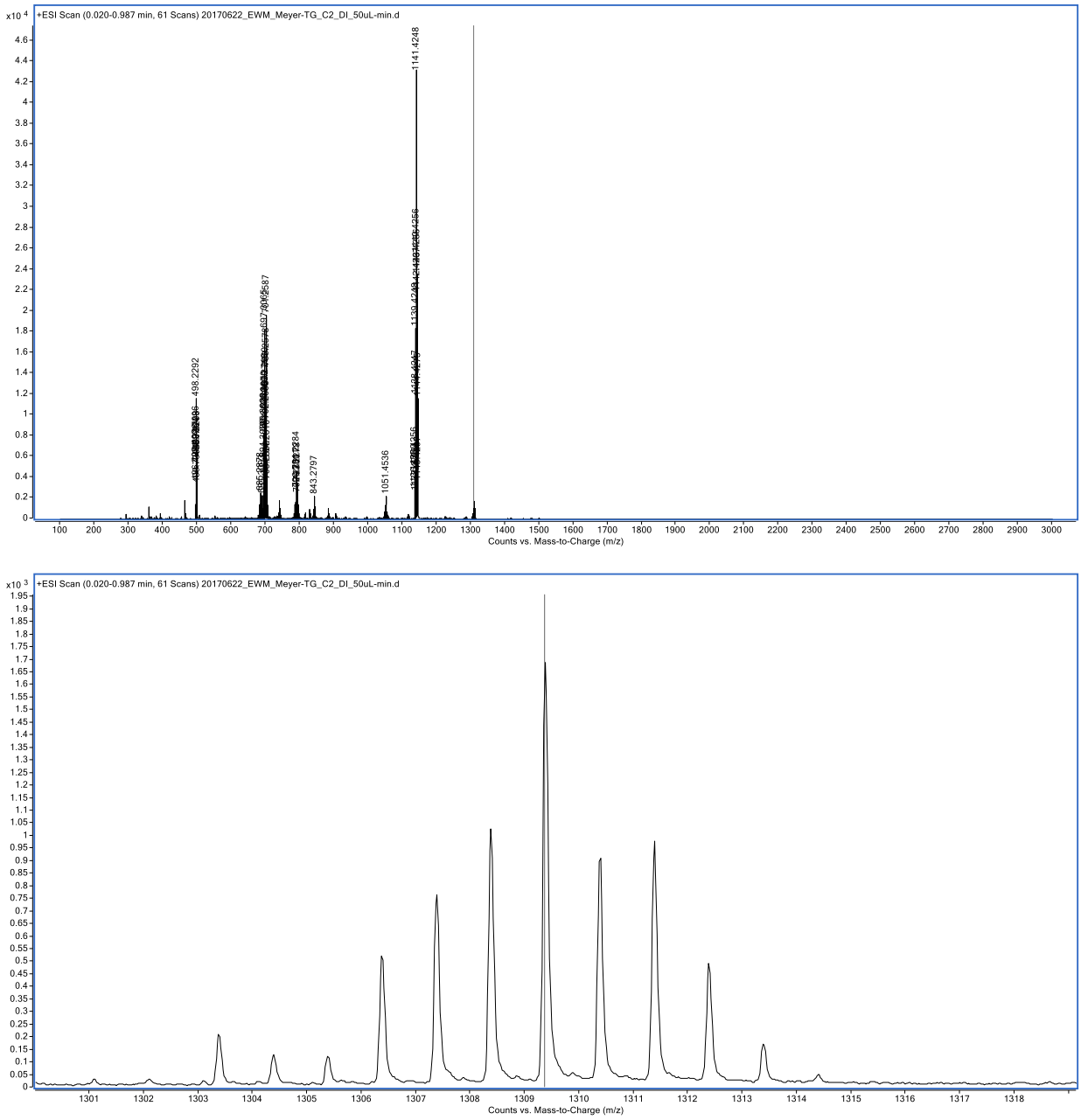

Figure S3.12: High-Resolution Mass Spectrum of Ru-dpaOH.

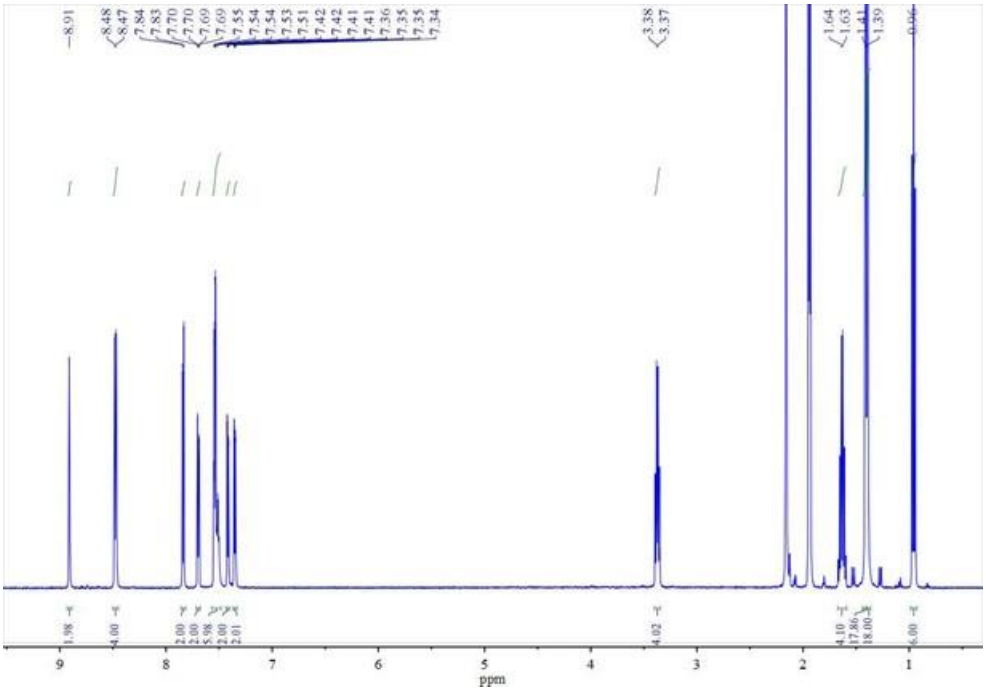

Figure S3.13: The ^{1}H NMR spectrum of Ru-dpa in CH_3CN at 298 K.

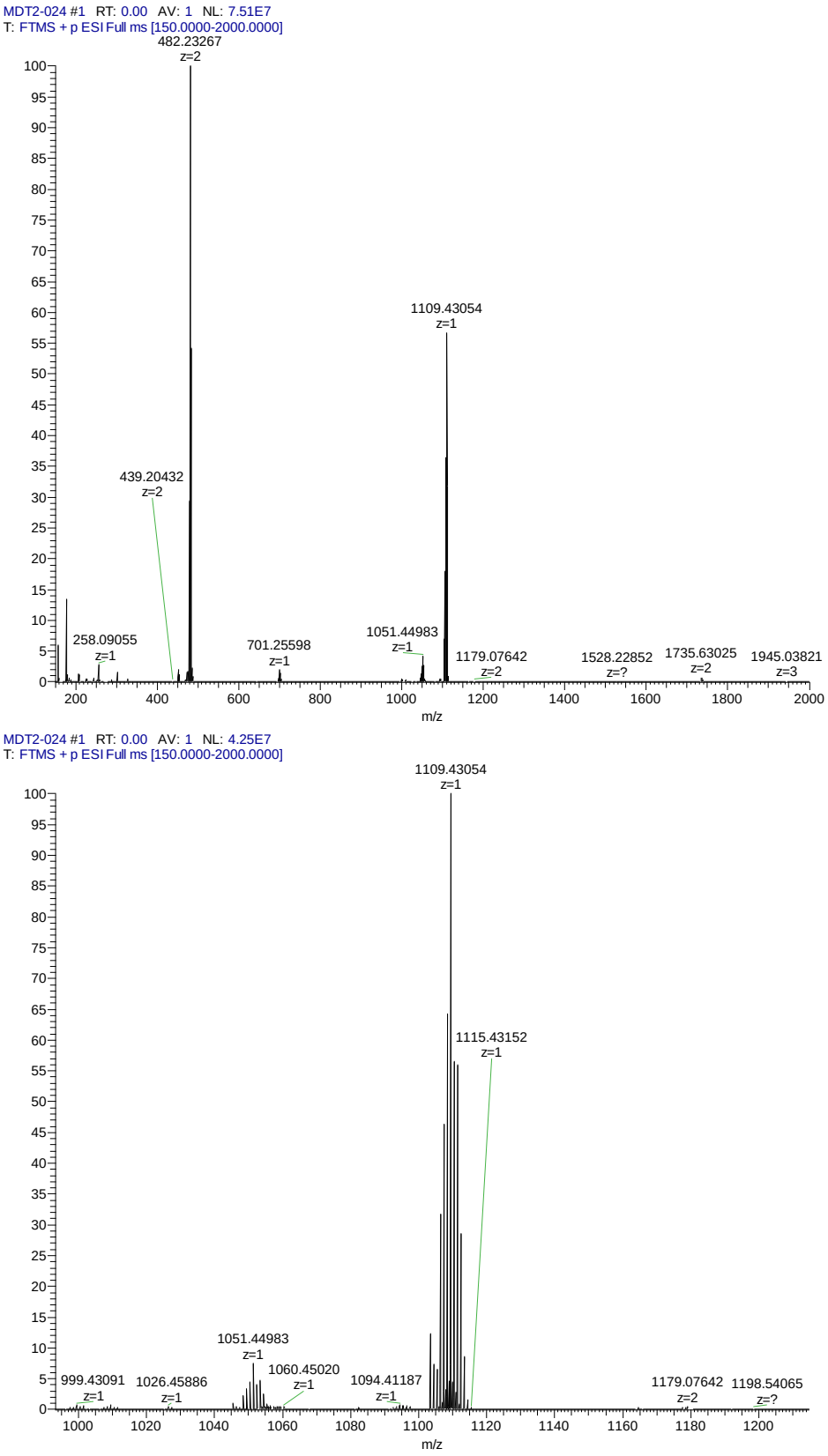

Figure S3. 14: High-Resolution Mass Spectrum of Ru-dpa.

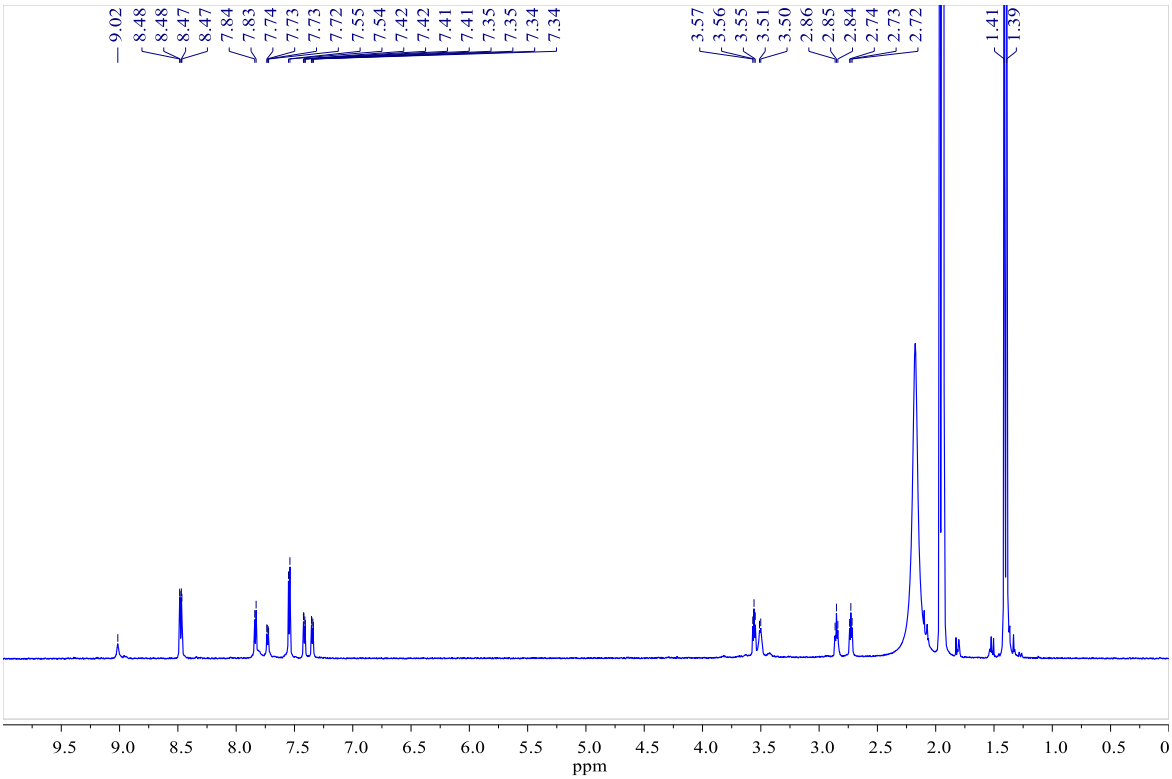

Figure S3.15: The ^{1}H NMR spectrum of Ru-daeaOH in CH_3CN at 298 K.

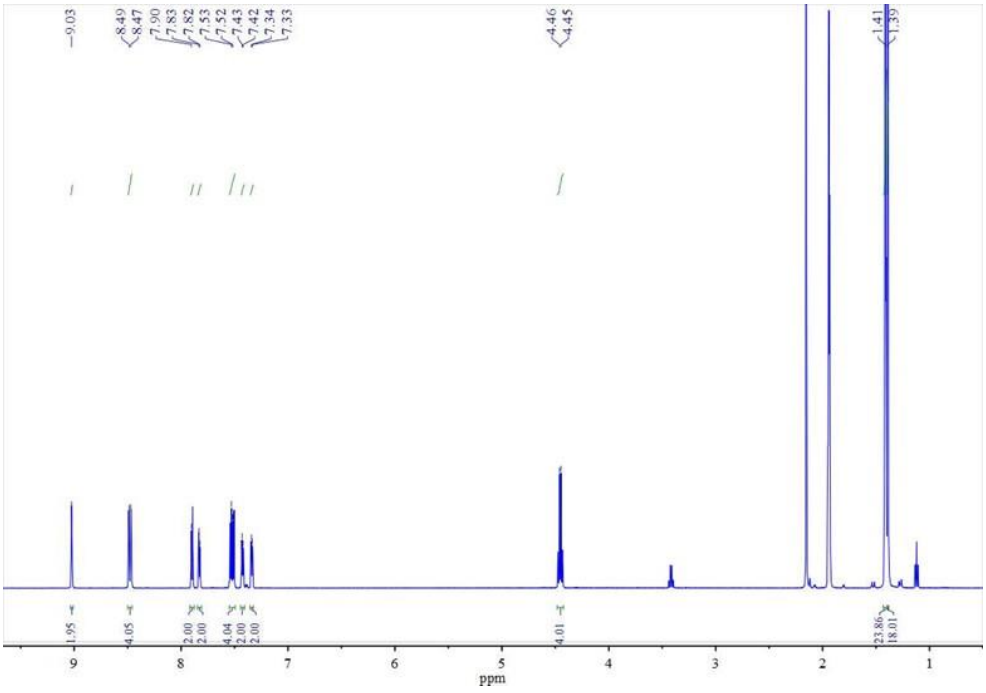

Figure S3.16: The ^{1}H NMR spectrum of Ru-deeb in CH_3CN at 298 K.

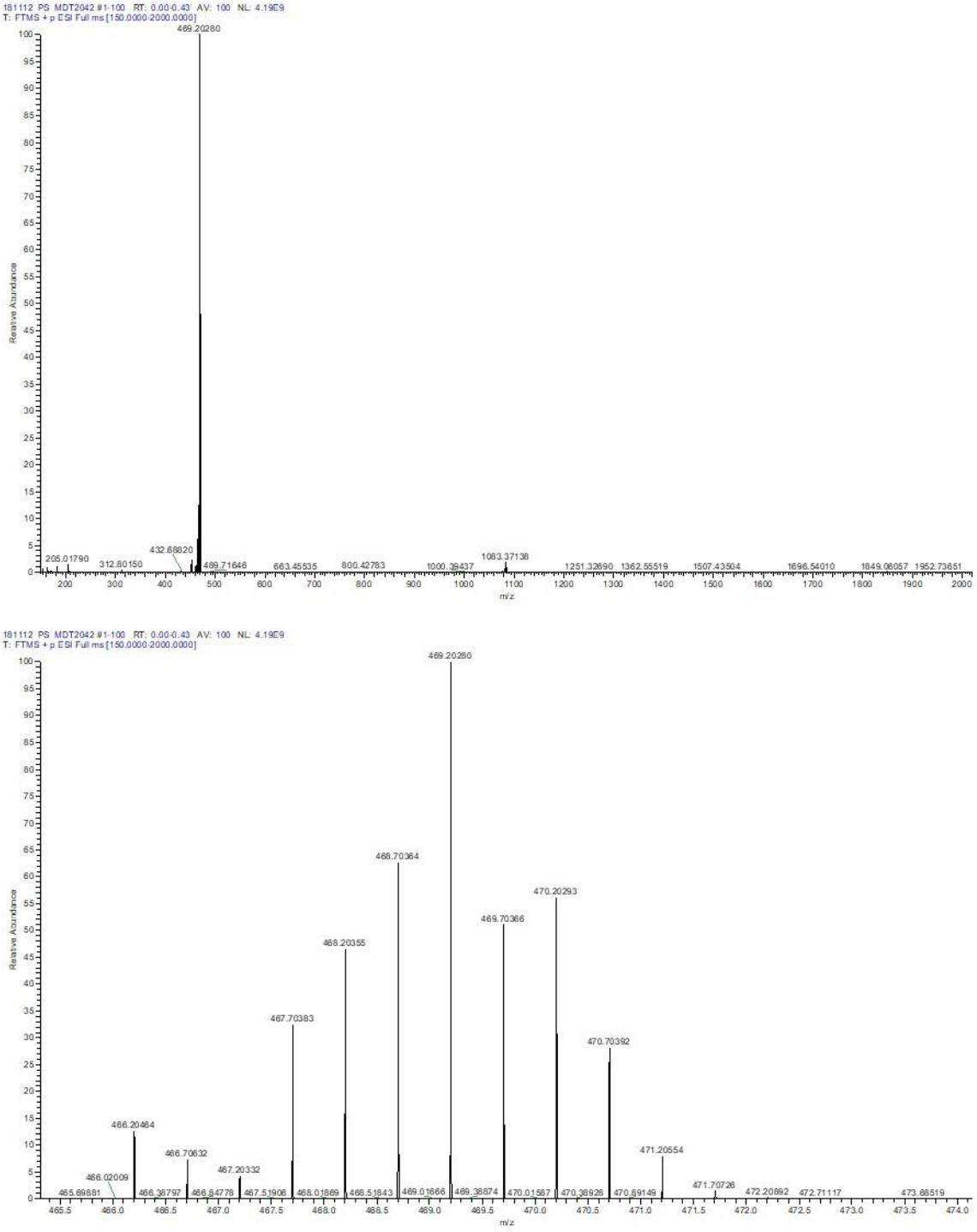

Figure S3.17: High-Resolution Mass Spectrum of Ru-deeb.

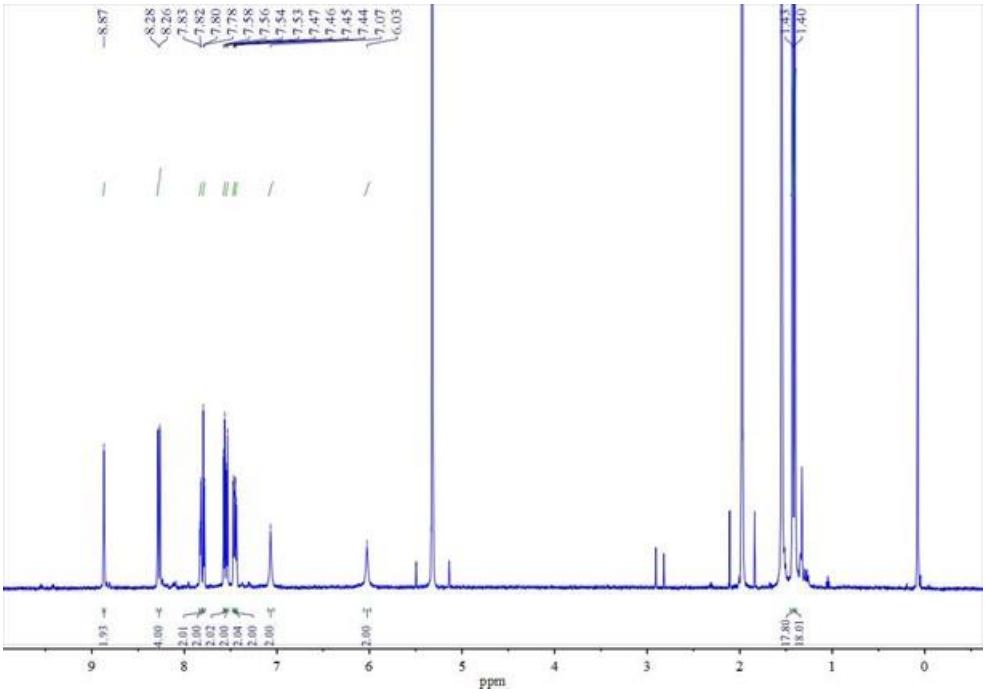

Figure S3.18: The ^{1}H NMR spectrum of Ru-da in CH_2Cl_2 at 298 K.

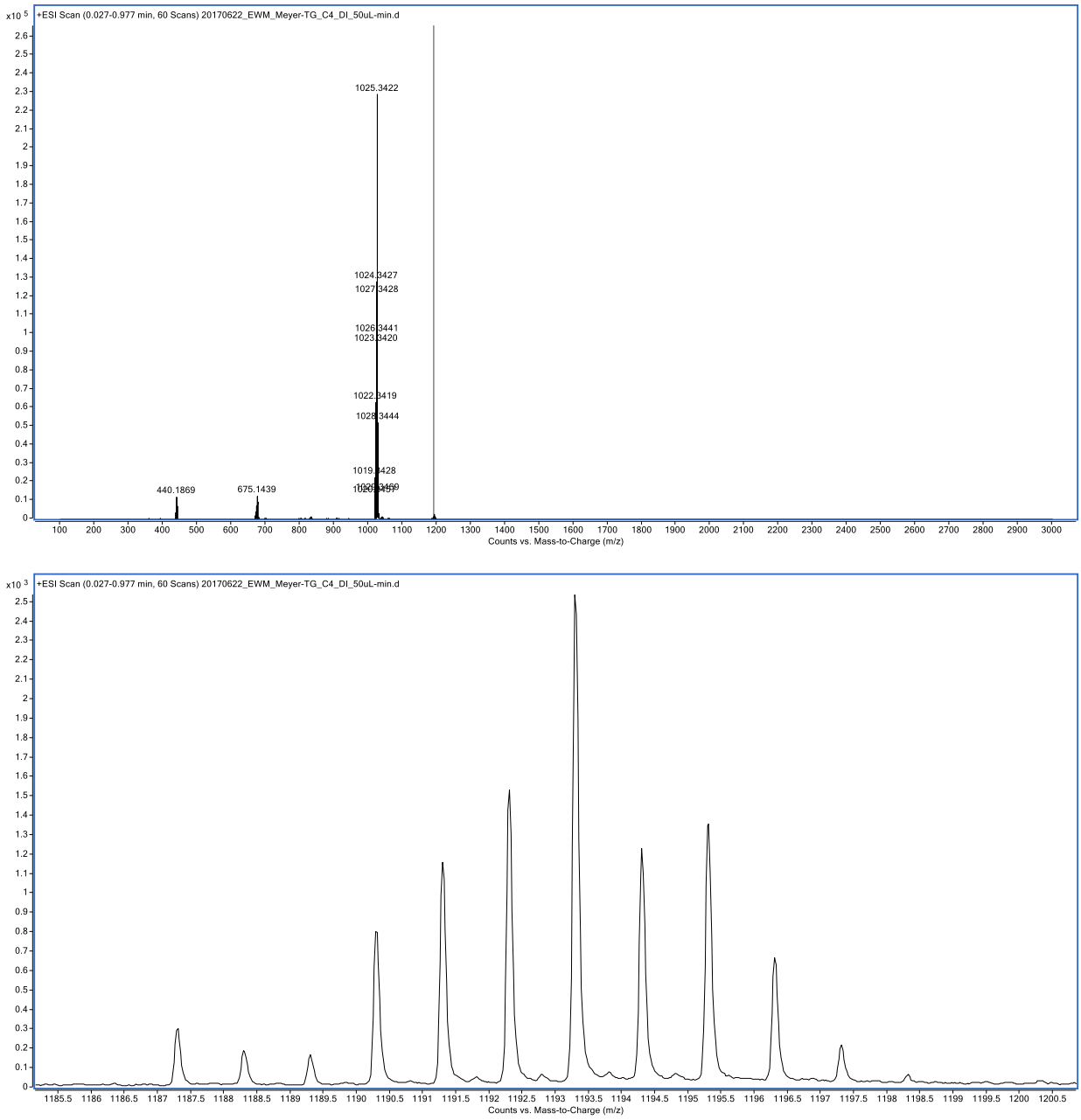

Figure S3.19: High-Resolution Mass Spectrum of Ru-da.

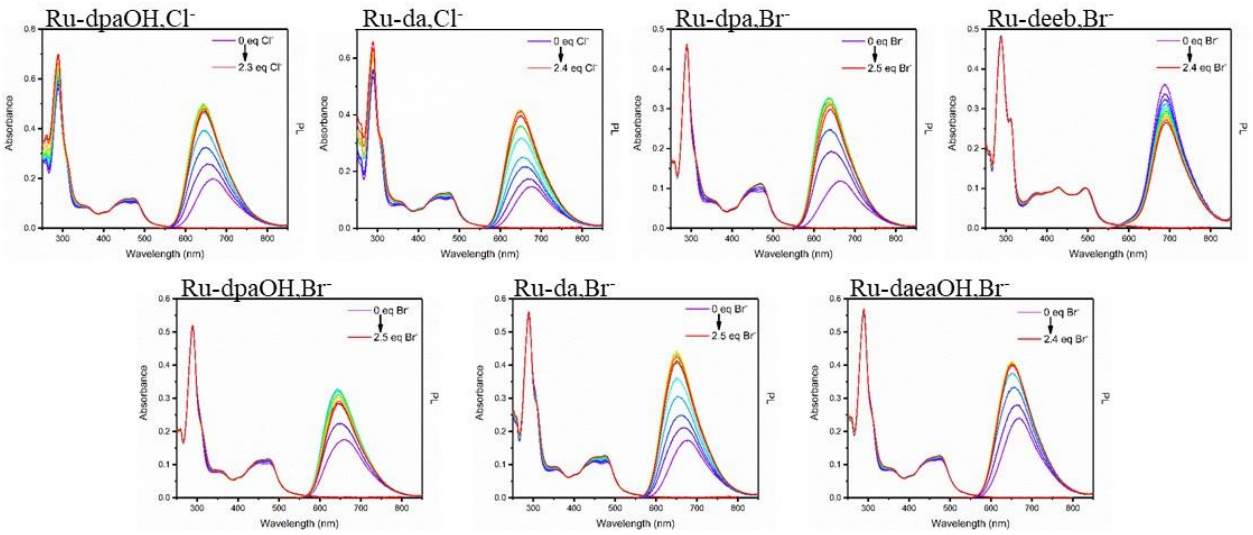

Figure S3.20: Absorbance and PL (λ_{ex} = 450 nm) spectra of the complexes in CH_2Cl_2 at room temperature as TBA chloride or bromide was titrated into solution. Titrations of TBA chloride into Ru-dpa and Ru-deeb are shown in Figure 3, while the titrations for Ru-deaOH[15] (TBA chloride and bromide) and Ru-daeaOH[17] (TBA chloride) are in references 15 and 17.

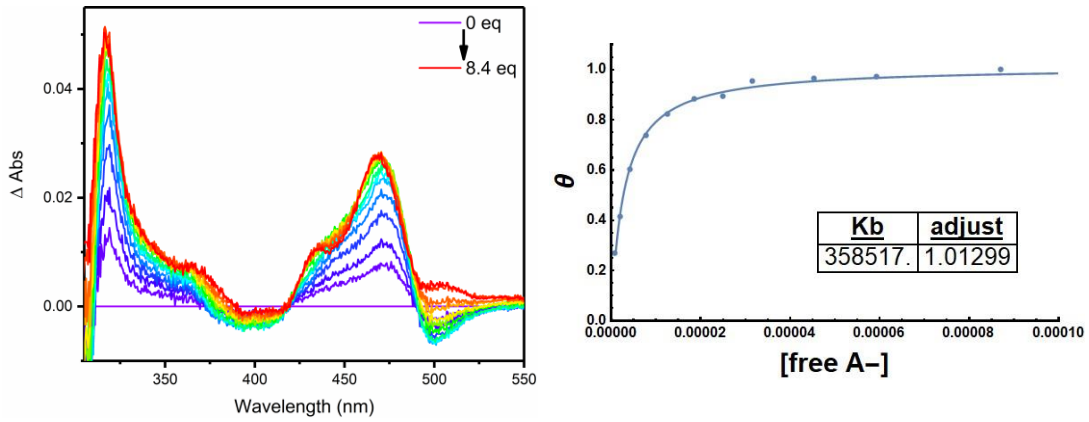

Figure S3.21: The UV-Vis difference spectra of Ru-deaOH with TBA triflate in CH_2Cl_2 at room temperature (left) and Benesi-Hildebrand analysis (right). The average K_{eq} at 470 nm with TBA triflate was found to be 2.82×10^5 M^{-1}.

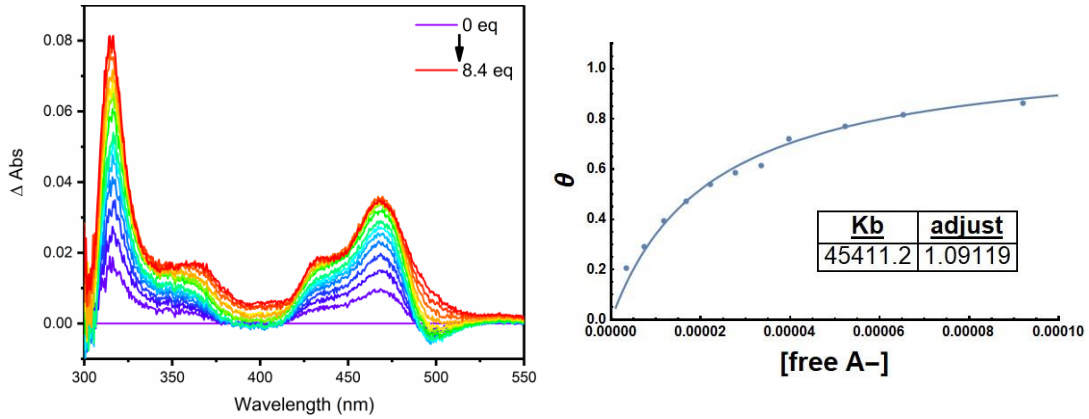

Figure S3.22: The UV-vis difference spectra of Ru-dpa with TBA BF_4 in CH_2Cl_2 at room temperature (left) and Benesi-Hildebrand analysis (right). The K_{eq} at 315 nm was 4.54×10^4 M^{-1}.

Table S3.1. Observed (K_{obs}) and Calculated (K_{eq}) Equilibrium Constants for Halide Association in the Presence of a Competitor. Average K_{eq}s for each Halide at the Three Competitor Concentrations are shown in Table 3.1.

Complex/ Competitor	Halide	[Competitor] ($\times10^{-4}$ M)	K_{obs} ($\times10^4$ M^{-1})	K_{eq} ($\times10^7$ M^{-1})
Ru-deaOH/ TBA triflate	Cl^-	3.06	73	6.3
		6.23	13	2.3
		11.70	7	2.2
	Br^-	2.86	42	3.4
		6.03	40	6.8
		12.00	9	3.0
Ru-dpa/ TBA BF_4	Cl^-	2.80	78	1.1
		6.10	118	3.4
		11.90	73	3.9
	Br^-	2.92	65	0.9
		5.95	26	0.7
		11.70	14	0.7

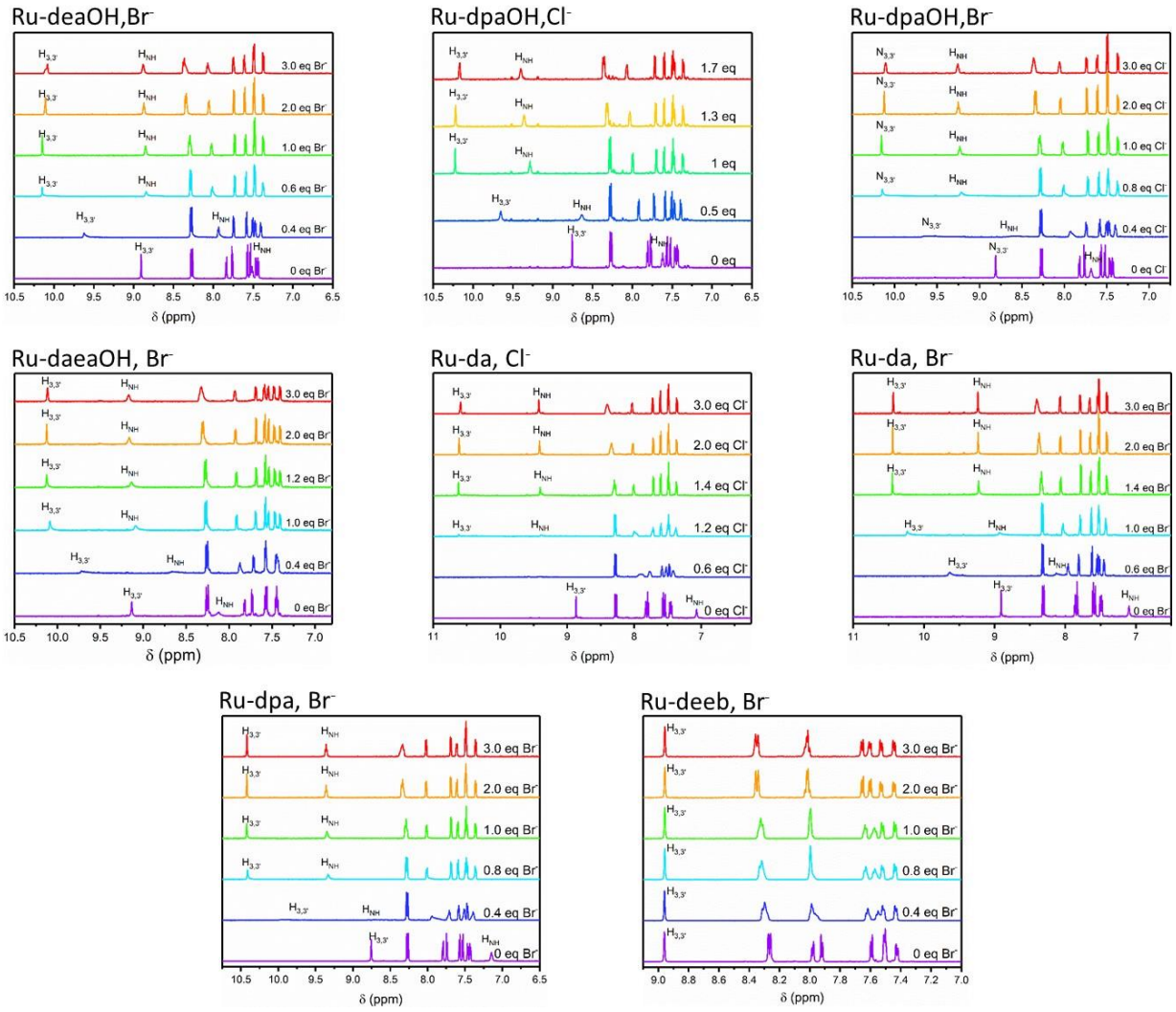

Figure S3. 23: The aromatic region of the ^{1}H NMR spectra of the complexes as TBA chloride and bromide were titrated into solution. Recorded in CD_2Cl_2 at room temperature on a 500 MHz spectrometer. Titrations of TBA chloride into Ru-dpa and Ru-deeb are shown in Figure 4, while the TBA chloride titrations for Ru-deaOH[1] and Ru-daeaOH[2] are in references 1 and 2.

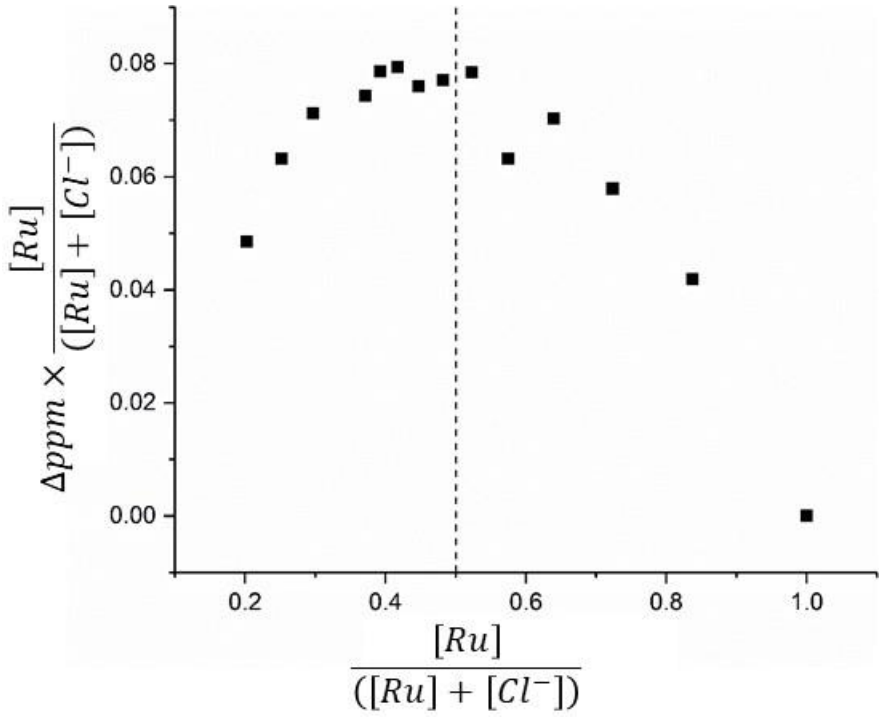

Figure S3.24: Job plot analysis of the ^{1}H NMR titration of Ru-deeb with TBA chloride. The maximum at a mol fraction of approximately 0.5 is indicative of 1:1 ion pair formation.

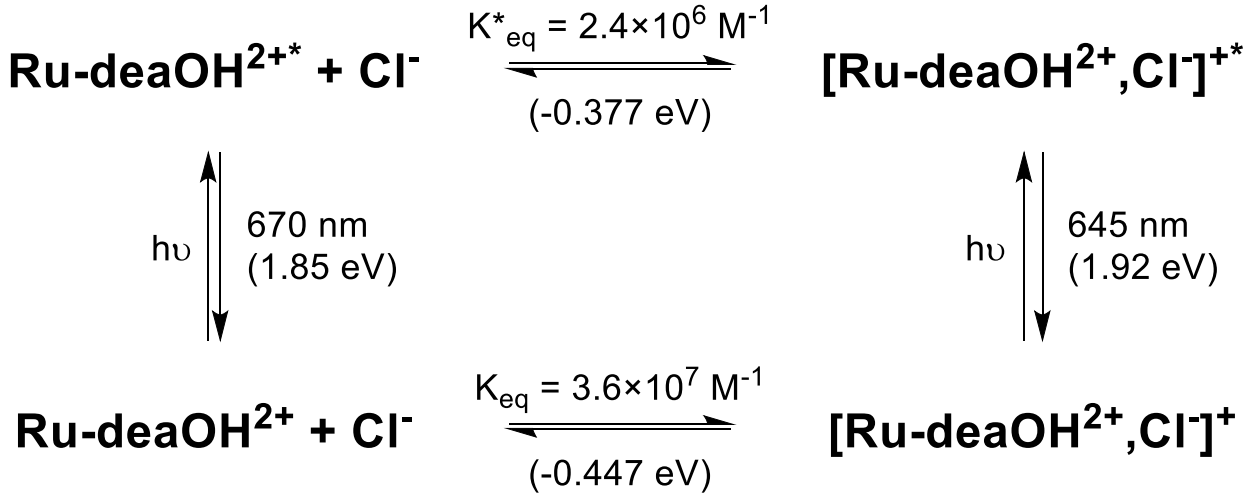

Figure S3.25: Representative Förster Cycle analysis for Ru-deaOH with chloride. This method was used to calculate the excited-state equilibrium constants with halides shown in Table 3.1.

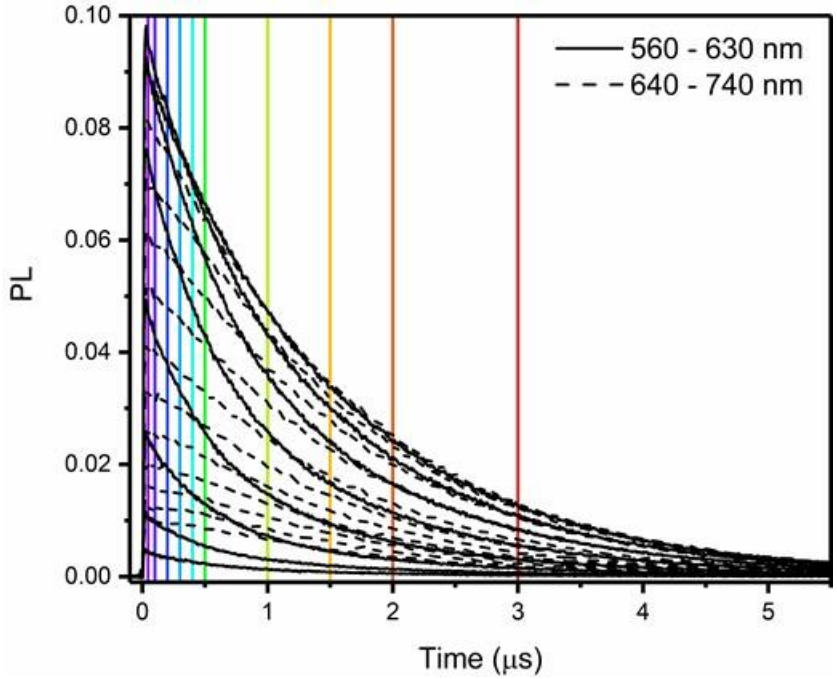

Figure S3.26: Time-resolved PL of Ru-deaOH with one equivalent of TBA chloride in CH_2Cl_2 at 298 K. Time-resolved PL traces were obtained every 10 nm from 560 – 740 nm. The amplitude of the traces at various times (colored lines) were plotted versus the wavelength and normalized to produce a transient PL spectrum. This procedure was used to generate the transient PL spectra shown in Figure 5 and S27.

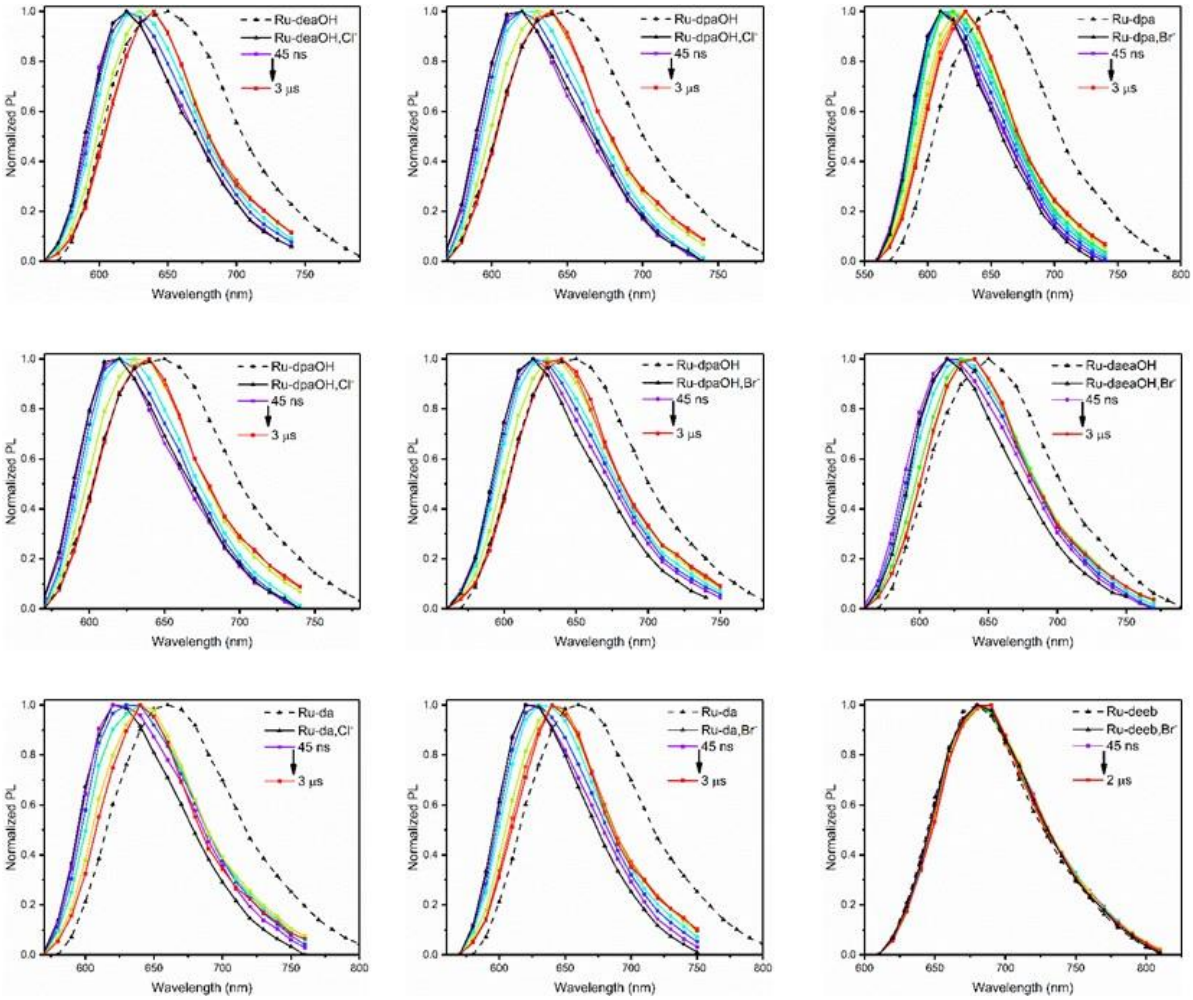

Figure S3.27: Transient PL spectra of the complexes at 45 ns and longer time delays after pulsed 500 nm excitation in the presence of one equivalent of chloride or bromide in CH_2Cl_2. For reference, the PL of the non-ion-paired complexes are included (black triangles, dashed line). The transient PL of Ru-dpa and Ru-deeb with chloride are shown in Figure 5, while the transient PL of Ru-daeaOH[2] with chloride is in reference 2.

Appendix: Calculation of the diffusion limit[57] for Ru^*, Cl^- interactions in CH_2Cl_2.

$$\boldsymbol{k_{diff} = 4\pi N_A (D_{Cl^-} + D_{Ru^*})\beta} \qquad \textbf{(S1)}$$

$$\beta = \frac{R_C}{\left(exp^{R_C/R} - 1\right)} \qquad \text{(S2)}$$

$$R_C = z_{Cl^-} z_{Ru^*} e^2 / 4\pi\varepsilon_r\, \varepsilon_0 k_B T \qquad \text{(S3)}$$

Where N_A is Avogadro's constant, D is the diffusion constant for chloride and the ruthenium excited state, z is the ionic charge, e is the elementary charge, ε_r is the vacuum permittivity, ε_r is the solvent dielectric, k_B is the Boltzmann constant, and T is temperature.

The diffusion constants, D_{Cl^-} and D_{Ru^*}, were calculated through the Stokes-Einstein relationship:

$$D = \frac{k_B T}{6\pi\eta r} \quad \text{(S4)}$$

Where η is the solvent viscosity of CH_2Cl_2 ($\eta = 4.5\times10^{-4}$ Pa•s) and r is the spherical radius of the molecule ($r_{Ru^*} = 7$Å[4], $r_{Cl^-} = 1.67$Å), $D_{Ru^*} = 6.9\times10^{-10}$ m^2 s^{-1} and $D_{Cl^-} = 2.9\times10^{-9}$ m^2 s^{-1}.

Under these conditions, k_{diff} is calculated to be 3.4×10^{11} M^{-1} s^{-1}.

Note: As written, the equation for k_{diff} gives units of m^3 mol^{-1} s^{-1}. To convert to units of M^{-1} s^{-1}, it is necessary to multiply by 1000.

REFERENCES

(1) Beer, P. D.; Gale, P. A. Anion Recognition and Sensing: The State of the Art and Future Perspectives. *Angew. Chem,. Int. Ed.* **2001**, *40*, 486–516.

(2) Barendt, T. A.; Ferreira, L.; Marques, I.; Félix, V.; Beer, P. D. Anion- and Sovent-Induced Rotary Dynamics and Sensing in a Perylene Diimide [3]Catenane. *J. Am. Chem. Soc.* **2017**, *139*, 9026–9037.

(3) Lim, J. Y. C.; Marques, I.; Félix, V.; Beer, P. D. A Chiral Halogen-Bonding [3]Rotaxane for the Recognition and Sensing of Biologically Relevant Dicarboxylate Anions. *Angew. Chem. Int. Ed.* **2018**, *57*, 584–588.

(4) Ramos, S.; Alcalde, E.; Doddi, G.; Mencarelli, P.; Pérez-García, L. Quantitative Evaluation of the Chloride Template Effect in the Formation of Dicationic [1_4]Imidazoliophanes. *J. Org. Chem.* **2002**, *67*, 8463–8468.

(5) Raheem, I. T.; Thiara, P. S.; Peterson, E. A.; Jacobsen, E. N. Enantioselective Pictet-Spengler-Type Cyclizations of Hydroxylactams: H-Bond Donor Caalysis by Anion Binding. *J. Am. Chem. Soc.* **2007**, *129*, 13404–13405.

(6) Reisman, S. E.; Doyle, A. G.; Jacobsen, E. N. Enantioselective Thiourea-Catalyzed Additions to Oxocarbenium Ions. *J. Am. Chem. Soc.* **2008**, *130*, 7198–7199.

(7) Brown, A. R.; Kuo, W. H.; Jacobsen, E. N. Enantioselective Catalytic α-Alkylation of Aldehydes via an S_N1 Pathway. *J. Am. Chem. Soc.* **2010**, *132*, 9286–9288.

(8) Birrell, J. A.; Desrosiers, J. N.; Jacobsen, E. N. Enantioselective Acylation of Silyl Ketene Acetals through Fluoride Anion-Binding Catalysis. *J. Am. Chem. Soc.* **2011**, *133*, 13872–13875.

(9) Koulov, A. V.; Lambert, T. N.; Shukla, R.; Jain, M.; Boon, J. M.; Smith, B. D.; Li, H.; Sheppard, D. N.; Joos, J. B.; Clare, J. P.; Davis, A. P. Chloride Transport Across Vesicle and Cell Membranes by Steroid-Based Receptors. *Angew. Chem. Int. Ed.* **2003**, *42*, 4931–4933.

(10) McNally, B. A.; Koulov, A. V.; Lambert, T. N.; Smith, B. D.; Joos, J. B.; Sisson, A. L.; Clare, J. P.; Sgarlata, V.; Judd, L. W.; Magro, G.; Davis, A. P. Structure-Activity Relationships in Cholapod Anion Carriers: Enhanced Transmembrane Chloride Transport through Substituent Tuning. *Chem. Eur. J.* **2008**, *14*, 9599–9606.

(11) Hussain, S.; Brotherhood, P. R.; Judd, L. W.; Davis, A. P. Diaxial Diureido Decalins as Compact, Efficient, and Tunable Anion Transporters. *J. Am. Chem. Soc.* **2011**, *133*, 1614–1617.

(12) Berezin, S. K.; Davis, J. T. Catechols as Membrane Anion Transporters. *J. Am. Chem. Soc.*

2009, *131*, 2458–2459.

(13) Sessler, J. L.; Eller, L. R.; Cho, W. S.; Nicolaou, S.; Aguilar, A.; Lee, J. T.; Lynch, V. M.; Magda, D. J. Synthesis, Anion-Binding Properties, and In Vitro Anticancer Activity of Prodigiosin Analogues. *Angew. Chem. Int. Ed.* **2005**, *44*, 5989–5992.

(14) Winstanley, K. J.; Allen, S. J.; Smith, D. K. Encapsulated Binding Sites-Synthetically Simple Receptors for the Binding and Transport of HCl. *Chem. Commun.* **2009**, 4299–4301.

(15) Troian-Gautier, L.; Beauvilliers, E. E.; Swords, W. B.; Meyer, G. J. Redox Active Ion-Paired Excited States Undergo Dynamic Electron Transfer. *J. Am. Chem. Soc.* **2016**, *138*, 16815–16826.

(16) Wehlin, S. A. M.; Troian-Gautier, L.; Sampaio, R. N.; Marcélis, L.; Meyer, G. J. Ter-Ionic Complex that Forms a Bond Upon Visible Light Absorption. *J. Am. Chem. Soc.* **2018**, *140*, 7799–7802.

(17) Turlington, M. D.; Troian-Gautier, L.; Sampaio, R. N.; Beauvilliers, E. E.; Meyer, G. J. Ligand Control of Supramolecular Chloride Photorelease. *Inorg. Chem.* **2018**, *57*, 5624–5631.

(18) Werber, J. R.; Osuji, C. O.; Elimelech, M. Materials for Next-Generation Desalination and Water Purification Membranes. *Nat. Rev. Mater.* **2016**, *1*, 1–15.

(19) White, W.; Sanborn, C. D.; Reiter, R. S.; Fabian, D. M.; Ardo, S. Observation of Photovoltaic Action from Photoacid-Modified Nafion Due to Light-Driven Ion Transport. *J. Am. Chem. Soc.* **2017**, *139*, 11726–11733.

(20) Cutting, G. R. Cystic Fibrosis Genetics: From Molecular Understanding to Clinical Application. *Nat. Rev. Genet.* **2015**, *16*, 45–56.

(21) Benesi, H. A.; Hildebrand, J. H. A Spectrophotometric Investigation of the Interaction of Iodine with Aromatic Hydrocarbons. *J. Am. Chem. Soc.* **1949**, *71*, 2703–2707.

(22) Ward, W. M.; Farnum, B. H.; Siegler, M.; Meyer, G. J. Chloride Ion-Pairing with Ru(II) Polypyridyl Compounds in Dichloromethane. *J. Phys. Chem. A* **2013**, *117*, 8883–8894.

(23) Tse, J. K. Y.; Giannetti, A. M.; Bradshaw, J. M. Thermodynamics of Calmodulin Trapping by Ca^{2+}/Calmodulin-Dependent Protein Kinase II: Subpicomolar K_d Determined Using Competition Titration Calorimetry. *Biochemistry* **2007**, *46*, 4017–4027.

(24) Bellelli, A.; Carey, J. *Reversible Ligand Binding: Theory and Experiment*; John Wiley and Sons, Inc.: Hoboken, NJ, 2018; p 1–30.

(25) Le, V. H.; Yanney, M.; McGuire, M.; Sygula, A.; Lewis, E. A. Thermodynamics of Host-Guest Interactions between Fullerenes and a Buckycatcher. *J. Phys. Chem. B* **2014**, *118*,

11956–11964.

(26) Marton, A.; Clark, C. C.; Srinivasan, R.; Freundlich, R. E.; Narducci Sarjeant, A. A.; Meyer, G. J. Static and Dynamic Quenching of Ru(II) Polypyridyl Excited States by Iodide. *Inorg. Chem.* **2006**, *45*, 362–369.

(27) Wehlin, S. A. M.; Troian-Gautier, L.; Li, G.; Meyer, G. J.; Chloride Oxidation by Ruthenium Excited-States in Solution. *J. Am. Chem. Soc.* **2017**, 139, 12903–12906.

(28) Li, G.; Ward, W. M.; Meyer, G. J. Visible Light Driven Nanosecond Bromide Oxidation by a Ru Complex with Subsequent Br-Br Bond Formation. *J. Am. Chem. Soc.* **2015**, *137*, 8321–8323.

(29) Li, G.; Brady, M. D.; Meyer, G. J. Visible Light Driven Bromide Oxidation and Ligand Substitution Photochemistry of a Ru Diimine Complex. *J. Am. Chem. Soc.* **2018**, 140, 5447–5456.

(30) O'Donnell, R. M.; Sampaio, R. N.; Li, G.; Johansson, P. G.; Ward, C. L.; Meyer, G. J. Photoacidic and Photobasic Behavior of Transition Metal Compounds with Carboxylic Acid Group(s). *J. Am. Chem. Soc.* **2016**, *138*, 3891–3903.

(31) Loken, M. R.; Hayes, J. W.; Gohlke, J. R.; Brand, L. Excited-State Proton Transfer as a Biological Probe. Determination of Rate Constants by Means of Nanosecond Fluorometry. *Biochemistry*, **1972**, *11*, 4779–4786.

(32) Demas, J. N. *Excited State Lifetime Measurements*; Demas, J. N.; Academic Press: New York, 1983; p 43.

(33) Laws, W. R.; Brand, L. Analysis of Two-State Excited-State Reactions. The Fluorescence Decay of 2-Naphthol. *J. Phys. Chem.* **1979**, *83*, 795–802.

(34) Ireland, J. F.; Wyatt, P. A. H. *Advances in Physical Organic Chemistry*; Gold, V., Academic Press: New York, 1976; Vol. 12, p 131.

(35) Lakowicz, J. R. *Principles of Fluorescence Spectroscopy*, 2nd ed.; Kluwer Academic/Plenum Publishers: New York, 1999.

(36) Arunan, E.; Desiraju, G. R.; Klein, R. A.; Sadlej, J.; Scheiner, S.; Alkorta, I.; Clary, D. C.; Crabtree, R. H.; Dannenberg, J. J.; Hobza, P.; Kjaergaard, H. G.; Legon, A. C.; Mennucci, B.; Nesbitt, D. J. Definition of the Hydrogen Bond (IUPAC Recommendations 2011). *Pure Appl. Chem.* **2011**, *83*, 1637–1641.

(37) Bondy, C. R.; Loeb, S. J. Amide Based Receptors for Anions. *Coord. Chem. Rev.* **2003**, *240*, 77–99.

(38) Swords, W. B.; Li, G.; Meyer, G. J. Iodide Ion Pairing with Highly Charged Ruthenium

Polypyridyl Cations in CH_3CN. *Inorg. Chem.* **2015**, *54*, 4512–4519.

(39) Troian-Gautier, L.; Wehlin, S. A. M.; Meyer, G. J. Photophysical Properties of Tetracationic Ruthenium Complexes and their Ter-Ionic Assemblies with Chloride. *Inorg. Chem.* **2018**, *57*, 12232–12244.

(40) Ramalingam, V.; Domaradzki, M. E.; Jang, S.; Muthyala, R. S. Carbonyl Groups as Molecular Valves to Regulate Chloride Binding to Squaramides. *Org. Lett.* **2008**, *10*, 7946–7949.

(41) Amendola, V.; Bergamaschi, G.; Boiocchi, M.; Fabbrizzi, L.; Milani, M. The Squaramide Versus Urea Contest for Anion Recognition. *Chem. Eur. J.* **2010**, *16*, 4368–4380.

(42) Bondy, C. R.; Gale, P. A.; Loeb, S. J. Platinum(II) Nicotinamide Complexes as Receptors for Oxo-Anions. *Chem. Commun.* **2001**, 729–730.

(43) Beer, P. D.; Szemes, F.; Balzani, V.; Salà, C. M.; Drew, M. G. B.; Dent, S. W.; Maestri, M. Anion Selective Recognition and Sensing by Novel Macrocyclic Transition Metal Receptor Systems. ^{1}H NMR, Electrochemical, and Photophysical Investigations. *J. Am. Chem. Soc.* **1997**, *119*, 11864–11875.

(44) Szemes, F.; Hesek, D.; Chen, Z.; Dent, S. W.; Drew, M. G. B.; Goulden, A. J.; Graydon, A. R.; Grieve, A.; Mortimer, R. J.; Wear, T.; Weightman, J. S.; Beer, P. D. Synthesis and Characterization of Novel Acyclic, Macrocyclic, and Calix[4]arene Ruthenium(II) Bipyridyl Receptor Molecules that Recognize and Sense Anions. *Inorg. Chem.* **1996**, *35*, 5868–5879.

(45) Beer, P. D.; Dent, S. W.; Wear, T. J. Spectral and Electrochemical Recognition of Halide Anions by Acyclic Mononuclear Ruthenium(II) Bipyridyl Receptor Molecules. *J. Chem. Soc., Dalt. Trans.* **1996**, 2341–2346.

(46) Smith, D. K. Rapid NMR Screening of Chloride Receptors: Uncovering Catechol as a Useful Anion Binding Motif. *Org. Biomol. Chem.* **2003**, *1*, 3874–3877.

(47) Winstanley, K. J.; Sayer, A. M.; Smith, D. K. Anion Binding by Catechols-an NMR, Optical and Electrochemical Study. *Org. Biomol. Chem.* **2006**, *4*, 1760–1767.

(48) Li, Y.; Flood, A. H. Pure C-H Hydrogen Bonding to Chloride Ions: A Preorganized and Rigid Macrocyclic Receptor. *Angew. Chem. Int. Ed.* **2008**, *47*, 2649–2652.

(49) Li, Y.; Flood, A. H. Strong, Size-Selective, and Electronically Tunable C-H•••Halide Binding with Steric Control over Aggregation from Synthetically Modular, Shape-Persistent [3_4]Triazolophanes. *J. Am. Chem. Soc.* **2008**, *130*, 12111–12122.

(50) Meudtner, R. M.; Hecht, S. Helicity Inversion in Responsive Foldamers Induced by Achiral Halide Ion Guests. *Angew. Chem. Int. Ed.* **2008**, *47*, 4926–4930.

(51) Juwarker, H.; Lenhardt, J. M.; Pham, D. M.; Craig, S. L. 1,2,3-Triazole CH•••Cl^- Contacts Guide Anion Binding and Concomitant Folding in 1,4-Diaryl Triazole Oligomers. *Angew. Chem. Int. Ed.* **2008**, *47*, 3740–3743.

(52) Blakley, R. L.; Dearmond, M. K. Unique Spectroscopic Properties of Mixed-Ligand Complexes with 2,2′-Dipyridylamine: A Dual Luminescence from a Ruthenium(II) Complex. *J. Am. Chem. Soc.* **1987**, *109*, 4895–4901.

(53) Elliott, C. M.; Hershenhart, E. J. Electrochemical and Spectral Investigations of Ring-Substituted Bipyridine Complexes of Ruthenium. *J. Am. Chem. Soc.* **1982**, *104*, 7519–7526.

(54) Farnum, B. H.; Gardner, J. M.; Marton, A.; Narducci-Sarjeant, A. A.; Meyer, G. J. Influence of Ion Pairing on the Oxidation of Iodide by MLCT Excited States. *Dalt. Trans.* **2011**, *40*, 3830–3838.

(55) Martir, D. R.; Averardi, M.; Escudero, D.; Jacquemin, D.; Zysman-Colman, E. Photoinduced Electron Transfer in Supramolecular Ruthenium-Porphyrin Assemblies. *Dalton Trans.* **2017**, *46*, 2255–2262.

(56) Oh, D. H.; Boxer, S. G. Stark Effect Spectra of Ru(diimine)$_3^{2+}$ Complexes. *J. Am. Chem. Soc.* **1989**, *111*, 1131–1133.

(57) Gardner, J. M.; Abrahamsson, M.; Farnum, B. H.; Meyer, G. J. Visible Light Generation of Iodine Atoms and I-I Bonds: Sensitized I^- Oxidation and I_3^- Photodissociation. *J. Am. Chem. Soc.* **2009**, *131*, 16206–16214.

(58) Liu, Y.; Sengupta, A.; Raghavachari, K.; Flood, A. H. Anion Binding in Solution: Beyond the Electrostatic Regime. *Chem* **2017**, *3*, 411–427.

(59) Adams, S. R.; Kao, J. P. Y.; Grynkiewicz, G.; Minta, A.; Tsien, R. Y. Biologically Useful Chelators that Release Ca^{2+} upon Illumination. *J. Am. Chem. Soc.* **1988**, *110*, 3212–3220.

(60) Kimura, K.; Mizutani, R.; Yokoyama, M.; Arakawa, R.; Sakurai, Y. Metal-Ion Complexation and Photochromism of Triphenylmethane Dye Derivatives Incorporating Monoaza-15-crown Moieties. *J. Am. Chem. Soc.* **2000**, *122*, 5448–5454.

(61) Kaplan, J. H.; Ellis-Davies, G. C. R. Photolabile Chelators for the Rapid Photorelease of Divalent Cations. *Proc. Natl. Acad. Sci. USA* **1988**, *85*, 6571–6575.

(62) Cui, J.; Gropeanu, R. A.; Stevens, D. R.; Rettig, J.; Campo, A. New Photolabile BAPTA-Based Ca^{2+} Cages with Improved Photorelease. *J. Am. Chem. Soc.* **2012**, *134* (18), 7733–7740.

(63) Lednev, I. K.; Hester, R. E.; Moore, J. N. Direct Observation of Photocontrolled Ion Release: A Nanosecond Time-Resolved Spectroscopic Study of a Benzothiazolium Styryl Azacrown Ether Dye Complexed with Barium. *J. Phys. Chem. A* **1997**, *101*, 7371–7378.

(64) Malval, J. P.; Gosse, I.; Morand, J. P.; Lapouyade, R. Photoswitching of Cation Complexation with a Monoaza-crown Dithienylethene Photochrome. *J. Am. Chem. Soc.* **2002**, *124*, 904–905.

(65) MacQueen, D. B.; Schanze, K. S. Cation-Controlled Photophysics in a Re(I) Fluoroionophore. *J. Am. Chem. Soc.* **1991**, *113*, 6108–6110.

(66) Lewis, J. D.; Moore, J. N. Photoinduced Ba^{2+} Release and Thermal Rebinding by an Azacrown Ether Linked by an Alkynyl Pyridine to a (bpy)$Re(CO)_3$ Group. *Chem. Commun.* **2003**, 2858–2859.

(67) Lewis, J. D.; Perutz, R. N.; Moore, J. N. Light-Controlled Ion Swithcing: Direct Observation of the Complete Nanosecond Release and Microsecond Recapture Cycle of an Azacrown-Substituted $[(bpy)Re(CO)_3L]^+$ Complex. *J. Phys. Chem. A* **2004**, *108*, 9037–9047.

(68) Lewis, J. D.; Clark, I. P.; Moore, J. N. Ground and Excited State Resonance Raman Spectra of an Azacrown-Substituted $[(bpy)Re(CO)_3L]^+$ Complex: Characterization of Excited States, Determination of Sturcture and Bonding, and Observation of Metal Cation Release from the Azacrown. *J. Phys. Chem. A* **2007**, *111*, 50–58.

(69) Lewis, J. D.; Towrie, M.; Moore, J. N. Ground- and Excited-State Infrared Spectra of an Azacrown-Substituted $[(bpy)Re(CO)_3L]^+$ Complex: Sturcture and Bonding in Ground and Excited States and Effects of Ba^{2+} Binding. *J. Phys. Chem. A* **2008**, *112*, 3852–3864.

(70) Hadda, T. Ben; Le Bozec, H. Preparation and Characterization of Ruthenium Complexes with the New 4,4′,4″-tri-*tert*-butyl-terpyridine Ligand and with 4,4′-di-*tert*-butyl-bipyridine. *Polyhedron* **1988**, *7*, 575–577.

(71) Hoertz, P. G.; Staniszewski, A.; Marton, A.; Higgins, G. T.; Incarvito, C. D.; Rheingold, A. L.; Meyer, G. J. Toward Exceeding the Shockley-Queisser Limit: Photoinduced Interfacial Charge Transfer Processes that Store Energy in Excess of the Equilibrated Excited State. *J. Am. Chem. Soc.* **2006**, *128*, 8234–8245.

(72) Gillaizeau-Gauthier, I.; Odobel, F.; Alebbi, M.; Argazzi, R.; Costa, E.; Bignozzi, C. A.; Qu, P.; Meyer, G. J. Phosphonate-Based Bipyridine Dyes for Stable Photovoltaic Devices. *Inorg. Chem.* **2001**, *40*, 6073–6079.

(73) Crosby, G. A.; Demas, J. N. The Measurement of Photoluminescence Quantum Yields. A Review. *J. Phys. Chem.* **1971**, *75*, 991–1024.

(74) Connelly, N. G.; Geiger, W. E. Chemical Redox Agents for Organometallic Chemistry. *Chem. Rev.* **1996**, *96*, 877–910.

(75) Noviandri, I.; Brown, K. N.; Fleming, D. S.; Gulyas, P. T.; Lay, P. A.; Masters, A. F.; Phillips, L. The Decamethylferrocenium/Decamethylferrocene Redox Couple: A Superior

Redox Standard to the Ferrocenium/Ferrocene Redox Couple for Studying Solvent Effects on the Thermodynamics of Electron Transfer. *J. Phys. Chem. B* **1999**, 103, 6713–6722.

CHAPTER 4: IODIDE PHOTO-OXIDATION MECHANISMS IN 1:2 RUTHENIUM: HALIDE ASSEMBLIES

4.1 Introduction

Excited-state electron transfer reactions coupled with bond formation are of significant interest in chemistry, particularly in the fields of photoredox catalysis[1] and solar energy conversion.[2] However, first order radiative and non-radiative excited-state decay pathways often are competitive with the reaction of interest, leading to deactivation of the photocatalyst until another photon is absorbed. To impart greater control over these excited-state reactions, the tools of supramolecular assembly have been utilized to preorganize the redox partners in the ground state, thereby precluding the need for diffusion. In photoredox catalysis, this preorganization strategy has recently been implemented in asymmetric catalysis, enabling high enantioselectivity in a number of reactions that utilize chiral hydrogen-bonding photosensitizers.[3–6] However, more fundamental work is needed to elucidate the role that preorganization plays in these excited-state electron transfer/ bond formation reactions. Mechanistic studies probing the excited state reactivity between preorganized ruthenium polypyridyl complexes and iodide have revealed that association of the two species often affects the mechanism in unexpected ways.[7–9] In many of these cases, preorganization has indeed provided access to novel iodide oxidation mechanisms, but the formation of strong ground-state assemblies may also have unintended consequences, such as a stabilization that prevents the desired reactivity from occurring.[8]

To better understand how supramolecular assembly affects excited-state electron transfer/ bond forming reactions, it is necessary to develop new catalysts that promote assembly and initiate

excited-state reactivity. Ruthenium polypyridyl complexes are suited for this role, as numerous $[Ru(bpy)_3]^{2+}$ derivatives have been rigorously studied for anion sensing,[10] while the photophysical and photochemical properties are well-understood and have been routinely exploited for their excited-state reactivity. Of particular interest to this work is a class of ruthenium polypyridyl complex bearing amide functional groups in the 4,4′ or 5,5′ positions of a bipyridine ligand.[8,11–15] These complexes are known to associate with halides in a number of organic solvents, as changes in the electrochemical and optical properties report on the ground-state assembly. Reductive quenching of the ruthenium excited-state by iodide (a reaction of significant interest, as it involves both electron transfer, $I^{\bullet/+}$, and bond formation, $I^{\bullet} + I^- \rightarrow I_2^{\bullet-}$) has also been investigated, providing insights into the interplay between the reactivity and stability of an assembled halide.[8] Characterization of the excited-state assembly structure has also been achieved, suggesting that the interaction between the assembled halide and excited-state dipole is of importance.[14,15]

Herein, a series of ruthenium polypyridyl complexes bearing amide substituents in the 5,5′ position of a bipyridine ligand are presented. This change in the position of the amide functional groups drastically impacted the ground-state halide association, as 1:2 ruthenium: halide assemblies with chloride, bromide, and iodide were resolved in CH_3CN. Large equilibrium constants for the association of the first and second halide (K_{11} from 10^4 -10^6 M^{-1}, K_{12} from 10^3 - 10^5 M^{-1}) were determined. The ground-state assembly structure also had a significant impact on the excited-state quenching reaction with iodide. When this reaction was observed, a Stern-Volmer analysis revealed static and dynamic quenching of the excited state. However, both the static and dynamic components revealed two distinct quenching mechanisms at low and high iodide concentrations. The quenching rate constants obtained from the dynamic quenching ($k_{q,\ low\ [I-]}$ = 6.8×10^{10} M^{-1} s^{-1}, $k_{q,\ high\ [I-]} = 4.0 \times 10^{10}$ M^{-1} s^{-1}) were consistent with diffusional quenching of Ru^{2+}

and $[Ru^{2+}, I^-]^+$, while the static component ($K_{S,\ low\ [I-]} = 2.4 \times 10^4\ M^{-1}$, $K_{S,\ high\ [I-]} = 1.3 \times 10^3\ M^{-1}$) were consistent with static quenching of $[Ru^{2+}, I^-]^+$ and $[Ru^{2+}, 2I^-]$.

4.2 Results

The synthesis of the amide-functionalized halide receptor ligand **5,5′-daea** was achieved through the modification of a literature procedure.[15] Briefly, the methyl groups of 5,5-dimethyl-2,2′-bipyridine were oxidized to carboxylic acids by excess potassium dichromate in sulfuric acid. Esterification of the carboxylic acid groups was performed in ethanol with catalytic sulfuric acid, yielding 5,5′-diethylester-2,2′-bipyridine, which, when refluxed in the presence of 2-(2-aminoethylamine)ethanol, gave **5,5′-daea** as a white precipitate. The yields for each step of the ligand synthesis ranged from 34-93%. The ruthenium complexes **Ru-dtb**, **Ru-bpy**, and **Ru-btfmb** (Figure 4.1), were prepared by refluxing the appropriate $Ru(LL)_2Cl_2$ (LL = dtb, bpy, btfmb) precursor with **5,5′-daea** in ethanol, purified by column chromatography, and precipitated as the PF_6 salt. The complexes were isolated as red solids in moderate yields (32-64%). All complexes were soluble in polar solvents such as CH_3CN, while the *t*-butyl groups of **Ru-dtb** provided enhanced solubility in less polar solvents like CH_2Cl_2. Characterization of the **5,5′-daea** ligand with ^1H and the ruthenium complexes with ^1H NMR and high resolution mass spectroscopy, is provided in the SI (Figures S4.1-S4.7).

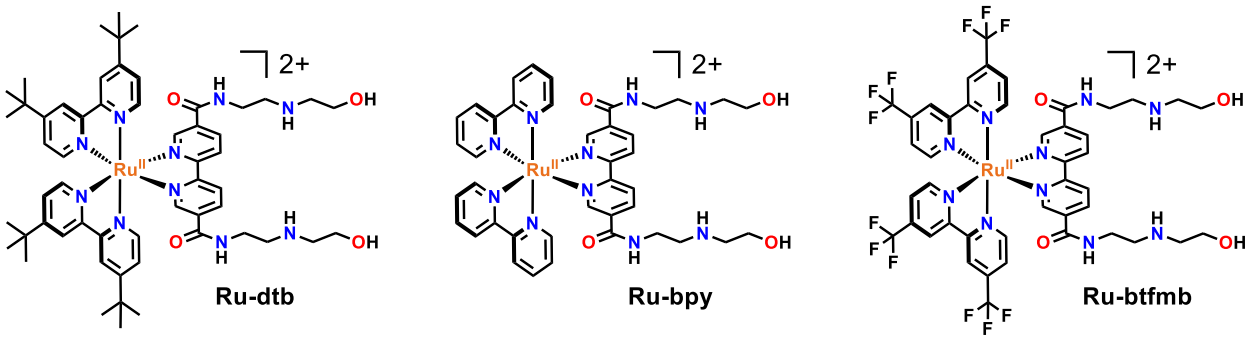

Figure 4.1: Ruthenium polypyridyl complexes reported in this study for supramolecular assembly with halides.

Square-wave voltammetry (Figure S4.8) was used to determine the metal and ligand based reduction potentials of each complex (Table 4.1). The metal based $Ru^{III/II}$ reduction potentials varied based on the electronic properties of the ancillary ligands, with electron withdrawing groups yielding the most anodic $Ru^{III/II}$ potential (1.84 V vs NHE for **Ru-btfmb**), while electron donating groups gave the most cathodic $Ru^{III/II}$ potential (1.46 V vs NHE **Ru-dtb**). A comparison of the ligand based reduction potentials with those of the homolyptic complexes indicated that for **Ru-btfmb**, the first reduction is of the btfmb ligand.[16] For **Ru-dtb** and **Ru-bpy**, the first reduction potential, which is approximately the same for both complexes, does not align with either dtb[17] or bpy,[18] and is therefore ascribed to reduction of the 5,5′-daea ligand. Blakley and DeArmond have shown that light-excitation of related complexes results in an excited-state dipole that is oriented towards the ligand that is most easily reduced.[19] Therefore, in **Ru-btfmb**, the excited-state dipole is oriented towards a btfmb ligand, while for **Ru-bpy** and **Ru-dtb**, the dipole is toward the 5,5′-daea ligand.

Table 4.1. Ground- and excited-state reduction potentials of ruthenium complexes

	(V vs NHE)			
Complex	$Ru^{III/II a}$	$Ru^{2+/+a}$	$Ru^{2+*/+}$	ΔG_{ES} (eV)
btfmb	1.84	-0.62	1.56	2.18
bpy	1.54	-0.72	1.31	2.03
dtb	1.46	-0.74	1.21	1.95

[a]Ground-state potentials measured in 0.1 M $NaClO_4$ in CH_3CN.

The UV-visible absorption spectra of the complexes are shown in Figure 4.2, solid lines. Characteristic features include a broad absorption between 400-550 nm ascribed to metal-to-ligand charge transfer (MLCT) transitions, and sharp absorption profiles at or below 300 nm attributed to ligand centered π-π* transitions.

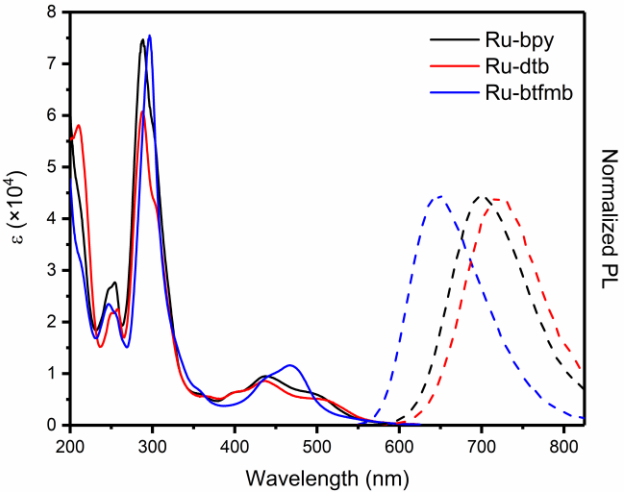

Figure 4.2: Absorbance (solid lines) and photoluminescence (dashed lines) spectra of the ruthenium complexes in CH_3CN.

The addition of tetrabutylammonium (TBA) chloride, bromide, or iodide salts into CH_3CN (or CH_2Cl_2) solutions of the ruthenium complexes (~ 40-60 μM) resulted in shifts in the UV-visible absorption spectrum consistent with halide assembly. In one instance, TBA chloride additions to **Ru-dtb** in CH_2Cl_2 resulted in such significant shifts that the color change was visible to the naked eye (Figure S4.9). In CH_3CN, where the bulk of this work was performed, the spectral changes upon halide addition were still significant (Figure 4.3) but not discernable by eye. In CH_3CN, the addition of halide to **Ru-dtb** (Figure 4.3, left, and Figure S4.10) and **Ru-bpy** (Figure S4.11) resulted in a blue shift of the low energy MLCT transitions, while for **Ru-btfmb**, the presence of halide resulted in a red-shift of the low energy feature (Figure 4.3, right, and Figure S4.12). Notably, in all halide titrations, the isosbestic points shifted dramatically over the course of the experiment, while new isosbestic points were resolved at higher halide concentrations (Figure 4.3, dashed lines in insets). Binding isotherms were generated from the spectral changes upon halide addition and were fit using a 1:2 binding model (available at supramolecular.org) to determine equilibrium constants for halide assembly.[20,21] The equilibrium constants obtained from the fitting are shown for each complex with chloride, bromide, and iodide in Table 4.2. From the equilibrium

constants, the mole fractions of the Ru^{2+}, $[Ru^{2+},X^-]$, and $[Ru^{2+},2X^-]$ species at each halide concentration were also determined (Figure S4.13).

Table 4.2. Equilibrium constants with chloride, bromide, and iodide in CH_3CN

	M^{-1}	**Ru-dtb**	**Ru-bpy**	**Ru-btfmb**
TBACl	K_{11}	$4.7\pm0.1 \times 10^5$	$2\pm1 \times 10^6$	$2\pm1 \times 10^6$
	K_{12}	$1.3\pm0.2 \times 10^3$	$2.8\pm0.8 \times 10^5$	$2.0\pm0.7 \times 10^4$
TBABr	K_{11}	$2.5\pm0.5 \times 10^5$	$7\pm3 \times 10^5$	$5\pm3 \times 10^5$
	K_{12}	$5\pm4 \times 10^3$	$3\pm1 \times 10^4$	$9\pm4 \times 10^3$
TBAI	K_{11}	$4\pm1 \times 10^4$	$4\pm2 \times 10^4$	$1.1\pm0.1 \times 10^5$
	K_{12}	$9\pm2 \times 10^2$	$1\pm1 \times 10^3$	$1.4\pm0.3 \times 10^3$

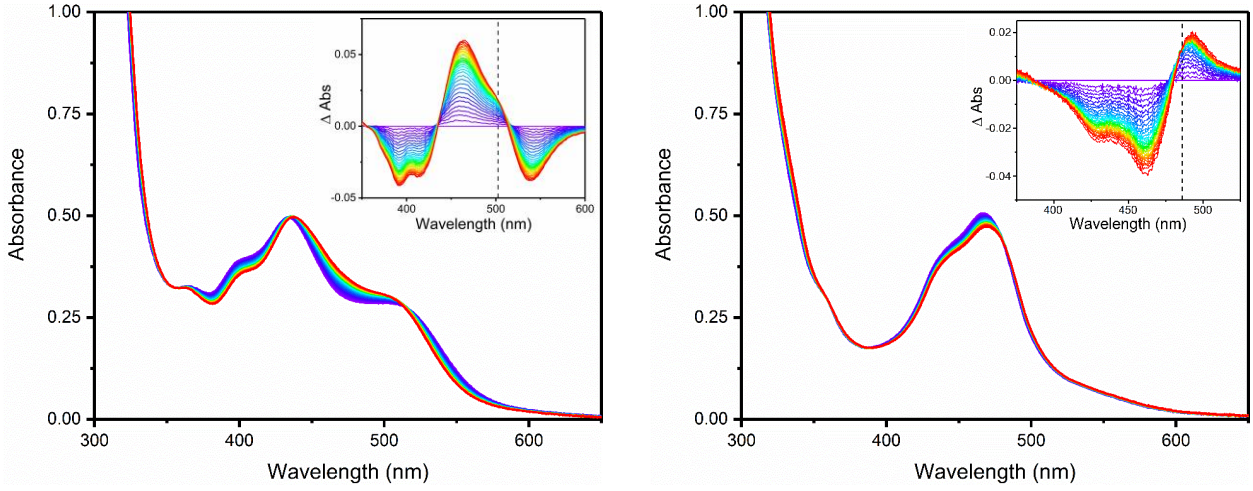

Figure 4.3: Absorption changes upon the titration of TBA chloride into CH_3CN solutions of **Ru-dtb** (left) and **Ru-btfmb** (right). The Δ absorption spectra in the insets (obtained by subtracting the absorbance at each halide concentration from the initial spectrum) show shifts in the isosbestic points and the appearance of new isosbestic points (dashed lines).

Halides titrations into approx. 1 mM CD_3CN solutions of **Ru-dtb**, **Ru-bpy**, and **Ru-btfmb** were monitored by ^1H NMR spectroscopy (Figure 4.4, and Figure S4.14). The presence of halide resulted in characteristic downfield shifts of resonances in the aromatic region, consistent with halide assembly. For **Ru-dtb**, the most prominent shifts were observed for the amide and 4,4′ hydrogens on the 5,5′-daea ligand, which shifted downfield by 1.84 and 0.57 ppm, respectively. The changes associated with the 4,4′ hydrogens saturated at approximately 2.5 equivalents of chloride, while the amide hydrogens shifted continuously throughout the course of the titration.

Small and continuous downfield shifts were also observed for the 6,6′ hydrogens (δppm = 0.16) on the 5,5′-daea ligand, and the 5,5′ hydrogens (Δppm = 0.12) on the dtb ligand. The results for **Ru-btfmb** and **Ru-bpy** were qualitatively similar, as the same signals (amide, 4,4′, and 6,6′ hydrogens on 5,5′-daea, and 5,5′ on the ancillary ligand) shifted downfield in the presence of halide, but also displayed a few minor differences. Namely, for **Ru-btfmb**, the Δppm for the 4,4′ hydrogens on the amide-functionalized ligand was much smaller (0.13 ppm) than that of **Ru-dtb**, while the 6,6′ hydrogens on that ligand had a larger Δppm of 0.20.

Chloride titrations in the less polar solvent CD_2Cl_2 provided additional insight into supramolecular assembly with **Ru-dtb** (Figure S4.15). Although the resonances that shifted downfield were the same in both solvents, (amide, 4,4′ and 6,6′ hydrogens on the 5,5′-daea ligand, and 5,5′ hydrogens on the dtb ligand), the 4,4′ hydrogens on the 5,5′-daea ligand displayed a much larger Δppm (0.73 at 1.5 eq. of chloride) in CD_2Cl_2 than in CH_3CN. However, further increasing the chloride concentration resulted in an upfield shift of 0.29 ppm, which was not observed in CH_3CN. Additionally, the 5,5′ hydrogens on the dtb ligand, which shifted continuously downfield in the titration in CD_3CN, did not shift in CD_2Cl_2 until 1.5 mM (~1.5 eq) of chloride was added, after which increasing the chloride concentration caused a shift of 0.21 ppm.

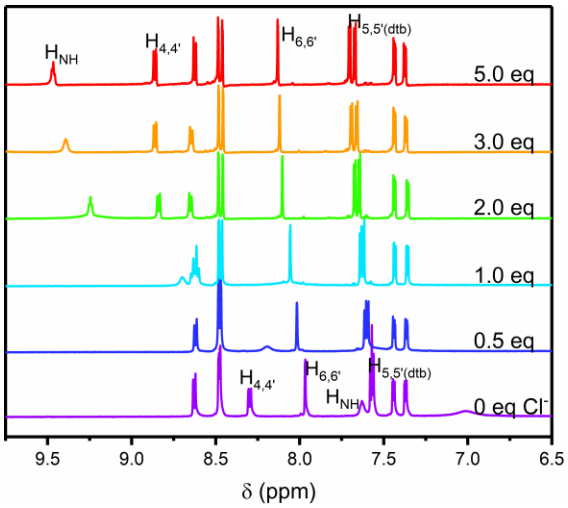

Figure 4.4: ^{1}H NMR titration of **Ru-dtb** with TBA chloride in CD_3CN.

Light excitation into the MLCT states of **Ru-dtb**, **Ru-bpy**, and **Ru-btfmb** resulted in photoluminescence (Figure 4.2, dashed lines) with maxima centered between 650-750 nm. Pulsed light excitation resulted in time resolved photoluminescence intensity changes that followed a first order-kinetic model with lifetimes that ranged from 44 ns (**Ru-dtb**) to 875 ns (**Ru-btfmb**) ns (Table 4.3). Photoluminescence quantum yields, as well as radiative and non-radiative rate constants for decay back to the ground-state, were determined through comparative actinometry using $[Ru(bpy)_3](Cl_2)$ as actinometer (Table 4.3).[22] The free energy stored in the excited-state, ΔG_{ES}, was estimated by fitting the high energy portion of the PL spectrum to a line and extrapolating to the photon energy-intercept (Table 4.1). Using the $Ru^{2+/+}$ potential, ΔG_{ES}, and equation 1, the excited state reduction potential for each complex, $Ru^{2+*/+}$, was calculated (Table 4.1).

$$E^{\circ}\left(Ru^{2+*/+}\right) = \Delta G_{ES} + E^{\circ}(Ru^{2+/+}) \qquad (1)$$

Table 4.3. Photphysical properties of the ruthenium complexes

Complex	λ_{max} PL (nm)	τ (ns)	Φ_{PL}	k_r ($\times 10^4$ s^{-1})	k_{nr} ($\times 10^6$ s^{-1})
Ru-dtb	720	44	0.002	4.5	22.58
Ru-bpy	700	57	0.003	5.2	17.58
Ru-btfmb	645	875	0.046	5.3	1.09

The addition of halides resulted in changes to the time-resolved and steady-state photoluminescence spectra. For **Ru-dtb** and **Ru-bpy**, the presence of halide resulted in a blue shift in the λ_{max} and an increase in the photoluminescence intensity (Figures S16), along with an increase in the photoluminescence lifetime. However, for **Ru-btfmb**, the addition of chloride and bromide led to a red shift and decrease in the photoluminescence intensity (Figures S17), while the addition of iodide resulted in excited-state quenching (Figure 4.5). The excited-state quenching of **Ru-btfmb** by iodide consisted of both a static and dynamic component, as both the initial intensity and photoluminescence lifetime in the time-resolved photoluminescence decreased with increasing iodide concentration. A Stern-Volmer analysis (equation 2) of the static and dynamic component (Figure 4.5, right inset), yielded two sloped regions at low (0-10 μM) and high (20-100 μM) iodide concentrations. The dynamic quenching rate constants (k_q, calculated from equation 3) were 6.8×10^{10} M^{-1} s^{-1} and 4.0×10^{10} M^{-1} s^{-1}, and the static quenching constants were 2.4×10^4 M^{-1} and 1.3×10^3 M^{-1} at low and high iodide concentrations, respectively.

$$I_0/I \ or \ \tau_0/\tau = 1 + K_{SV}[Q] \quad (2)$$

$$k_q = K_{SV}/\tau_0 \quad (3)$$

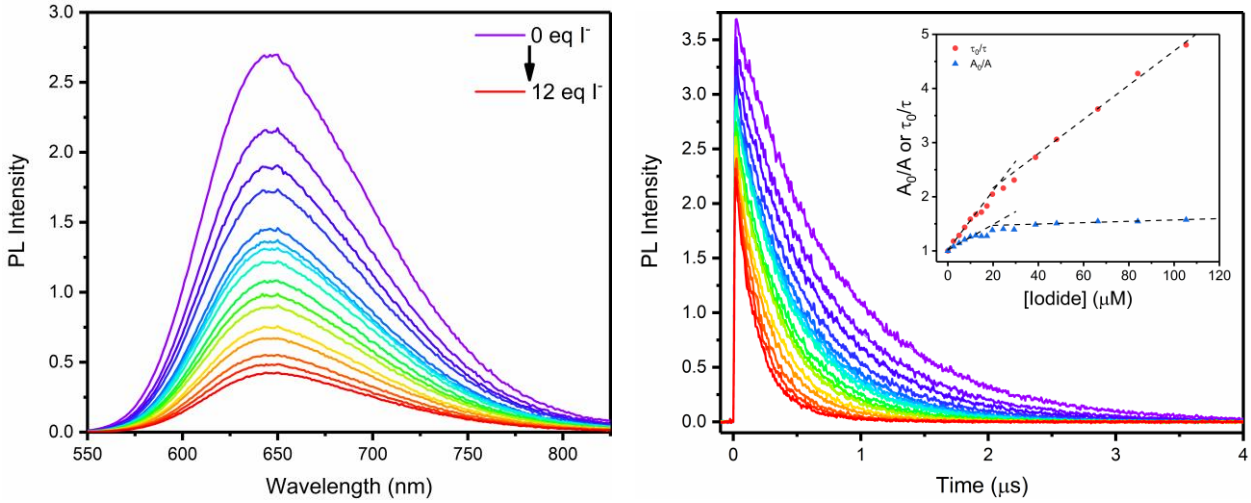

Figure 4.5: Excited-state quenching of **Ru-btfmb** by TBA iodide. The inset shows a Stern-Volmer plot for the addition of iodide with dynamic (red dots) and static (blue triangles) quenching.

The excited-state quenching of **Ru-btfmb** was further probed at fixed ionic strengths (μ = 0.005 – 0.1 M) using TBA perchlorate as an inert electrolyte. In the electrolyte solutions, the static quenching was drastically attenuated, consistent with decreased supramolecular assembly with iodide. Increasing the ionic strength resulted in a decrease in the dynamic quenching rate constants (k_q) (Figure S4.18), allowing a Debye-Hückel analysis (equation 4) to be performed.

$$\log(k) = \log(k_0) + \frac{2Az_a z_b \mu^{1/2}}{1 + \alpha\beta\mu^{1/2}} \qquad (4)$$

In this analysis, a plot of $2A\mu^{1/2}/(1+\alpha\beta\mu^{1/2})$ (where A and β are constants, 1.1611 and 3.274×10^9,[23] and α , the reactive radius is 5.5Å) versus $\log(k_q)$ is expected to result in a linear relationship where the y-intercept equals k_q at μ = 0, and the slope equals the charge of the two ionic species ($z_a z_b$). For this data, a linear fit gave a k_q at μ = 0 of 6.3×10^{10} M^{-1} s^{-1} and a slope of -2.

Transient absorption spectroscopy was performed on ~40 μM **Ru-btfmb** solutions in CH_3CN. The transient spectra of **Ru-btfmb** upon 532 nm pulsed-laser excitation displays a ground-state bleach centered at 460 nm, growths below 400 nm and above 520 nm, and isosbestic points at 419 and 520 nm (Figure 4.6, left). When excess iodide (~1 mM, 25 eq. with respect to

Ru-btfmb) was present in the solution, new absorption features were observed (Figure 4.6, middle), consistent with diiodide, $I_2^{\bullet-}$, (λ_{max} = 385 nm) and a reduced ruthenium polypyridyl complex which shows absorption features centered around 520 nm.[8] The kinetics monitoring the formation of these two photoproducts were probed at various iodide concentrations. At all iodide concentrations, the rate of formation of the reduced ruthenium complex was faster than that of $I_2^{\bullet-}$ (Figure 4.6, right) suggesting that the reduced ruthenium is a primary photoproduct, while $I_2^{\bullet-}$ is a secondary photoproduct.

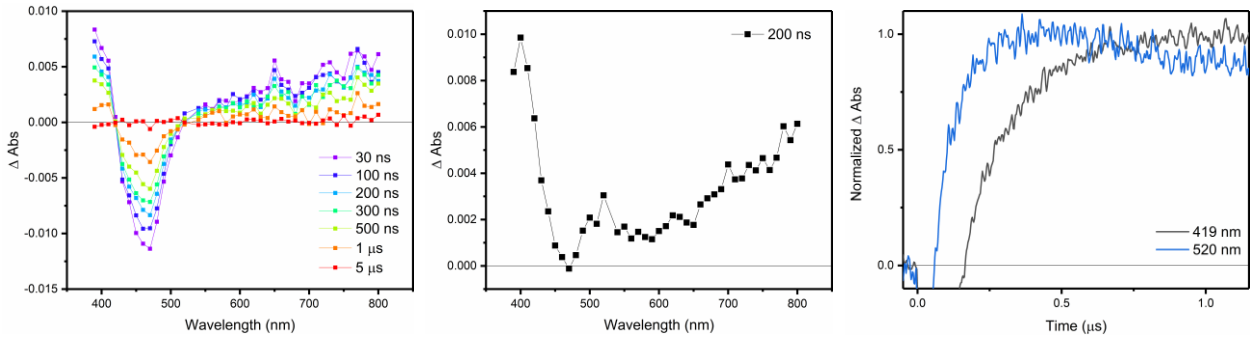

Figure 4.6: Transient absorption spectrum of **Ru-btfmb** in CH_3CN in the absence of iodide (left), and in the presence of 20 eq of iodide (middle). (Right) Kinetic traces at 419 and 520 nm with 5 eq of iodide. The laser fluence in each experiment was ~5 mJ/pulse.

4.3 Discussion

In this work, a series of ruthenium polypyridyl complexes are presented that assembly with two halides in CH_3CN. Few examples of such assembly structures are known, and in cases where two halides were able to overcome their intrinsic coulombic repulsion and associate with a host in close proximity, it was necessary to use highly charged cationic complexes and/ or low dielectric solvents.[9,24,25] The approach described herein makes use of amide functional groups in the 5,5′ position of a bipyridine ligand to facilitate large equilibrium constants with halide in a significantly more polar solvent. This result was somewhat unexpected, as one-to-one ruthenium-to-halide assembly was exclusively observed for related complexes with amide functional groups in the 4,4′ position.[8,14,15,26] As discussed in previous reports, the excited-states of ruthenium polypyridyl

complexes are potent photo-oxidants. For **Ru-dtb** and **Ru-bpy**, little to no driving force for halide oxidation was present, but for **Ru-btfmb**, both static and dynamic quenching by iodide was observed. A Stern-Volmer analysis of the static and dynamic quenching yielded two values of k_q and K_S at low and high iodide concentrations, behavior which suggests that the supramolecular assembly structure impacts the quenching mechanism. Transient absorption experiments revealed that the quenching proceeds through an electron transfer reaction, yielding reduced ruthenium and $I_2^{\bullet-}$ as products.

4.3.1 Supramolecular Assembly Structure

The complexes presented in this study were prepared by refluxing the appropriate $Ru(LL)_2Cl_2$ (LL = dtb, bpy, or btfmb) precursor with the 5,5′-daea ligand in EtOH, giving **Ru-dtb**, **Ru-bpy**, and **Ru-btfmb** in moderate yields of 32-64%. The absorption spectra of the complexes show the characteristic MLCT and ligand centered π-to-π* transitions at approximately 450 and 300 nm, respectively. For **Ru-dtb** and **Ru-bpy**, two broad and overlapping MLCT absorption bands are observed with the higher energy being assigned to Ru → dtb (or bpy) and the lower energy to Ru → **5,5′-daea**. The presence of the four electron withdrawing -CF_3 groups increases the $Ru^{III/II}$ potential giving rise to a blue shifted absorption and photoluminecesce spectrum. The MLCT absorption band for **Ru-btfmb** is also significantly sharper, presumably because the π* levels of the 5,5′-daea and btfmb ligands are close in energy.

Initial chloride titrations into CH_2Cl_2 solutions of **Ru-dtb** provided clear evidence for a 1:2 ruthenium:chloride assembly. In the UV-visible absorption spectrum, three species with distinct absorption profiles were resolved during the titration (Figure S4.10), while the binding isotherms provided evidence of two halide association steps to form $[Ru^{2+},Cl^-]^+$ and $[Ru^{2+},2Cl^-]$. In CH_2Cl_2, the spectral change associated with chloride assembly was observable by eye, as the red solution

turned yellow-orange during the course of the titration (Figure S4.10). These visible changes suggest that the complex may be promising for applications in colorimetric halide sensing. The ^{1}H NMR spectrum of **Ru-dtb** in CD_2Cl_2 provided additional evidence for the formation of 1:2 assemblies with chloride (Figure S4.15). In particular, the 4,4′ hydrogens on the 5,5′-daea ligand experienced a significant downfield shift (Δppm = 0.73) up to 1.5 equivalents of chloride, behavior which has been attributed to hydrogen-bonding interactions that lengthen the C-H bond and deshield the hydrogen. However, increasing the chloride concentration past 1.5 equivalents resulted in an upfield shift of 0.29 ppm for these same hydrogens. This upfield shift suggests that the association of a second anion destabilizes the first chloride associated with the 4,4′ hydrogens, which results in less hydrogen bonding at this position. The total downfield shift of 0.43 ppm (0.73 downfield minus 0.29 upfield) experienced during the course of the titration indicates that the 4,4′ hydrogens contribute to beneficial hydrogen-bonding interactions in the 1:2 halide assembly, but to a less extent than in the 1:1 assembly. Although CH_2Cl_2 proved to be a useful solvent for identifying the presence of 1:2 ruthenium-to-halide assemblies, a more complete characterization of halide association and excited-state quenching was performed in CH_3CN, a solvent in which all three complexes were soluble.

Significant research on anion association and sensing has shown that equilibrium constants for assembly are inversely proportional to the solvent dielectric,[27] as beneficial solvation interactions with the anion compete with stabilization by the host. As CH_3CN (ε = 37.5) is significantly more polar than CH_2Cl_2 (ε = 8.93), the equilibrium constants with halide were expected to decrease, possibly to such an extent that a second halide association would not occur. However, addition of halide salts (chloride, bromide, and iodide) to CH_3CN solutions of **Ru-dtb**, **Ru-bpy**, and **Ru-btfmb** resulted in several distinct spectral features that were consistent with 1:2

ruthenium-to-halide assembly. Three main points in favor of this assignment are: 1) For all complexes, the isosbestic points shifted significantly (approx. 7-10 nm, Figure 4.3, left and right insets) in the presence of halide. This behavior is not consistent with the presence of only two species, as prior studies on related ruthenium complexes that are known to form 1:1 assemblies do not, within the error of the spectrometer, display shifts in the isosbestic points during halide titrations.[14,15] For the complexes studied herein, the presence of secondary isosbestic points were resolved at high halide concentrations (Figure 4.3, dashed lines in insets), as would be expected after the concentration of Ru^{2+} is approximately zero and only conversion of $[Ru^{2+},X^-]^+$ to $[Ru^{2+},2X^-]$ is observed. 3) Fitting the binding isotherms with a 1:2 model generated residuals that were randomly distributed around zero, unlike the 1:1 model, where systematic trends in the residual plots were observed. Thordarson suggests that such systematic trends in residuals provide evidence against that binding model,[20,21] suggesting that the 1:1 model should not be used in this case. Based on these observations, a 1:2 ruthenium-to-halide stoichiometry was used to describe the data in CH_3CN, and modeling the data in this way gave the equilibrium constants (K_{11} and K_{12}) for halide association shown in Table 4.2. From the equilibrium constants, the mole fractions (χ) of the ruthenium species, Ru^{2+}, $[Ru^{2+},X^-]^+$, and $[Ru^{2+},2X^-]$, at each point during the titration were determined (Figure S4.13). The mole fraction plots showed that with each halide, $[Ru^{2+},X^-]^+$ was the dominate species after approximately one equivalent of chloride, bromide, or iodide was added. With chloride and bromide, K_{12} was so large that by the end of the titration (~10 eq X^-), the majority (70-80%) of ruthenium complexes in solution were present as the 1:2 $[Ru^{2+},2X^-]$ assembly.

A brief inspection of the equilibrium constants reveals that the complexes are most selective for chloride association, with large K_{11} (0.5 to 2×10^6 M^{-1} s^{-1}) and K_{12} (.01 to 3×10^5 M^{-1}

s^{-1}) values. As the charge-to-size ratio of the halide decreases, K_{11} decreased anywhere from a factor of two to ten going from chloride to bromide, and again from bromide to iodide. Comparing the equilibrium constants for each complex in the presence of the same halide provided some insight into the supramolecular assembly structure. For example, **Ru-dtb**, **Ru-bpy**, and **Ru-btfmb** association with chloride gave values of K_{11} that were within a factor of four, while association with bromide and iodide gave K_{11} values that varied by a factor of two or less. As the ancillary ligands do not dramatically impact K_{11}, the first association is likely occurring with the 5,5′-daea ligand. Inspection of the K_{12} values for chloride association revealed equilibria that varied much more significantly as the identity of the ancillary ligand was changed. For association of a second halide, increasing the steric bulk of the functional group at the 4,4′ position of the ancillary ligand resulted in nearly an order of magnitude decrease going from H to CF_3, and again from CF_3 to *t*-butyl. This suggests that the second halide interacts, at least in part, with the ancillary ligand, and that the sterics of the ancillary ligands inhibit this interaction. For iodide and bromide however, the sterics of the ancillary ligands appears less influential, as K_{12} is approximately the same for all complexes. This suggests that the size of the larger halides already inhibits the approach to the second receptor site.

Additional insight into the assembly structures was gained through ^{1}H NMR spectroscopy (Figure 4.4). In chloride titrations performed in CD_3CN, the most significant downfield shifts in the ruthenium complexes were observed for the amide and 4,4′ hydrogens on the 5,5′-daea ligand. It is interesting to note that in these titrations, the downfield shifts of the 4,4′ hydrogens on the daea ligand saturate before those of the amide hydrogens and other resonances that shift in the presence of chloride. The larger equilibrium observed for the 4,4′ resonance suggests that this interaction is between the ruthenium and the first halide (Scheme 4.1, left), and is predominately

with the 4,4′ and amide hydrogens on the 5,5′-daea ligand. During the titration, downfield shifts were also observed for the 6,6′ hydrogens on the 5,5′-daea ligand, and for the 5,5′ hydrogens on the ancillary ligands. Therefore, the second halide with the smaller equilibrium constants (Scheme 4.1, right) likely associates between the amide functionalized and ancillary ligand, close to the ruthenium metal center. Free rotation of the second amide group is proposed to allow additional stabilization of this halide, which is in agreement with the amide hydrogens continual downfield shift. Although this proposed structure would break the symmetry of the complex, fast exchange on the NMR timescale is expected and would lead to averaging of the hydrogens in different environments.

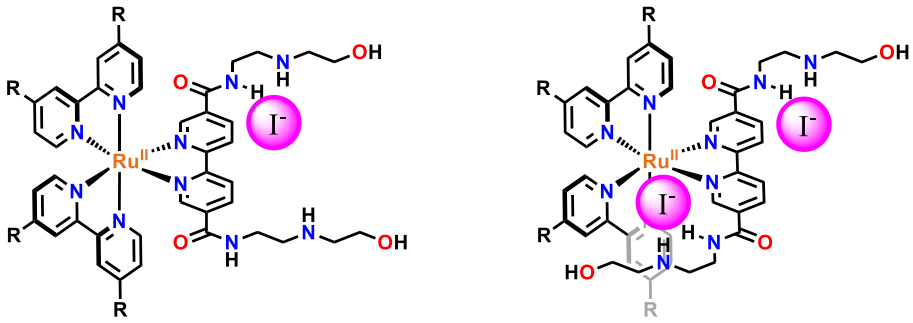

Scheme 4.1: Proposed structure of the $[Ru^{2+},X^{-}]^{+}$ (left) and $[Ru^{2+},2X^{-}]$ (right) assemblies.

4.3.2 Excited-State Behavior

Light-excitation into the MLCT excited-states of **Ru-dtb**, **Ru-bpy**, and **Ru-btfmb** resulted in room temperature photoluminescence with λ_{max} values of 720, 700, and 645 nm, with lifetimes of 44, 57, and 875 ns, respectively. Unusually low photoluminescence quantum yields (Φ) and large non-radiative rate constants (k_{nr}) were observed for **Ru-dtb** and **Ru-bpy**. As the luminescence from these complexes is at quite low energy, the low quantum yields are in agreement with the energy gap law, which predicts that k_{nr} will increase as the free energy stored in the excited-state (ΔG_{ES}) decreases, a trend which is observed in Table 4.3.

As described in the results section, the orientation of the excited-state dipole was determined through electrochemistry. For **Ru-dtb** and **Ru-bpy**, the excited-state dipole is oriented towards the 5,5′-daea ligand, while for **Ru-btfmb**, the excited-state dipole is oriented away from that ligand. The assembly of halide anions was found to perturb the luminescent excited-state in predictable ways, depending on the interaction of the halide with the excited-state dipole. For example, the addition of halide (X^- = chloride, bromide, and iodide) to CH_3CN solutions of **Ru-dtb** and **Ru-bpy** was found to result in a blue-shift and increase in the photoluminescence intensity. This behavior was ascribed to a Coulombic repulsion between the excited-state dipole and assembled halide, resulting in a destabilization of the excited state. For **Ru-btfmb**, where the excited-state dipole is oriented away from assembled halide (X^- = chloride and bromide), a red-shift and decrease in the photoluminescence intensity is observed, as is expected from a stabilization of the excited state.

The excited-state behavior of **Ru-btfmb** in the presence of iodide could not be explained by the interaction between the excited-state dipole and assembled halide, as the photoluminescence maximum did not shift with increasing iodide concentration, even though the photoluminescence intensity decreased. Determination of the excited state reduction potential ($Ru^{2+*/+}$) of **Ru-btfmb** (Table 4.1), showed that this complex is a potent photooxidant ($Ru^{2+*/+}$ = 1.56 V vs NHE) capable of performing iodide oxidation ($I^{\bullet/-}$ = 1.23 V vs NHE), unlike the excited states of **Ru-dtb** and **Ru-bpy**, which have significantly less driving force for iodide oxidation. Indeed, the addition of TBA iodide into **Ru-btfmb** solutions resulted in significant static and dynamic quenching of the excited-state (Figure 4.5). A Stern-Volmer analysis of the static and dynamic components yielded unusual quenching behavior, as both plots deviated from the expected linear relationship between τ_0/τ (dynamic) or A_0/A (static) and the iodide concentration. To describe the unusual Stern-Volmer

behavior, it was helpful to consider the possible quenching mechanisms of the various ruthenium:iodide assemblies present in solution, depicted in Scheme 4.2.

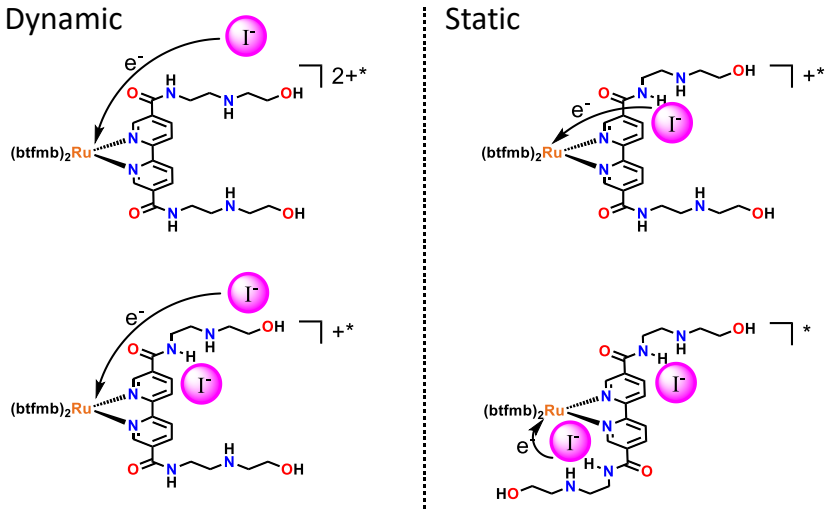

Scheme 4.2: Proposed dynamic and static quenching mechanisms of **Ru-btfmb** by iodide.

As determined from the characterization of the ground state halide assembly, **Ru-btfmb** can be present in CH_3CN solution with zero, one, or two assembled iodide anions. At low iodide concentrations (<1 eq. with regard to ruthenium), Ru^{2+} is the predominate species in solution. However, after this point, the equilibrium favors formation of $[Ru^{2+},I^-]^+$, and the Ru^{2+} concentration approaches zero. At ~2.5 eq. of iodide, the concentration of $[Ru^{2+},I^-]^+$ reaches its maximum value, after which its gradual decrease is concomitant with an increase in the $[Ru^{2+},2I^-]$ concentration. Quenching of the luminescent excited-state reaches 85% by ~12 eq. of iodide, which is well before $[Ru^{2+},2I^-]$ becomes the dominate species in solution. Under the conditions described above, at various points in the titration, Ru^{2+} and $[Ru^{2+},I^-]^+$ are present in concentrations where dynamic quenching would be observed, assuming that the excited-state lifetimes are long-lived enough for diffusional quenching. Additionally, static quenching of both $[Ru^{2+},I^-]^+$ and $[Ru^{2+},2I^-]$ would be expected.

In the Stern-Volmer analysis of the dynamic quenching (Figure 4.5), two distinct slopes are observed at low (0-10 μM, 0-1 eq.) and high (20-100 μM, 2-12 eq.) iodide concentrations, with k_q values of 6.8×10^{10} M^{-1} s^{-1} and 4.0×10^{10} M^{-1} s^{-1}, respectively. To probe the origin of these two slopes, the excited-state quenching was performed in the presence of an inert electrolyte (TBA perchlorate) at several fixed ionic strengths (μ = 0.005 – 0.1 M). The presence of the inert electrolyte had two effects: 1) static quenching was drastically decreased or not observed, suggesting that the equilibrium constants with iodide were much lower, and 2) the quenching rate constant (k_q) decreased as μ increased. As supramolecular assembly with iodide was greatly reduced under these conditions, it was possible to solely monitor the dynamic quenching of the Ru^{2+} excited-state. A Debye-Hückel analysis of the quenching rate constants at various ionic strengths (Figure S4.18) was performed, which provided insights into the dynamic component. In this analysis, the slope of the linear fit is equal to the product of the ionic charge, which in this case was equal to -2, consistent with excited-state quenching of Ru^{2+} by I^-. Additionally, extrapolation of the fit to the y-axis, where the ionic strength is equal to zero, yields the quenching rate constant for the reaction when no inert salt is present. Extrapolation to μ = 0 gave a k_q of 6.3×10^{10} M^{-1} s^{-1}, which is in good agreement with the slope obtained at low iodide concentrations in the Stern-Volmer analysis. These values are also in agreement with the calculated diffusion-limited rate constant for excited-state quenching reactions between related 2+ ruthenium polypyridyl complexes and iodide.[28] Therefore, at low iodide concentrations, the dynamic quenching mechanism is attributed to diffusional quenching of Ru^{2+} by iodide (Scheme 4.2, top left), as this is consistent with both Ru^{2+} as the main species in solution and the k_q and ionic charge obtained from the Debye- Hückel analysis.

At high iodide concentrations (20-100 μM) where $[Ru^{2+},I^-]^+$ accounts for the majority of ruthenium species, the slope from the dynamic Stern-Volmer quenching decreases to 4.0×10^{10} M^{-1} s^{-1}. In this instance, the Debye- Hückel analysis could not be used to probe diffusional quenching of $[Ru^{2+},I^-]^+$, as the presence of the inert electrolyte attenuates supramolecular assembly to such an extent that it is not significantly observed. Instead, the diffusion limited rate constant for the monocationic assembly $[Ru^{2+},I^-]^+$ and iodide was calculated using the Stokes-Einstein equation (Appendix A, SI). This equation predicts, when all other variables are kept constant, that decreasing the charge of the ruthenium species by one (here through assembly with an iodide anion) will slow the diffusion limit to 3.7×10^{10} M^{-1} s^{-1}, which is in excellent agreement with the value obtained from the Stern-Volmer plot at high iodide concentrations. This suggests that diffusion limited excited-state quenching of $[Ru^{2+},I^-]^+$ by free iodide is responsible for the second slope observed in the dynamic quenching (Scheme 4.2, bottom left).

Concurrent with the dynamic excited-state quenching, static quenching of the ruthenium excited-state was manifest as a decrease in the initial photoluminescence amplitude. The Stern-Volmer analysis of the static quenching also resulted in two sloped regions, with a slope at low iodide concentrations (0-10 μM) of 2.4×10^4 M^{-1}, and a slope of 1.3×10^3 M^{-1} at high iodide concentrations (20-100 μM). These values are similar to the ground-state equilibrium constants obtained for the complexes through absorption spectroscopy ($K_{11} = 1.1\times10^5$ M^{-1}, $K_{12} = 1.4\times10^3$ M^{-1}). Therefore, this behavior is ascribed to static quenching of $[Ru^{2+},I^-]^+$ (Scheme 4.2, top right) and $[Ru^{2+},2I^-]$ (Scheme 4.2, bottom right) by an assembled halide at low and high iodide concentrations, respectively.

The products of the excited-state quenching reaction were monitored with time-resolved transient absorption spectroscopy. The absorption profile of excited-state **Ru-btfmb** shows

growths below 400 nm and above 520 nm, with a ground-state bleach centered at 460 nm and ground/excited-state isosbestic points at 419 and 520 nm. The transient absorption spectrum in the presence of excess iodide (~25 eq.) however, displayed significant absorption features at these isosbestic points. These features are consistent with the spectra of $I_2^{\bullet-}$ (λ_{max} = 385 nm) and a reduced ruthenium complex. The kinetics of $I_2^{\bullet-}$ formation monitored at 419 nm grow in at a slower rate than those of Ru^+, suggesting that $I_2^{\bullet-}$ is a secondary photoproduct. Additionally, the formation of $I_2^{\bullet-}$ was dependent on the free iodide concentration, suggesting that I-I bond formation occurred with a solvated iodide, and not one associated with the ruthenium complex. This is consistent with previous studies that suggest the mechanism for iodide oxidation by ruthenium excited states depicted in equations 5-6.

$$Ru^{2+*} + I^- \rightarrow Ru^+I^\bullet \quad (5)$$

$$I^\bullet + I^- \rightarrow I_2^{\bullet-} \quad (6)$$

From the transient absorption data, no evidence was obtained for an iodide oxidation mechanism in which the electron transfer and bond formation occurred within the $[Ru^{2+},2I^-]$ assembly, as might have been expected. In fact, even static quenching of the ruthenium excited-state was not observed with this method. To explain this, we suggest that when electron transfer occurs within the excited-state assembly, diffusion of the iodine atom is precluded by fast back-electron transfer. Fast back-electron transfer and a low cage escape yield would result in small amounts of product formed by this pathway, which would render detection difficult within the time-resolution of our instrument. In the diffusional reaction, cage escape of the oxidized halide is expected to be larger, which is in agreement with the data presented above.

4.4 Conclusion

A series of ruthenium polypyridyl complexes with amide functionalized bipyridine ligands and electron donating or withdrawing ancillary ligands were studied for halide assembly and oxidation. In CH_3CN (and when soluble, CH_2Cl_2), spectral evidence was obtained for 1:2 ruthenium:halide assemblies, and large equilibrium constants for association of the first (K_{11} from 10^4-10^6 M^{-1}) and second halide (K_{12} from 10^3-10^5 M^{-1}) were measured. The electronic properties of the ancillary ligands tuned the excited-state reduction potential ($Ru^{2+*/+}$) by 350 meV. For the most potent photo-oxidant, static and dynamic quenching of the luminescent excited state by iodide was resolved. A Stern-Volmer analysis of the both the static and dynamic components revealed two sloped regions at low and high iodide concentrations, consistent with diffusion limited quenching of Ru^{2+} and $[Ru^{2+},I^-]^+$, and static quenching of $[Ru^{2+},I^-]^+$ and $[Ru^{2+},2I^-]$. Transient absorption experiments were consistent with reductive quenching of the excited state to form Ru^+ and $I^\bullet$, while $I^\bullet$ subsequently reacted with free iodide, yielding $I_2^{\bullet-}$. Monitoring the kinetics of Ru^+ and $I_2^{\bullet-}$ formation suggested that only photoproducts from the diffusional reaction were able to escape the solvent cage, while fast back-electron transfer hindered mechanistic characterization of the electron transfer reaction within the assembly.

4.5 Experimental

4.5.1 Materials

Sulfuric acid (H_2SO_4, Fisher, 98 %, Certified ACS Plus), methanol (Fisher, Certified ACS), ethanol (Fisher, Certified ACS), 2-(2-aminoethylamine)ethanol (Sigma-Aldrich, ≥ 98 %), acetone (Sigma-Aldrich, Certified ACS), acetonitrile (CH_3CN, Burdick and Jackson, 99.98 %), and dichloromethane (CH_2Cl_2, Burdick and Jackson, 99.98 %) were used as received. Argon gas (Airgas, 99.998 %) was passed through a Drierite drying tube before use. Ammonium

hexafluorophosphate (NH_4PF_6, Sigma-Aldrich, ≥ 98 %), tetrabutylammonium chloride (TBACl, Sigma-Aldrich, purum ≥ 97 %), tetrabutylammonium bromide (TBABr, Acros Organics, 99+ %), tetrabutylammonium iodide (TBAI, Sigma-Aldrich ≥ 99 %), tetrabutylammonium perchlorate ($TBAClO_4$, Sigma-Aldrich, for electrochemical analysis, ≥ 99 %), and ruthenium trichloride hydrate (Oakwood Chemicals, 97 %) were used as received. NMR solvents were purchased from Cambridge Isotope Laboratories, Inc. 5,5′-dicarboxylic acid-(2,2′)-bipyridine,[29] 5,5′-diethylester-(2,2′)-bipyridine,[30] $Ru(dtb)_2Cl_2$,[31] $Ru(bpy)_2Cl_2$,[32] and $Ru(btfmb)_2Cl_2$[33] were synthesized according to previous procedures. All solutions were sparged with argon for at least 30 minutes before titration, photoluminescence, and transient absorption experiments were performed.

4.5.2 Synthesis

Synthesis of the 5,5′-daea ligand:

To a 100 mL round bottom flask was added 5,5′-diethylester-(2,2′)-bipyridine (1.0 g, 3.3 mmol), methanol (25 mL), and excess 2-(2-aminoethylamine)ethanol (~5 mL, ~50 mmol). The mixture was sparged with argon for ~30 min and refluxed overnight. Upon cooling, the mixture was poured into acetone (60-70 mL) causing a precipitate to form, and the solid was collected by vacuum filtration on a sintered glass frit. The precipitate was washed with excess acetone and dried under vacuum at 100 °C, yielding 5,5′-daea (0.466 g, 34%) as a white powder. ^{1}H NMR (d_6-DMSO, 400 MHz): 9.12 (2H, dd), 8.76 (2H, t,), 8.51 (2H, dd), 8.37 (2H, dd), 4.50 (2H, t), 3.45 (4H, q), 3.42 – 3.36 (4H, m), 2.72 (4H, t), 2.61 (4H, t).

Synthesis of ruthenium complexes:

General method for synthesis of ruthenium complexes **Ru-dtb**, **Ru-bpy**, and **Ru-btfmb**. To a 50 mL round bottom flask was added the appropriate ruthenium precursor ($Ru(dtb)_2Cl_2$, $Ru(bpy)_2Cl_2$,) one equivalent of 5,5′-daea, and EtOH. The mixture was sparged with argon for ~30

min and refluxed overnight. (For **Ru-btfmb**, one equivalent of ruthenium precursor and the ligand, two equivalents of silver nitrate, and 5 mL of EtOH, were heated at 150 °C for 10 min under microwave irradiation. After this point, the procedure is the same for all three complexes.) After cooling, the red solution was filtered, and the solvent was removed by rotary evaporation. The resulting solid was dissolved in minimal MeOH and eluted through a sephadex column with MeOH. The red band was collected, and the solvent was removed by rotary evaporation. The solid was dissolved in minimal H_2O, and a few drops of saturated aqueous NH_4PF_6 was added, causing a precipitate to form. The solid was collected with vacuum filtration, washed with excess H_2O, and dried under vacuum at 100 °C overnight, yielding a red solid.

$[Ru(dtb)_2(5,5'\text{-daea})](PF_6)_2$, (Ru-dtb): $Ru(dtb)_2Cl_2$ (177 mg, 0.22 mmol), 5,5′-daea (90 mg, 0.22 mmol) and ~20 mL EtOH was refluxed overnight, yielding 96 mg (33%) of **Ru-dtb**. ^1H NMR (CD_3CN, 400 MHz): 8.60 (2H, d), 8.48 (4H, dd), 8.33 (2H, d), 7.99 (2H, s), 7.58 (6H, m), 7.45 (2H, dd), 7.38 (2H, dd), 3.64 (4H, t), 3.48 (4H, m), 3.05 (4H, t), 2.97 (4H, t), 1.41 (36H, d). HRMS (ESI-MS). Calcd for $C_{56}H_{76}N_{10}O_4Ru$ ($[M]^{2+}$): *m/z* = 527.18 Found: *m/z* = 527.25.

Note: After the sephadex column, a luminescent impurity was still observed in the PL spectrum of **Ru-dtb**. To remove this impurity, the solid was dissolved in an CH_3CN: H_2O mixture (2% H_2O containing 1% $NaNO_3$ by mass) and eluted through a basic alumina column. A yellow band quickly eluted and was discarded, while a second red band was collected at higher percentages of H_2O (8-10%). The solvent was removed from the second fraction, yielding a red solid which was dissolved in minimal water. The addition of and a few drops of saturated aqueous NH_4PF_6 caused a precipitate to form. The solid was collected with vacuum filtration, washed with excess H_2O, and dried under vacuum at 100 °C overnight, yielding a red solid.

[Ru(bpy)$_2$(5,5′-daea)](PF$_6$)$_2$, (Ru-bpy): Ru(bpy)$_2$Cl$_2$ (100 mg, 0.21 mmol), 5,5′-daea (86 mg, 0.21 mmol), silver nitrate (70 mg, 4.1 mmol) and 10 mL EtOH was refluxed overnight, yielding 75 mg (32%) of **Ru-bpy**. ^{1}H NMR (CD_3CN, 500 MHz): 8.65 (2H, d), 8.51 (4H, d), 8.33 (2H, d), 8.08 (4H, t), 8.01 (2H, s) 7.72 (4H, t), 7.65 (2H, m), 7.41 (4H, dt), 3.70 (4H, t), 3.54 (4H, m), 3.18 (4H, t), 3.10 (4H, t). HRMS (ESI-MS). Calcd for $C_{40}H_{44}N_{10}O_4Ru$ ($[M]^{2+}$): *m/z* = 415.13 *m/z* = 415.13.

[Ru(btfmb)$_2$(5,5′-daea)](PF$_6$)$_2$, (Ru-btfmb): Ru(btfmb)$_2$Cl$_2$ (100 mg, 0.13 mmol), 5,5′-daea (55 mg, 0.13 mmol), silver nitrate (45 mg, 2.6 mmol) and ~5 mL EtOH was heated at 150 °C for 10 min under microwave irradiation, yielding 118 mg (64%) of **Ru-btfmb**. ^{1}H NMR (CD_3CN, 500 MHz): 8.96 (4H, d), 8.70 (2H, d), 8.43 (2H, d), 8.00 (4H, dd), 7.93 (2H, s), 7.72 (6H, m), 3.70 (4H, t), 3.54 (4H, m), 3.17 (4H, t), 3.10 (4H, t). HRMS (ESI-MS). Calcd for $C_{40}H_{44}F_{12}N_{10}O_4Ru$ ($[M]^{2+}$): *m/z* = 551.11 *m/z* = 551.10.

4.5.3 Nuclear Magnetic Resonance

Characteristic NMR spectra were obtained at room temperature on a Bruker Avance III 400 or 500 MHz spectrometer. Solvent residual peaks were used as internal standards for ^{1}H (δ =2.50 ppm for DMSO, 5.32 for CD_2Cl_2, 1.94 for CD_3CN) and ^{13}C (39.52 ppm for DMSO) chemical shift referencing. NMR spectra were processed using MNOVA.

4.5.4 Mass Spectrometry

Samples were analyzed with a Q Exactive HF-X (ThermoFisher, Bremen, Germany) mass spectrometer. Samples were introduced via a heated electrospray source (HESI) at a flow rate of 10 µL/min. One hundred time domain transients were averaged in the mass spectrum. HESI source conditions were set as: nebulizer temperature 100 deg C, sheath gas (nitrogen) 15 arb, auxillary gas (nitrogen) 5 arb, sweep gas (nitrogen) 0 arb, capillary temperature 250 degrees C, RF voltage

100 V. The mass range was set to 600-2000 m/z. All measurements were recorded at a resolution setting of 120,000. Solutions were analyzed at 0.1 mg/mL or less based on responsiveness to the ESI mechanism. Xcalibur (ThermoFisher, Breman, Germany) was used to analyze the data. Molecular formula assignments were determined with Molecular Formula Calculator (v 1.2.3). All observed species were singly charged, as verified by unit *m/z* separation between mass spectral peaks corresponding to the ^{12}C and $^{13}C^{12}C_{c-1}$ isotope for each elemental composition.

4.5.5 UV−Vis Absorption

UV−vis absorption spectra were recorded on a Varian Cary 60 UV−vis spectrophotometer with a resolution of 1 nm.

4.5.6 Steady-State PL

Steady-state PL spectra were recorded on a Horiba Fluorolog 3 fluorimeter and corrected by calibration with a standard tungsten-halogen lamp. Samples were excited at 450 nm. The intensity was integrated for 0.1 s at 1 nm resolution and averaged over 3 scans. The PL quantum yields were measured by the optically dilute method using $[Ru(bpy)_3]Cl_2$ in acetonitrile (Φ = 0.062) as a quantum yield standard.[22]

4.5.7 Time-Resolved Photoluminescence

Time-resolved PL data were acquired on a nitrogen dye laser with excitation centered at 445 nm. Pulsed light excitation was achieved with a Photon Technology International (PTI) GL-301 dye laser that was pumped by a PTI GL-3300 nitrogen laser. The PL was detected by a Hamamatsu R928 PMT optically coupled to a ScienceTech Model 9010 monochromator terminated into a LeCroy Waverunner LT322 oscilloscope. Decays were monitored at the PL maximum and averaged over 180 scans. Nonradiative and radiative rate constants were calculated from the quantum yields, $\Phi = k_r/(k_r + k_{nr})$ and lifetimes, $\tau = 1/(k_r + k_{nr})$.

4.5.8 Electrochemistry

Square wave voltammetry was performed with a BASi Epsilon potentiostat in a standard three-cell in CH_2Cl_2 electrolytes. The cells consisted of a platinum working electrode and a platinum mesh as an auxiliary electrode. A non-aqueous silver/silver chloride electrode (Pine) was used as a reference electrode that was referenced to an internal ferrocene (630 mV vs. NHE) standard.

4.5.9 Halide Titrations

UV−vis, PL, and time-resolved measurements were performed in CH_2Cl_2 or CH_3CN using ~10-50 μM solutions of the ruthenium complexes. Titration measurements were performed for each of the spectroscopies with TBACl, TBABr, or TBAI through additions of 0.25 equivalents. Throughout all titrations, the concentration of complexes remained unchanged. For the UV-vis titrations used to determine equilibrium constants, a stock solution of each complex was prepared with an absorbance of ~0.5 at the λ_{max}, and 5 mL was added to a quartz cuvette. A titration solution was then prepared with 10 mL of the stock solution. TBACl, TBABr, and TBAI were added to the stock solution such that a 10 μL addition to the cuvette was ~0.1 eq of halide with respect to ruthenium.

For the PL titrations, the same procedure was used, except that an absorbance of ~0.1 at the λ_{max} was used, and the concentration of halide was adjusted such that a 10 μL addition to the cuvette was ~0.25 eq of halide with respect to ruthenium. For titrations performed at a fixed ionic strength, the stock ruthenium solution was prepared in CH_3CN solution with a fixed concentration of TBA perchlorate ranging from $\mu = 0.005 – 0.1$ M.

The ^{1}H NMR titrations were performed using a Bruker Avance III 500 MHz spectrometer equipped with a broadband inverse (BBI) probe using 1 mM ruthenium complex in 600 μL of

deuterated solvent and 0.25 equivalent additions of TBACl or TBAI were added in 10 μL additions. The ruthenium concentration was kept unchanged through preparation of a titration solution that contained both the ruthenium complex and the desired halide. Each spectrum was averaged over 16 scans.

Data analysis for all experiments was performed using Origin 2017. Data fitting was preformed using a Levenberg-Marquardt iteration method. Benesi-Hildebrand type analysis was performed in Mathematica, version 11.

4.5.10 Transient Absorption

Nanosecond transient absorption measurements were acquired on a setup published previously.[34] Briefly, a Q-switched, pulsed Nd:YAG laser (Quantel USA (BigSky) Brilliant B 5−6 ns full width at half-maximum (fwhm), 1 Hz, ~ 10 mm in diameter) doubled to 532 nm. The laser irradiance at the sample was attenuated to 3 mJ/pulse. The probe lamp consisted of a 150 W xenon arc lamp and was pulsed at 1 Hz with 70 V during the experiment. Signal detection was achieved using a monochromator (SPEX 1702/ 04) optically coupled to an R928 photomultiplier tube (Hamamatsu) at a right angle to the excitation laser. Transient data were acquired with a computer-interfaced digital oscilloscope (LeCroy 9450, Dual 330 MHz) with an overall instrument response time of ~10 ns. An average of 30 laser pulses was acquired averaged at each wavelength of interest over the 370−800 nm range. Intervals of 10 nm were used for wavelength between 370 and 600 nm and intervals of 20 nm were used between 600 and 800 nm. Time-resolved PL data were also acquired at the same laser intensity at 532 nm.

4.6 Supporting Information

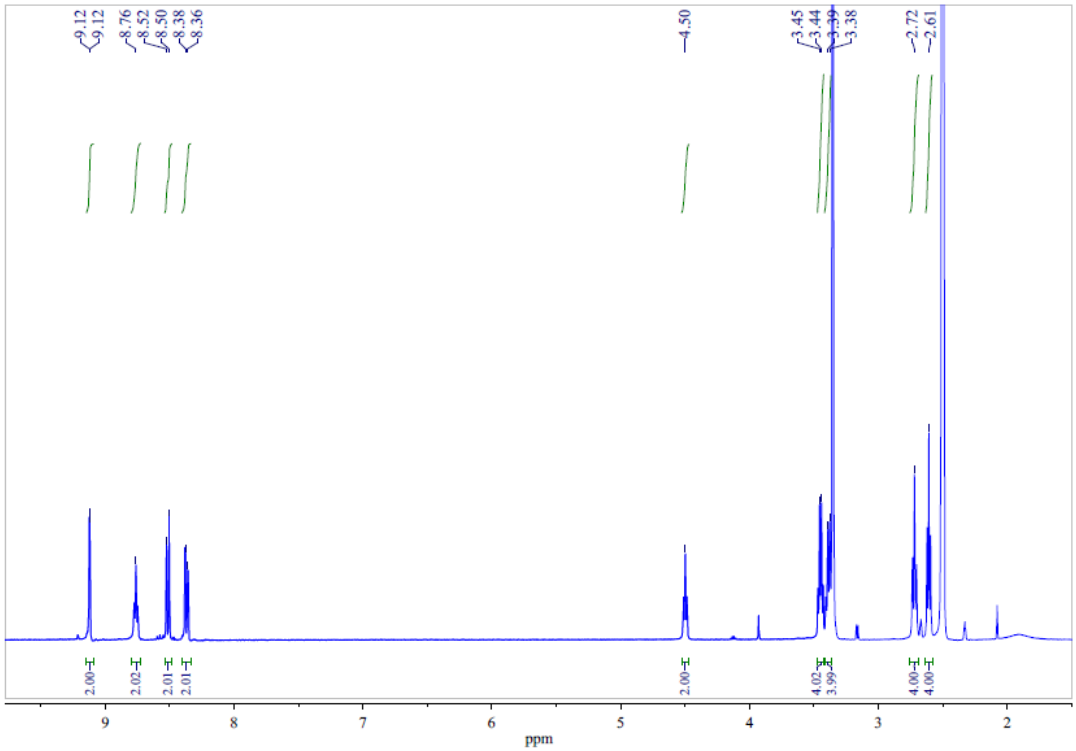

Figure S4.1: ^{1}H NMR spectrum of 5,5′-daea in d_6-DMSO.

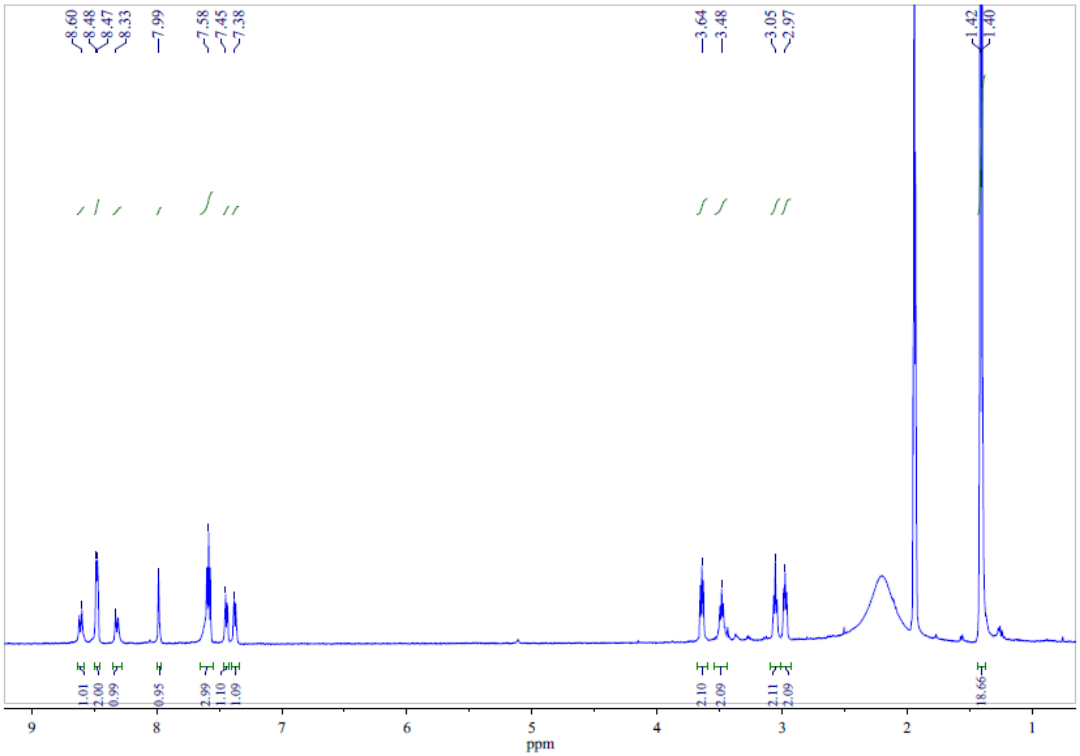

Figure S4.2: ^{1}H NMR spectrum of **Ru-dtb** in CD_3CN.

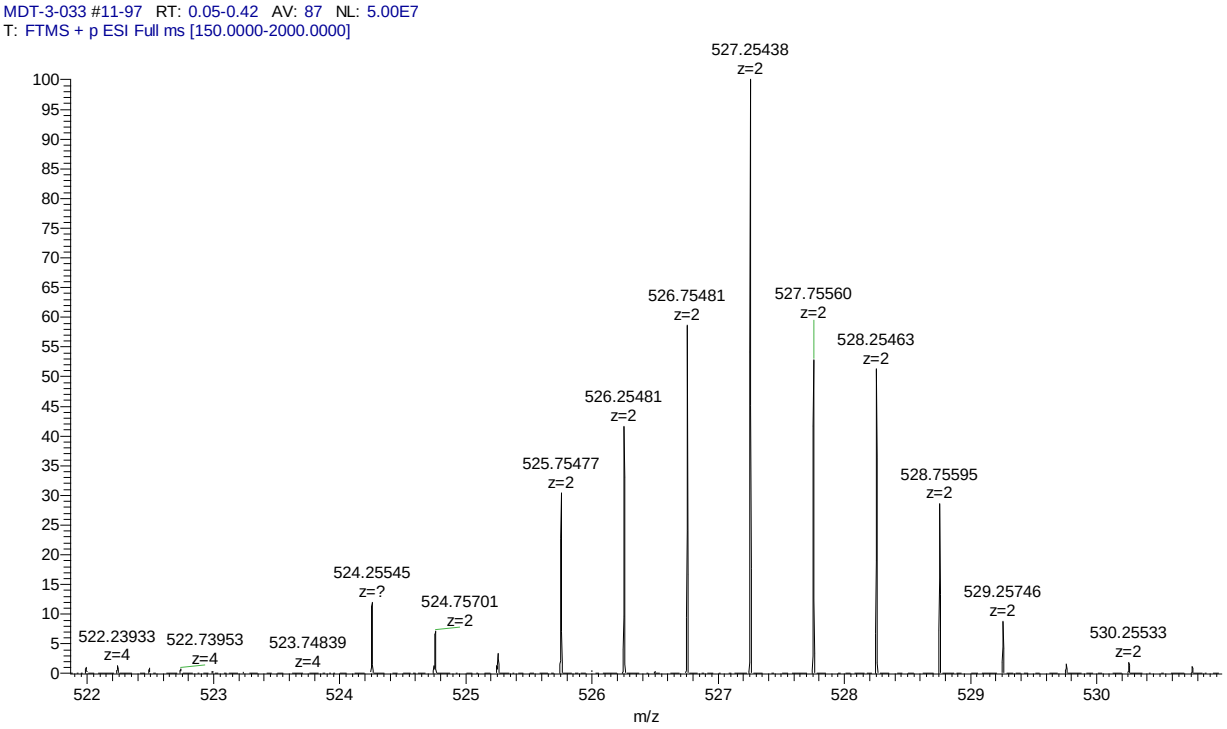

Figure S4.3: High resolution mass spectrum of **Ru-dtb.**

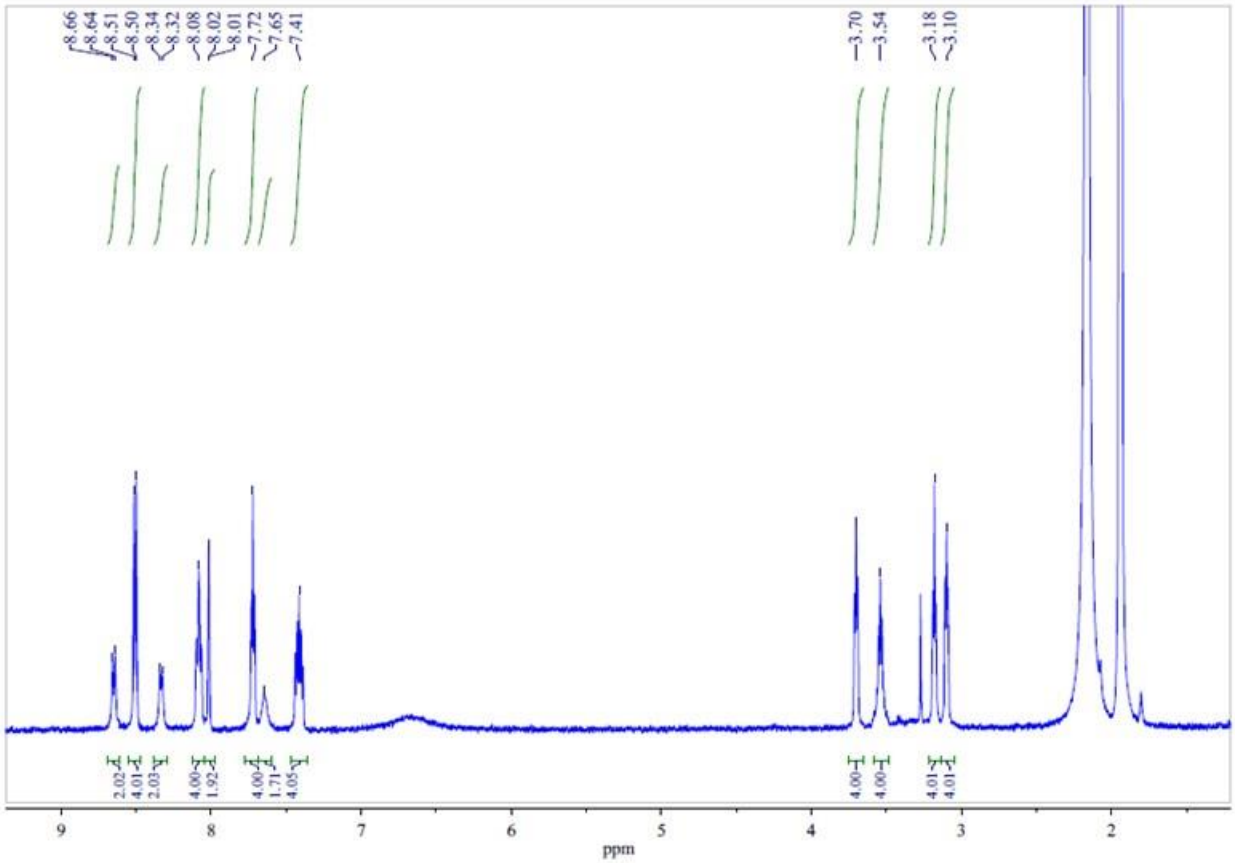

Figure S4.4: ^{1}H NMR spectrum of **Ru-bpy** in CD_3CN.

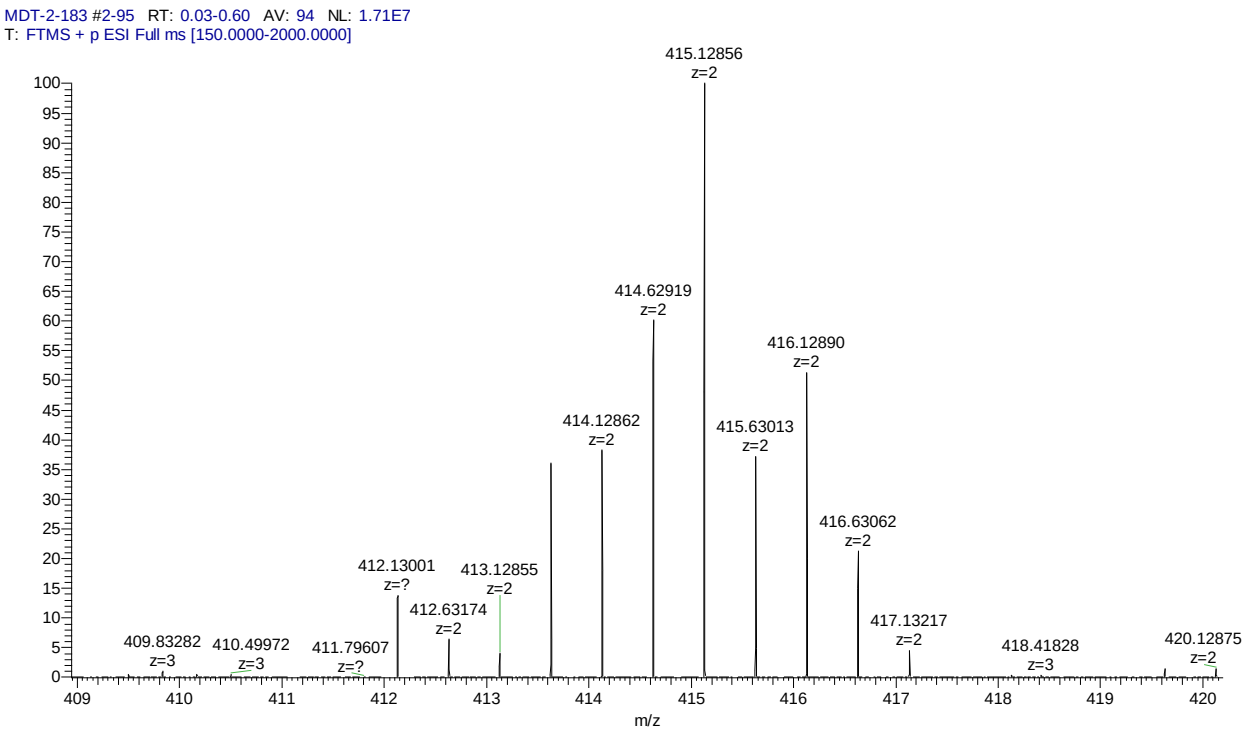

Figure S4.5: High resolution mass spectrum of **Ru-bpy.**

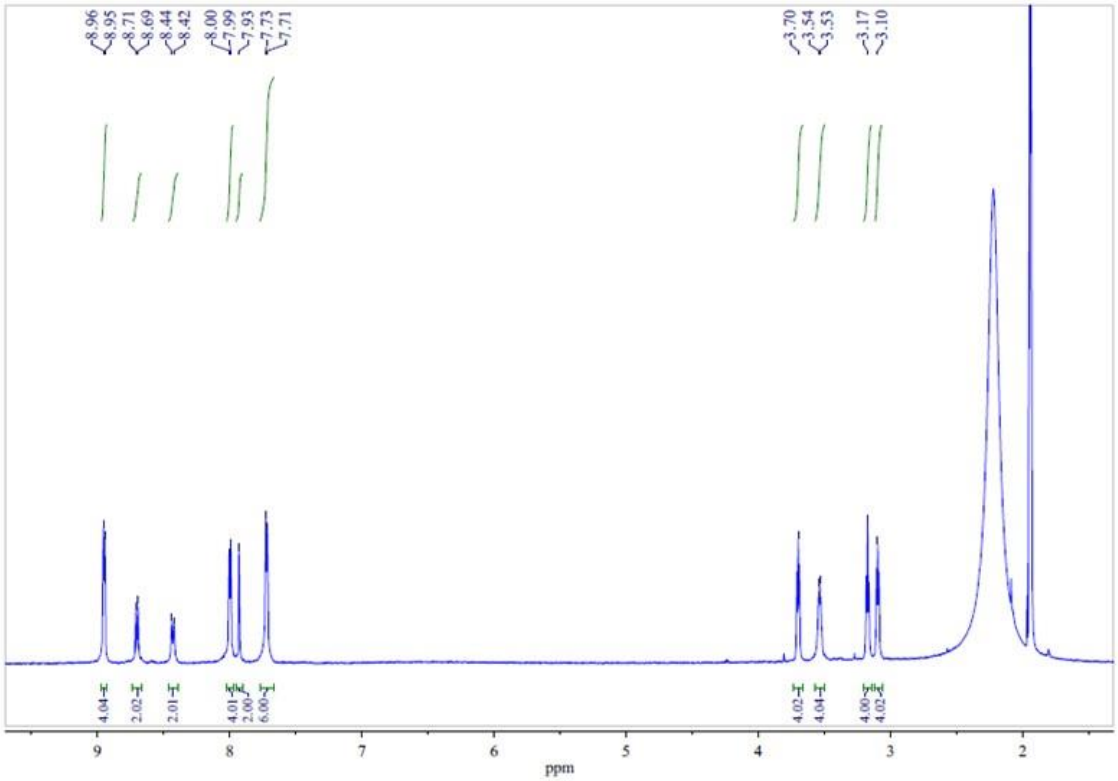

Figure S4.6: ^{1}H NMR spectrum of **Ru-btfmb** in CD_3CN.

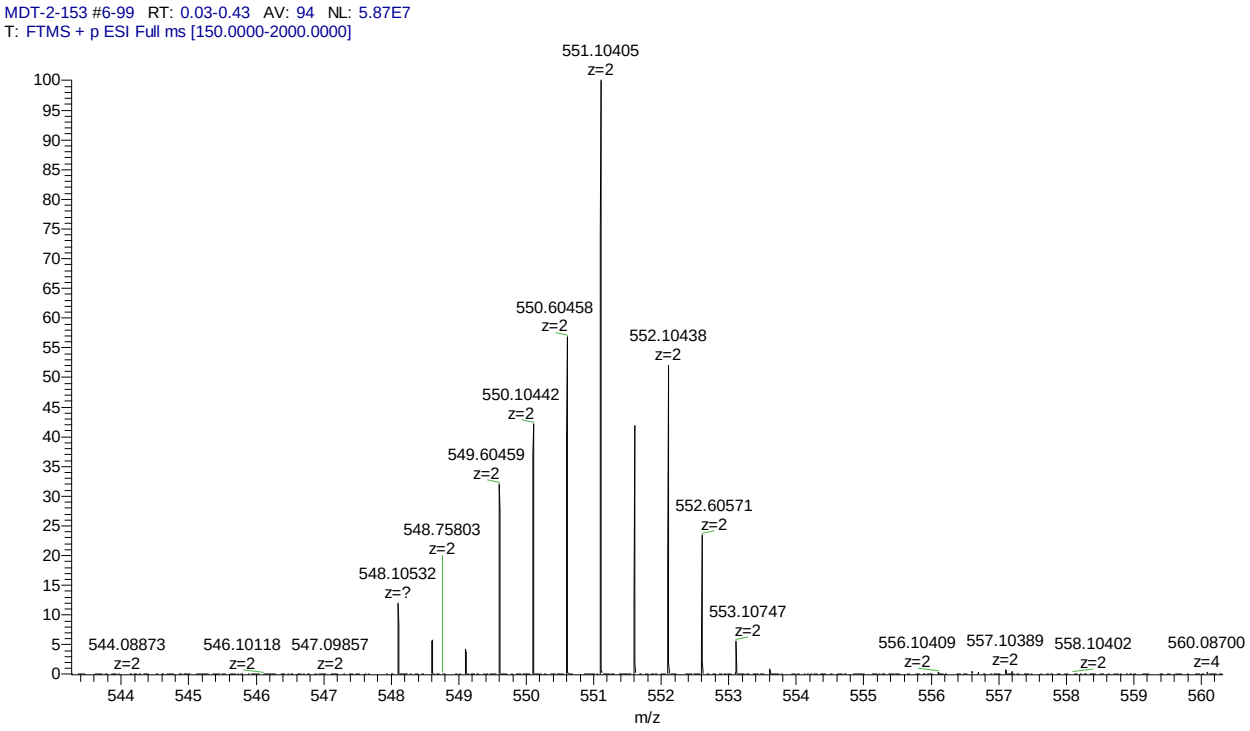

Figure S4.7: High resolution mass spectrum of **Ru-btfmb**.

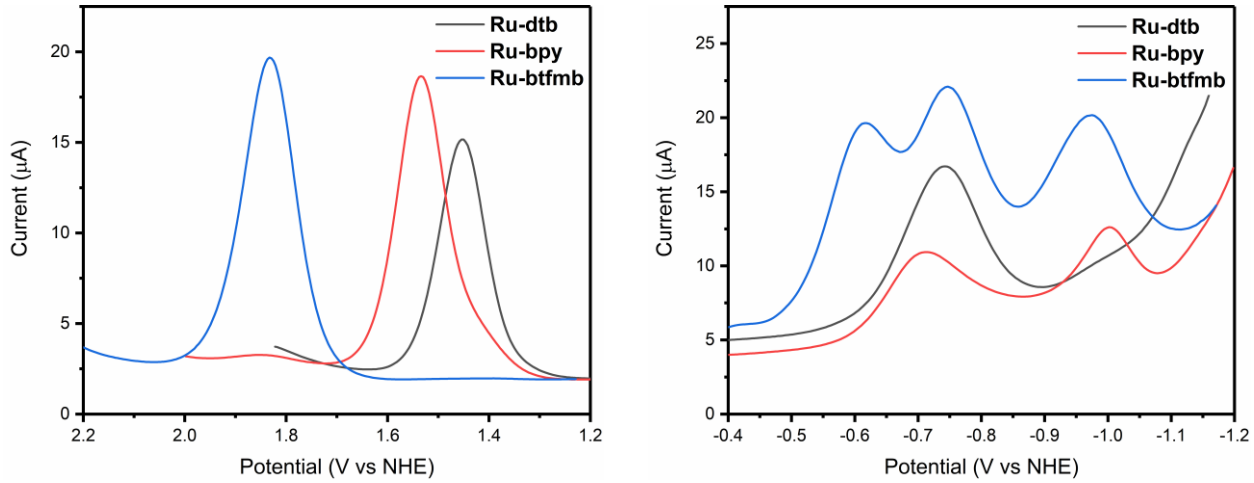

Figure S4.8: Square-wave voltammograms of **Ru-dtb**, **Ru-bpy**, and **Ru-btfmb** in 0.1 M $NaClO_4$ in CH_3CN. The left panel shows the $Ru^{III/II}$ reduction, and the left panel shows the ligand based reductions.

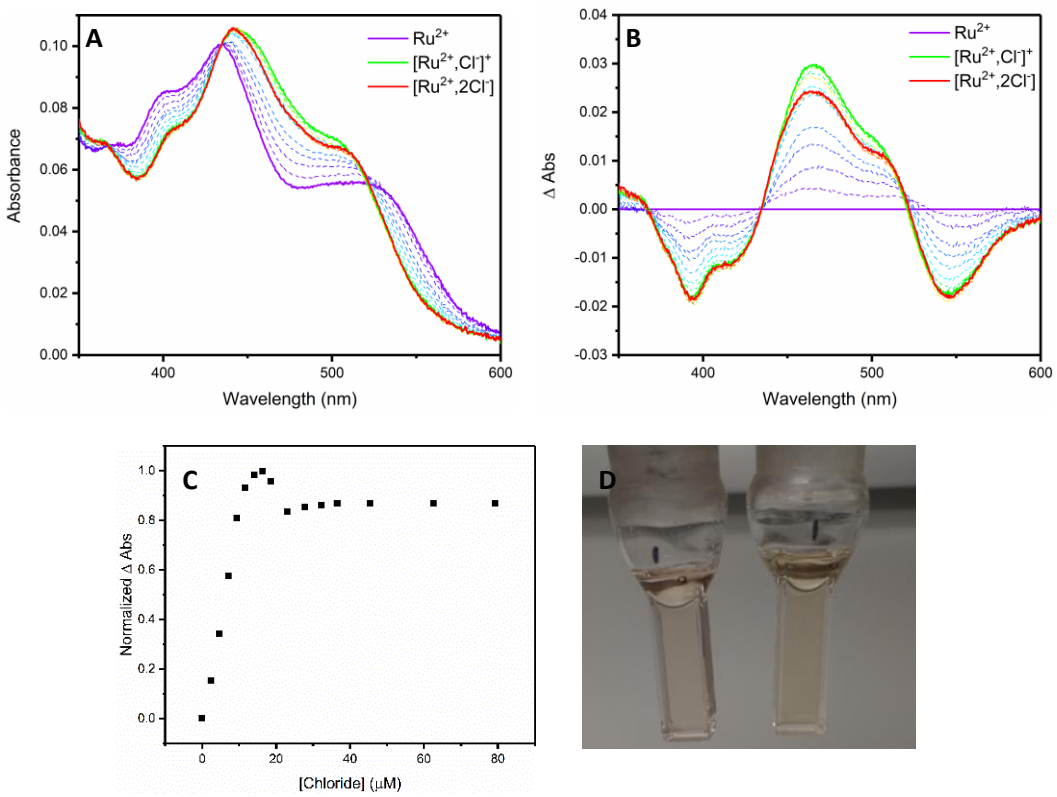

Figure S4.9: (A) Absorption spectra of **Ru-dtb** in CH_2Cl_2 as TBA chloride is added. The solid lines show the spectral features of Ru^{2+} (purple), $[Ru^{2+},Cl^-]^+$ (green), and $[Ru^{2+},2Cl^-]$ (red). (B) Δ absorption spectrum obtained by subtracting the absorption at each chloride concentration from the initial spectrum. (C) Binding isotherm at 465 nm, showing two halide association steps. (D) Visible color change upon chloride association in CH_2Cl_2 solutions of **Ru-dtb**.

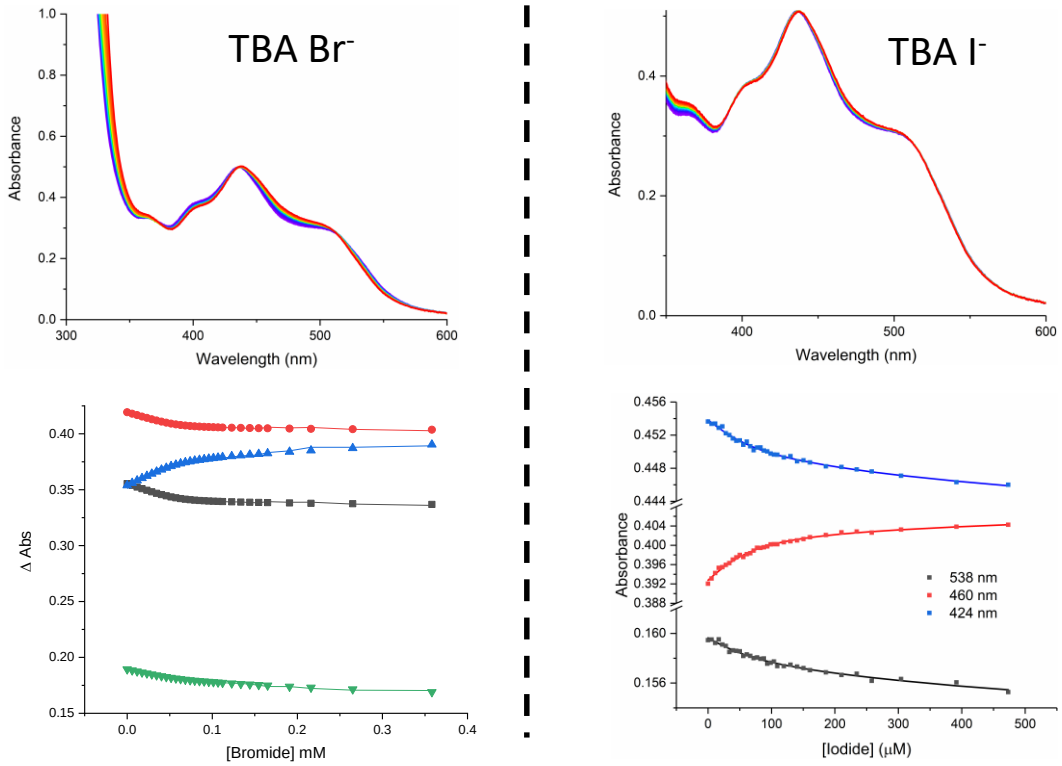

Figure S4.10: UV-vis absorption spectra of Ru-dtb monitoring TBA bromide (left) and iodide (right) titrations. Binding isotherms and resulting fits from supramolecular.org are shown below the absorption spectra.

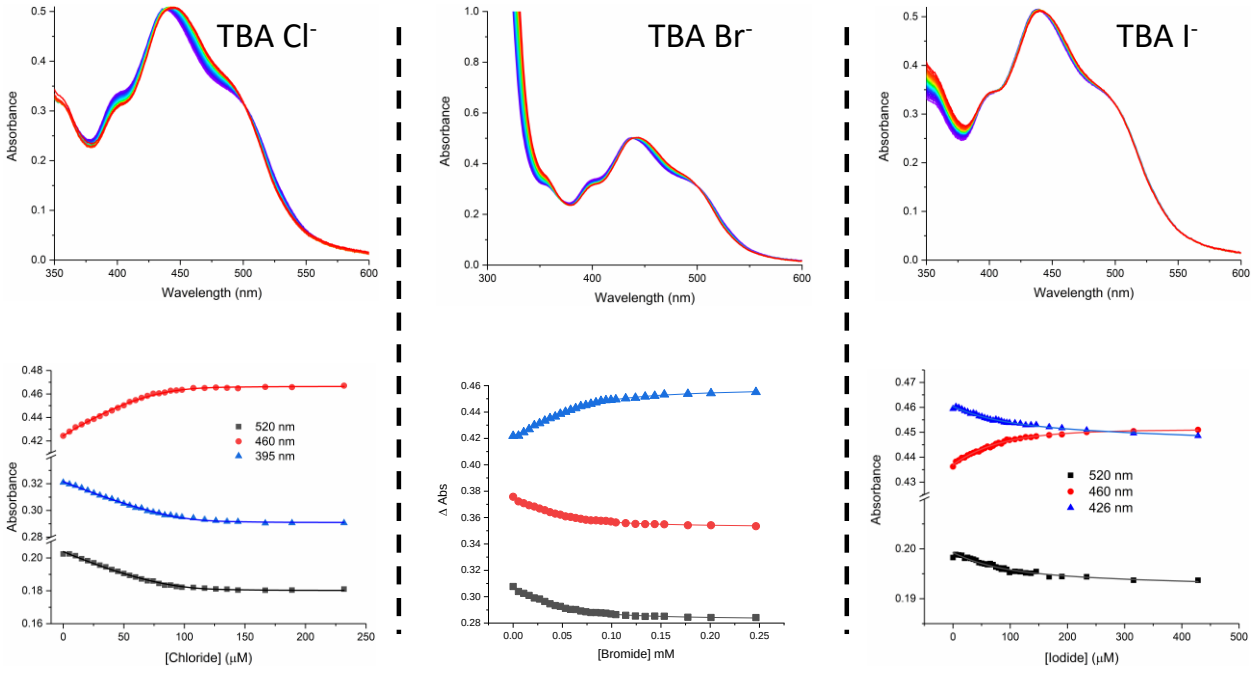

Figure S4.11: UV-vis absorption spectra of Ru-bpy monitoring TBA chloride (left), bromide (middle) and iodide (right) titrations. Binding isotherms and resulting fits from supramolecular.org are shown below the absorption spectra.

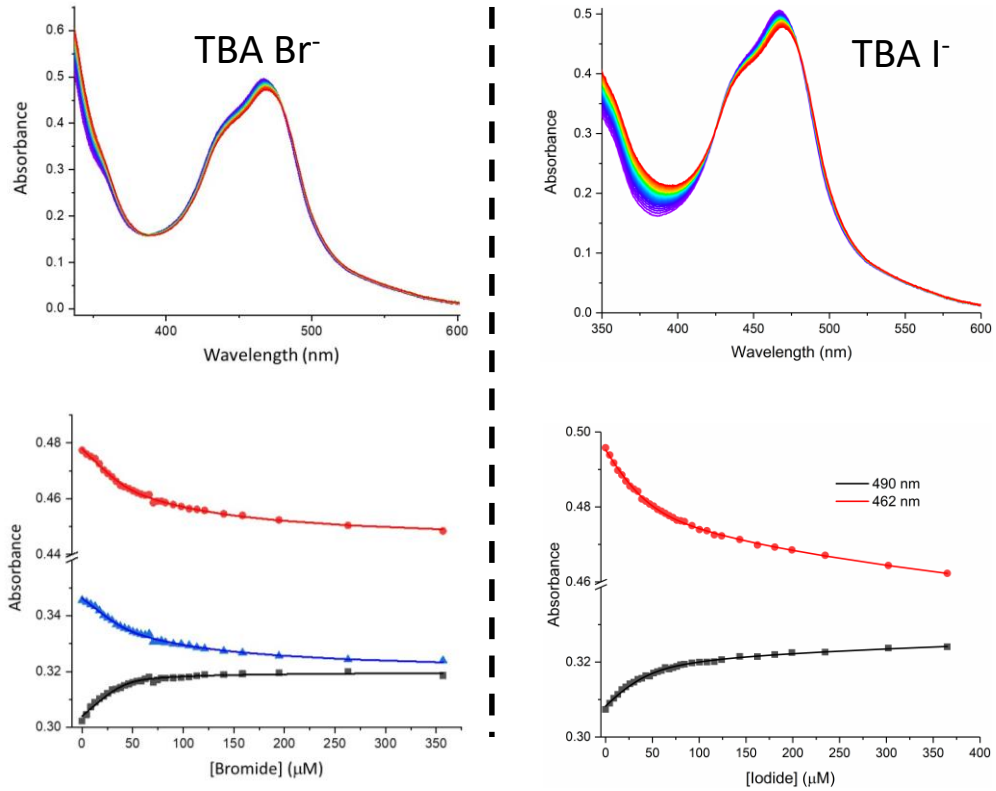

Figure S4.12: UV-vis absorption spectra of Ru-btfmb monitoring TBA bromide (left) and iodide (right) titrations. Binding isotherms and resulting fits from supramolecular.org are shown below the absorption spectra.

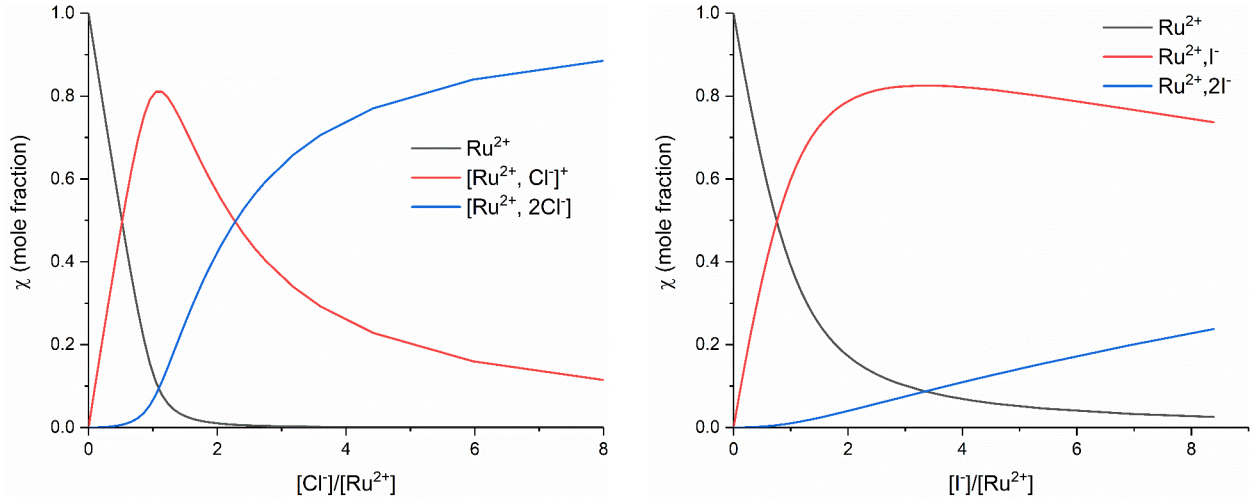

Figure S4.13: Mole fraction plots of Ru-btfmb with increasing chloride (left) and iodide (right) concentrations.

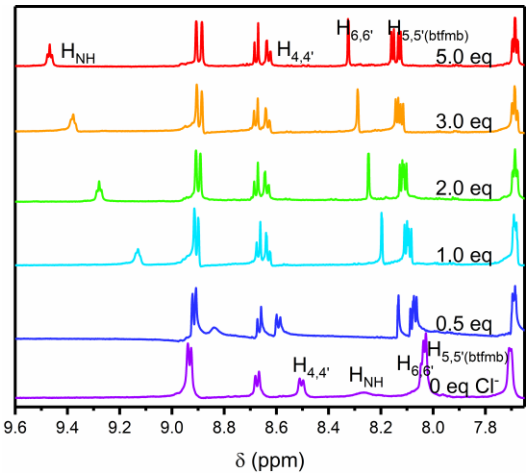

Figure S4.14: ^{1}H NMR titration of Ru-btfmb with TBA chloride in CD_3CN.

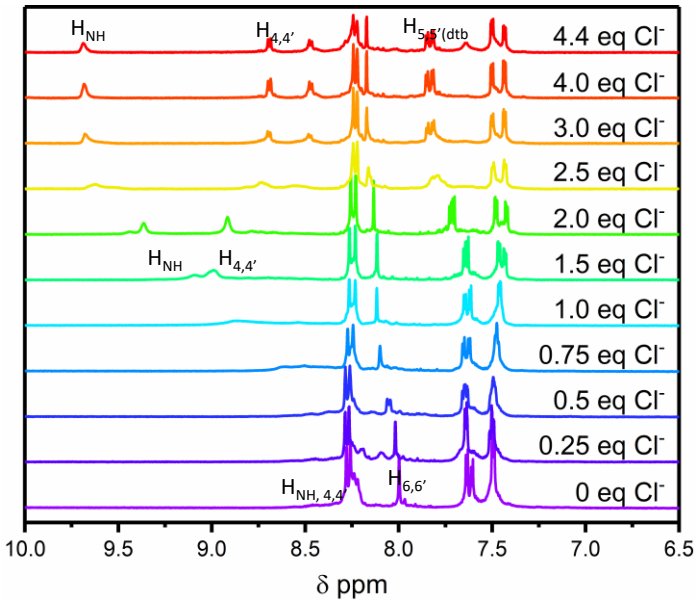

Figure S4.15: ^{1}H NMR titration of Ru-dtb with TBA chloride in CD_2Cl_2.

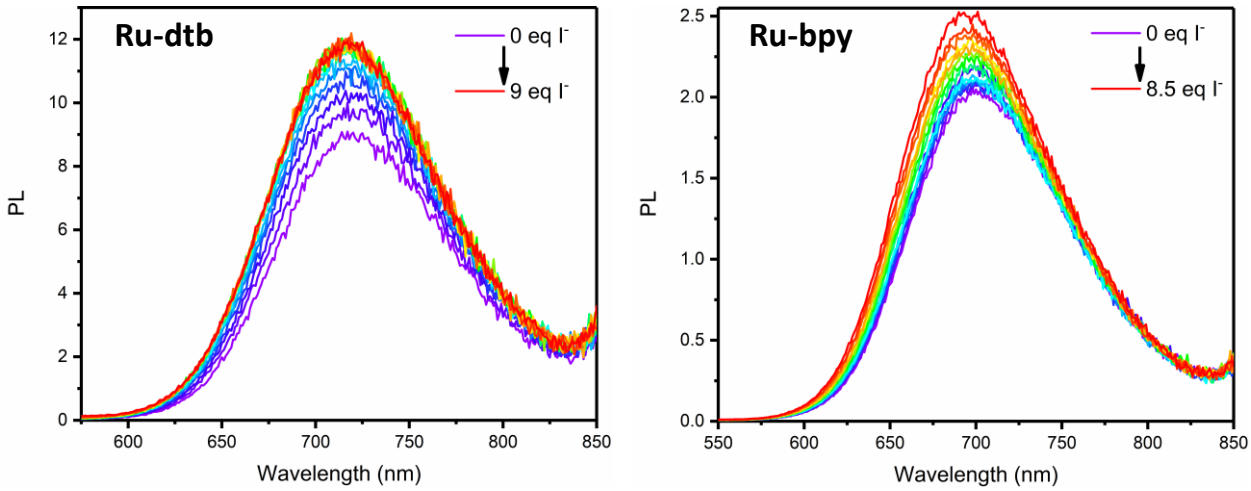

Figure S4.16: Photoluminescence spectrum of Ru-dtb (left) and Ru-bpy (right) as TBA iodide is titrated into CH_3CN solution. In both cases, the photoluminescence blue shifts and increases in intensity.

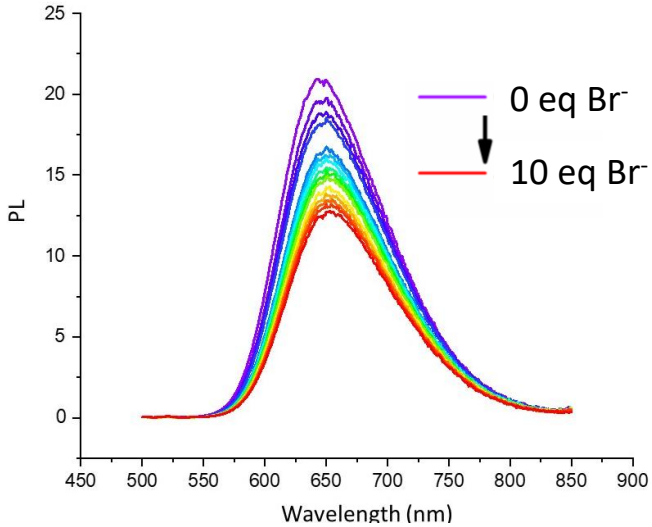

Figure S4.17: Photoluminescence spectrum of Ru-btfmb as TBA iodide is titrated into CH_3CN solution. The photoluminescence red shifts and decreases in intensity.

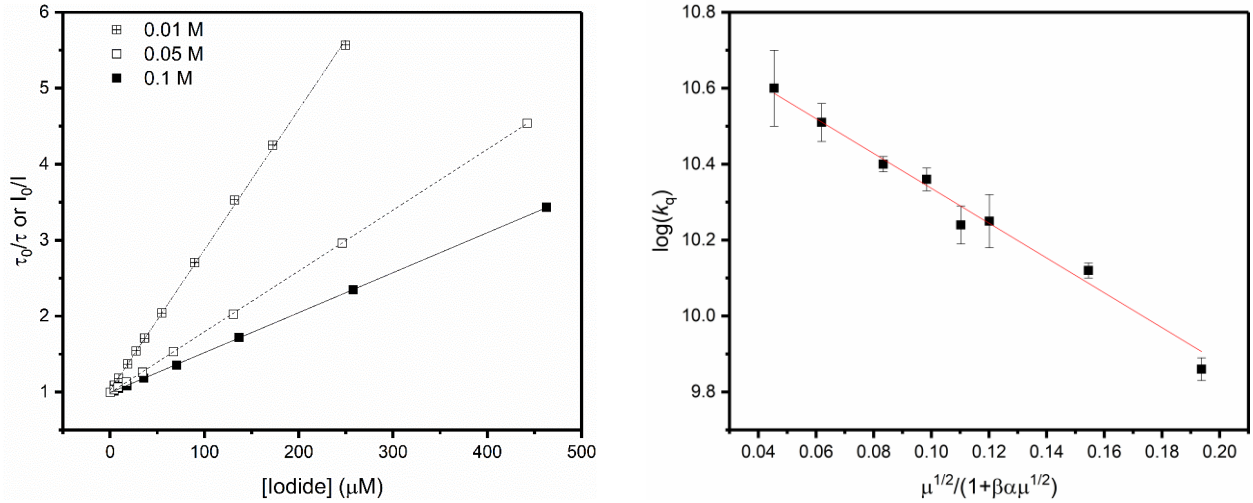

Figure S4.18: (Left) Stern-Volmer analysis of Ru-btfmb quenching with iodide in CH_3CN at various fixed ionic strengths. (Right) Debye-Hückel analysis of the excited-state quenching the fixed ionic strengths.

Appendix: Calculation of the diffusion limit for $[Ru^{2+},I^-]^+$ and I^- interactions in CH_3CN.

$$\boldsymbol{k_{diff} = 4\pi N_A(D_{Cl^-} + D_{Ru^*})\beta} \qquad \text{(S1)}$$

$$\beta = \frac{R_C}{\left(exp^{R_C/R} - 1\right)} \qquad \text{(S2)}$$

$$R_C = z_{Cl^-} z_{Ru^*} e^2 / 4\pi\varepsilon_r\,\varepsilon_0 k_B T \qquad \text{(S3)}$$

Where N_A is Avogadro's constant, D is the diffusion constant for iodide and the ruthenium excited state, z is the ionic charge, e is the elementary charge, ε_r is the vacuum permittivity, ε_r is the solvent dielectric, k_B is the Boltzmann constant, and T is temperature.

The diffusion constants, D_{Cl^-} and D_{Ru^*}, were calculated through the Stokes-Einstein relationship:

$$D = \frac{k_B T}{6\pi\eta r} \text{ (S4)}$$

Where η is the solvent viscosity of CH_3CN ($\eta = 3.4\times10^{-4}$ Pa•s) and r is the spherical radius of the molecule (r_{Ru^*} = 7Å, r_{I^-} = 2.2 Å), $D_{Ru^*} = 6.9\times10^{-10}$ m^2 s^{-1} and $D_{Cl^-} = 1.7\times10^{-9}$ m^2 s^{-1}.

Under these conditions, k_{diff} is calculated to be 3.7×10^{10} M^{-1} s^{-1}.

Note: As written, the equation for k_{diff} gives units of m^3 mol^{-1} s^{-1}. To convert to units of M^{-1} s^{-1}, it is necessary to multiply by 1000.

REFERENCES

(1) Prier, C. K.; Rankic, D. A.; Macmillan, D. W. C. *Chem. Rev.* **2013**, *113*, 5322–5363.

(2) House, R. L.; Yukie, N. M. I.; Coppo, R. L.; Alibabaei, L.; Sherman, B. D.; Kang, P.; Brennaman, M. K.; Hoertz, P. G.; Meyer, T. J. *J. Photochem. Photobiol. C Photochem. Rev.* **2015**, *25*, 32–45.

(3) Rigotti, T.; Aleman, J. *Chem. Commun.* **2020**, *56*, 11169–11190.

(4) Fanourakis, A.; Docherty, P. J.; Chuentragool, P.; Phipps, R. J. *ACS Catal.* **2020**, *10*, 10672–10714.

(5) Proctor, R. S. J.; Colgan, A. C.; Phipps, R. J. *Nat. Chem.* **2020**, *12*, 990–1004.

(6) Zheng, J.; Swords, W. B.; Jung, H.; Skubi, K. L.; Kidd, J. B.; Meyer, G. J.; Baik, M.; Yoon, T. P. *J. Am. Chem. Soc.* **2019**, *141*, 13625–13634.

(7) Gardner, J. M.; Abrahamsson, M.; Farnum, B. H.; Meyer, G. J. *J. Am. Chem. Soc.* **2009**, *131* (44), 16206–16214.

(8) Troian-Gautier, L.; Beauvilliers, E. E.; Swords, W. B.; Meyer, G. J. *J. Am. Chem. Soc* **2016**, *138*, 16815–16826.

(9) Wehlin, S. A. M.; Troian-Gautier, L.; Sampaio, R. N.; Marcélis, L.; Meyer, G. J. *J. Am. Chem. Soc.* **2018**, *140* (25), 7799–7802.

(10) Beer, P. D.; Gale, P. a. *Angew. Chem. Int. Ed. Engl.* **2001**, *40* (3), 486–516.

(11) Beer, P. D.; Szemes, F.; Balzani, V.; Salà, C. M.; Drew, M. G. B.; Dent, S. W.; Maestri, M. *J. Am. Chem. Soc.* **1997**, *119*, 11864–11875.

(12) Uppadine, L. H.; Drew, M. G. B.; Beer, P. D. *Chem. Commun.* **2001**, 291–292.

(13) Beer, P. D.; Fletcher, N. C. *Polyhedron* **1996**, *8*, 1339–1347.

(14) Turlington, M. D.; Troian-Gautier, L.; Sampaio, R. N.; Beauvilliers, E. E.; Meyer, G. J. *Inorg. Chem.* **2018**, *57* (9), 5624–5631.

(15) Turlington, M. D.; Troian-Gautier, L.; Sampaio, R. N.; Beauvilliers, E. E.; Meyer, G. J. *Inorg. Chem.* **2019**, *58*, 3316–3328.

(16) Jang, H. J.; Hopkins, S. L.; Siegler, M. A.; Bonnet, S. *Dalt. Trans.* **2017**, *46*, 9969–9980.

(17) Juris, A.; Balzani, V.; Belser, P.; Zelewsky, A. von. *Helv. Chim. Acta* **1981**, *64*, 2175–2182.

(18) Thompson, D. W.; Ito, A.; Meyer, T. J. *Pure Appl. Chem.* **2013**, *85* (7), 1257–1305.

(19) Blakley, R. L.; DeArmond, M. K. *J. Am. Chem. Soc.* **1987**, *109*, 4895–4901.

(20) Thordarson, P. *Chem. Soc. Rev.* **2011**, *40*, 1305–1323.

(21) Hibbert, D. B.; Thordarson, P. *Chem. Commun.* **2016**, *52*, 12792–12805.

(22) Demas, J. N.; Crosby, G. A. *J. Phys. Chem.* **1971**, *75*, 991–1024.

(23) Bigger, S. W.; Watkins, P. J.; Verity, B. *Int. J. Chem. Kinet.* **2000**, *32*, 473–477.

(24) Troian-Gautier, L.; Wehlin, S. A. M.; Meyer, G. J. *Inorg. Chem.* **2018**, *57* (19), 12232–12244.

(25) Li, G.; Swords, W. B.; Meyer, G. J. *J. Am. Chem. Soc.* **2017**, *139*, 14983–14991.

(26) Beer, P. D.; Dent, S. W.; Wear, T. J. *J. Chem. Soc., Dalt. Trans.* **1996**, 2341–2346.

(27) Liu, Y.; Sengupta, A.; Raghavachari, K.; Flood, A. H. *Chem* **2017**, *3*, 411–427.

(28) Gardner, J. M.; Abrahamsson, M.; Farnum, B. H.; Meyer, G. J. *J. Am. Chem. Soc.* **2009**, *131*, 16206–16214.

(29) Szeto, K. C.; Kongshaug, O. K.; Jakobsen, S.; Tilset, M.; Lillerud, K. P. *Dalt. Trans.* **2008**, 2054–2060.

(30) An, B.; Zeng, L.; Jia, M.; Li, Z.; Lin, Z.; Song, Y.; Zhou, Y.; Cheng, J.; Wang, C.; Lin, W. *J. Am. Chem. Soc.* **2017**, *139*, 17747–17750.

(31) Hadda, T. Ben; Le Bozec, H. *Polyhedron* **1988**, *7* (7), 575–577.

(32) Adamson, K.; Dolan, C.; Moran, N.; Forster, R. J.; Keyes, T. E. *Bioconjug. Chem.* **2014**, *25*, 928–944.

(33) O'Donnell, R. M.; Sampaio, R. N.; Li, G.; Johansson, P. G.; Ward, C. L.; Meyer, G. J. *J. Am. Chem. Soc.* **2016**, *138* (11), 3891–3903.

(34) Argazzi, R.; Bignozzi, C. A.; Heimer, T. A.; Castellano, F. N.; Meyer, G. J. *Inorg. Chem.* **1994**, *33*, 5741–5749.

CHAPTER 5. DUAL-SENSITIZER PHOTOANODE FOR BROMIDE OXIDATION[3]

5.1 Introduction

Water splitting provides a viable means of generating a sustainable and storable fuel from sunlight.[1–10] This "holy grail" of solar energy storage has been performed with a dye-sensitized photoelectrosynthesis cell, with the oxidation ($2H_2O \rightarrow O_2 + 4e^-$) at a dye-sensitized anode and reduction ($2H_2O + 4e^- \rightarrow 2H_2$) at a dark Pt electrode.[11,12,21–26,13–20] In a typical cell, the photoanode is composed of a wide band gap semiconducting metal oxide sensitized to visible light by a molecular dye often called a sensitizer, S^0. Photoexcitation of S^0 results in excited-state electron injection into the semiconductor yielding an interfacial charge-separated state $TiO_2(e^-)|S^+$. The oxidizing equivalent is then transferred from S^+ to a catalyst via thermal electron transfer, which regenerates S^0. After four oxidizing equivalents have accumulated on the catalyst, water oxidation occurs, completing the anodic half reaction. The photoinjected electrons are transported to a platinum cathode that catalyzes proton reduction, Figure 5.1A. Herein are described first steps toward an alternative strategy wherein bromine is generated as a redox mediator for water oxidation through dye-sensitization, Figure 5.1B.

The efficiency of water splitting is generally limited by the oxidation half reaction, as the accumulation of four redox equivalents on a single catalyst occurs in kinetic competition with deleterious charge recombination reactions.[27–30] Recent literature reports have shown that

[3] This chapter previously appeared as an article in the journal ACS Applied Energy Materials. The original citation is as follows: Turlington, M. D.; Brady, M. D.; Meyer, G. J. Dual-Sensitizer Photoanode for Bromide Oxidation. *ACS Appl. Energy Mater.* **2021**, *4*, 745-754.

unwanted back-electron transfer reactions from the semiconductor to the oxidized dye and/or catalyst can be inhibited through the use of core/shell metal oxide materials,[31] redox gradients that vectorally separate charge,[12,32] chemical linkers that position the catalyst farther from the dye-sensitized interface,[33] or a combination of these strategies.[34] However, the solar conversion efficiency still remains far from optimal. An alternative strategy is to physically separate water oxidation catalysis from the dye-sensitized photoanode. In this design, dye-sensitization creates a mobile oxidant that is thermodynamically capable of initiating water oxidation at a remote catalytic site.[35] The efficient dye-sensitized generation of potent oxidants that serve as mediators for water oxidation is therefore crucial to the successful implementation of this strategy.[36] Iodine generation, for example, is well known to occur nearly quantitatively in dye-sensitized solar cells, but I_2 is not a strong enough oxidant for water oxidation in neutral or acidic aqueous solutions.

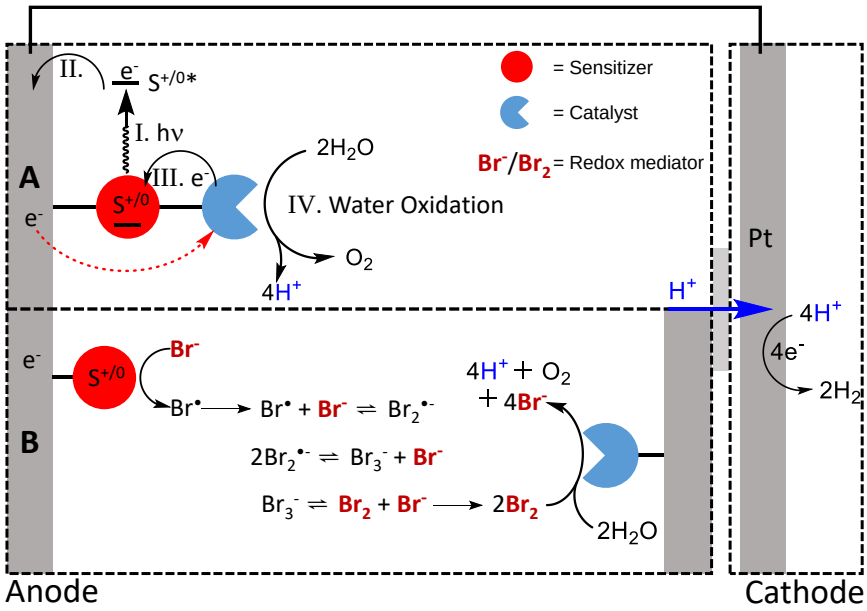

Figure 5.1: Dye-sensitized water splitting photoelectrosynthesis cells. The left half-cell shows the dye-sensitized processes that lead to water oxidation at the anode. The right half-cell depicts proton reduction at the cathode. (A) I. Photoexcitation of the sensitizer. II. Excited-state electron injection from the sensitizer to the semiconductor. III. Thermal electron transfer from the water oxidation catalyst to the sensitizer. IV. Water oxidation occurs after four oxidizing equivalents have been transferred to the catalyst. (B) After excited state injection, S^+ oxidizes bromide to yield the bromine atom, $Br^{\cdot}$. In acidic aqueous solutions concentrated with bromide ions, the photogenerated bromine atom reacts with Br^- to form dibromide, $Br_2^{\cdot-}$, that is unstable with respect to disproportionation to yield tribromide that is in equilibrium with elemental bromine, Br_2, that is thermodynamically competent of initiating water oxidation at a remote catalytic cite.

A challenge associated with the dye-sensitized generation of strong oxidants at semiconductor interfaces is that S* must be a potent excited-state reductant for quantitative electron injection and S^+ must react with the oxidant precursor more rapidly than the competitive back reaction. As was recently described, there is a delicate interplay between ground- and excited-state reduction potentials that make it difficult to tune both for optimal behavior while still maintaining light absorption throughout the visible region.[37]

A dual-sensitizer photoanode approach with a molecular catalyst has been reported for water oxidation.[34] The approach was successful, but the conversion efficiencies were low even when losses associated with transmitted light were taken into account.[34] Herein is reported a mechanistic study designed to identify loss mechanism(s) in the dual-sensitizer approach. Two sensitizers were utilized that have more favorable energetics for inter-sensitizer electron transfer, Figure 5.2. The sensitizer 1-cyano-2-(4-(di-p-tolylamino)phenyl)vinyl)phosphonic acid (**Org**, Figure 5.2, left) is linked directly to core/shell SnO_2/TiO_2 nanoparticles in a mesoporous thin film photoanode. An Al_2O_3 overlayer stabilizes **Org** and provides a binding site for a second sensitizer, $[Ru(bpz)_2(4,4'\text{-}(PO_3H_2)_2\text{-}2,2'\text{-bipyridine}]^{2+}$ (**Ru**, Figure 5.2, right). The desired sequence of electron transfer reactions are as follows. Upon blue light absorption **Org*** injects an electron into the core-shell nanoparticle thin film. Longer wavelength light absorption creates **Ru*** that reduces $\mathbf{Org^{ox}}$ and oxidizes bromide at an aqueous electrolyte interface. Time resolved anisotropy measurements with Monte-Carlo simulations revealed that the Ru* undergoes lateral intermolecular energy transfer across the oxide surface. In addition, an unproductive excited-state electron transfer pathway was identified that lowers the efficiency. This fundamental research shows that a dual-sensitizer photoanode is indeed capable of generating Br_2 that is known to mediate water oxidation catalysis.[35]

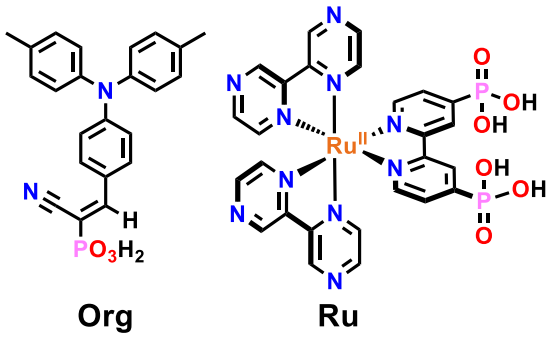

Figure 5.2: Structures and abbreviations of the dual-sensitizers utilized herein.

5.2 Experimental

5.2.1 Materials

Sodium Acetate (Sigma-Aldrich, ≥99%), glacial acetic acid (Fisher, certified ACS), sodium bromide (EM Science), and sodium perchlorate (Acros Organics, 98%), were used as received. Argon gas (Airgas, 99.998%) was passed through a Drierite drying tube before use. All solvents were ACS grade and used as received. The two sensitizers, **Org** and **Ru** were available from previous studies. SnO_2/TiO_2 core/shell[33] and ZrO_2[38] thin films were prepared as previously published. Fluorine-doped tin oxide (FTO) was purchased from Hartford Glass (15 Ω/sq).

5.2.2 Thin Film Preparation

The mesoporous thin films were made from a colloidal SnO_2 or ZrO_2 solution. The SnO_2 or ZrO_2 solutions were doctor bladed onto a methanol-cleaned FTO glass substrate using Scotch tape (~50 μm thick) as a spacer to ensure uniform thickness. The doctor bladed films were covered and allowed to dry at room temperature for 30 min, then sintered under an O_2 atmosphere (~1 atm) for 30 min at 450 °C. These films were stored in a ~70 °C oven until use. The thin films were placed into ~1 mM methanol sensitizer solutions to allow for surface functionalization. Films reacted for at least 48 h to ensure that uniform, saturation surface coverages were achieved. Prior to use, films were rinsed with neat MeOH to remove any weakly adsorbed molecules from the surface. The dual-sensitizer photoanode CS|**Org**|Al_2O_3|**Ru**$^{2+}$ was prepared by first reacting **Org** to

the SnO_2/TiO_2 core/shell films. The subsequent deposition of Al_2O_3 by atomic layer deposition (see below) presented a fresh surface by which the **Ru^{2+}** sensitizer could be functionalized.

5.2.3 Atomic Layer Deposition

Atomic layer deposition (ALD) was performed in a commercial reactor (Savannah S200, Cambridge Nanotech). The core/shell SnO_2/TiO_2 films were prepared by atomic layer deposition of TiO_2 onto the SnO_2 films using tetrakis-dimethyl amine titanium, (TDMAT), held at 75 °C, and water as the precursors. The deposition conditions were 130 °C under 20 sccm carrier N_2 gas. An ALD "cycle" consisted of a 1 s TDMAT pulse, 15 s hold, 50 s N_2 purge, 0.02 s H_2O pulse, 15 s hold, and 50 s N_2 purge. These core/shell thin films were annealed for 30 min under an O_2 flow at 450 °C.

Aluminum oxide (Al_2O_3) was deposited using trimethylaluminum (TMA). The reactor temperature was held at 130 °C, whereas the TMA reservoir was kept at room temperature. The TMA was pulsed into the reactor for 0.02 s and then held for 30 s before opening the pump valve and purging for 35 s. ALD coating conditions were 130 °C with a 20 sccm N_2 carrier gas flow rate with a sequence of 0.02 s TMA dose, 30 s hold, 35 s N_2 purge, 0.02 s H_2O dose, 30 s hold, 35 s N_2 purge for 10 cycles, with ∼1.1 Å Al_2O_3 deposited per cycle.

5.2.4 Spectroscopy

UV−Visible Absorption. All steady-state UV− visible spectra were obtained on an Agilent Cary 60 spectrophotometer at room temperature in 1.0 cm path length glass cuvettes with the functionalized thin films placed along the diagonal at a 45° angle to the incident probe light.

Nanosecond Transient Absorption. Nanosecond transient absorption measurements were obtained with an apparatus which has been previously described.[39] Briefly, samples were excited by a Qswitched, pulsed Nd:YAG laser (Quantel U.S.A. (Big Sky) Brilliant B; 5−6 ns full

width at half-maximum (fwhm)) tuned to 532 nm or a laser of the same model, frequency tripled (355 nm) coupled to an optical parametric oscillator (OPO, Opotek, Inc.) tuned to 488 nm with the appropriate nonlinear optics. The excitation fluence was measured with a Thor Laboratories PM100D laser powermeter that was typically 3−5 mJ/pulse. The laser beam was directed 45° to the film surface. A 150 W Xe arc lamp served as the probe beam and was aligned orthogonal to the laser excitation light. The probe lamp was pulsed for measurements on sub-100 μs time scales. Detection was achieved with a monochromator (SPEX 1702/04) optically coupled to an R928 photomultiplier tube (Hamamatsu). Transient data were acquired with a computer-interfaced digital oscilloscope (LeCroy 9450, Dual 330 MHz) with an overall instrument response time of ∼10 ns. Typically, 30 laser pulses were averaged at each observation wavelength over the range 390−760 at 10 nm intervals. Full spectra were generated by averaging 2−10 points on either side of the desired time value to reduce noise in the raw data. Single wavelength kinetic traces typically consisted of 90 laser pulses averaged at the observed wavelength.

Nanosecond Transient Anisotropy. Nanosecond transient anisotropy measurements were obtained with the apparatus described above for transient absorption experiments. One difference was that the probe was directed through a 1/4 m monochromator (Spectral Energy Corp., GM 252) before arriving at the sample. Typically, 60 laser pulses were averaged at each observation wavelength and 5−10 identical measurements were taken and averaged to help increase the signal-to-noise ratio of the anisotropy data. All measurements utilized a Glan−Taylor polarizer (Thorlabs, GL 10-A) for excitation (Pex) and a second Glan−Taylor polarizer (Pdet) for the probe beam. For anisotropy measurements, Pex was set to vertical, the same polarization as the laser, and Pdet was set to either vertical (V) or horizontal (H). Magic angle and anisotropy values were calculated via eqs 1 and 2, respectively:

$$\Delta\, Abs_{magic\ angle} = \frac{(VV+2VH)}{3} \quad (1)$$

$$r = \frac{(VV-VH)}{3\Delta Abs_{magic\ angle}} \quad (2)$$

where VY is the change in absorbance observed with excitation polarization V and detection polarization Y = V or H and r is the anisotropy value.

5.2.5 Data Analysis

Data fitting was performed in OriginPro 2017, with least-squares error minimization achieved using the Levenberg−Marquardt method. The errors reported for fitting parameters are the standard errors.

5.2.6 Simulations of Anisotropy Data

Monte Carlo simulations were employed to simulate the random-walk anisotropy decay observed after vertically polarized light excitation. The simulation utilized a 20 nm spherical nanocrystallite with sensitizers spaced at approximately the intermolecular distance, δ, extracted from surface coverage (Γ0) measurements, vide infra. The simulated sensitizers were distributed across the surface of the sphere through an iterative Coulomb's law force minimization, which produced a nearly even sensitizer distribution. To simulate the low laser power utilized experimentally, one hole was generated per nanocrystallite for each simulation. The probability of an initial hole being generated at a specific location was proportional to $\cos^2 \varphi$, where φ is the inclination angle of the vertical plane, i.e., vertically polarized light has φ = 0. For each initialization, the excited-state sensitizer generated after vertically polarized excitation was assumed to quantitatively inject an electron. After formation of the oxidized sensitizer, or hole, a random-walk simulation was performed. For each sensitizer, 10000 random walks consisting of 1000 iterations were averaged to determine the simulated anisotropy decay as a function of the iteration step. Self-exchange electron transfer was modeled with an exponential distance

dependence for the probability of transfer with β = 1.2 Å−1 , as previously determined.[40] The anisotropy, r, at any time during the random walk was calculated via eq 3, where ⟨cos^2 φ⟩ was the average of the square of the cosine of the inclination angle of the position of the hole.

$$r = \frac{3\langle cos^2\varphi\rangle - 1}{2} \quad (3)$$

With the time per iteration step as the only adjustable parameter, the experimentally determined anisotropy decays were modeled directly with the simulated anisotropy decays. The best fit with respect to time per iteration was then utilized to determine the resulting self-exchange rate constant, k_{MC}, for each sensitizer. The Monte Carlo simulations were performed with Wolfram Mathematica 11.0.1.0.

5.2.7 Photoelectrochemical Cells

Photocurrent measurements were performed on a BASi Epsilon potentiostat with a standard three-electrode configuration (working electrode, photocatalyst sensitized SnO_2/TiO_2 core/shell on FTO with 500 mV applied potential; reference electrode, Ag/AgCl (4 M KCl, externally referenced to SCE); counter electrode, Pt mesh) in a custom-built H-cell with the two half-cells separated by a Nafion proton-exchange membrane. **White Light Illumination**. Under white light illumination from a Cole Parmer 41720-Series fiber optic illuminator, thin film slides were positioned to receive 100 mW cm^2 with the light intensity determined with a Coherent Molectron PM 5200 laser power detector. A 400 nm long-pass filter was used to inhibit direct bandgap excitation of the metal oxide layer. The geometric area of the photoanode was used for reporting current densities. Unless otherwise stated, solutions were sparged with argon for 30 min prior to running the experiment. **Monochromatic Illumination for Incident and Absorbed Photon-to-Current Efficiencies (IPCE and APCE)**. For monochromatic light excitation, a

Coherent Genesis MX 460 or 532 nm solid-state laser was utilized as the illumination source with photon output calibrated using a Thor Laboratories PM100D laser power meter. Photocurrents were measured with both excitation wavelengths at various laser power intensities. The reported IPCE and APCE values were calculated with a laser power of 20 mW cm^{-2}. The geometric area of the detector was used for reporting power per unit area. For all experiments utilizing an applied potential, a Ag/AgCl reference electrode externally calibrated to a SCE electrode (241 mV vs NHE) was used. All potentials are reported versus NHE.

5.2.8 Faradaic Efficiency

The Faradaic efficiency was quantified via coulometric determination of the number of electrons in the integrated photocurrent and spectroscopic determination of the number of Br_2 and Br3−generated. The tribromide (Br_3^-) and bromine (Br^2) are in equilibrium (eq 4):

$$Br^- + Br_2 \leftrightarrow Br_3^- \; K_{eq} = 16 \tag{4}$$

Using the known extinction coefficient of Br_3^- (ε(266 nm) = 40,900 M^{-1} cm^{-1}) and the equilibrium constant, the total photoproduct concentration was calculated. Thin-film photoanodes immersed in a known volume of pH 4.76 solution (0.2 M acetate buffer, 0.3 M NaBr) were illuminated with 460 nm steady-state illumination for fixed periods of time (Figure S5.1, left). After illumination, an aliquot of the electrolyte solution was removed and the absorption spectrum was measured (Figure S5.1, right). The ratio of the oxidized bromide photoproducts to the total charge passed during illumination while taking into account the two-electron oxidation provided a Faradaic efficiency of 14% for CS|**Org**|Al_2O_3|**Ru**. In the control experiment with CS|**Org** where the laser power was attenuated to give the same photocurrent magnitude, no Br_3^- photoproduct was observed over the same time frame (Figure S5.2).

5.3 Results

The two sensitizers utilized (1-cyano-2-(4-(di-p-tolylamino)phenyl)vinyl)phosphonic acid (**Org**) and $[Ru(bpz)_2(4,4'\text{-}(PO_3H_2)_2\text{-}2,2\text{-bipyridine}]^{2+}$ (**Ru**) (Figure 5.2), have been characterized previously in solution and on mesoporous metal oxide surfaces.[37,41] The target photoanode, herein referred to as CS|**Org**|Al_2O_3|**Ru**, was prepared sequentially starting with previously described $SnO_2|TiO_2$ core shell (CS) nanoparticles interconnected in a mesoporous thin film. The thin film was surface functionalized with **Org** to saturation surface coverages. Atomic layer deposition of an ~11 Å insulating Al_2O_3 overlayer CS|**Org**|Al_2O_3 stabilized the sensitizer and providing an oxide surface to which **Ru** was functionalized yielding CS|**Org**|Al_2O_3|**Ru**.

The UV-visible absorption spectra in methanol solution are shown in Figure 5.3A, while the relevant ground- and excited-state reduction potentials are reported in Table 1. The absorption spectrum of the two-sensitizer sensitized photoanode is shown in Figure 5.3B. Notably, subtraction of contributions from **Org** results in a broad band at 465 nm, consistent with the presence of the metal-to-ligand charge-transfer (MLCT) absorption of **Ru**. Significant broadening of the surface bound **Org** and **Ru** sensitizers was observed as compared to the solution spectra. The spectroscopically determined surface coverages (Γ_0) were calculated with Equation 4, where A is the absorbance at λ_{max} and ε is the molar extinction coefficient, which was assumed to retain its value upon surface binding. Surface coverages were approximately equal for the two sensitizers, 4.3 and 3.7×10^{-8} mol/cm^2 for **Org** and **Ru**, respectively.

$$A = 1000 \times \Gamma_0 \times \varepsilon \tag{4}$$

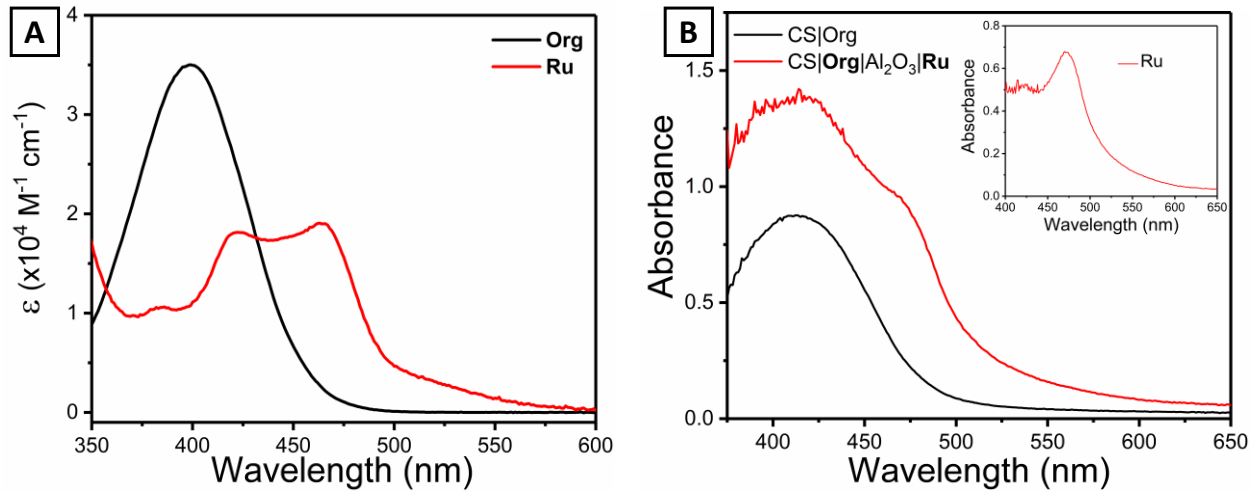

Figure 5.3: (A) Visible absorption spectra of **Org** (black) and **Ru**(red) in MeOH solution. (B) Visible absorption spectra of the CS|**Org** (black) and CS|**Org**|Al_2O_3|**Ru** (red) photoanodes. The inset shows the spectrum obtained by subtraction of the CS|**Org** spectrum from that of CS|**Org**|Al_2O_3|**Ru** that was assigned to the MLCT state of Ru.

Table 5.1. Absorption and Electrochemical Characterization of **Org** and **Ru**

	λmax (ε×10^4 M^{-1} cm^{-1})	E° ($S^{*0/+}$)	E° ($S^{0/+}$)
Org	400 nm (3.5)	-1.88	0.99
Ru	465 nm (1.9)	-0.25	1.85

5.3.1 Excited-State Electron Injection

Pulsed 488 nm laser excitation of CS|**Org** resulted in an absorption feature centered at 700 nm corresponding to **Org^{ox}** (Figure S5.1).[41] This transient feature formed within the instrument response time, consistent with $k_{inj} > 10^8$ s^{-1}.[42,43] The kinetics for back-electron transfer (BET) from a CS electron to **Org^{ox}** monitored at 700 nm (Figure S5.2) were nonexponential and successfully modeled by the Kohlrausch−Williams−Watts (KWW) function (Equation 4), where A_0 is the initial amplitude, k_{obs} is the characteristic rate constant, and β is inversely proportional to the width of an underlying Lévy distribution. The average rate constant was determined with equation 5 (where Γ is the gamma function), yielding a rate constant for $k_{KWW} = 5\times10^2$ s^{-1}.

$$\mathrm{Abs(t)} = \mathrm{A_0 e^{-(k_{obs}t)^{\beta}}} \qquad (5)$$

$$k_{\mathrm{KWW}} = \frac{k_{\mathrm{obs}}\beta}{\Gamma\left(\frac{1}{\beta}\right)} \tag{6}$$

5.3.2 Time-Resolved Absorption Anisotropy

Light absorption by **Ru** yielded an MLCT excited state that was not quenched by the CS acceptor states. The fate of the excited state was probed by time-resolved absorption anisotropy, a technique that has recently been utilized to quantify lateral self-exchange reactions occurring on nanoparticle surfaces.[44–46] Initial studies were frustrated by a reductive quenching pathway (see below), so an insulating zirconium oxide (ZrO_2) mesoporous thin film was utilized, abbreviated ZrO_2|**Ru**. Vertically polarized 532 nm laser excitation produced the MLCT excited state that was detected with either vertically (VV) or horizontally (VH) oriented polarizers, Figure 5.4A. A time-resolved anisotropy resulted that was used to determine the anisotropy decay, Figure 5.4B.

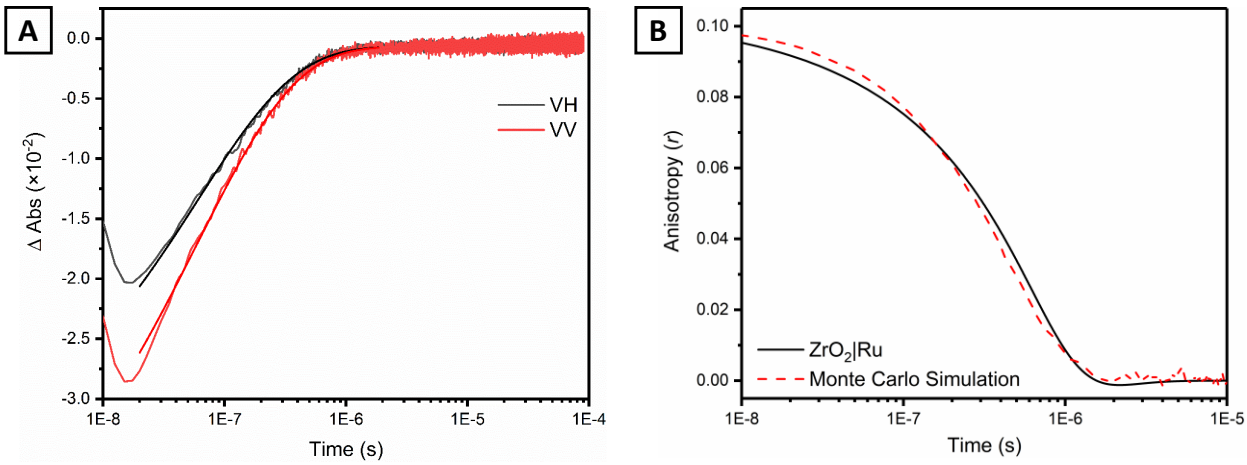

Figure 5.4: (A) Time-resolved absorption anisotropy decays and overlaid fits of the MLCT excited-state with VV (red) and VH (black) polarization. (B) Calculated anisotropy (black) overlaid with the results of the Monte Carlo simulation, resulting in an energy transfer rate constant of 4×10^7 s^{-1}.

This anisotropy decay was modeled with previously described Monte Carlo simulations.[45,46] An intermolecular energy transfer rate constant of 4×10^7 s^{-1} was found that corresponds to ~ 25 ns per energy transfer consistent with reports of related ruthenium complexes, Figure 5.3B.[47] Therefore

in the absence of excited state electron transfer, energy transfer across the surface of the nanoparticle occurs an average of 26 times within the excited state lifetime.

5.3.3 Regeneration of ***Ru^{ox}*** *with* Br^-

To test the utility of the CS|**Org**|Al_2O_3|**Ru** photoanode in generating strong oxidizing equivalents, the reaction of photogenerated **Ru^{ox}** with Br^- was investigated. The formal one electron reduction potentials for $Br^{-/\bullet}$ and **Ru**$^{III/II}$ are 1.92 and 1.85 V vs. NHE, respectively. Although the oxidation of Br^- in this reaction is unfavorable by 70 mV, large rate constants for formally uphill reactions have been observed previously when a large excess of Br^- is present.[37,48] As prior reports show, **Ru*** is not a potent photoreductant and does not inject electrons into the CS acceptor states in the pH range (4-6) targeted for this study.[37] Therefore, photoanodes were prepared on a SnO_2 semiconductor with more positive acceptor states. Pulsed 532 nm laser excitation of SnO_2|**Ru** anode resulted in a transient bleach at the 402 nm ground/excited-state isosbestic point (Figure 5.5, purple trace), consistent with the formation of **Ru^{ox}**. This transient bleach was observed at both pH 4 and 5.6, indicated that **Ru*** is able to inject electrons into SnO_2, yielding $SnO_2(e^-)$|**Ru^{ox}**

As shown in Figure 5.5, increasing the Br^- concentration resulted in faster **Ru^{ox}** regeneration. The kinetic data were successfully fit to the KWW function. A plot of k_{KWW} verses the Br^- concentration (Figure 5.5, inset) was linear with a slope that provided the regeneration rate constant $k_{reg} = 2\times10^7\ M^{-1}\ s^{-1}$.

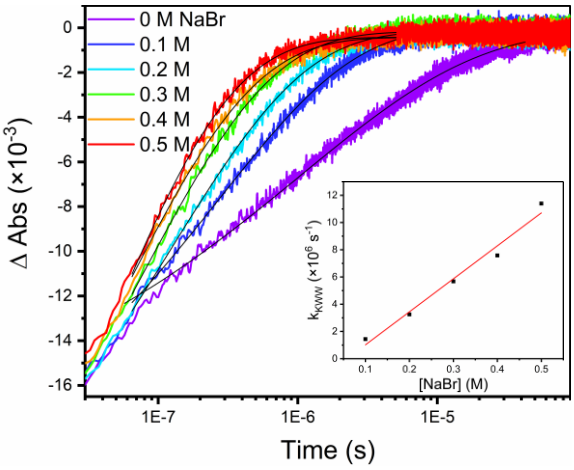

Figure 5.5: Regeneration of the oxidized ruthenium complex in pH 4 acetate buffer (0.2 M) with increasing Br^- concentrations. The inset shows the observed rates verses the Br^- concentration, the slope of which corresponds to the second order rate constant, $k_{reg,} = 2\times10^7\ M^{-1}\ s^{-1}$.

5.3.4 Photocurrents

To assess the performance of the dual-sensitizer photoanode for Br^- oxidation in pH 5.6 solutions, photocurrent measurements were obtained in a three electrode H-cell. The photoanode and reference electrode were placed in one compartment of the H-cell and illuminated with 100 mW cm^{-2} (1 sun), while a counter electrode was kept in a dark compartment. The photocurrent responses displayed a typical spike in intensity indicative of electrode polarization and fast electron transfer, followed by decay to the steady-state photocurrent.[12,27] In control experiments, white light excitation of CS|**Org** or CS|**Ru** photoanodes resulted in 40 or 2 μA cm^{-2} of sustained photocurrent, respectively. For the dual sensitizer CS|**Org**|Al_2O_3|**Ru**, 200 μA cm^{-2} of sustained photocurrent was measured indicating that the two sensitizers have a synergistic effect on the current output, Figure 5.6.

Incident and adsorbed photon-to-current efficiencies (IPCE and APCE) for Br^- were measured for the photoanode with 460 and 532 nm excitation in pH 4 solution (Figures S5.3 and S5.4, Table S1). As shown in Figure 5.3, both sensitizers absorb light at 460 nm, while only the ruthenium sensitizer absorbs significantly at 532 nm. The IPCE and APCE values were an order

of magnitude greater with 460 nm excitation (IPCE = 1.2%, APCE = 1.4%) as compared to 532 nm excitation (IPCE = 0.08%, APCE = 0.13%), revealing that the photoanode efficiency decreases drastically when only the ruthenium sensitizer absorbed light. With 460 nm light excitation the photocurrent increased linearly with the light intensity.

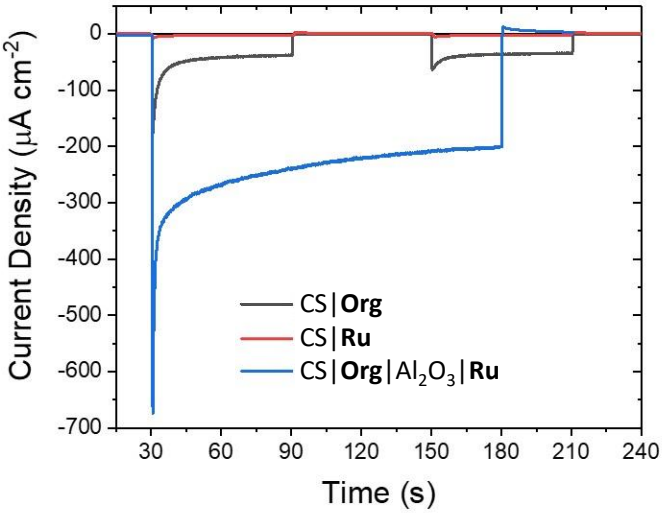

Figure 5.6: Light on/off current responses for CS|**Org** (black), CS|**Ru** (red), and CS|**Org**|Al_2O_3|**Ru** (blue) photoanodes. The current responses were measured under 100 mW cm^{-2} white light illumination with a 0.5 V vs. NHE applied potential in 0.2 M acetate buffer (pH 5.6) and 0.3 M NaBr.

*5.3.5 Reductive Quenching of **Ru*** by **Org***

In the dual-sensitizer assembly, the magnitude of the photocurrent response indicated that the efficiency of Br^- oxidation was suboptimal.[37,48] This suggested the presence of a nonproductive electron transfer pathway. The absorption difference spectra measured after pulsed 488 or 532 nm excitation of MOx|**Org**|Al_2O_3|**Ru** (MOx = CS or TiO_2) revealed a positive absorption growth at 500 nm assigned to the reduced complex, **Ru**^{red},[49–51] and the characteristic abortion of **Org**^{ox} centered near 700 nm, Figure S5.5.

Additional insights were gained by successfully isolating this reaction through photoanode design. To accomplish this, a dual-sensitizer assembly was prepared with the insulator ZrO_2

instead of the CS semiconductor, yielding the following structure, ZrO_2|**Org**|Al_2O_3|**Ru**. In this assembly, excited-state electron injection from **Org*** was not observed. Pulsed 532 nm excitation resulted in the appearance of absorption at 500 and 700 nm, consistent with the formation of **Org**^{ox} and **Ru**^{red}, Figure 5.7A. Varying the Al_2O_3 layer thickness from 5.5 to 22 Å (5 – 20 cycles) was found to have a dramatic impact on the yield, Figure 5.7B. With thin shells (5.5 – 11 Å Al_2O_3), significant amplitude remained and when the thickness was increased to 22 Å, the yield was near zero.

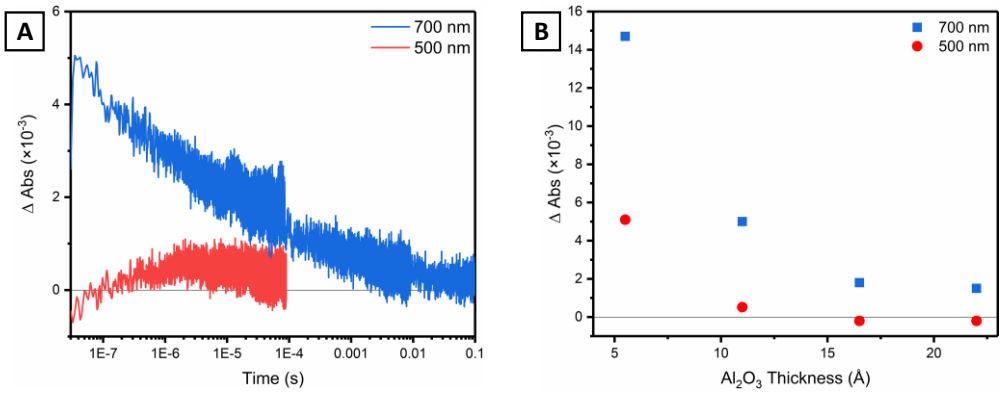

Figure 5.7: (A) Time-resolved absorption changes at 500 (red) and 700 (blue) nm upon 532 nm excitation of ZrO_2|**Org**|Al_2O_3|**Ru** anodes in 0.2 M acetate buffer (pH 5.6). (B) The maximum ΔAbs for the transient signal at 500 and 700 nm plotted vs. the insulating Al_2O_3 layer thickness.

5.4 Discussion

Dye-sensitized Br^- oxidation through the use of a dual-sensitizer photoanode design has been realized in pH 5.6 aqueous solution. Previous research has been limited to organic solvents or highly acidic (pH 0-1) aqueous solutions, conditions that simplify many of the challenges associated with dye-sensitized Br^- oxidation. For instance, the $Br^{\bullet/-}$ potential is less positive in organic solvents (1.42 V vs NHE in acetone)[52] as compared to water (1.92 V vs NHE),[53] allowing weaker ground-state oxidants to turn over catalysis.[54,55] In aqueous conditions, acidic electrolytes shift the semiconductor acceptor states to lower energy, facilitating excited-state injection.

A generalized depiction of the dual-sensitizer photoanode is shown in the left panel of Figure 5.8. The photoanode was designed such that the inner sensitizer (**Org**) a potent photoreductant was positioned for excited-state electron injection, while the outer sensitizer (**Ru**) a potent oxidant was present at an Al_2O_3 electrolyte interface for Br^- oxidation.

In the right panel of Figure 5.8, the desired processes for an operational HBr splitting cell are plotted on an energy axis, along with the relevant ground- and excited-state reduction potentials of the sensitizers, which represents a Z-type scheme. The artificial Z-scheme is here applied to two molecular sensitizers, as compared to prior reports which utilized two semiconductors[56–60] or a semiconductor and a single sensitizer[61,62] as light harvesters. In CS|**Org**|Al_2O_3|**Ru**, blue light absorption by **Org** ($h\nu_1$) yields an electronic excited-state that quantitatively injects an electron into the core/shell metal oxide. Green light excitation of the outer **Ru** sensitizer ($h\nu_2$), yields the MLCT excited-state **Ru***, which undergoes excited-state energy transfer across the surface until it encounters $\mathbf{Org^{ox}}$. A large driving force (1.24 V) for the electron-transfer reaction ($k_{reg,1}$), $\mathbf{Org^{ox} + Ru^{*} \rightarrow Org + Ru^{ox}}$ translates the oxidizing equivalent to the electrolyte interface. Despite a strong thermodynamic driving force for this reaction, $-\Delta G^o = 1.24$ eV, it was not found to be quantitative. Excited state injection was efficient and Br^- oxidation occurred with a large rate constant $k_{reg} = 2\times10^7\ M^{-1}\ s^{-1}$, however the measured photocurrents were sub-optimal, indicative of an unwanted charge recombination pathway.

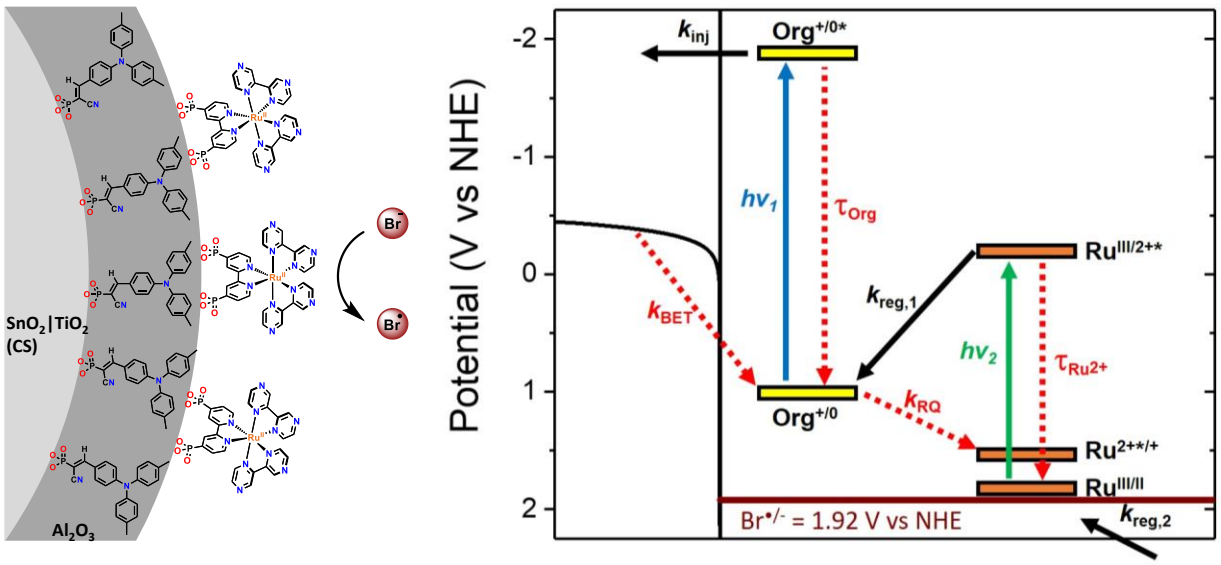

Figure 5.8: A depiction of the dual-sensitizer photoanode used for bromide oxidation at pH 4-6 (left panel). The right panel shows the proposed electron transfer reactions (beneficial in solid arrows, non-beneficial in dashed arrows) on an energy axis.

In addition to the desired electron transfer reactions, a variety of non-productive pathways (right panel Figure 5.8, dashed arrows) were envisioned. Prior work revealed that despite a short < 1 ns **Org** excited-state lifetime, excited-state injection quantum yields of unity were obtained.[41] The **Ru***excited-state lifetime of τ = 0.67 μs is approximately three orders of magnitude longer than that of **Org**, but **Ru*** did not undergo measureable excited state injection; behavior attributed to weak electronic coupling to the core/shell oxide and a low driving force. Instead, the excited state was found to undergo lateral intermolecular energy transfer across a ZrO_2 interface. Monte-Carlo simulations indicated that on average the Ru* 'hops' to a neighbor sensitizer 26 times before recombination. Such energy migration should increase the likelihood that **Ru*** encounters **Org^{ox}**. In principle, the **Org^{ox}** could undergo lateral **Org^{ox}/Org** self-exchange reactions often called hole-hopping,[63,64] but prior research has shown that hole-hopping is inhibited when sensitizers are buried in Al_2O_3 overlayers.[46,65] Hence **Ru*** energy transfer to the injection site or the statistical photo-creation of proximate **Ru*** and **Org*** provide the only mechanisms for efficient bromide

oxidation prior to $k_{BET}= 5\times10^2\ s^{-1}$. Mechanistic studies revealed that this does not occur efficiently as an unwanted reaction pathway competes kinetically.

The energy diagram of Figure 5.8 shows a significant driving force for reductive quenching (500 meV) of **Ru*** by ground state **Org** (**Org** + **Ru*** → **Org**$^+$ + **Ru**^{red}) with a rate constant of k_{RQ}. To determine whether this nonbeneficial pathway was operative under normal cell conditions, a related oxidestructure was prepared, in which an insulating metal oxide,ZrO_2, was employed to create a ZrO_2|**Org**|Al_2O_3|**Ru** structure. The acceptor states of ZrO2are high in energy and precludeOrg*excited-state electron injection. In the absence of the excited-state injection, **Ru*** was indeed quenched by **Org** by reductive electron transfer to yield **Org**^{ox} that returned to ground-state products on a millisecond time scale.

In principle, this nonproductive rate constant k_{RQ} could be controlled through the driving force for electron transfer ($-\Delta G^o$), the reorganization energy (λ), or the electronic coupling (H_{AB}) between the two sensitizers. Increasing the thickness of the Al_2O_3 overlayer was expected to impact both H_{AB} and λ. A decrease in H_{AB} was expected due to the larger distance between the **Org** and **Ru** sensitizers. An increase reorganization energy was anticipated as the insulating overlayer inhibits solvents and ion motion. Varying the thickness of the insulating layer did in fact have a dramatic impact on the yield of reductive quenching. In anodes with thin insulating layers (5.5 and 11 Å), both **Org**^{ox} and **Ru**^{red} were observed transiently. However, the concentration of products from the reductive quenching reaction were significantly less with 11 Å of Al_2O_3 as opposed to 5.5 Å. At shell thicknesses of 16.5 and 22 Å, the magnitude of reductive quenching plateaued, with only a small concentration of **Org**$^+$ being resolved. In future research, it will be of interest to examine whether the thicker Al_2O_3 overlayers also inhibit the desired **Ru*** + **Org**^{ox} -→ **Ru**^{ox} + **Org** reaction. The use of alternative sensitizers, particularly a weaker oxidant as the inner-

sensitizer, would lower the reaction free energy change resulting in enhanced bromide photo-oxidation efficiency.

5.5 Conclusions

The photogeneration of the strong oxidant Br_2 has been achieved at a metal oxide/ electrolyte interface through the use of a dual-sensitizer photoanode design. The scope of dye-sensitized bromide oxidation has been extended from organic solvents and strongly acidic solutions to mildly acidic aqueous conditions (pH 5.6) where the kinetics for water oxidation catalysis are more ideal. The use of two sensitizers in an artificial z-scheme approach was found to simplify several of the challenges associated with photocatalytic bromide oxidation. First, the inclusion of two sensitizers allowed the properties of each to be tuned for its specific task ensuring near unity injection and large rate constants for bromide oxidation. This removed the necessity of finding a single sensitizer that was best able to balance these parameters. Second, the use of Br^- as a redox mediator ($E^o(Br^{-/\bullet}) = 1.92$ V vs. NHE) allows favorable disproportionation and equilibrium chemistry to be exploited, as the oxidized mediator ($Br^\bullet$) is known to yield Br_2 in bromide-containing acidic aqueous and organic solutions. The disadvantage of this strategy is that two photons are required to generate an injected electron and a Br instead of one. This stands in contrast to prior approaches that utilized a single chromophore, where it was necessary to balance the ground- and excited-state redox potentials so that both electron injection and bromide oxidation could be achieved.

This dual-sensitizer photoanode is ripe for further investigations. The modular design of the anode allows sensitizers to be chosen that have complimentary absorption spectra, such that more significant portions of the solar spectrum can be harvested. Optimization of intermolecular energy transfer and hole-hopping to enhance encounters between **Ru*** and $\mathbf{Org^{ox}}$ provide a rational

means to improve efficiency. The mechanistic study here reveals that efficient bromide oxidation requires an inner-sensitizer that is a weaker oxidant so as to prevent unwanted reduction of the outer sensitizer excited state. Dye-sensitized bromide oxidation to yield a $Br^{\bullet}$ atom undergoes a disproportionation like reaction that yields Br_2 that is a known redox mediator for water oxidation. Hence single photon one-electron transfer oxidations can drive the demanding multi-electron and multi-proton oxidation of water.

5.6 Supporting Information

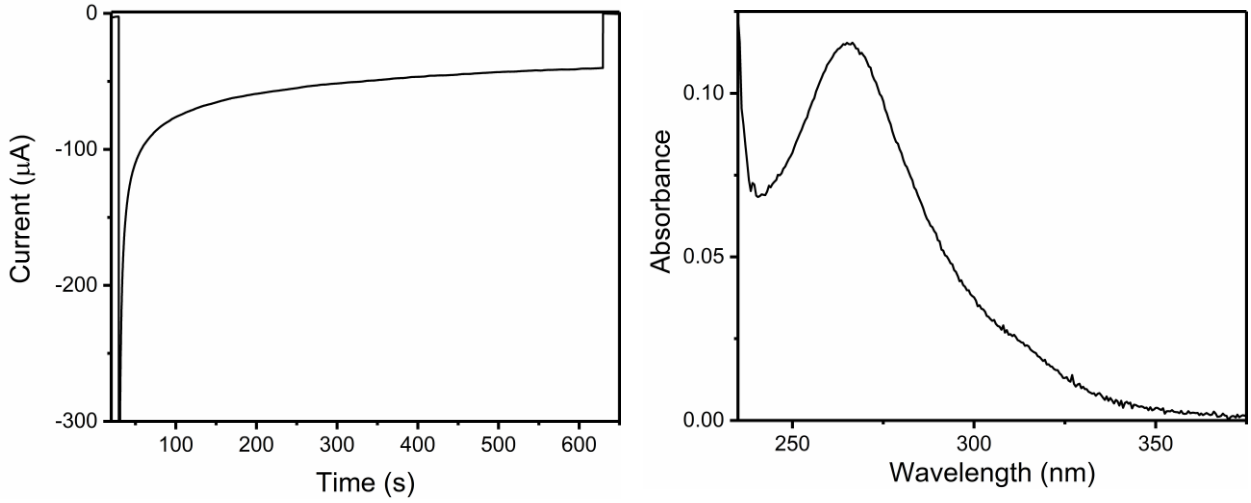

Figure S5.1: (Left) Photocurrent response with 460 nm illumination of CS|Org|Al_2O_3|Ru with a 500 mV applied potential. (Right) Absorption spectrum of the resultant solution, showing the absorption of Br_3^-. The Faradaic efficiency (14%) was calculated as 2 x the moles of product (Br_2 and Br_3^-) divided by the integrated number of electrons times 100%.

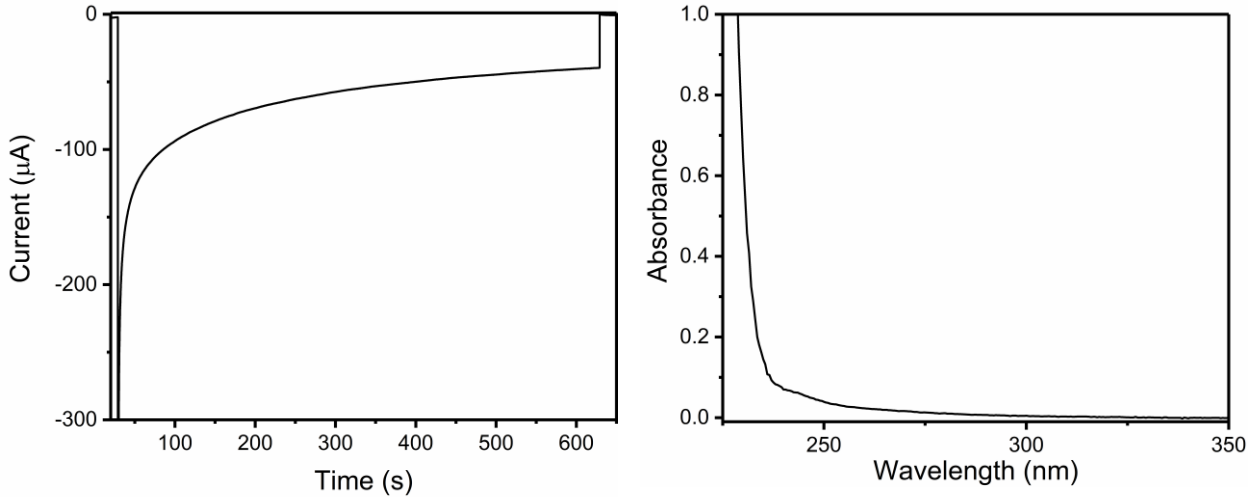

Figure S5.2: (Left) Photocurrent response with 460 nm illumination of CS|Org with a 500 mV applied potential. (Right) Absorption spectrum of the resultant solution, showing no evidence for oxidized Br^- products.

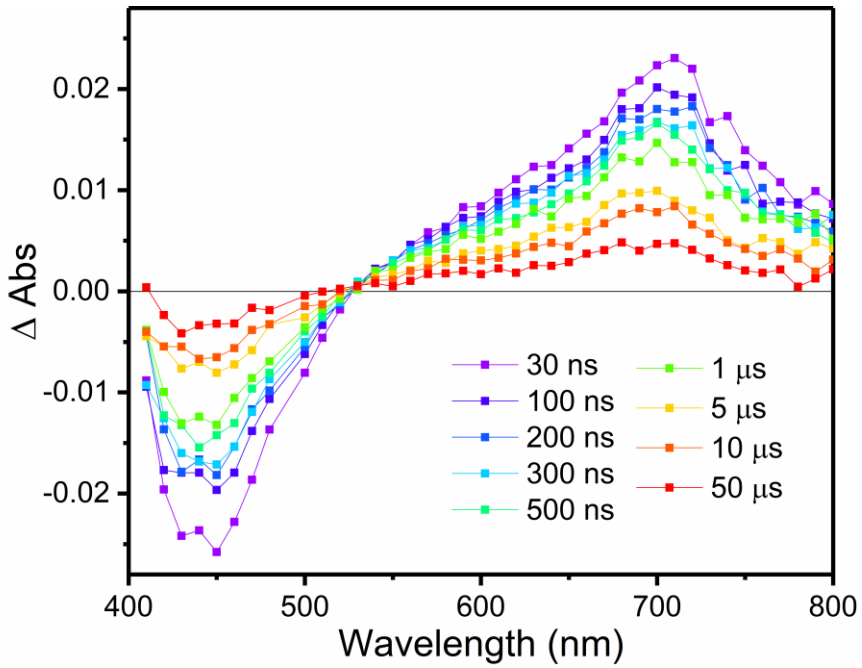

Figure S5.3: Transient absorption spectrum of CS|Org with 488 nm laser-pulse excitation in 0.2 M acetate buffer solution (pH 3.9). The laser power was attenuated to ~2 mJ/pulse. The positive signal centered at 700 nm was used as a spectroscopic handle to monitor the formation and decay of Org^{ox}.

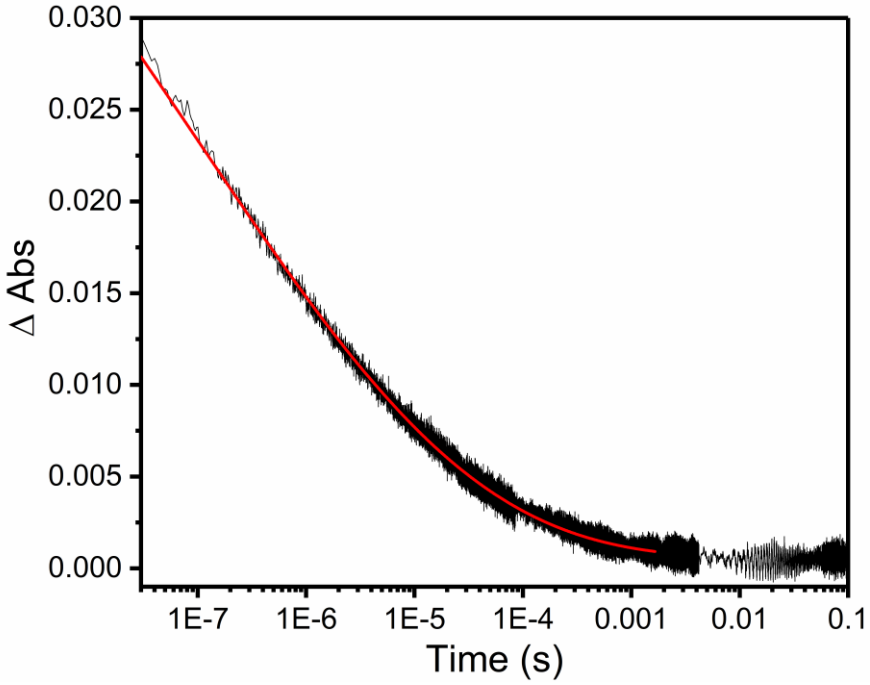

Figure S5.4: Transient absorption kinetics (black) with overlaid KWW fit (red) monitored at 700 nm and attributed to $CS(e^-)|Org^{ox} \rightarrow CS|Org$ interfacial electron transfer. The average rate constant for back-electron transfer (k_{BET}) extracted from the fit was 5×10^2 s^{-1}.

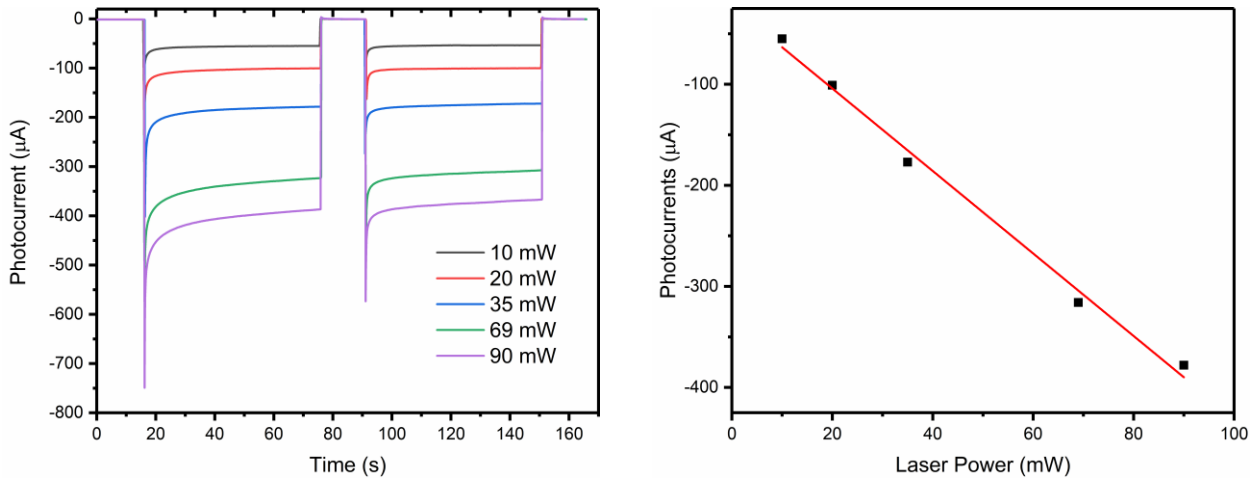

Figure S5.5: (Left) Light on/ off photocurrent response of the CS|Org|Al_2O_3|Ru anode in a three-electrode H-cell with 460 nm illumination at various laser power intensities. The photoanode (working electrode, surface area = 1.13 cm^2) and reference electrode (Ag/AgCl 4 M KCl, externally referenced to SCE) were placed in the illuminated half-cell, while a platinum mesh counter electrode was housed in the dark half-cell. The photocurrent responses were measured with a 0.5 V vs. NHE applied potential in 0.2 M acetate buffer (pH 3.9) and 0.3 M NaBr. (Right) Photocurrent response versus the laser power intensity.

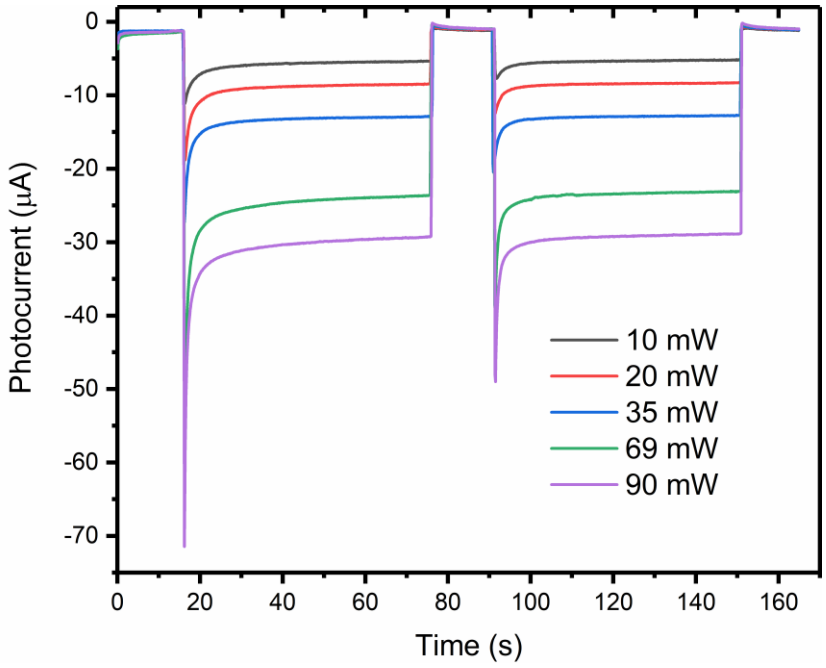

Figure S5.6: Light on/ off photocurrent response of the CS|Org|Al_2O_3|Ru anode in a three-electrode H-cell with 532 nm illumination. The photoanode (working electrode, surface area = 1.13 cm^2) and reference electrode (Ag/AgCl 4 M KCl, externally referenced to SCE) were placed in the illuminated half-cell, while a platinum mesh counter electrode was housed in the dark half-cell. The photocurrent responses were measured with a 0.5 V vs. NHE applied potential in 0.2 M acetate buffer (pH 3.9) and 0.3 M NaBr.

Table S5.1: Data used to calculate IPCE and APCE[a]

	460 nm	532 nm
Photcurrent (μA)	0.038	0.003
Absorptance at λ_{ex}	0.85	0.57
IPCE	1.2%	0.08%
APCE	1.4%	0.13%

[a]The surface area of the films was 1.13 cm^2

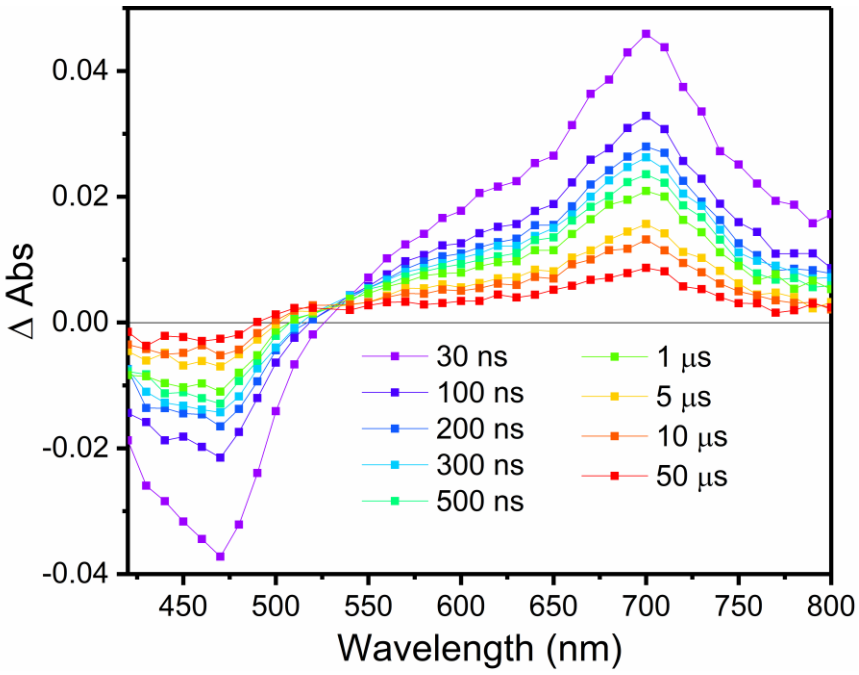

Figure S5.7: Transient absorption spectrum of TiO_2|Org|Al_2O_3|Ru with 532 nm laser-pulse excitation in 0.2 M acetate buffer solution (pH 3.9). The laser power was attenuated to ~6 mJ/pulse. The positive signal at 500 nm was attributed to the formation of the reduced complex Ru^{red}

REFERENCES

(1) Brennaman, M. K.; Dillon, R. J.; Alibabaei, L.; Gish, M. K.; Dares, C. J.; Ashford, D. L.; House, R. L.; Meyer, G. J.; Papanikolas, J. M.; Meyer, T. J. Finding the Way to Solar Fuels with Dye-Sensitized Photoelectrosynthesis Cells. *J. Am. Chem. Soc.* **2016**, *138*, 13085–13102.

(2) Song, W.; Chen, Z.; Brennaman, M. K.; Concepcion, J. J.; Patrocinio, A. O. T.; Iha, N. Y. M.; Meyer, T. J. Making solar fuels by artificial photosynthesis. *Pure Appl. Chem.* **2011**, *83*, 749–768.

(3) Ashford, D. L.; Gish, M. K.; Vannucci, A. K.; Brennaman, M. K.; Templeton, J. L.; Papanikolas, J. M.; Meyer, T. J. Molecular Chromophore−Catalyst Assemblies for Solar Fuel Applications. *Chem. Rev.* **2015**, *115*, 13006–13049.

(4) Alibabaei, L.; Luo, H.; House, R. L.; Hoertz, P. G.; Lopez, R.; Meyer, T. J. Applications of metal oxide materials in dye sensitized photoelectrosynthesis cells for making solar fuels: let the molecules do the work. *J. Mater. Chem. A* **2013**, *1*, 4133–4145.

(5) Youngblood, W. J.; Lee, S.-H. A.; Maeda, K.; Mallouk, T. E. Visible Light Water Splitting Using Dye- Sensitized Oxide Semiconductors. *Acc. Chem. Res.* **2009**, *42* (12), 1966–1973.

(6) Swierk, J. R.; Mallouk, T. E. Design and development of photoanodes for water-splitting dye-sensitized photoelectrochemical cells. *Chem. Soc. Rev.* **2013**, *42*, 2357–2387.

(7) Xu, P.; McCool, N. S.; Mallouk, T. E. Water splitting dye-sensitized solar cells. *Nano Today* **2017**, *14*, 42–58.

(8) Young, K. J.; Martini, L. A.; Milot, R. L.; Snoeberger III, R. C.; Batista, V. S.; Schmuttenmaer, C. A.; Crabtree, R. H.; Brudvig, G. W. Light-driven water oxidation for solar fuels. *Coord. Chem. Rev.* **2012**, *256*, 2503–2520.

(9) Berardi, S.; Drouet, S.; Francas, L.; Gimbert-Surinach, C.; Guttentag, M.; Richmond, C.; Stoll, T.; Llobet, A. Molecular artificial photosynthesis. *Chem. Soc. Rev.* **2014**, *43*, 7501–7519.

(10) Yu, Z.; Sun, L. Recent advances in dye-sensitized photoelectrochemical cells for solar hydrogen production based on molecular components. *Energy Environ. Sci.* **2015**, *8*, 760–775.

(11) Youngblood, W. J.; Lee, S.-H. A.; Kobayashi, Y.; Hernandez-Pagan, E. A.; Hoertz, P. G.; Moore, T. A.; Moore, A. L.; Gust, D.; Mallouk, T. E. Photoassisted Overall Water Splitting in a Visible Light-Absorbing Dye-Sensitized Photoelectrochemical Cell. *J. Am. Chem. Soc.* **2009**, *131*, 926–927.

(12) Zhao, Y.; Swierk, J. R.; Megiatto, J. D.; Sherman, B.; Youngblood, W. J.; Qin, D.; Lentz,

D. M.; Moore, A. L.; Moore, T. A.; Gust, D.; Mallouk, T. E. Improving the efficiency of water splitting in dye-sensitized solar cells by using a biomimetic electron transfer mediator. *Proc. Natl. Acad. Sci. U. S. A.* **2012**, *109* (39), 15612–15616.

(13) Alibabaei, L.; Brennaman, M. K.; Norris, M. R.; Kalanyan, B.; Song, W.; Losego, M. D.; Concepcion, J. J.; Binstead, R. A.; Parsons, G. N.; Meyer, T. J. Solar water splitting in a molecular photoelectrochemical cell. *Proc. Natl. Acad. Sci. U. S. A.* **2013**, *110*, 20008–20013.

(14) Alibabaei, L.; Sherman, B. D.; Norris, M. R.; Brennaman, M. K.; Meyer, T. J. Visible photoelectrochemical water splitting into H_2 and O_2 in a dye-sensitized photoelectrosynthesis cell. *Proc. Natl. Acad. Sci. U. S. A.* **2015**, *112*, 5899–5902.

(15) Sherman, B. D.; Ashford, D. L.; Lapides, A. M.; Sheridan, M. V; Wee, K. R.; Meyer, T. J. Light-Driven Water Splitting with a Molecular Electroassembly-Based Core/Shell Photoanode. *J. Phys. Chem. Lett.* **2015**, *6*, 3213–3217.

(16) Moore, G. F.; Blakemore, J. D.; Milot, R. L.; Hull, J. F.; Song, H.; Cai, L.; Schmuttenmaer, C. A.; Crabtree, R. H.; Brudvig, G. W. A visible light water-splitting cell with a photoanode formed by codeposition of a high-potential porphyrin and an iridium water-oxidation catalyst. *Energy Environ. Sci.* **2011**, *4*, 2389–2392.

(17) Yamamoto, M.; Wang, L.; Li, F.; Fukushima, T.; Tanaka, K.; Sun, L.; Imahori, H. Visible light-driven water oxidation using a covalently-linked molecular catalyst–sensitizer dyad assembled on a TiO_2 electrode. *Chem. Sci.* **2016**, *7*, 1430–1439.

(18) Sherman, B. D.; Xie, Y.; Sheridan, M. V; Wang, D.; Shaffer, D. W.; Meyer, T. J.; Concepcion, J. J. Light-Driven Water Splitting by a Covalently Linked Ruthenium-Based Chromophore− Catalyst Assembly. *ACS Energy Lett.* **2017**, *2*, 124–128.

(19) Swierk, J. R.; McCool, N. S.; Saunders, T. P.; Barber, G. D.; Strayer, M. E.; Vargas-Barbosa, N. M.; Mallouk, T. E. Photovoltage Effects of Sintered IrO_2 Nanoparticle Catalysts in Water-Splitting Dye-Sensitized Photoelectrochemical Cells. *J. Phys. Chem. C* **2014**, *118*, 17046–17053.

(20) Swierk, J. R.; Méndez-Hernádez, D. D.; McCool, N. S.; Liddell, P.; Terazono, Y.; Pahk, I.; Tomlin, J. J.; Oster, N. V; Moore, T. A.; Moore, A. L.; Gust, D.; Mallouk, T. E. Metal-free organic sensitizers for use in water-splitting dye-sensitized photoelectrochemical cells. *Proc. Natl. Acad. Sci. U. S. A.* **2015**, *112* (6), 1681–1686.

(21) Li, L.; Duan, L.; Xu, Y.; Gorlov, M.; Hagfeldt, A.; Sun, L. A photoelectrochemical device for visible light driven water splitting by a molecular ruthenium catalyst assembled on dye-sensitized nanostructured TiO_2. *Chem. Commun.* **2010**, *46*, 7307–7309.

(22) Gao, Y.; Ding, X.; Liu, J.; Wang, L.; Lu, Z.; Li, L.; Sun, L. Visible Light Driven Water Splitting in a Molecular Device with Unprecedentedly High Photocurrent Density. *J. Am.*

Chem. Soc. **2013**, *135*, 4219–4222.

(23) Gao, Y.; Zhang, L.; Sun, L. Artificial photosynthesis – functional devices for light driven water splitting with photoactive anodes based on molecular catalysts. *Phys. Chem. Chem. Phys.* **2014**, *16*, 12008–12013.

(24) Zhang, L.; Gao, Y.; Ding, X.; Yu, Z.; Sun, L. High-Performance Photoelectrochemical Cells Based on a Binuclear Ruthenium Catalyst for Visible-Light-Driven Water Oxidation. *ChemSusChem* **2014**, *7*, 2801–2804.

(25) Ding, X.; Gao, Y.; Zhang, L.; Yu, Z.; Liu, J.; Sun, L. Visible Light-Driven Water Splitting in Photoelectrochemical Cells with Supramolecular Catalysts on Photoanodes. *ACS Catal.* **2014**, *4*, 2347–2350.

(26) Li, F.; Fan, K.; Xu, B.; Gabrielsson, E.; Daniel, Q.; Li, L.; Sun, L. Organic Dye-Sensitized Tandem Photoelectrochemical Cell for Light Driven Total Water Splitting. *J. Am. Chem. Soc.* **2015**, *137*, 9153–9159.

(27) Swierk, J. R.; McCool, N. S.; Saunders, T. P.; Barber, G. D.; Mallouk, T. E. Effects of Electron Trapping and Protonation on the Efficiency of Water-Splitting Dye-Sensitized Solar Cells. *J. Am. Chem. Soc.* **2014**, *136*, 10974–10982.

(28) McCool, N. S.; Swierk, J. R.; Nemes, C. T.; Saunders, T. P.; Schmuttenmaer, C. A.; Mallouk, T. E. Proton-Induced Trap States, Injection and Recombination Dynamics in Water-Splitting Dye-Sensitized Photoelectrochemical Cells. *ACS Appl. Mater. Interfaces* **2016**, *8*, 16727–16735.

(29) Song, W.; Brennaman, M. K.; Concepcion, J. J.; Jurss, J. W.; Hoertz, P. G.; Luo, H.; Chen, C.; Hanson, K.; Meyer, T. J. Interfacial Electron Transfer Dynamics for $[Ru(bpy)_2((4,4'\text{-}PO_3H_2)_2bpy)]^{2+}$ Sensitized TiO_2 in a Dye-Sensitized Photoelectrosynthesis Cell: Factors Influencing Efficiency and Dynamics. *J. Phys. Chem. C* **2011**, *115*, 7081–7091.

(30) Swierk, J. R.; McCool, N. S.; Mallouk, T. E. Dynamics of Electron Recombination and Transport in Water- Splitting Dye-Sensitized Photoanodes. *J. Phys. Chem. C* **2015**, *119*, 13858–13867.

(31) Lee, S.-H. A.; Zhao, Y.; Hernandez-Pagan, E. A.; Blasdel, L.; Youngblood, W. J.; Mallouk, T. E. Electron transfer kinetics in water splitting dye-sensitized solar cells based on core–shell oxide electrodes. *Faraday Discuss.* **2012**, *155*, 165–176.

(32) Wang, D.; Sampaio, R. N.; Troian-Gautier, L.; Marquard, S. L.; Farnum, B. H.; Sherman, B. D.; Sheridan, M. V; Dares, C. J.; Meyer, G. J.; Meyer, T. J. Molecular Photoelectrode for Water Oxidation Inspired by Photosystem II. *J. Am. Chem. Soc.* **2019**, *141*, 7926–7933.

(33) Wang, D.; Marquard, S. L.; Troian-Gautier, L.; Sheridan, M. V; Sherman, B. D.; Wang, Y.; Eberhart, M. S.; Farnum, B. H.; Dares, C. J.; Meyer, T. J. Interfacial Deposition of Ru(II)

Bipyridine-Dicarboxylate Complexes by Ligand Substitution for Applications in Water Oxidation Catalysis. *J. Am. Chem. Soc.* **2018**, *140*, 719–726.

(34) Wang, D.; Eberhart, M. S.; Sheridan, M. V; Hu, K.; Sherman, B. D.; Nayak, A.; Wang, Y.; Marquard, S. L.; Dares, C. J.; Meyer, T. J. Stabilized photoanodes for water oxidation by integration of organic dyes, water oxidation catalysts, and electron-transfer mediators. *Proc. Natl. Acad. Sci. U. S. A.* **2018**, *115*, 8523–8528.

(35) Sheridan, M. V; Wang, Y.; Wang, D.; Troian-Gautier, L.; Dares, C. J.; Sherman, B. D.; Meyer, T. J. Light-Driven Water Splitting MediatedbyPhotogenerated Bromine. *Angew. Chemie Int. Ed. English* **2018**, *57*, 3449–3453.

(36) Parent, A. R.; Crabtree, R. H.; Brudvig, G. W. Comparison of primary oxidants for water-oxidation catalysis. *Chem. Soc. Rev.* **2013**, *42*, 2247–2252.

(37) Brady, M. D.; Troian-Gautier, L.; Sampaio, R. N.; Motley, T. C.; Meyer, G. J. Optimization of Photocatalyst Excited- and Ground-State Reduction Potentials for Dye-Sensitized HBr Splitting. *ACS Appl. Mater. Interfaces* **2018**, *10*, 31312–31323.

(38) Heimer, T. A.; D`Arcangelis, S. T.; Farzad, F.; Stipkala, J. M.; Meyer, G. J. An Acetylacetonate-Based Semiconductor-Sensitizer Linkage. *Inorg. Chem.* **1996**, *35*, 5319–5324.

(39) Argazzi, R.; Bignozzi, C. A.; Heimer, T. A.; Castellano, F. N.; Meyer, G. J. Enhanced Spectral Sensitivity from Ruthenium(II) Polypyridyl Based Photovoltaic Devices. *Inorg. Chem.* **1994**, *33*, 5741–5749.

(40) Motley, T. C.; Brady, M. D.; Meyer, G. J. Influence of 4 and 4′ Substituents on $Ru^{III/II}$ Bipyridyl Self-Exchange Electron Transfer Across Nanocrystalline TiO_2 Surfaces. *J. Phys. Chem. C* **2018**, *122*, 19385–19394

(41) Eberhart, M. S.; Wang, D.; Sampaio, R. N.; Marquard, S. L.; Shan, B.; Brennaman, M. K.; Meyer, G. J.; Dares, C.; Meyer, T. J. Water Photo-oxidation Initiated by Surface-Bound Organic Chromophores. *J. Am. Chem. Soc.* **2017**, *139*, 16248–16255.

(42) Kuciauskas, D.; Monat, J. E.; Villahermosa, R.; Gray, H. B.; Lewis, N. S.; McCusker, J. K. Transient Absorption Spectroscopy of Ruthenium and Osmium Polypyridyl Complexes Adsorbed onto Nanocrystalline TiO_2 Photoelectrodes. *J. Phys. Chem. B* **2002**, *106*, 9347–9358.

(43) Listorti, A.; Regan, B. O.; Durrant, J. R. Electron Transfer Dynamics in Dye-Sensitized Solar Cells. *Chem. Mater.* **2011**, *23*, 3381–3399.

(44) Ardo, S.; Meyer, G. J. Direct Observation of Photodriven Intermolecular Hole Transfer across TiO_2 Nanocrystallites: Lateral Self-Exchange Reactions and Catalyst Oxidation. *J. Am. Chem. Soc.* **2010**, *132*, 9283–9285.

(45) Ardo, S.; Meyer, G. J. Characterization of Photoinduced Self-Exchange Reactions at Molecule–Semiconductor Interfaces by Transient Spectroscopy: Lateral Intermolecular Energy and Hole Transfer Polarization across Sensitized TiO_2 Thin Films. *J. Am. Chem. Soc.* **2011**, *133*, 15384–15396.

(46) Brady, M. D.; Troian-Gautier, L.; Motley, T. C.; Turlington, M. D.; Meyer, G. J. An Insulating Al_2O_3 Overlayer Prevents Lateral Hole Hopping Across Dye-Sensitized TiO_2 Surfaces. *ACS Appl. Mater. Interfaces* **2019**, *11*, 27453–27463.

(47) Higgins, G. T.; Bergeron, B. V; Hasselmann, G. M.; Farzad, F.; Meyer, G. J. Intermolecular Energy Transfer across Nanocrystalline Semiconductor Surfaces. *J. Phys. Chem. B* **2006**, *110*, 2598–2605.

(48) Brady, M. D.; Sampaio, R. N.; Wang, D.; Meyer, T. J.; Meyer, G. J. Dye-Sensitized Hydrobromic Acid Splitting for Hydrogen Solar Fuel Production. *J. Am. Chem. Soc.* **2017**, *139*, 15612–15615.

(49) Marton, A.; Clark, C. C.; Srinivasan, R.; Freundlich, R. E.; Narducci Sarjeant, A. A.; Meyer, G. J. Static and Dynamic Quenching of Ru(II) Polypyridyl Excited States by Iodide. *Inorg. Chem.* **2006**, *45*, 362–369.

(50) Troian-Gautier, L.; Beauvilliers, E. E.; Swords, W. B.; Meyer, G. J. Redox Active Ion-Paired Excited States Undergo Dynamic Electron Transfer. *J. Am. Chem. Soc* **2016**, *138*, 16815–16826.

(51) Wehlin, S. A. M.; Troian-Gautier, L.; Sampaio, R. N.; Marcélis, L.; Meyer, G. J. Ter-Ionic Complex that Forms a Bond Upon Visible Light Absorption. *J. Am. Chem. Soc.* **2018**, *140* (25), 7799–7802.

(52) Li, G.; Brady, M. D.; Meyer, G. J. Visible Light Driven Bromide Oxidation and Ligand Substitution Photochemistry of a Ru Diimine Complex. *J. Am. Chem. Soc.* **2018**, *140*, 5447-5456.

(53) Wardman, P. Reduction Potentials of One-Electron Couples Involving Free Radicals in Aqueous Solution. *J. Phys. Chem. Ref. Data* **1989**, *18*, 1637–1755.

(54) Tsai, K. Y.-D.; Chang, I.-J. Photocatalytic Oxidation of Bromide to Bromine. *Inorg. Chem.* **2017**, *56*, 693–696.

(55) Tsai, K. Y.-D.; Chang, I.-J. Oxidation of Bromide to Bromine by Ruthenium(II) Bipyridine-Type Complexes Using the Flash-Quench Technique. *Inorg. Chem.* **2017**, *56*, 8497–8503.

(56) Wang, Y.; Suzuki, H.; Xie, J.; Tomita, O.; Martin, D. J.; Higashi, M.; Kong, D.; Abe, R.; Tang, J. Mimicking Natural Photosynthesis: Solar to Renewable H_2 Fuel Synthesis by Z-Scheme Water Splitting Systems. *Chem. Rev.* **2018**, *118*, 5201–5241.

(57) Wang, Y.; Shang, X.; Shen, J.; Zhang, Z.; Wang, D.; Lin, J.; Wu, J. C. S.; Fu, X.; Wang, X.; Li, C. Direct and indirect Z-scheme heterostructure- coupled photosystem enabling cooperation of CO_2 reduction and H_2O oxidation. *Nat. Commun.* **2020**, *11*, 1–11.

(58) Ng, B.-J.; Putri, L. K.; Kong, X. Y.; Teh, Y. W.; Pasbakhsh, P.; Chai, S.-P. Z-Scheme Photocatalytic Systems for Solar Water Splitting. *Adv. Sci.* **2020**, *7*, 1903171.

(59) Maeda, K. Z-Scheme Water Splitting Using Two Different Semiconductor Photocatalysts. *ACS Catal.* **2013**, *3*, 1486–1503.

(60) Hara, S.; Yoshimizu, M.; Tanigawa, S.; Ni, L.; Ohtani, B.; Irie, H. Hydrogen and Oxygen Evolution Photocatalysts Synthesized from Strontium Titanate by Controlled Doping and Their Performance in Two-Step Overall Water Splitting under Visible Light. *J. Phys. Chem. C* **2012**, *116*, 17458–17463.

(61) Sekizawa, K.; Maeda, K.; Domen, K.; Koike, K.; Ishitani, O. Artificial Z-Scheme Constructed with a Supramolecular Metal Complex and Semiconductor for the Photocatalytic Reduction of CO_2. *J. Am. Chem. Soc.* **2013**, *135*, 4596–4599.

(62) Oshima, T.; Nishioka, S.; Kikuchi, Y.; Hirai, S.; Yanagisawa, K.; Eguchi, M.; Miseki, Y.; Yokoi, T.; Yui, T.; Kimoto, K.; Sayama, K.; Ishitani, O.; Mallouk, T. E.; Maeda, K. An Artificial Z-Scheme Constructed from Dye-Sensitized Metal Oxide Nanosheets for Visible Light-Driven Overall Water Splitting. *J. Am. Chem. Soc.* **2020**, *142*, 8412–8420.

(63) Hu, K.; Meyer, G. J. Lateral Intermolecular Self-Exchange Reactions for Hole and Energy Transport on Mesoporous Metal Oxide Thin Films. *Langmuir* **2015**, *31*, 11164–11178.

(64) Moia, D.; Vaissier, V.; López-Duarte, I.; Torres, T.; Nazeeruddin, M. K.; O`Regan, B. C.; Nelson, J.; Barnes, P. R. F. The reorganization energy of intermolecular hole hopping between dyes anchored to surfaces. *Chem. Sci.* **2014**, *5*, 281–290.

(65) Hanson, K.; Losego, M. D.; Kalanyan, B.; Ashford, D. L.; Parsons, G. N.; Meyer, T. J. Stabilization of $[Ru(bpy)_2(4,4'\text{-}(PO_3H_2)bpy)]^{2+}$ on Mesoporous TiO2 with Atomic Layer Deposition of Al_2O_3. *Chem. Mater.* **2013**, *25*, 3–5.